Characterising the evaporation histories of exoplanets using X-ray observations of their host stars

by

Jorge Fernández Fernández

Thesis

Submitted to the University of Warwick

for the degree of

Doctor of Philosophy

Department of Physics

March 2025

THE UNIVERSITY OF
WARWICK

Contents

List of Tables

List of Figures

Declarations

I declare the work presented in this thesis is my own. It has not been submitted to any other academic institution as part of any other degree or qualification. The research here presented was undertaken at the University of Warwick between October 2020 and July 2024, under the supervision of Prof. Peter Wheatley. I acknowledge that this thesis includes material from the following publications and contributions from co-authors:

- The work presented on Chapter 3 on the planetary system around the star K2-136 is based on the publication "The shared evaporation history of three sub-Neptunes spanning the radius-period valley of a hyades star", as published in MNRAS 522, 4251 (2023).

- Chapter 4, where I study X-ray irradiation on the hot Neptune LTT 9779 b, is based on the publication "Survival in the Neptune desert: LTT 9779 b kept its atmosphere thanks to an unusually X-ray faint host star", as published in MNRAS 527, 911 (2023).

- The introduction and methodology chapters make use of material from the two publications above.

- Prof. Peter Wheatley provided guidance and aided in the interpretation of results of Chapters 3 to 7.

- Additional co-authors provided feedback on the two publications listed above.

Additionally, I acknowledge that research in this thesis has made use of data from the following telescopes and catalogues:

- Chapters 5 & 7 made use of data from the European Space Agency (ESA) mission *Gaia* (`https://www.cosmos.esa.int/gaia`), processed by the *Gaia* Data Processing and Analysis Consortium (DPAC, `https://www.cosmos.esa.int/web/gaia/dpac/consortium`). Funding for the DPAC has been provided by national institutions, in particular the institutions participating in the *Gaia* Multilateral Agreement.
- Chapters 3 & 4 made use of the NASA Exoplanet Archive, which is operated by the California Institute of Technology, under contract with the National Aeronautics and Space Administration under the Exoplanet Exploration Program.
- Chapters 5 & 7 made use of data obtained from the 4XMM *XMM-Newton* serendipitous source catalogue compiled by the *XMM-Newton* Survey Science Centre consortium.
- The research presented in Chapters 3 to 7 was based on observations obtained with XMM-Newton, an ESA science mission with instruments and contributions directly funded by ESA Member States and NASA.

The work presented in this thesis was supported by UK Science and Technology Facilities (STFC).

Abstract

The discovery of the first extrasolar planet by Mayor and Queloz [1995] sparked a gold rush in the field of exoplanetology, with thousands of exoplanets uncovered in the three decades that followed. Many of these planets are only two to three times larger than Earth and orbit very closely to their host stars. As a result, they are strongly irradiated by high energy X-ray and EUV photons emitted from their host stars. The energy deposited by these photons in the upper atmospheres of these planets is thought to drive vigorous atmospheric escape that can fully remove their gaseous envelopes, sculpting exoplanet populations.

In my first published study, presented in Chapter 3, I used *XMM-Newton* observations to characterise the high energy environment of three planets which straddle the radius valley around the star K2-136, with a mini-Neptune (planet c) lying interior to a super-Earth (planet d). I simulated their evaporation histories and found that planet c held onto its gaseous atmosphere thanks to its higher mass. Similarly, in Chapter 6, I also investigate the evaporation histories of four mini-Neptunes around two young stars with *XMM-Newton*, TOI-451 and TOI-1098. I find the three outermost planets are likely to retain their gaseous atmospheres in the future, with their futures hinging on better constraints on their masses.

My second published work, presented in Chapter 4, concerns LTT 9779 b, the only hot Neptune deep in the Neptunian desert with a gaseous atmosphere. Its presence so close to its host G-type star (with a 19 h period) is puzzling, as the intense X-ray irradiation it receives should have already stripped it of its atmosphere. If the star was unusually X-ray faint, however, the planet might have been able to survive. In this chapter, I test out this hypothesis by characterising the coronal activity of the star using observations from *XMM-Newton*, which I find to be 15 times fainter than expected, allowing LTT 9779 b to survive to the present day.

The final two chapters focus on characterising stellar X-ray emission across the HR diagram. In Chapter 5 I study X-ray emission in the Pleiades open cluster, placing cluster stars in context with their spin periods. After accounting for binaries, I determine that the X-ray activities of FGK stars to be 2–3 times fainter than predicted by X-ray evolution models. Lastly, in Chapter 7, I study the stellar content of the *4XMM* catalogue using Gaia, and characterise the X-ray variability of single FGKM stars across 25 years of *XMM-Newton* observations. I find that FGK stars vary in the X-rays half as much as M-dwarfs, and thus the scatter induced by their variability cannot fully account for the spread seen in rotation-activity relations.

Abbreviations

NUV	Near Ultraviolet
FUV	Far Ultraviolet
UV	Ultraviolet
EUV	Extreme Ultraviolet
XUV	X-ray and Extreme Ultraviolet
Lyα	Lyman-α
TESS	Transiting Exoplanet Survey Satellite
HST	Hubble Space Telescope
XMM	X-ray Multi-Mirror Mission
EPIC	European Photon Imaging Camera
CCD	Charge-Coupled Device
ISM	Interstellar Medium
ENA	Energetic Neutral Atom
SED	Spectral Energy Distribution
APEC	Astrophysical Plasma Emission Code
TBABS	Tuebingen-Boulder ISM Absorption Model
SAS	Science Analysis System
RV	Radial Velocity
TTV	Transit timing variation
TOI	TESS Object of Interest
HJ	Hot Jupiter
USP	Ultra-Short Period
RLO	Roche Lobe Overflow
$\mathrm{M_E}$	Earth mass
$\mathrm{R_E}$	Earth radius
$\mathrm{M_J}$	Jupiter mass
$\mathrm{R_J}$	Jupiter radius
$\mathrm{M}_\odot$	Solar mass
$\mathrm{R}_\odot$	Solar radius

Chapter 1

Introduction

> There are then innumerable suns, and an infinite number of earths revolve around those suns, just as the seven we can observe revolve around this sun which is close to us.
>
> Giordano Bruno (1584), *De l'infinito, universo et mondi*

The study of stars and planets in the night sky has been present in every human civilisation since the Bronze age, possibly much earlier. The so-called "wandering stars" from antiquity were only recognised, together with Earth, as solid spherical bodies orbiting the Sun by the action of gravitation during the scientific revolution some 300 years ago. In the period that followed, this view was applied to other stars, which were also recognised as far away Suns possibly with their own planets too, making the Solar System only one tiny part of a considerably broader and possibly infinite Universe.

It was only 30 years ago that a planet beyond our Solar System was first detected, 51 Pegasi b, by Mayor and Queloz [1995]. Since then, the number of new planet discoveries has been growing rapidly with the launch of new observatories tasked with finding them (particularly *Kepler* and *TESS*). These faraway worlds would later be known as extrasolar planets, or simply exoplanets.

These observatories have uncovered a great diversity in planet sizes and system architectures with no analogue in our own Solar System. These include exotic planetary systems around stellar remnants such as white dwarfs and neutron stars [e.g. PSR 1257+12 bcd, Wolszczan and Frail, 1992] and circumbinary planets orbiting two stars at the same time [e.g. TOI-1338, Kostov et al., 2020]; as well as large populations of massive gas giants orbiting extremely close to their stars [hot Jupiters, e.g. 51 Pegasi b, Mayor and Queloz, 1995] and a surprisingly large number of small worlds between Earth and Neptune in size [e.g. NGTS-4 b, West et al., 2019] with no counterpart in our own Solar System. Some of these worlds belong to multi-planet systems of up to 6-8 constituents tightly packed within a fraction of an astronomical unit (au), the separation between Earth and the Sun. Many of these small worlds also orbit extremely close to their stars, with orbital periods below 30 days, well within the orbit of Mercury around the Sun. In part, the prevalence of such worlds in the observed populations of exoplanets is due to the biases of our own methods, which are amenable to short-period planets.

These planets have also sparked an interest in studying their evolution under the influence of the high stellar radiation they are expected to receive, particularly since many also have low densities consistent with large gaseous atmospheres and are hence vulnerable to evaporation/atmospheric escape. Such themes constitute the central thesis of this work, where I discuss our current knowledge of planet populations, the processes that shape them (particularly atmospheric escape), and how stellar radiation fits into this picture.

1.1 Exoplanet detection methods

In this section, I introduce some of the methods used to find extrasolar planets as well as their performance and sensitivity in planet radius-mass-period parameter space. I pay particular attention to the transit and radial velocity methods, which have been by far the most successful, and were responsible for the discovery and characterisation of the planetary systems I studied in this thesis (K2-136 bcd in Chapter 3, LTT 9779 b in Chapter 4, and TOI-451 bcd and TOI-1908 b in Chapter 6). I also briefly discuss some additional detection methods, namely direct imaging, microlensing, and transit timing variations, and how they compliment the transit and radial velocity methods.

1.1.1 Transit method

The presence of a planet can be inferred from the periodic dips it produces in the brightness of its host star as it orbits in front of it when viewed edge-on, during a so-called *transit*. These transits will occur at regular intervals that match the orbital period of the planet. The fraction of starlight blocked by a planet as it transits is given by the ratio of the cross-sectional areas of the planet and the star, the transit depth δ, expressed as:

$$\delta = \frac{\Delta F}{F_*} = \frac{R_\mathrm{p}^2}{R_*^2}, \tag{1.1}$$

where F_* is the flux from the star, ΔF is the change in flux during a transit, R_p is the radius of the planet, and R_* is the radius of the star. Since the transit method provides observational constraints on the quantity R_p/R_*, knowledge of the stellar radius allows the planet radius to be determined. A Jupiter-sized planet ($1\,\mathrm{R_J}$) around a Sun-like star will produce a transit depth of 1%, whilst an Earth-sized planet ($1\,\mathrm{R_E}$or $0.09\,\mathrm{R_J}$) will produce a much shallower transit depth of 0.008%, 120 times lower. We can immediately infer that detecting transits of Earth-like planets requires much greater precision than larger planets.

Transit depth is also unaffected by the separation between the star and the planet, as star systems are distant enough from Earth that the effects of perspective become negligible. Two identical planets transiting the same star, one at an orbital separation of 0.1 au and another at 10 au, will produce the same transit depth. The outer planet, though, has a much longer orbital period and thus will transit much more infrequently, every 31 years, compared to just 11 days for the inner planet. Consequently, detecting transiting planets in wide orbits will require longer observing periods.

Moreover, in order for a planet to transit, its orbit must lie edge-on relative to an observer on Earth, such that the planet crosses the stellar disc when it transits, producing a dip in its brightness. If orbital inclinations are randomly distributed, transiting planets make up only a tiny fraction of all planets. This also implies that planets that are further out are much less likely to be seen transiting, as their orbits must be more precisely edge-on. Planets orbiting larger stars are also more likely to transit, since the larger area of the star will cover a greater range of orbital inclinations, although their transits will also be shallower for the same reason.

The transit method therefore lends itself towards large planets that orbit close to their stars as well as edge-on relative to Earth. Indeed, the first population of planets discovered with the transit method were Jupiter-sized worlds ($> 0.7\,\mathrm{R_J}$) at short orbital periods [$<$ 10 d, e.g. Wright et al., 2012]. These so-called hot Jupiters were named as such due to the high equilibrium temperatures they endure as a result of their short separations.

Transit surveys are carried out by monitoring a patch of the sky for a certain amount of time. Stars in that patch are then identified and their lightcurves are searched for transits. The choice of observing period, however, will limit the populations of planets that can be characterised. Since at least two transits are required to determine the orbital period of a planet, the survey will be limited to orbital periods shorter than half the observing window. For longer orbital periods that are still within the observing window, a planet may transit only once, which provides constraints on its radius but not on its orbital period.

For orbits longer than the observing window, however, a transit is not guaranteed. For instance, the Transiting Exoplanet Survey Satellite (*TESS*) surveys regions of the sky 24° × 96° in size, known as *sectors*, continuously for 27 days at a time [Ricker et al., 2015] in search of planetary transits. Within this observing window, a planet with an orbit of 54 days will thus have a 50% chance of transiting, and for a 1 year orbit, like Earth, this falls to only 7%.

Additionally, reaching down to the smallest Earth-sized planets requires targeting bright stars with highly precise photometers, which are able to pick up very shallow transits, as well as mitigating the effects of stellar activity, which may drown the planetary signal [Barros et al., 2020].

Stellar activity presents itself in lightcurves as photometric variability, which can be inducted by several phenomena, such as rotation, oscillations, and granulation, which induce variability in different timescales and amplitudes. Stellar rotation causes active regions and features in the stellar surface to move in and out of view, inducing variability with amplitudes of up to 1000 ppm and timescales matching the stellar rotation period [Lagrange et al., 2010b], which range between a day for young stars to more than a hundred days for old stars. P-mode oscillations are standing waves within stellar interiors generated by convection which cause regions in the surface to rise and sink, inducing variability with amplitudes of tens of ppm and timescales of a few minutes [Kjeldsen and Bedding, 1995; Kallinger et al., 2014]. Finally, granulation is caused by convective cells rising to the stellar surface as bright patches, then cooling down and sinking into dark edges, which result in signals with amplitudes of up to a hundred ppm and timescales of tens of minutes to days [Kallinger et al., 2014; Meunier et al., 2015].

These phenomena are similar in period and amplitude to the transit signals of small exoplanets, which produce transit depths of tens to hundreds of ppm with transit durations of hours and ingress/egress timescales of minutes. Whilst variability originated in rotation is quasi-periodic and much longer than transit timescales, granulation is stochastic and thus much harder to predict. Several statistical and numerical methods, namely Gaussian process (GP) regression, have proven successful in mitigating stellar variability in order to accurately recover planetary parameters [e.g. Haywood et al., 2014; Faria et al., 2016; Barros et al., 2020].

Despite this, transit surveys have been the most prolific of all discovery methods by far at uncovering extrasolar planets – 75% of all confirmed planets to date have been discovered with the transit method, as per the NASA Exoplanet Archive[1]. Since transit surveys only require optical photometry, these can be carried out with both space-based and ground-based photometric monitoring, which are able to target a large number of stars simultaneously. Ground-based observatories benefit from large mirrors and extended collecting areas, whilst space-based observatories, despite their smaller sizes, circumvent the adverse effects of weather and optical distortion caused by Earth's atmosphere and, depending on the orbit of the spacecraft, can benefit from uninterrupted monitoring of the sky.

Amongst ground-based surveys targeting transiting exoplanets, SuperWASP [Pollacco et al., 2006] and HAT/HAT-South [Bakos et al., 2004] have been the most productive, particularly with hot Jupiters (e.g. WASP-193 b, Barkaoui et al. 2024; HAT-P-7 b, Pál et al. 2008), but also Neptune-sized planets (e.g. HAT-P-11 b, Bakos et al. 2010; WASP-156 b, Demangeon et al. 2018).

Other surveys such as *OGLE* [Udalski et al., 1992], *TrES* [Alonso et al., 2004], *KELT* [Pepper et al., 2004], *MEarth* [Irwin et al., 2009b], and *NGTS* [Wheatley et al., 2018], have also achieved success, with discoveries such as the hot Neptune NGTS-4 b [West et al., 2019] and the the ultra-hot Jupiter KELT-9 b [Gaudi et al., 2017].

The first space-based observatory dedicated to planet discovery via the transit method was *CoRoT* [Auvergne et al., 2009], which operated between 2007 and 2012. The mission uncovered close to 100 planet candidates, mostly Saturn to Jupiter sized ($> 0.7\,\mathrm{R_J}$), although a number of small planets were also found, including CoRoT-7 b, the first terrestrial planet to be discovered [Léger et al., 2009]. This mission was succeeded by *Kepler*, which operated between 2009 and 2015 and monitored a region of the sky $115\,\mathrm{deg}^2$ in size continuously, targeting stars as faint as $V = 16$. Kepler carried out by far the most prolific transit survey to date, uncovering more than 2700 confirmed planets. Among these planets, it discovered a new population of worlds between Earth and Neptune in size, the

---

[1] The NASA Exoplanet Archive is accessible via `https://exoplanetarchive.ipac.caltech.edu/`

so-called super-Earths and sub-Neptunes, including features in their populations , namely the *radius valley* [Fulton et al., 2017] and the *Neptunian desert* [Szabó and Kiss, 2011], which I examine further in depth in Sections 1.2.1 & 1.2.2, respectively. After failure of two of its reaction wheels, Kepler was repurposed into the K2 mission [Howell et al., 2014], which continued transit searches until 2018, when its fuel was exhausted. In Chapter 3, I explore the evaporation history of the planets K2-136 bcd, which were originally discovered with K2.

Kepler was succeeded by the Transiting Exoplanet Survey Satellite [*TESS*, Ricker et al., 2015], launched in 2018 and is still operational to this day. It targets brighter stars than *Kepler*, with $V < 16$, throughout most of the sky, observing large sectors of $24° \times 96°$ deg continuously for 27 days at a time. Since some of the sectors overlap, some regions of the sky benefit from a greater coverage, in some cases up to a year. So far, *TESS* has uncovered 7200 planet candidates, 480 of which have been confirmed.

Since both telescopes make use of the transit method, they are both most amenable to large short-period planets. Their observing strategies, however, differ somewhat, influencing the populations of planets they are sensitive to. *Kepler*, given its greater photometric precision, was able to uncover a larger fraction of Earth-sized planets, and it's strategy of continuously observing one region of the sky allowed it to uncover more long-period planets. *Kepler*, however, was limited to only 0.25% of the sky. *TESS*, on the other hand, despite its lower sensitivity and short observing window per sector, has the flexibility of an all-sky survey, which has allowed it to seek a wider diversity of targets, particularly young stars.

In Chapters 4 & 6, I study atmospheric escape from the planets LTT 9779 b as well as TOI-451 bcd and TOI-1098 b, all of which were discovered with *TESS*.

Regarding the future of the field, *PLATO* [Rauer et al., 2014], with an expanded field of view of 2250 deg^2, will target brighter stars with the objective of measuring planetary radii with unprecedented accuracy, reaching down to Earth-sized planets in the habitable zones of their stars. *PLATO* is predicted to achieve uncertainties in planet radii below 3% by characterising their stars with asteroseismology.

1.1.2 Radial velocity method

In a binary system, the two bodies orbit around their common centre of mass with the same orbital period. This holds true even for planetary systems, where one of the bodies (the star) is much more massive than the other (the planet). Their orbital speeds, however, will differ greatly. For instance, in the Earth-Sun system, Earth has an orbital speed of $30\,\mathrm{km\,s^{-1}}$ whereas the motion induced by Earth in the Sun is only around $0.1\,\mathrm{m\ s^{-1}}$. A hot Jupiter, on the other hand, will induce a much stronger motion on its star of 20–$50\,\mathrm{m\,s^{-1}}$. The radial velocity (RV) technique infers the presence of a planet orbiting a star by measuring the motion of the star as induced by its planetary companion. These radial velocities can be measured by detecting the Doppler effect that this orbital motion creates in the spectrum of the star, where emission lines are blueshifted when the star moves towards the observer and redshifted when it moves away from it. The radial velocity method has been responsible for $\sim$1090 discoveries to date, over 25% of all confirmed planets as per the NASA Exoplanet Archive, including the first exoplanet to be discovered, 51 Pegasi b [Mayor and Queloz, 1995].

RV observations are carried out by ground-based spectrographs that measure stellar spectra over long timescales to capture the shift in wavelength of spectral lines. The resulting spectra must then be corrected for telluric contamination from Earth's atmosphere (using comparison stars with known spectra) and for stellar activity signals caused by granulation, rotation, and oscillations (using, for instance, Gaussian process regression). Then, a cross-correlation function is used on each spectrum to search for the peak wavelengths of several spectral lines, and the offsets from their expected rest frame wavelengths are calculated, which then reveal a radial velocity curve.

The semi-amplitude of this curve K_1 can be used to calculate the minimum mass $M_\mathrm{p}\sin i$, which requires knowledge of the orbital inclination i relative to the line of sight to calculate the true planet mass M_p. The inclination can be obtained from follow-up observations with the transit or astrometry methods. As for the orbital period of the planet, this is equivalent to the period of the RV curve.

More massive planets will produce stronger radial velocity signals and planets in shorter orbits require a shorter temporal baseline to detect. Therefore, this method is more sensitive to massive planets in close-in orbits, akin to the transit method. Although, unlike the transit method, RV signals can still be detected even if the planet does not orbit along the line of sight.

Radial velocity surveys include high-resolution spectrographs such as *CORALIE* [Queloz et al., 2000], *ELODIE* [Baranne et al., 1996], *HIRES* [Vogt et al., 1994], *HARPS/HARPS-N* [Mayor et al., 2003], *CARMENES* [Quirrenbach et al., 2014], and more recently *ESPRESSO* [Pepe et al., 2021], among others.

Mayor and Queloz [1995] discovered the first exoplanet around a Sun-like star, the hot Jupiter 51 Pegasi b, using radial velocity observations from *ELODIE*. The spectrograph had a precision of $7\ \mathrm{m\,s^{-1}}$, which readily detected the planetary signal of $56\,\mathrm{m\,s^{-1}}$. Newer spectrographs aim to improve their precision in order to reach the less massive Earth-like planets, which produce signals of only a few tens of $\mathrm{cm\,s^{-1}}$. *HARPS* has achieved a precision of $1\,\mathrm{m\,s^{-1}}$, and the newer *ESPRESSO* can reach down to $25\,\mathrm{cm\,s^{-1}}$. In this regime, stellar variability becomes the limiting factor for the precision of RV measurements, inducing RV signals of $\geq 50\,\mathrm{cm\,s^{-1}}$ that cannot be easily mitigated [see Hara and Ford, 2023, and references within].

Stellar variability in radial velocity measurements is primarily originated in granulation, p-mode oscillations, and rotation (spots and faculae). These phenomena induce motion in the stellar plasma, which in turn redshift or blueshift light directed towards the observer. The amplitudes and frequencies of the radial velocity signals created by these phenomena strongly depend on the magnetic activity level of the star, ranging from tens of $\mathrm{cm\,s^{-1}}$ to several $\mathrm{m}\,s^{-1}$ Cegla et al. [2019]; Hara and Ford [2023]. Granulation induces a net blueshift as the rising convective cells are larger and brighter than the darker gaps between the cells where plasma sinks back into the star. These stochastic fluctuations are correlated to timescales of minutes to hours. P-mode oscillations are produced by standing pressure waves within stellar interiors of Sun-like stars, which induce radial velocity variations in timescales of 5 to 10 minutes. Finally, stellar rotation brings spots and faculae (regions of the stellar surface that are darker or brighter than the surrounding plasma) in and out of view in timescales matching the spin period, varying the amount of blue/redshifted light travelling towards the observer. The number and shape of spots and faculae also evolve in timescales of months to years [Dumusque et al., 2011; Kallinger et al., 2014; Meunier et al., 2015; Cegla et al., 2019; Sulis et al., 2023]. These phenomena can increase uncertainties in the fitted planet masses, or mimic planetary signals in amplitude and frequency, which may drown real planet signatures, or cause stellar variability signals to be mistaken for real planets.

1.1.3 Other methods

Additional methods for detecting exoplanets include direct imaging, microlensing, and transit timing variations (TTVs).

The **direct imaging** method involves measuring the infrared light directly emitted by exoplanets. These planets start out with thermal energy within their interiors, which they radiate away in infrared wavelengths throughout their life, cooling down, and thus becoming fainter in the infrared [Bowler, 2016]. Since very young planets are hotter, they will be brighter and thus easier to detect. However, as planets cool down with age, their host stars maintain a constant luminosity throughout the main sequence, creating a luminosity bifurcation and increasing the contrast between the plant and its host star. This method is thus sensitive to young ($< 200\,\mathrm{Myr}$) massive planets ($> 1\,\mathrm{M_J}$) at large separations ($> 10\,\mathrm{au}$), mapping a region of parameter space unavailable to the transit and radial velocity methods. In order to detect the planets, it is necessary to block the starlight with a coronagraph; in the case of ground-based observatories, adaptive-optics (AO) systems are also required to correct for the distortion caused by Earth's atmosphere. Keck/NIRC2, for instance, can reach a contrast of 10^{-7} at angular separation of 0.5" [Kunimoto et al., 2023]. Despite the difficulties in the way of detecting the infrared emission from exoplanets, this method has been moderately successful with 77 confirmed discoveries so far as per the NASA Exoplanet Archive, such as HR 8799 [Marois et al., 2008], 51 Eridani b [Macintosh et al., 2015], and β Pictoris b [Lagrange et al., 2010a].

Microlensing uses the gravitational lensing effect observed when a star system moving across the sky aligns with a background star. The light from the background star will be magnified by both the gravity of the foreground star and of its orbiting planet. This method is sensitive to planets from Earth to Jupiter mass at orbital separations of 1–10 au; this includes the habitable zones of Sun-like stars, a region of parameter space available to other methods. These are also very rare events, which require constant monitoring of large areas of the sky, and do not repeat. Follow-up with other detection methods is also not possible due to the large distances of these systems, up to several kpc. The microlensing method has been responsible for 217 confirmed exoplanet discoveries to date, including the cold super-Earth OGLE-2005-BLG-390L b [Beaulieu et al., 2006] and the cold Neptune OGLE-2005-BLG-169L b [Gould et al., 2006].

Transit timing variations (TTVs) are fluctuations in the timing of the transits of a planet caused by the gravitational pull from additional planets in the system, which subtly alter its orbit and ephemerides. This method is particularly effective on tightly packed multiplanetary systems, such as TRAPPIST-1 [Gillon et al., 2017], to measure the masses of the planets using photometry alone without additional radial velocity observations. TTVs are also particularly pronounced when the planets are in near first-order mean motion resonance orbits, where the ratio of their orbital periods have specific values [e.g. 2:1, 3:2, 4:3, Steffen et al., 2013a]. N-body simulations are performed to find the mass and orbital period of the additional planet or planets that can induce the observed TTVs. Moreover, TTVs also nicely compliment the transit method since, it can constrain planet masses using the same observations as the transit method uses to determined planet radii, if the right orbital configurations are present.

1.2 Exoplanet populations

Together, these detection methods have not only uncovered but also characterised the masses, radii, and orbital separations (amongst other parameters) of more than 5600 planets to date, as per the NASA Exoplanet Archive. Follow-up observations are equally important to confirm these discoveries; this involves detecting a planet independently with two methods, most commonly transits and RVs. These two methods also compliment each other – with knowledge of planet's radius from transits and its mass from RVs, we obtain the planet's bulk density and thus constraints on its internal structure and its past formation and evolution. Indeed, the planetary systems studied in Chapters 3, 4, and 6 were first discovered by *Kepler* and *TESS* with the transit method and later characterised with radial velocity measurements to determine their masses.

Such large numbers of planet discoveries allows us to perform statistics on their populations and identify different groups as imprints of formation and evolution mechanisms. In Figure 1.1 I plotted the radii (top) and masses (bottom) against the orbital period of all confirmed planets to date from the NASA Exoplanet Archive. In period-radius space, discoveries are dominated by the transit method, particularly from *Kepler*, with populations spanning a wide range of radii of $0.5-20\,\mathrm{R_E}$ and periods of $0.5-200\,\mathrm{d}$. In period-mass space, these transit discoveries span $1-10^4\,\mathrm{M_E}$ and are less numerous, as these were later characterised with radial velocity follow-up to measure their masses, although it also includes discoveries of small planets made with this method. We can also see a new population of giant planets appear discovered with the radial velocity method, with greater planet masses of $> 100\mathrm{M_E}$ and longer periods of 1–20 years. Due to their long orbital periods, these planets are seldom characterised with the transit method and thus their radii are left unknown. Finally, the few discoveries via direct imaging stand out due to their long orbital periods of 10 to 10^5 years at large radii and

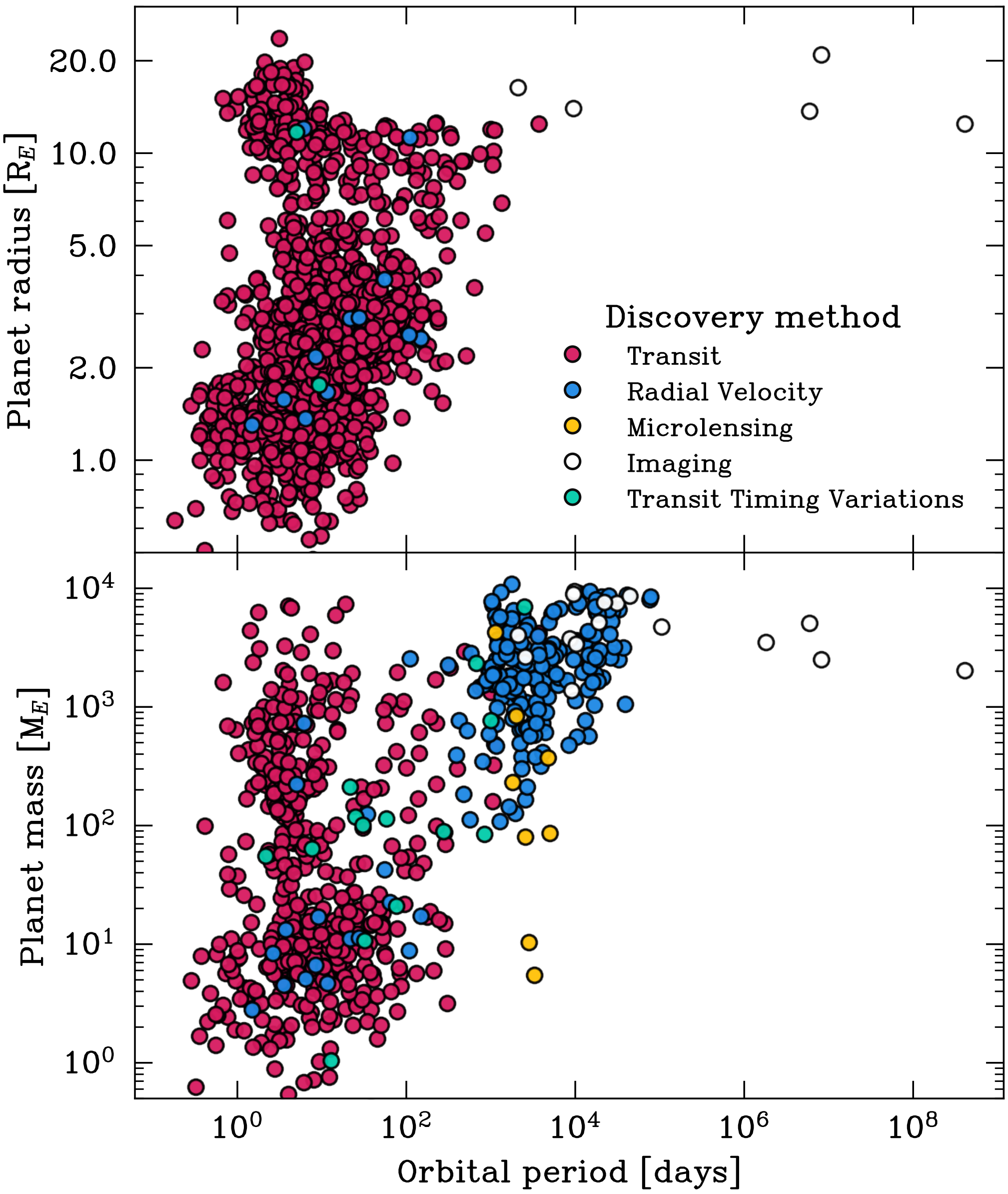

Figure 1.1: **Top:** planet radius against orbital period with the confirmed exoplanets on the NASA Exoplanet Archive. The planets are colour-coded by their original discovery method: transit (red), radial velocity (blue), microlensing (yellow), and direct imaging (dark green). **Bottom:** planet mass against orbital period with confirmed exoplanets, following the top panel.

masses. This is a direct result of the limitations of this method, which requires planets to be young, massive, and far away from their stars to be more easily detected.

The first class of exoplanet to be discovered in large numbers were the so-called hot Jupiters (HJs). These are Jupiter-mass planets ($0.3 - 2.0\,\mathrm{M_J}$, $100 - 600\,\mathrm{M_E}$) that orbit extremely close to their host stars, with orbital periods ranging from a week down to less than a day. These planets raised many questions. They had no analogue in the solar system, and challenged contemporaneous models of planet formation and evolution. The leading theory for their existence is that they formed further away where the protoplanetary disk is denser, cooler, and water-rich, and migrated inward via the high eccentricity mechanism [e.g. Dawson and Johnson, 2018; D'Angelo and Lissauer, 2018; Owen and Lai, 2018].

Other authors have also suggested alternative origins for the population of hot Jupiters. Batygin et al. [2016] and Boley et al. [2016] argued hot Jupiters may also have formed in-situ close to their current orbital periods; where close-in multi-planet systems become unstable and merge into cores with masses $M > 15\,\mathrm{M_E}$ which experience runaway gas accretion from the protoplanetary disk, turning into hot Jupiters. Alternatively, Ida and Lin [2008] and Mordasini et al. [2009] have also argued that hot Jupiters may also have arrived to their current locations via disk-driven migration, where nascent cores form beyond the ice line, and then slowly migrate inward collecting solids until they reach the critical mass to undergo runaway mass accretion, ending their migration at short orbital periods.

Moreover, due to their short orbital periods, these worlds were also expected to receive large amounts of high energy radiation from their host stars. The idea that stellar high energy radiation could have significant effects in the atmospheres of close-in planets was first born [e.g. Lammer et al., 2003; Baraffe et al., 2004], although later observations [e.g. HD 209458 b Vidal-Madjar et al., 2003, 2004] and simulations [Yelle, 2004; Murray-Clay et al., 2009b] determined hot Jupiters were too massive to experience significant mass loss.

In 2009, the *Kepler* mission was launched, with the objective to continue the search for exoplanets with the capability of detecting transits from planets as small as Earth. In its nine years of operation, the *Kepler* mission, and later K2, would uncover more than 2700 exoplanets, many of which are between Earth and Neptune in size, and thus are collectively known as super-Earths and mini-Neptunes [Borucki et al., 2011]. These planets range between Earth and Neptune in size, with radii between 1 and $4\,\mathrm{R_E}$. Akin to hot Jupiters, many of these

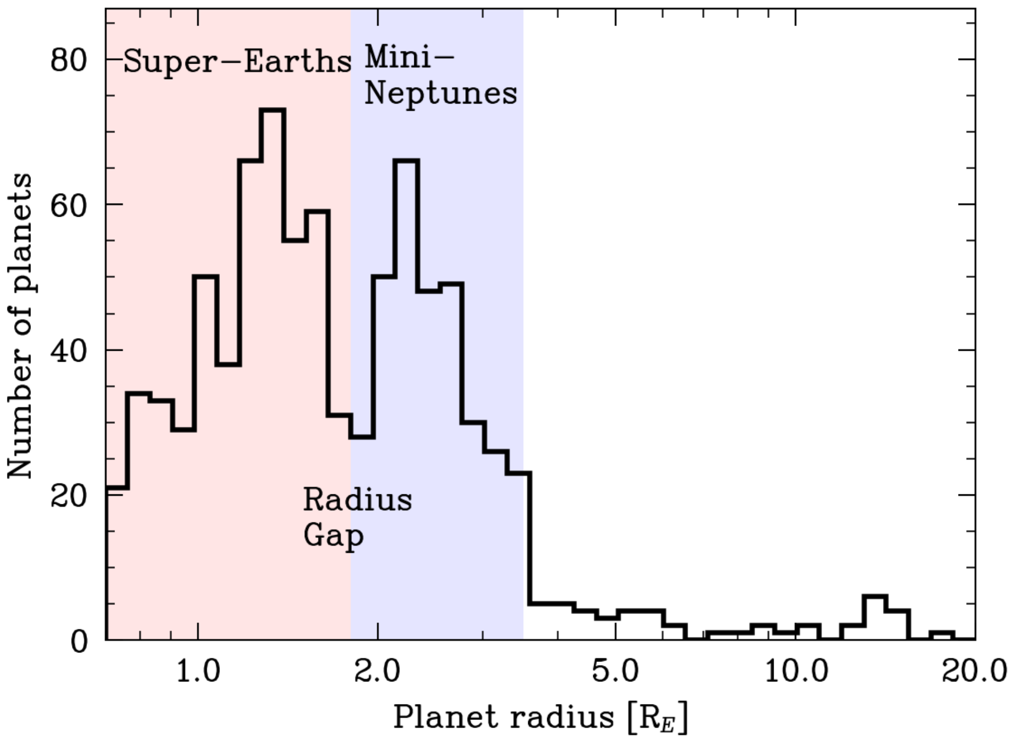

Figure 1.2: Histogram of the radii of planets from the California-Kepler Survey (CKS) filtered by Fulton et al. [2017], showing a bimodal distribution. The two populations of super-Earths (red) and mini-Neptunes (blue) have been highlighted.

planets lie very close to their stars, with orbital periods of only a few days. These discoveries of much smaller worlds sparked renewed interest in studying the impact of atmospheric escape on their atmospheres.

1.2.1 The radius valley

Whilst *Kepler* photometry constrained the ratio of planet radius to stellar radius R_p/R_* of these small worlds quite well, with a median uncertainty of $\sim 3\%$, stellar radii were less constrained, with uncertainties around 40%, leading to poor constraints on the planetary radii.

Petigura et al. [2017] introduced the California-Kepler Survey (CKS), which contained 1300 planet-hosting stars previously observed by *Kepler*, hosting a total of 2000 planets. Petigura et al. [2017] obtained high-precision optical spectral for these stars with the Keck/HIRES spectrograph and Johnson et al. [2017] then fitted these spectra to stellar interior models using the isochrone models by Dotter

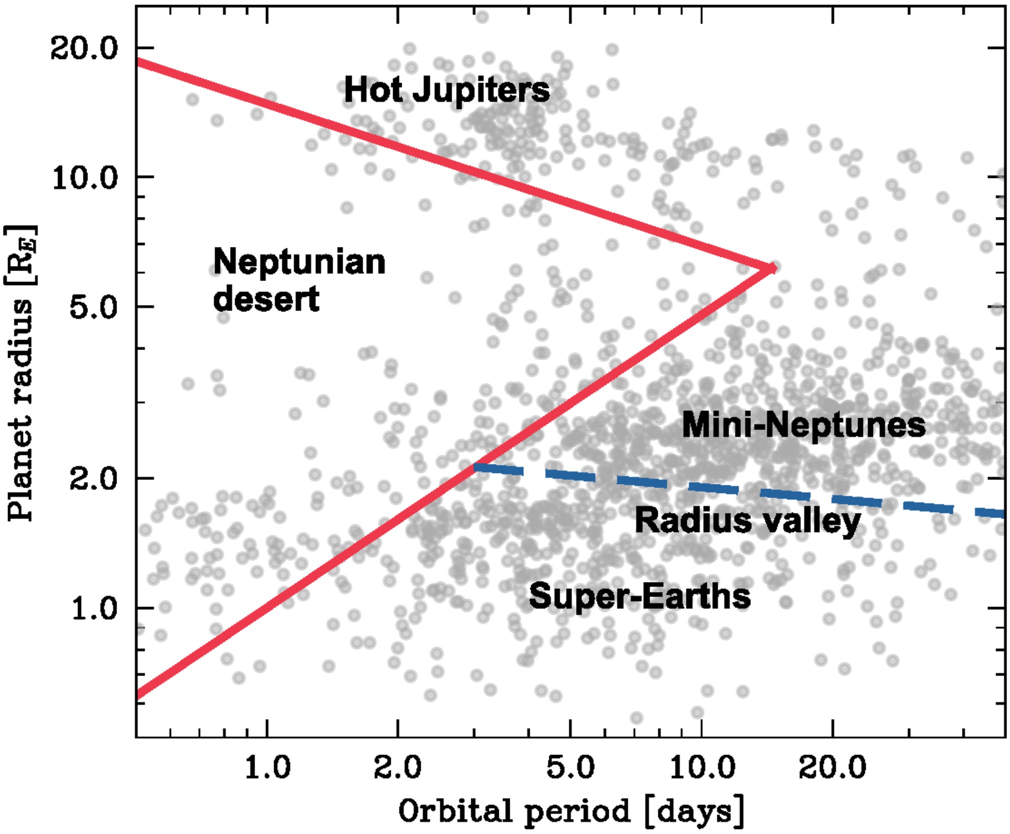

Figure 1.3: Planet radius against orbital period showing the populations of close-in exoplanets. The edges of the Neptunian desert as defined by Mazeh et al. [2016] are shown as red lines, and the radius valley as defined by Van Eylen et al. [2018] is shown as a blue line.

et al. [2008] to place tighter constraints on their parameters, which they validated by comparing with results from asteroseismology and *Gaia* parallaxes. They thus reduced the average errors on stellar radii down to $\sim 11\%$ and updated the radii of their transiting planets to similar uncertainties.

Fulton et al. [2017], using a subset of the most well characterised stars from the CKS dataset, uncovered a bimodal distribution in the radii of these planets, with two peaks at 1.6 and $2.0\,\mathrm{R_E}$ and a gap at $1.8\,\mathrm{R_E}$. This *radius gap* thus separates two populations of exoplanets: a population small planets with radii $1 - 1.8\,\mathrm{R_E}$, known as super-Earths, and a population of larger planets with radii $1.8 - 3.0\,\mathrm{R_E}$, known as mini-Neptunes. In Figure 1.2, I plotted this bimodal distribution of planet radii, highlighting the two populations. Fulton et al. [2017] also traced this radius gap as a function of orbital period, and found it tends to greater radii at shorter periods, extending the radius gap into a *radius valley*.

These results were confirmed by Van Eylen et al. [2018] who recovered this radius valley using a smaller sample of stars with highly accurate parameters with *asteroseismology*. Asteroseismology studies oscillations in stellar interiors, which are observed as photometric variability. The spacing between the oscillation modes as well as the frequency at which they have maximum power are fundamental asteroseismic parameters that can be used to probe into stellar interiors and place tight constraints on the masses and radii of stars [e.g. Huber et al., 2013; Silva Aguirre et al., 2015; Lundkvist et al., 2016]. These precise stellar radii can then be used to greatly improve the uncertainties on the radii of transiting planets. The sample Van Eylen et al. [2018] presented included 117 planets and further reduced the uncertainties in radii down to $\sim 3.3\%$, which allowed them to determine that the radius gap moves to smaller radii for longer orbital periods. Their fit to the radius valley as a function of orbital period is plotted in Figure 1.3.

Moreover, mass measurements of these worlds from radial velocities [e.g. Affer et al., 2016; Lacedelli et al., 2022] and TTVs [e.g. Ballard et al., 2011; Steffen et al., 2013b; Gillon et al., 2017] would also reveal that these two populations not only differ in their radii but also in their densities. Super-Earths are smaller and have high densities ($\sim 5\,\mathrm{g\ cm^{-3}}$), consistent with a rocky Earth-like composition. Mini-Neptunes, on the other hand, are larger and have lower densities ($\sim 1\,\mathrm{g\,cm^{-3}}$), suggesting the presence of extended volatile-rich atmospheres that can double the size of a planet and yet comprise less than a percent of its mass [Lopez et al., 2012].

In actuality, the existence of a radius valley had already been predicted by Lopez et al. [2012] and Owen and Wu [2013], who argued the radius valley arises as a result of the escape of the gaseous atmospheres of mini-Neptunes. Since mini-Neptunes also have short orbital periods of only a few days, placing them remarkably close to their host stars, they were also expected to receive considerable amounts of high energy irradiation from their host stars. This energy would be absorbed and deposited in the upper atmospheres of exoplanets, heating up the gas and causing it to expand beyond the planet's Roche lobe, resulting in a flow of gas escaping the planet [e.g. Lecavelier Des Etangs, 2007; Davis and Wheatley, 2009].

The radius gap discovered by Fulton et al. [2017] was also later reproduced by Owen and Wu [2017], who simulated atmospheric escape on mini-Neptunes powered by the high energy emission from their host stars. They found that atmospheric escape is able to completely remove the gaseous envelopes of certain planets down to barren rocky cores. As such, some planets that start out as sub-Neptunes with a sizeable H/He envelope later lose it entirely to escape, becoming super-Earths, whilst other planets are able to hold onto their atmospheres and remain above the radius valley as mini-Neptunes. Moreover, they determined that planets at shorter orbital periods are more susceptible to escape, as they are more strongly irradiated; this is also true for low-mass worlds, as less energy is required to remove gas from a shallower gravitational potential. Their predictions naturally explained not only the existence of a radius gap, but also its relation with orbital period where the locus of the gap moves to larger radii at shorter periods (as seen in Figure 1.3).

Ginzburg et al. [2016] and Ginzburg et al. [2018] proposed an alternative atmospheric escape mechanism, core-powered mass loss, where the energy for escape comes from the bolometric flux from the host star aided by the thermal energy from the rocky core which puffs up the atmosphere from within. Gupta and Schlichting [2020], using simulations of atmospheric escape on synthetic populations of exoplanets, showed that core-powered mass loss can reproduce the observed properties of the radius valley.

Wyatt et al. [2020] instead argued that impacts from planetesimals early in the life of a planetary system are able to deliver enough energy to planets to remove their primordial envelopes. The efficiency of this mechanism hinges on the rate of atmospheric stripping versus the rate of delivery of volatiles as a result of impacts from planetesimals, where the balance between the two creates a so-called *impact shoreline*. High mass planets would accrete volatiles at a greater rate and planets at longer periods would suffer from impacts less frequently. Wyatt et al. [2020] found that the impact shoreline coincides with the location radius gap, and were able to reproduce the evaporation valley and its dependence with planet mass, orbital period, and stellar mass, although the precise width and depth of the resulting radius gap would depend on the properties of the impacting planetesimals.

Other studies have instead interpreted the valley as imprints of planet formation. Some authors have argued a gas-poor formation, where super-Earths never accreted a H/He envelope and remained gas-free since formation, can reproduce the location of the radius valley [e.g. Lee et al., 2014; Lee and Chiang, 2016; Lopez and Rice, 2018; Cloutier and Menou, 2020]. Other authors have argued planets above the valley are water-rich worlds with low bulk densities, mimicking gaseous H/He envelopes [e.g. Ida and Lin, 2008; Zeng et al., 2019; Mousis et al., 2020; Venturini et al., 2020; Luque and Pallé, 2022], in contrast with Owen and Wu [2017], who assumed such planets can be described as rocky cores surrounded by pure H/He envelopes. Indeed, water worlds are predicted to be plentiful by formation models [e.g. Seager et al., 2007; Jin et al., 2014; Jin and Mordasini, 2018]. These water worlds would originally be formed further at greater orbital separations, where the protoplanetary disk cooler allowing water to condense into solids; this occurs past the so-called *ice line*. As a result, the planets accrete large fractions of ices relative to their rocky masses, and later migrate inward within the protoplanetary disk [Ida and Lin, 2008; Mordasini et al., 2009]. A population of planets that match the densities of water-rich worlds can indeed be observed in mass-radius relations [e.g. Zeng et al., 2019]. Their internal compositions, however, are degenerate as they are also consistent with having small rocky cores enveloped in thin H/He envelopes and no water content [e.g. Owen, 2019].

Luque and Pallé [2022] found that, around M-dwarfs, the radius valley has no dependence on orbital period, contrary to predictions from thermal mass loss mechanisms. They instead argued their results could be explained by the presence of three classes of planets: barren rocky worlds that lie below the valley, icy worlds with 50% water fraction by mass along the upper edge of the valley, and large H/He-rich sub-Neptunes at greater radii. However, the widespread presence of water-rich worlds in the populations of close-in planets is still under debate.

Rogers et al. [2023] showed that an additional mass loss mechanism, "boil-off", could explain the results from Luque and Pallé [2022] without the presence of water-rich worlds. Boil-off consists on a rapid loss of hot atmospheres on small worlds that have accreted significant H/He envelopes during their formation, caused by the pressure from the protoplanetary disc being lifted as the disc is dispersed.

Moreover, Ho et al. [2024] found that the radius valley also becomes shallower around M-dwarfs. Photoevaporation and other thermal mass loss mechanisms, however, predict that the “depth” of the valley should not have a dependence on stellar mass. Ho et al. [2024] suggested three scenarios that could explain their observations and populate the valley on M-dwarfs: (1) the presence of icy bodies, in agreement with Luque and Pallé [2022]; (2) planetary collisions being more frequent on M-dwarfs creating large barren rocky worlds whose radii lie in the valley [as suggested by dynamical simulations, e.g. Naponiello et al., 2023a; Childs et al., 2025]; and (3) scatter in the stellar emission of M-dwarfs inducing a diversity of irradiation histories for these planets that would blur the valley.

1.2.2 The Neptunian desert

The Neptunian desert is a second region of parameter space where close-in ($P < 4\,\mathrm{d}$) Neptune-sized ($2 - 4\,\mathrm{R_E}$) exoplanets become scarce. I labelled this region in Figure 1.3, where I show the populations of confirmed exoplanets with periods below 40 days.

Szabó and Kiss [2011] first noticed a lack of hot Neptunes with periods below 2.5 d in the full sample of 106 transiting exoplanets known at the time. This region, which they labelled the “sub-Jovian desert”, contrasts with the numerous hot Jupiters with orbital periods of $> 1\,\mathrm{d}$ (see Figure 1.3). Benítez-Llambay et al. [2011] reported the same results independently, and performed simulations of disk and orbital migration of these close-in hot Jupiters and Neptunes. They argued that the inner edge of the protoplanetary disk, located roughly at 2.5 d period for Sun-like stars, prevents planets from forming closer to the star. This inner edge would be carved by the stellar magnetic field disrupting the disk and accreting material onto the star, and would be located at the corotation radius, where the disk no longer follows keplerian rotation but is forced to match the stellar rotation period [e.g. Miranda and Lai, 2018].

Instead, the population of hot Jupiters at shorter periods would then arise from orbital migration via tidal interactions with their host star, which only occurs for planets above some critical mass $m_c \sim \mathrm{M_J}$. Beaugé and Nesvorný [2013] confirmed the results of Szabó and Kiss [2011] and Benítez-Llambay et al. [2011], and found that this underdensity of hot Neptunes was present in period-radius space as well as period-mass space.

Subsequently, the *Kepler* mission, thanks to its greater photometric precision, offered unprecedented insight into the populations of smaller worlds, uncovering a large number of exoplanets with radii between 1 and $4\,\mathrm{R_E}$. Sanchis-Ojeda et al. [2014], using data from *Kepler*, presented the discovery of 106 ultra-short period (USP) planets with radii 1–$2\,\mathrm{R_E}$ and orbital periods below one day. They found that these small close-in worlds are as abundant as hot Jupiters, with similar orbital periods but much smaller radii. They additionally reported a lack of USP planets with radii $R_\mathrm{p} > 2\,\mathrm{R_E}$, which would constitute a lower bound in planet radius for the sub-Jovian desert that Szabó and Kiss [2011] uncovered. Lundkvist et al. [2016] later confirmed these results with a smaller sample of well characterised stars with using asteroseismology. This hot Neptune desert could not be explained as an observational bias, since *Kepler* was sensitive to short period planets spanning radii from Earth to Jupiter size. Instead, it must be caused by underlying physical mechanisms affecting these planets during their formation and/or evolution.

Mazeh et al. [2016] defined upper and lower boundaries of this Neptunian desert by finding the linear contours in period-radius space with the largest drop in planet number density. I show their boundaries in Figure 1.3. Mazeh et al. [2016] found that the upper boundary of the desert, above which hot Jupiters lie, decreases in radius with increasing period; whilst the lower boundary, lying over a population of super-Earths, follows the opposite trend, increasing in both radius and orbital period. Moreover, the upper boundary is much more well defined than the lower boundary, as the occurrence of hot Jupiters experiences a much sharper decline whilst the depletion of super-Earths is much more gradual.

Owen and Lai [2018] performed simulations of orbital migration and photoevaporation on close-in planets from Earth to Jupiter in size. They found that the Neptunian desert originates from two parallel mechanisms which result in a scarcity of Neptune-mass worlds at short orbital periods, each giving rise to the upper and lower boundaries of this region separately. They found that the lower boundary is sculpted by photoevaporation, where Neptunes with masses $M_\mathrm{p} < 25\,\mathrm{M_E}$ that formed very close to their host stars would experience strong X-ray and extreme ultra violet (together, XUV) irradiation from their host stars and would be stripped of their gaseous envelopes, joining the large population of hot super-Earths at smaller radii.

Regarding the upper boundary, Owen and Lai [2018] found that photoevaporation is ineffective at evaporating the more massive ($M_\mathrm{p} > 0.5\,\mathrm{M_J}$) hot

Jupiters in this region thanks to their deep gravitational potentials. Instead, they argued that this region arises from a tidal disruption barrier in planet migration. Following previous literature [e.g. Matsakos and Königl, 2016], they argued the population of hot Jupiters arises from high eccentricity migration, where planets form at wider orbits (1–2 au) and are subsequently pushed into a highly eccentric orbit by scattering with an additional outer massive planet. At this point, interaction with stellar tides ends up circularising its orbit at a final close-in semi-major axis that is mass-dependent, giving rise to a tidal disruption barrier. This can be observed in exoplanet populations as more massive giant planets orbiting closer to their host stars at the location expected by such migration models [Owen and Lai, 2018]; these define the upper boundary of the Neptune desert, which is a strong function of planet mass.

These mechanisms also explained the scatter in the two boundaries. High-eccentricity migration results in a well-defined boundary in period-mass space as the final location to which the mechanism delivers planets depends strongly on the ratio between planet mass and stellar mass. On the other hand, the photoevaporative boundary is less well-defined as it additionally depends on the particular irradiation history of each planet and its starting envelope mass fraction. The lower boundary is also less populated than the upper boundary, particularly in period-mass space, due to the low number of super-Earths with measured masses.

Alternatively, Jackson et al. [2017] and Koskinen et al. [2022] argued that the Neptunian desert could also arise from Neptunes migrating too close to their stars, where they would be stripped of their gaseous atmospheres via the Roche Lobe Overflow (RLO) mechanism, turning into hot rocky worlds. Under this mechanism, the upper atmosphere of the planet becomes unbound due to the close proximity to its star and as a result material is pulled from the planet into the star. Koskinen et al. [2013] predicted this mechanism would dominate over XUV photoevaporation at planet radii below 15 $\mathrm{R_E}$and orbital periods under 1.5 days, matching the location of the Neptunian desert. The resulting mass loss rates can be several orders of magnitude greater than what photoevaporation can achieve, carving out the Neptunian desert in relatively short timescales.

More recently, a handful of hot Neptunes have been discovered deep in the Neptune desert, which may have followed more exotic and unusual routes for formation and evolution. These rare worlds thus offer new opportunities to explore the limits of our theories. One of these is LTT 9779 b, the only hot Neptune deep in the Neptunian desert with a low density that requires a gaseous envelope [Jenkins et al., 2020]. In Chapter 4, I study the evaporation history of this planet under X-ray irradiation with constraints from the *XMM-Newton* telescope.

1.3 Atmospheric escape

The super-Earths and mini-Neptunes that the *Kepler* mission uncovered are much less massive than hot Jupiters, but experienced the same high energy environment. This led to the idea that these small planets could be experiencing vigorous atmospheric escape as a result of irradiation from their host star, in some cases completely stripping them of their envelopes [e.g. Davis and Wheatley, 2009; Lopez et al., 2012; Owen and Wu, 2013].

Owen and Wu [2013] simulated the evolution of the atmospheres of exoplanets under evaporation powered by stellar radiation. They assembled a population of synthetic planets spanning masses between 6.5 and 15 $\mathrm{M_E}$ and separations under 0.5 AU, with an initial atmospheric mass fraction of at least 1%. The evolution of these planets was then simulated using the *MESA* code [Paxton et al., 2015] to model the structure of the planetary atmospheres and the models by Owen and Jackson [2012] to compute the mass loss rates. Overall, their results showed that these small close-in planets lost a significant fraction of their gaseous atmospheres as a result of the energy delivered by their host stars. The resulting distribution of planetary radii after 1 Gyr of evolution was bimodal, with a population of small planets whose atmospheres had been fully stripped and another population of larger planets that retained their envelopes. Ultimately, Owen and Wu [2013] showed that stellar radiation could sculpt the populations of super-Earths and mini-Neptunes, carving a gap in the distribution of their radii and giving way to the radius valley. They concluded that the radius-period valley is consistent with a picture in which atmospheric escape plays an important role in shaping the population of close-in small exoplanets, with some planets having their envelopes completely stripped down to their core, as predicted by Lopez and Fortney [2013], Owen and Wu [2013] and Jin et al. [2014].

Similarly, the origin of the Neptunian desert has been attributed at least in part to the inability of planets in this region to hold onto their gaseous envelopes due to atmospheric escape [Kurokawa and Kaltenegger, 2013; Kurokawa and Nakamoto, 2014; Ionov et al., 2018; Owen and Lai, 2018]. Neptune-sized planets that formed in the desert, or migrated there in their youth, would be stripped of their H/He envelopes joining the more abundant population of hot rocky worlds with smaller radii, and those that underwent later high-eccentricity migration would have been delivered to larger orbital separations [Castro-González et al., 2024]. Hot Jupiters ($> 0.5\,\mathrm{M_E}$), on the other hand, do migrate to very short periods in part thanks to their high mass but are also stable against atmospheric loss for the same reason [Yelle, 2004; Murray-Clay et al., 2009b; Vissapragada et al., 2022]. Unlike hot Neptunes, in which the core dominates its mass and the envelope constitutes less than half fo the total mass of the planet, hot Jupiters have H/He masses many times the mass of the rocky core. In this regime, the gas layers compress under their own gravity. This phenomenon, known as envelope self-gravity, results in smaller radii in comparison to what envelope structure models for sub-Neptunes predict, extending the lifetimes of their envelopes Owen and Wu [2017]; Owen and Lai [2018].

In this section, I present the evidence we have so far of ongoing atmospheric escape, and discuss the different mechanisms that drive evaporation as well as their relative contributions to shaping exoplanet populations.

1.3.1 Observational evidence

In theory, atmospheric escape creates a cloud of escaping gas that surrounds a planet and extends for several planetary radii, beyond the Roche lobe of the planet, at which point it is no longer gravitationally bound. This extended atmosphere can potentially block a greater fraction of starlight at certain wavelengths, producing deeper transits. Observational evidence has for the most part been obtained by means of detecting this excess transit depth that the gas escaping the planet's atmosphere (the planetary wind) induces.

The ideal wavelengths for such observations are those which will create the strongest absorption signatures given the composition and chemistry of the escaping gas as well as its high energy environment. So far, observations of the Lyman-α line of hydrogen at 1215 Å and the metastable helium line triplet at 10830 Å have been by far the most fruitful.

Lyman-α

Lyman-α (Lyα) absorption is originated in photons at 1215.67 Å (10 eV) bringing neutral hydrogen from its ground level at $n = 1$ to an excited state at $n = 2$. This makes it an important tracer for atmospheric escape, as neutral hydrogen atoms that were swept away from the planet by the hydrodynamic wind readily absorb

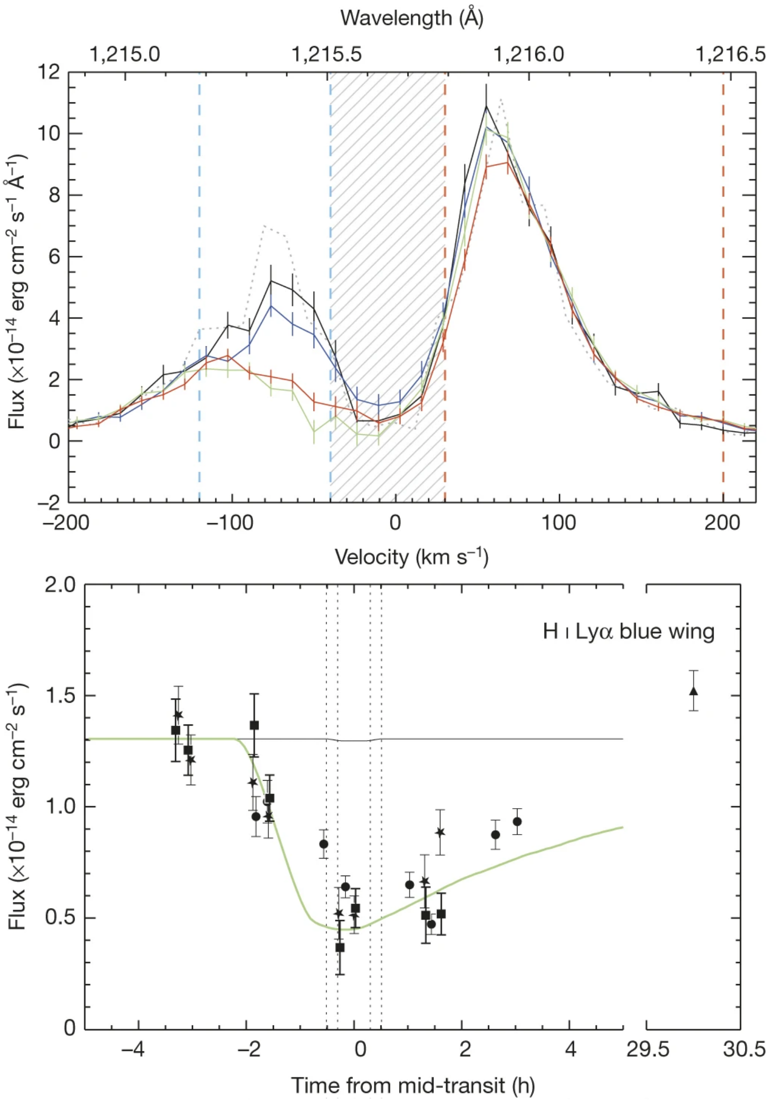

Figure 1.4: **Top:** Figure from Ehrenreich et al. [2015] showing transit spectra of GJ 436 b around the Lyα line, including out-of-transit (black), pre-transit (blue), in-transit (green), and post-transit (red). The shaded region is the core of the line, which has been erased by ISM absorption and geocoronal emission. The red and blue wings are produced by the escaping atmosphere leaving the planet. **Bottom:** figure from Ehrenreich et al. [2015] showing the Lyman-α transit curve of the warm Neptune GJ 436 b integrated over the blue wing (-120 to -40 km s^{-1}). There is significant absorption, reaching a 50% transit depth, during and after the transit caused by the planet's extended atmosphere and comet-like tail of escaping gas blocking starlight.

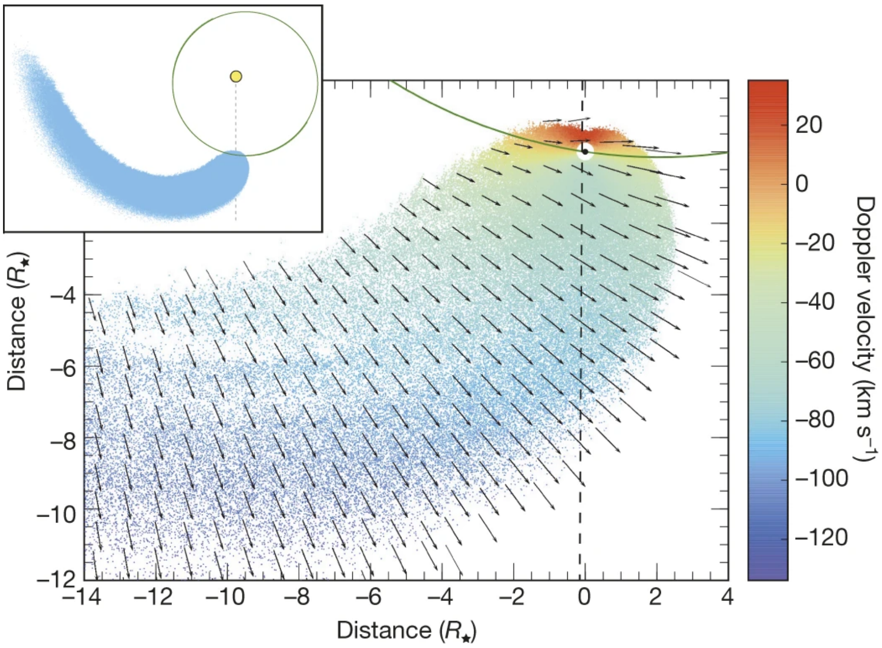

Figure 1.5: Figure from Ehrenreich et al. [2015] showing a particle simulation of the comet-like structure produced by the planetary wind escaping the warm Neptune GJ 436 b.

stellar photons at this wavelength, producing deep transits compared to optical transits.

Observations of Lyα, however, are hampered by absorption from neutral H atoms in the interstellar medium (ISM), which erases the core of the line (see Fig 1.4, top panel). Lyα wavelengths can also be contaminated by Earth's geocoronal emission, which originates in solar Lyα photons scattering in Earth's exosphere.

For that reason, atmospheric escape in Lyα must be studied using the wings of the line instead, which can additionally trace the high-velocity structure of the cloud. Planetary wind flowing away from the star (towards the observer during transit) will produce in-transit excess absorption on the blue wing, whereas wind flowing towards the star will produce excess absorption in the red wing.

Vidal-Madjar et al. [2003] first detected atmospheric escape in Lyα from the hot Jupiter HD 209458 b. Observations with *HST*/STIS revealed an absorption of $15 \pm 4\%$ in the blue wing of the Lyα feature during the transit, compared to an optical transit of only 1.5%. This corresponds to an extended atmosphere that reaches beyond the Roche lobe of the planet. Excess absorption in the wings of the Lyα feature also revealed the planetary outflow reaches velocities of up to $130\,\mathrm{km\,s^{-1}}$, with outflow models constraining a minimum mass loss rate of $10^{10}\,\mathrm{g\,s^{-1}}$. Despite such high mass loss rates, the planet is unlikely to be stripped of its atmosphere in its lifetime. Indeed, a constant mass loss rate of $10^{10}\,\mathrm{g\,s^{-1}}$ would cause the planet to lose only 0.25% of its mass over 10 Gyr.

Another key example is the hot Jupiter HD 189733 b, which Lecavelier Des Etangs et al. [2010] observed with HST/ACS and found a deep transit in the Lyα line with depth $5.05 \pm 0.75\%$, which is 70% deeper than its optical transit depth of 2.9% [Bouchy et al., 2005]. Later observations by Lecavelier des Etangs et al. [2012] revealed a dramatic variability in the Lyα signature of atmospheric escape from the planet. Whilst a first epoch found no evidence for escape, observations of a second epoch 1.5 years later revealed a surprisingly deep transit of depth $14.4 \pm 3.6\%$ contemporaneous with an X-ray flare from its host star detected with Swift. Their simulations showed the upper atmosphere was heated to $10^5\,\mathrm{K}$, driving planetary winds with speeds of $190\,\mathrm{km\,s^{-1}}$ and escape rates of $10^9\,\mathrm{g\,s^{-1}}$.

Atmospheric escape has also been detected on Neptune-sized planets in the Lyman-α line. Ehrenreich et al. [2015] detected a deep transit in Lyα on the hot Neptune GJ 436 b with an absorption depth of over 50%, significantly greater than the optical transit depth of 0.7%. Figure 1.4 shows the spectra of the host star as the planet transits (top panel) and the time series of the transit integrated over the blue wing (bottom panel), which show strong excess absorption in-transit and post-transit, particularly in the blue wing. Indeed, the authors found an excess in the blue wing of $56.2 \pm .6\%$ in-transit and $47.2 \pm 4.1\%$ post-transit relative to out-of-transit levels, with excess absorption up to 4 h after egress. The authors interpreted the observations to be caused by an extended comet-like tail of escaping gas. Figure 1.5 shows their simulations of the spatial structure of this tail of escaping gas. Moreover, the absorption is predominantly detected in the blue wing of the Lyα feature, which suggests most of the wind is being pushed away from the star by radiation pressure with speeds between 70 and 120 $\mathrm{km\,s^{-1}}$, far greater than the planet's escape velocity of $36\,\mathrm{km\,s^{-1}}$.

Since these discoveries, an increasing number of studies have found evidence of atmospheric escape in Lyα from Jupiter-sized planets, such as WASP-12 b [Jensen et al., 2018], WASP-121 b [Yan et al., 2021], HAT-P-32 b [Czesla et al., 2022], and 55 Cancri b [Ehrenreich et al., 2012]; as well as Neptune-sized planets, such as GJ 3470 b [Bourrier et al., 2018], HAT-P-11 b [Ben-Jaffel et al., 2022], HD 63433 c [Zhang et al., 2022], and AU Mic b [Rockcliffe et al., 2023].

Observations of Lyα, however, require space-based observatories that target the ultraviolet. To date, the only such observatory with the capabilities to perform spectroscopy in the Lyα line is the *Hubble* Space Telescope (HST). The HST has only one fully functioning gyroscope left as of June 2024 out of six originally, which, if it were to fail, would render the spacecraft unusable and thus Lyα unobservable. There is also no clear space-based successor to the HST that targets the UV. The Large Ultraviolet Optical Infrared Surveyor [LUVOIR, Bolcar et al., 2017] currently in its concept stage, has been proposed as one such candidate, targeting UV, optical, and near IR wavelengths.

Helium triplet

More recently, deep planetary transits have also been detected around 10830 Å [e.g. Spake et al., 2018; Palle et al., 2020; Zhang et al., 2023]. This absorption feature is produced by helium atoms in the metastable state found in the planetary outflow, which have an absorption line at 10830 Å. Metastable helium is produced when He atoms in the wind escaping the planet are photoionised by stellar EUV photons with energies $> 24.6\,\mathrm{eV}$ ($\lambda < 50.4\,\mathrm{nm}$) which then undergo recombination, cascading until reaching the 2^3S triplet state. This state can then undergo spontaneous radiative decay back to the ground state with a long lifetime of 2.2 hours as it is a forbidden transition, making it metastable, or depopulated by either mid-UV stellar photons or collisions. Whilst in this state, helium can then be temporarily excited by stellar EUV radiation into the 2^3P state, producing an absorption line at 10830 Å.

Seager and Sasselov [2000] first predicted that metastable helium would produce strong absorption signals in planet transmission spectra and thus its potential in probing exoplanet atmospheres, and Oklopčić and Hirata [2018] predicted its absorption could be readily observed in the planetary winds of escaping atmospheres with excess transit depths of a few percent.

Spake et al. [2018] first detected atmospheric escape from an exoplanet using the metastable helium triplet with HST/WFC3. They measured the transmission spectrum of the warm Jupiter WASP-107 b and detected a $2.105 \pm 0.010\%$ transit depth at 10830 Å, compared to an optical depth of $2.056 \pm 0.005\%$, and thus an He absorption excess of $0.05 \pm 0.01\%$. Using a 1D photoionisation model for escaping atmospheres, which can predict the in-transit He absorption signature, they fitted a mass loss rate of $10^{10} - 10^{11}$ g s^{-1}to their observations. Later this signature would be confirmed with high-resolution ground-based observations by Allart et al. [2019] with CARMENES and by Kirk et al. [2020] with Keck II/NIRSPEC, which were able to resolve the line and uncovered much deeper He excess absorptions of 5.5% and 7.2%, respectively. The apparent disagreement between the two studies arises from differences in the measured white-light planet size, which, when accounted for, result in excellent agreement between the two. They also resolved the velocity structure of the escaping cloud, with evidence of increased absorption in the blue wing of the triplet line, suggesting planetary material is being blown away from the star by radiation pressure.

Shortly after, Allart et al. [2018] observed the hot Neptune HAT-P-11 b with CARMENES and measured an excess absorption of $1.08 \pm 0.05\%$ at 10830 Å, which is five times greater than its optical transit. They then interpreted their observations with 3D simulations of the planet's upper atmosphere and escaping wind, and found that the absorption feature is unlikely to originate in a escaping wind but instead in layers of the upper atmosphere that are still bound to the planet, with mass loss rates no greater than 10^5 g s^{-1}. This was evidenced by the symmetry observed on both the time series about the transit and the absorption profile near the He I triplet. If the absorption happened in a planetary outflow, these signatures would be asymmetric in both the time series (due to the comet-like tail of escaping gas), as well as in the He I absorption profile (due to its velocity structure producing excess absorption blue wind).

Since then, subsequent studies have found this feature in the transits of other exoplanets, both hot Jupiter-sized and Neptune-sized worlds, using spectrographs such as *HST*/WFC3 [e.g. Spake et al., 2018; Mansfield et al., 2018], CARMENES [e.g. Nortmann et al., 2018; Palle et al., 2020], and Keck II/NIRSPEC [e.g. Kirk et al., 2020; Zhang et al., 2023]. See Dos Santos [2023] for an in-depth review.

Observations of escaping atmospheres at 10830 Å offer several advantages over Lyα. Firstly, the triplet lies in the infrared and so it is unaffected by extinction by the interstellar medium, unlike Lyα which lies in the UV and experiences strong extinction, making the core of the line unusable [Oklopčić and Hirata, 2018]. Helium triplet absorption can also be observed with ground-based infrared observatories, which provide much higher spectral resolutions and coverage. Metastable helium also has a long lifetime – it decays back into the ground state in relatively long ($\sim$2 h) timescales.

The detection of metastable helium, however, is also elusive, and many observations have also yielded non-detections [e.g. Kreidberg and Oklopčić, 2018; Bennett et al., 2023; Vissapragada et al., 2024]. The number of He atoms in the triplet state corresponds to a tiny fraction of the total helium in the planetary wind, and its population is highly sensitive to the amount of helium in the planet's atmosphere as well as the stellar activity. Oklopčić [2019] found a correlation between stronger He absorption and higher stellar activity, and Poppenhaeger [2022] also uncovered a correlation with iron abundance in stellar coronae, since most of the stellar EUV emission is produced by iron emission lines in the corona.

On the other hand, metastable helium is also depopulated by mid-UV photons. The balance between the stellar emission on these two wavelength ranges determines whether the escaping gas will produce a detectable absorption signal. Therefore, stars with high XUV fluxes and low UV fluxes are the most efficient at populating the metastable state. According to Oklopčić [2019], young active K-dwarfs strike such a balance between emission in these two bands, and should be the best targets for studies of helium escape.

Moreover, estimating a mass loss rate from absorption spectra is not straightforward, with significant challenges in current modelling efforts such as estimating the population and depletion of the metastable state, accounting for geometrical effects from the transit and the escaping wind, and the strong degeneracy between EUV flux and the H-to-He ratio in the upper atmospheres of exoplanets. Together, these effects can introduce considerable uncertainty into the predicted mass loss rates [Biassoni et al., 2024].

Metal lines

Species heavier than hydrogen and helium have also been detected in the extended exospheres of exoplanets. In order to produce these deep excess transits, these heavy elements must first be carried away from the planet by a strong hydrodynamic wind. These detections come mostly from absorption lines in the UV detected with HST. Moreover, observations of metal lines offer advantages over Lyα, as they are not affected by ISM absorption, and thus can observed from much further away.

An archetypal example is the hot Jupiter HD 209458 b, which Vidal-Madjar et al. [2004] observed with HST/STIS and detected absorption in the O I and C II lines in the near UV with deep transit depths of $13 \pm 4.5\%$ and $7.5 \pm 3.5\%$, respectively, even deeper than its Lyα absorption of $5 \pm 2\%$. Such transit depths not only placed these species at radii beyond the planet's Roche lobe, suggesting they were entrapped in a hydrodynamic wind escaping the planet, but also placed constraints on the composition of the planetary wind and thus of the planet's atmosphere. Linsky et al. [2010a] additionally detected a deep transit of $8.2 \pm 1.4\%$ in the Si III line in the near ultraviolet (NUV), and Cubillos et al. [2020] detected a deep $0.18 \pm 0.05\%$ transit from Fe^{+} transition lines.

Fe and Mg absorption has also been detected in the extended atmosphere of the hot Jupiter WASP-121 b by Sing et al. [2019], who reported deep absorption at the Fe II UV1 and UV2 lines ($0.11 \pm 0.05\%$) as well as the Mg II lines ($0.08 \pm 0.02\%$) in NUV spectra from HST. Fossati et al. [2010] also reported a deep absorption at the Mg II lines during transits of the hot Jupiter WASP-12 b uncovering an extended atmosphere 40% larger than the planet's optical radius.

Despite these discoveries, evidence of escape from absorption lines of metals has been elusive, with a number studies reporting non-detections even when strong signatures were predicted by absorption from other species [e.g. Loyd et al., 2017; dos Santos et al., 2021; Cubillos et al., 2023]. The interpretation of these non-detections has also been unclear, as models differ in their description of the structure of upper atmospheres and their predictions for the mass loss rates. These degeneracies between models could be mitigated by expanding our inventory of spectral lines that trace atmospheric escape [Linssen and Oklopčić, 2023].

1.3.2 Atmospheric escape mechanisms

Deep absorption during the transits of exoplanets in Lyα, He triplet, and metal lines are thought to be caused by escape of their gaseous atmospheres. Such escape can be driven by a number of physical processes occurring in the upper atmospheres of these exoplanets. Characterising such mechanisms, their origins, efficiencies, and their relative contributions to escape is necessary to uncover the origin of the radius valley and the Neptunian desert. In this section, I discuss a number of these mechanisms thought to be important in driving atmospheric escape.

Jeans escape

The distribution of velocities and kinetic energies of atoms in a gas can be described with a Maxwell-Boltzmann distribution. In cool planetary atmospheres, atoms on the high tail of the distribution can have speeds greater than the escape velocity of the planet and will escape into space, as long as they don't collide with another atom in their path and dissipate their kinetic energy. In the upper layers of the atmosphere, where the rate of collisions is very low, these high-speed atoms will therefore be able to escape the planet's gravity unhindered. This occurs in the exosphere, above the exobase, where the mean free path is longer than one pressure scale height. In this case, atmospheric escape is said to be collisionless.

This thermal escape mechanism, dubbed Jeans escape, was first proposed by Jeans [1926], and later developed by Chamberlain [1963]. The rate at which Jeans escape occurs depends on the number of atoms in the high end of the kinetic energy distribution, which depends on the average temperature of the upper atmosphere. Jeans escape can be described with the Jeans parameter λ, the ratio between the average gravitational potential energy U of a gas and its average kinetic energy kT,

$$\lambda = \frac{U}{k_B T}. \tag{1.2}$$

The Jeans parameter can also be written in terms of the ratio between the escape velocity v_{esc} and the most probably velocity of the gas v_{mp} as follows,

$$\lambda = \left(\frac{v_{esc}}{v_{mp}}\right)^2. \tag{1.3}$$

Jean escape dominates in the regime where $v_{mp} << v_{esc}$ and thus $\lambda >> 1$, where the atmosphere is cool and tightly bound, with the vast majority of the atoms having speeds below the escape velocity. This regime applies to planets with high masses (and thus high escape velocities) and/or low equilibrium temperatures and thus low incident bolometric fluxes, which reduce the temperature of the upper atmosphere, pushing the distribution of velocities to lower speeds. Despite that Jean escape lies in a regime of low mass loss rates, it can also be important in driving significant atmospheric escape on long timescales, preferentially targeting the lightest particles, such as hydrogen.

Hydrodynamic escape

However, if the atmosphere is heated up to a high enough temperature, such that $v_{mp} \sim v_{esc}$ then λ becomes small and the atmosphere below the exobase is no longer tightly bound. Hydrostatic equilibrium ceases to apply as a large number of particles begin to escape the planet. The escape becomes a *hydrodynamic* flow that is collisional, carrying other atoms along with it [Hunten, 1982], with escape rates several orders of magnitude greater than Jeans escape.

Watson et al. [1981] first presented an analytical model to describe such a scenario in the context of the Solar System planets. In their model, EUV photons from the Sun are the source of energy – they are absorbed in the upper atmosphere, heating up and expanding the gas, launching a hydrodynamic flow that escapes the planet. This hydrodynamic flow is similar to the flow of solar wind that had been described by Parker [1960] and Parker [1964] earlier.

The discovery by Vidal-Madjar et al. [2003] of an escaping atmosphere from the hot Jupiter HD 209458 b in the Lyα line of hydrogen sparked renewed interest in studying the physical and chemical conditions of evaporating exoplanets. Lammer et al. [2003] first showed that the highly irradiated exospheres of hot Jupiter can be heated up to temperatures of $\sim 10^4$ K, a regime where hydrostatic equilibrium does not hold as the upper atmosphere expand dynamically, driving an outflow.

Subsequent studies modelled hydrodynamic flows in the atmospheres of hot Jupiters [e.g. Yelle, 2004; Tian and Toon, 2005; García Muñoz, 2007; Penz et al., 2008; Guo, 2011, 2013]. These models predicted that escape occurs in the form of a hydrodynamic outflow that reaches a temperature of $\sim 10^4$ K and remains collisional at the sonic point, at which point it becomes supersonic and thus causally detached from the atmosphere below it.

These models all require a source of energy for heating the upper atmosphere. In the sections below, I discuss two of the mechanisms thought to be dominant in providing energy for escape: energy deposited by XUV photons from the star (photoevaporation) and the bolometric flux from the star aided by thermal energy from the rocky core (core-powered mass loss).

Photoevaporation

Close-in exoplanets can receive large amounts of optical photons ($\times 10^2 - 10^3$ Earth insolations), as well as intense X-ray irradiation ($\times 10^2 - 10^5$ the X-ray flux incident on Earth). Despite the fact that the optical flux is typically 4–5 orders of magnitude greater than the X-ray flux, it is the X-rays that are responsible for driving the planetary outflow in the context of photoevaporation. This is because optical photons reach deep into the atmosphere and heat it up from within, contributing to puffing up the atmosphere. XUV photons, on the other hand, are much more readily absorbed in the upper layers, creating an ionisation front where the atmosphere is heated and the planetary wind is launched.

The model of hydrodynamic escape that Watson et al. [1981] introduced is powered by stellar EUV photons. They derived an expression for atmospheric mass loss purely from energetic arguments – balancing the incident energy deposited by EUV photons against the potential energy required for a certain amount of mass to overcome the planet's gravitational well and reach escape velocity. This is known as the *energy-limited* formulation. To derive the mass loss rate, we first consider the work required for a parcel of gas with mass m to overcome the planet's gravitational potential,

$$W_{esc} = \frac{GM_{\mathrm{p}}m}{R_{\mathrm{p}}}, \tag{1.4}$$

where M_{p} and R_{p} are the planet's mass and radius, and G is the gravitational constant. Secondly, we consider the energy deposited in the atmosphere by XUV heating,

$$E_{XUV} = F_{XUV}\mathrm{d}A\mathrm{d}t = F_{XUV}\pi R_{\mathrm{p}}^2\mathrm{d}t, \tag{1.5}$$

where F_{XUV} is the incident XUV flux on the planet. Equating both equations and solving for the quantity $\mathrm{d}m/\mathrm{d}t$ yields the mass loss rate for the energy-limited formulation,

$$\frac{\mathrm{d}m}{\mathrm{d}t} = \frac{\pi R_{\mathrm{p}}^3 F_{XUV}}{GM_{\mathrm{p}}}. \tag{1.6}$$

Lecavelier Des Etangs [2007] and Erkaev et al. [2007] provided a correction

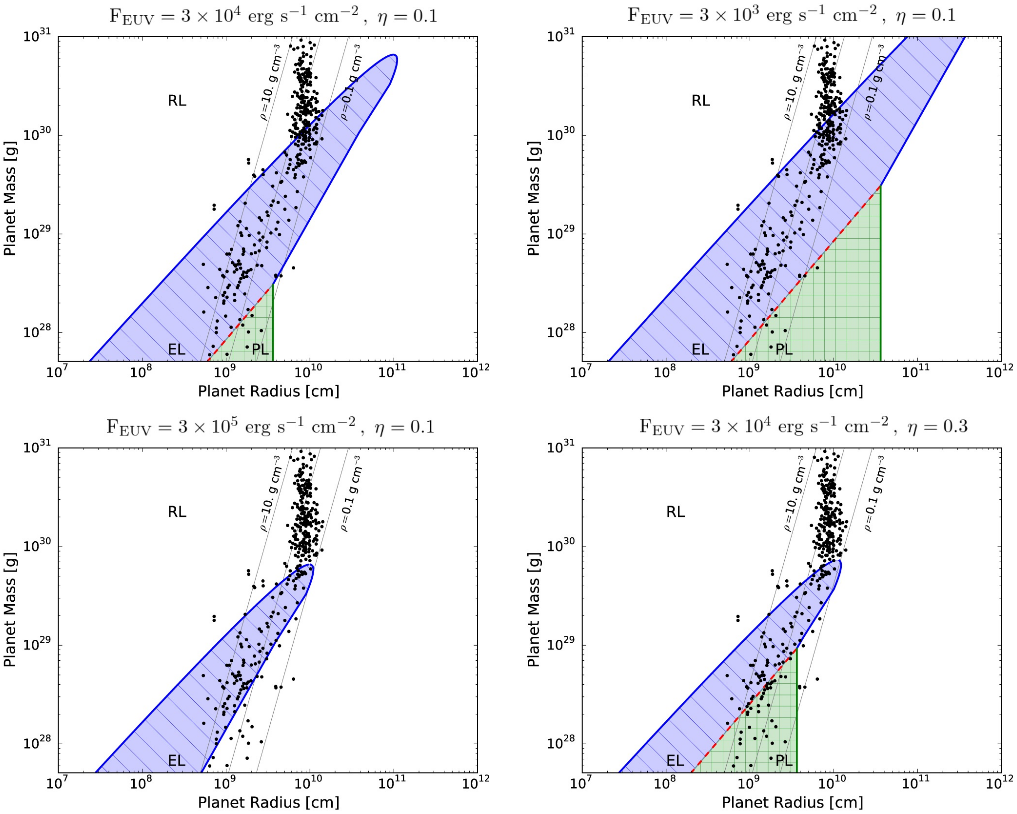

Figure 1.6: Diagram from Owen and Alvarez [2016] showing the locations of different atmospheric escape regimes in planet radius-mass space under a range of EUV irradiation levels (3×10^3–3×10^5 erg cm^{-2} s^{-1}) and mass loss efficiencies ($\eta = 0.1$ and 0.3). The regimes depicted are energy-limited (blue), photon-limited (green), and recombination-limited (white). Exoplanets on the Open Exoplanet Catalogue as of February 2015 are shown as black circles.

to this equation which considers that planetary material does not need to reach infinity to escape, but only the boundary where the gravitational pull from the star dominates over that of the planet, the Roche lobe. This correction factor K, applied to the formula, reduces the energy needed to remove a certain amount of mass, and thus enhances mass loss rates.

Additional parameters that expand the energy-limited formulation are the energetic efficiency η, which corresponds to the fraction of incident flux that goes into heating the atmosphere, and R_{XUV}, the radius at which XUV photons are absorbed [e.g. Salz et al., 2016]. Since XUV radiation is more readily absorbed higher in the atmosphere, its absorption radius is likely larger than the optical radius, such that $R_{XUV} \geq R_{\mathrm{p}}$, reducing the energy required to drive escape. This parameter is often represented as a function of planet radius instead $\beta = R_{XUV}/R_{\mathrm{p}}$; it is also squared ($\beta^2$) to represent a factor increase in cross-sectional area of absorption. All together, these parameters yield the following expression for the energy-limited model:

$$\frac{\mathrm{d}m}{\mathrm{d}t} = \frac{\eta \beta^2 \pi R_{\mathrm{p}}^3 F_{XUV}}{K G M_{\mathrm{p}}}, \tag{1.7}$$

where K is the correction by Erkaev et al. [2007] to account for the Roche lobe.

The choice of efficiency η and XUV absorption radius β, however, mask additional physics that the energy-limited model alone does not account for. Instead, some of the input energy that is absorbed in the upper atmosphere may be dissipated; atoms that become ionised and subsequently undergo recombination, cooling down via Lyα emission. As such, the energy-limited model provides an upper limit to the total mass loss rate possible from a hydrodynamic outflow.

Murray-Clay et al. [2009a] studied mass loss from hot Jupiters via EUV irradiation (with energy of 20 eV), and also improved upon previous models of atmospheric escape by including additional cooling mechanisms that further limit the temperature and speed of the outflow under certain conditions. They considered a hot Jupiter orbiting a main sequence Sun-like star under two scenarios: a low irradiation scenario, with $F_{\mathrm{EUV}} = 500\,\mathrm{erg\,cm^{-2}\,s^{-1}}$, and a high irradiation scenario, with $F_{\mathrm{EUV}} = 5 \times 10^5\,\mathrm{erg\,cm^{-2}\,s^{-1}}$.

In the low flux scenario, they found most of the input EUV energy goes into PdV work, lifting the gas out of the planet's potential well and resulting in mass loss. Moreover, the photoionisation rate from the EUV photons is balanced for the most part by gas advection (loss of ions via escape). In this case, they found that atmospheric escape is well described by the energy-limited model with efficiency $\eta \sim 0.3$, where the mass loss rate scales almost linearly with incident flux ($\dot{M} \propto F_{\mathrm{EUV}}^{0.9}$)

In the high flux scenario, on the other hand, Murray-Clay et al. [2009a] determined that most of the input energy is dissipated in the form of Lyα radiation emitted by ions as they undergo radiative recombination. In this scenario, the photoionisation rate is thus balanced by recombination instead. In this *recombination-limited* regime, mass loss rates scale more slowly with incident flux ($\dot{M} \propto F_{\mathrm{EUV}}^{0.6}$), demonstrating a significant deviation from energy-limited models.

There are additional processes that aid in either heating or cooling the flow, increasing or decreasing the escape rates, respectively. For instance, a fraction of the photons emitted during Lyα cooling may be reabsorbed, reducing the efficiency of this cooling mechanism. The atmosphere can also be cooled via H_3^+ emission [Miller et al., 2013] and metal emission lines [C, N, O, Si, and their ions, Koskinen et al., 2013].

Stellar wind can also interact with the escaping outflow, shaping it into comet-like tails of gas which have been observed in Lyα transits [Ehrenreich et al., 2015], as well a propelling the escaping wind to the speeds of hundreds of $\mathrm{km\,s^{-1}}$ observed in Lyα and He triplet transits (see Section 1.3.2), compared to $\sim 10\,\mathrm{km\,s^{-1}}$ that XUV heating drives [Holmström et al., 2008; Khodachenko et al., 2017]. If the upper atmosphere expands beyond the planet's magnetosphere, which is more likely to occur on planets with shallow potentials and/or weak magnetospheres, stellar wind may contribute to Lyα absorption non-thermally even when almost no mass is actually escaping the planet [Kislyakova et al., 2013, 2014], interacting with the extended atmosphere and producing energetic neutral atoms (ENAs) via charge exchange. Vidotto and Cleary [2020] also found that, on high gravity planets, stellar wind can confine the outflow instead, reducing the escape rates. On the other hand, Kubyshkina et al. [2022] found that if the stellar wind is dense and fast, it can reach down to the upper atmosphere and can suppress Lyα signatures whilst at the same time contributing to the erosion of the upper atmosphere, increasing the mass loss rates significantly.

Such studies have also highlighted that super-Earths and mini-Neptunes lie in a regime of atmospheric escape characterised by low gravity and high ionising fluxes. This is particularly true during the early stages of their evolution, when their atmospheres are hot and puffy, and their host stars are the most X-ray active [Johnstone et al., 2015b]. In this regime, the energy-limited model tends to underpredict the mass loss rates on small planets. On the other hand, the energy-limited model over-predicts escape rates on stable hydrostatic atmospheres, such as those on cool massive Neptunes and sub-Neptunes, where Jeans escape dominates instead [Kubyshkina et al., 2018].

Owen and Alvarez [2016] identified an additional regime of escape, dubbed the “photon-limited” regime, which applies to planets with shallow gravitational potentials and low XUV fluxes, where atmospheric escape is limited by the number of incident XUV photons instead. Figure 1.6, produced by Owen and Alvarez [2016], shows the regions in planet mass-radius parameter space where the three different regimes of atmospheric escape apply to planets subjected to a range of EUV fluxes.

In practice, many models of atmospheric escape also assume a single energy for the incident ionising photons. Stellar high energy emission, however, is not limited to a single wavelength, and absorption cross-sections depend very strongly on wavelength. Consequently, photons of different energies are absorbed at different depths in the upper atmosphere, heating different layers of the atmosphere. Cecchi-Pestellini et al. [2009] found that X-ray photons ($> 100\,\mathrm{eV}$) can penetrate further into the atmosphere, heating deeper layers, whilst EUV photons are absorbed higher up. Moreover, King and Wheatley [2021] showed that whilst X-ray emission dominates in young active stars, EUV emission takes over for older less active stars. In Section 1.4.4, I discuss the relative X-ray and EUV emission of stars in more detail.

Owen and Jackson [2012] identified two regimes in which the escape is driven by either X-rays or EUV. They argued the regime a planet is in depends on the relative location of two points in the atmosphere: the ionisation front, where the atmosphere is heated and the wind is launched, and the sonic point, where the flow becomes supersonic and causally detached from the atmosphere below. At high XUV fluxes, the ionisation front lies above the sonic point. Here, X-rays are absorbed by a flow that is already supersonic and detached from the planet, and hence the EUV photons absorbed above will not contribute to escape. At low XUV fluxes, on the other hand, the ionisation front lies below the sonic point. Here, X-ray heating produces a highly sub-sonic flow that then crosses into the EUV ionisation front above, which launches a supersonic flow. Since stellar X-ray emission declines with the age of the star (as I discuss in Section 1.4.3), there is also a cross-over time at which escape turns from X-ray dominated to EUV-dominated, although under certain circumstances the escape may remain entirely X-ray or EUV driven for the entirety of the lifetime of the envelope.

But how far away from the planet's optical radius are XUV photons absorbed? Kubyshkina et al. [2018] modelled the absorption of high energy photons in planet atmospheres at two wavelengths (60 nm/20 eV for EUV and 5 nm/250 eV for X-rays) along the path between the star and the planet, taking into account their absorption cross-sections and the density profile of the atmosphere. Their results suggested the XUV absorption radius, R_{XUV}, typically takes values between 1 and 3 planet radii, and in some cases (very low gravity planets) it can reach 10+ planet radii; in such regime, which I describe in the section below, the atmosphere would be freely escaping due to bolometric heating, not XUV photons.

Core-powered mass loss

The source of energy that powers hydrodynamic escape need not be stellar XUV photons. Ginzburg et al. [2016] instead proposed that stellar bolometric flux can achieve the same result if the atmosphere is also heated and inflated by the thermal energy from the solid core leftover from the formation and gravitational contraction of the planet. This mechanism would have the greatest impact on low gravity planets with high equilibrium temperatures. They predict this proposed mechanism, core-powered mass loss, may completely remove the gaseous envelope of planets with atmospheric mass fractions below 5%.

Ginzburg et al. [2018] and Gupta and Schlichting [2019] showed that simulations of atmospheric escape with core-powered mass loss can reproduce the period-radius valley, and Gupta and Schlichting [2020] showed that this mechanism acts on timescales of several Gyr, much longer than typically assumed for photoevaporation. This occurs because this mechanism is driven only by (1) the thermal energy in the core and (2) the stellar bolometric flux incident on the planet. Bolometric heating stays nearly constant for several Gyr whilst the host star is in the main sequence, and planets cool down slowly also in Gyr timescales, contracting by a relatively small amount as well (no more than 1-2 R_E). As a result, core-powered mass loss predicts small (but constant) mass loss rates on sub-Neptunes.

Indeed, Ho and Van Eylen [2023] analysed short cadence observations from the *Kepler* satellite and refitted the transits of 431 planets. They found that the period-radius valley is weakly dependent on stellar age, consistent with core-powered mass loss, which acts on Gyr timescales [Gupta and Schlichting, 2020], and less consistent with photoevaporation, which is expected to act in ~ 100 Myr timescales [Owen and Wu, 2017]. King and Wheatley [2021] also argued that, whilst X-ray emission declines steeply with age, EUV decay is likely to be more gradual, remaining significant for several Gyr, matching the predicted evaporation timescales of core-powered mass loss.

Distinguishing between XUV photoevaporation and core-powered mass loss is not trivial. Both mechanisms rely on atmospheric heating to drive a hydrodynamic outflow from the planet, and both produce very similar signatures in exoplanet populations (i.e. the radius valley and its dependence on orbital period). However, the two mechanisms can also predict very different mass loss rates on some planets (up to several orders of magnitude) and act differently depending on the mass of a planet and its equilibrium temperature. This means that, for each model to reproduce the observed distribution of exoplanet radii, they require planet populations to follow a distinct (albeit similar) distribution in core mass and starting envelope mass fraction [Rogers and Owen, 2021; Owen and Schlichting, 2024]. Unfortunately, few exoplanets have mass measurements, and those that do often lack the necessary precision to resolve which mass loss mechanism is dominant. This problem is also exacerbated by the uncertainty in the internal composition of planetary cores [e.g. Zeng et al., 2019; Venturini et al., 2020]. Moreover, efforts to robustly distinguish between the two models using the observed location of the radius valley as a function of orbital period, stellar mass, and age simultaneously have so far been met with little success [Rogers et al., 2021; Ho and Van Eylen, 2023].

The two models may also differ to a degree in the timescales in which they sculpt exoplanet populations. Whilst XUV photoevaporation predicts faster evolution in the first 500 Myr when stellar X-ray emission is the strongest and slower evolution in the subsequent 1-2 Gyr when the emission becomes fainter and EUV-dominated [King and Wheatley, 2021], core-powered mass loss predicts only a gradual evolution during the first few Gyr [Gupta and Schlichting, 2020]. Resolving the relative distribution of super-Earths and mini-Neptunes as a function of age accurately, particularly at early ages, could prove to be an important piece of evidence to distinguish between the two models. Unfortunately, there have been few discoveries of young exoplanets to date [Battley et al., 2020], and the age estimates of older planets are poorly constrained. The upcoming *PLATO* mission, which will enable precise characterisation of stellar ages using asteroseismology [Rauer et al., 2014], could prove vital in breaking the degeneracy between photoevaporation and core-powered mass loss.

From a theoretical point of view, Owen and Schlichting [2024] compared the relative impact of photoevaporation and core-powered mass loss over the lifetimes of gaseous exoplanets. They found that which mechanism is dominant will depend on the relative depth in the atmosphere at which each mechanism launches the outflow. In photoevaporation, the hydrodynamic wind is launched from the radius at which XUV photons are absorbed (R_{XUV}), whereas in core-powered mass loss, this occurs at the planet's Bondi radius (R_B), the point where a bolometric-driven outflow becomes supersonic. Owen and Schlichting [2024] argued that photoevaporation is dominant on high gravity planets with low equilibrium temperatures, where the XUV absorption radius is below the Bondi radius ($R_{XUV} < R_B$). On the other hand, core-powered mass loss dominates on low gravity planets with high equilibrium temperatures, where the Bondi radius lies below the XUV absorption radius ($R_{XUV} > R_B$). This also means that, if XUV flux is weak enough, the planet would instead launch an outflow driven by the core-powered mechanism.

The two processes, however, can also be significant simultaneously. In this regime, which they termed "enhanced photoevaporation", the core's thermal energy can puff-up the envelope, reducing its density, and thus increasing the efficiency of photoevaporation. The existence of these two regimes also implies that a planet may start out dominated by core-powered escape and later transition into XUV-dominated escape once the core has cooled down enough.

Boil-off

Owen and Wu [2016] showed that an additional mass loss mechanism, "boil-off", can shape the populations of small close-in exoplanets at the very beginning of their lives, whilst they are still embedded in the proto-planetary disk. Boil-off consists on a rapid loss of hot atmospheres on small worlds that have accreted significant H/He envelopes during their formation, caused by the pressure from the protoplanetary disc being lifted as the disc is dispersed. This mechanism takes place when disk dispersal timescales are much shorter than a planet's cooling timescale, such that the planet's atmosphere cannot thermally respond quickly enough to the loss of pressure from the protoplanetary disk causing it to expand adiabatically. External heating (from the star or the disk) would then induce a hydrodynamic flow from the planet, causing it to loose a large part of its atmosphere. The adiabatic expansion of the atmosphere also cools it, reducing both its cooling timescale and the escape rate; when the planet has cooled down enough, it no longer expands rapidly and boil-off stops. [Rogers et al., 2024], using numerical evolution models for gaseous accretion and boil-off, determined that even though most small planets can accrete large gaseous envelopes consisting of 10% of their masses, boil-off then truncates these envelopes to mass fractions of only 1-2% after disc dispersal in timescales under 10 Myr, and for very close-in super-Earths it can also completely remove the accreted atmosphere. After boil-off finishes shaping the distribution of starting gaseous envelopes, their subsequent evolution will be dictate by other mass loss processes, such as photoevaporation and/or core-powered mass loss, over longer timescales of 100 Myr to several Gyr.

1.4 X-ray emission of stars

As discussed in Section 1.3, X-ray and EUV photons of stellar origin deposit large amounts of energy in the upper atmospheres of exoplanets, enough to drive atmospheric escape and sculpt exoplanet populations. In order to test our models of atmospheric escape and our predictions for exoplanet populations, we need to characterise the high energy environment of exoplanets and how it evolves throughout their lifetimes. To do so, we must characterise the current X-ray emission of their host stars as well as their emission *histories*.

This can be achieved with X-ray surveys of the sky, characterising the X-ray emission from many stars across spectral types, ages, and activity levels. Sensitive X-ray surveys were pioneered by the Einstein observatory, launched by NASA in 1978, the first space-based single-purpose X-ray imaging telescope. It performed the first population-level study of the X-ray emission of stars across the HR diagram [Vaiana et al., 1981]. Its X-ray survey of 126 stars classified most FGKM stars as soft (low energy) X-ray sources with luminosities $10^{26} - 10^{31}\,\mathrm{erg\,s^{-1}}$. Since then, deep X-ray surveys of the sky carried out by further missions, namely ROSAT, XMM-Newton, & Chandra, have greatly expanded our inventory of X-ray emitting stars.

1.4.1 Stellar coronae

As the brightest X-ray source in the sky, the field of X-ray astronomy began with observations of the Sun. X-ray emission from the Sun was predicted by Grotrian [1939] and Edlén [1943], and later observed by Burnight [1949]. These X-ray photons were attributed to an extended atmosphere of hot plasma around

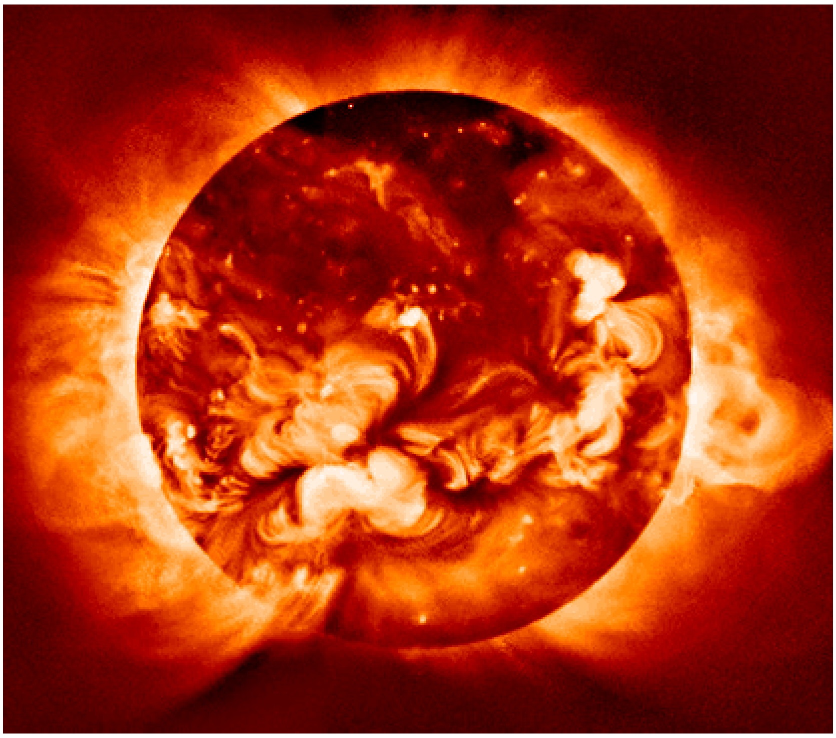

Figure 1.7: Image of the Sun in X-ray wavelengths taken by the Yohkoh satellite in 1992. The image was obtained by combining multiple observations of the Sun at 1 keV. *Credit: Yohkoh Soft X-ray Telescope, ISAS, Japan.*

the Sun, an X-ray corona. Later high-resolution observations, pioneered by the *Yohkoh* satellite launched in 1991, revealed the presence of complex structures in this corona, as seen in Figure 1.7: active regions with a multitude of arch-like loops of plasma extending tens of thousands of kilometres above the surface, as well as X-ray dark regions or coronal holes which have been interpreted as cool regions from which stellar material is launched into space. These X-ray observations of the Sun highlighted the importance of magnetic fields in shaping and understanding the solar corona and thus the mechanism responsible for the emission of high energy photons.

The atmosphere of the Sun is highly structured into layers of plasma with different temperatures. The lowest layer, the photosphere, defines the visible surface of the Sun under which the plasma becomes opaque to visible wavelengths. This layer is 10–100 km thick and has a blackbody temperature of about 5770 K. Over that is the chromosphere, characterised by strong emission lines, particularly Hα and Lyα, but also Ca II H and K lines in the UV. These Ca lines can be used to estimate the Mount Wilson S-index, a measure of the chromospheric activity level. This layer is a few thousand kilometers thick; its temperature remains constant at at 6000 K initially but then rises to $\sim 30,000$ K towards the top.

Above it sits the transition region, a thin layer $\sim$ 200 km thick where the temperature of the plasma rises drastically to $\sim$2 million K and where magnetic forces begin to dominate over gravity and fluid dynamics in shaping the plasma. In this region, emission lines transition from IR, visible, and NUV wavelengths to FUV, EUV, and X-rays.

The transition region is followed by the corona, the outermost layer of the solar atmosphere, which extends several solar radii into space. The plasma in the corona is optically thin with a very low density of 10^5 cm^{-1}; its temperature reaches 2 million K and it is shaped by magnetic fields into arch-like coronal loops. As a result of such extreme temperatures, the corona shines brightly in the X-rays and EUV, with most radiation dominated by line emission from highly ionised species (e.g. Fe, Ne, Mg, Si, Ca) which still retain few electrons in their inner shells [Del Zanna and Mason, 2018, and references therein].

The stark contrast in temperature between the photosphere ($\sim$5000 K) and the corona ($\sim$2 million K) necessitates a mechanism by which energy is transported from the stellar interior and the photosphere to the much hotter corona and then dissipated into heat. The dominant mechanism for energy transport is still under debate, giving rise to the so-called coronal heating problem [Klimchuk, 2006].

The two leading mechanisms in literature are magnetic waves and magnetic reconnection. Magneto-hydrodynamic (MHD) waves in the solar atmosphere arise from convection in the photosphere which induces an oscillatory motion. These waves are carried by structures called flux tubes, which are cylindrical regions of space enclosed by parallel magnetic field lines acting as very efficient waveguides. Once they reach above the photosphere, the flux tubes expand rapidly due to the drastic decrease in density as magnetic pressure pushes the magnetic field lines apart. As a result, the MHD waves dissipate their energy into heat via resonant absorption and phase mixing mechanisms [Nakariakov and Verwichte, 2005; Erdélyi and Ballai, 2007].

Magnetic reconnection, on the other hand, arises from the topology of the magnetic field. Convection, rotation, and turbulence in stellar interiors can cause magnetic field lines with opposite directions to cross. In such regions, current is forced into a thin surface between the two opposite field lines (a "current sheet") where the density of the magnetic field is increased, storing large amounts of energy in the magnetic field. The local properties of the plasma allow the magnetic field to diffuse through the plasma, causing these magnetic field lines to snap and rejoin into a different topology that relieves the pressure. This releases the stored magnetic energy as thermal and kinetic energy [Priest and Forbes, 2000; Klimchuk, 2006; Hesse and Cassak, 2020]. This mechanism is also thought to be responsible for solar flares.

Moreover, plasma in the corona presents an array of complex shapes and structures guided by magnetic fields [Rosner et al., 1978]. Coronal loops consist of hot plasma entrapped by magnetic flux tubes, which may interact and release their energy as flares. Coronal holes, on the other hand, are regions of low X-ray emission with open magnetic field lines that launch stellar wind into space.

Beyond the Sun, chromospheric and coronal activity are prevalent on main sequence stars. Catura et al. [1975] first observed the star Capella in the X-rays and measured an X-ray luminosity of $10^{31}\,\mathrm{erg\,s^{-1}}$, four orders of magnitude greater than the Sun. Moreover, Vaiana et al. [1981] presented an X-ray survey of the sky with the *Einstein* mission and found that the presence of X-ray emission and coronae is ubiquitous in stellar populations across the HR diagram, with detections of X-ray emission originating in main sequence stars from OB to M type, as well as pre-main sequence and evolved stars. They also found a great diversity in coronal activity levels across late-type stars, spanning three orders of magnitude in X-ray luminosity.

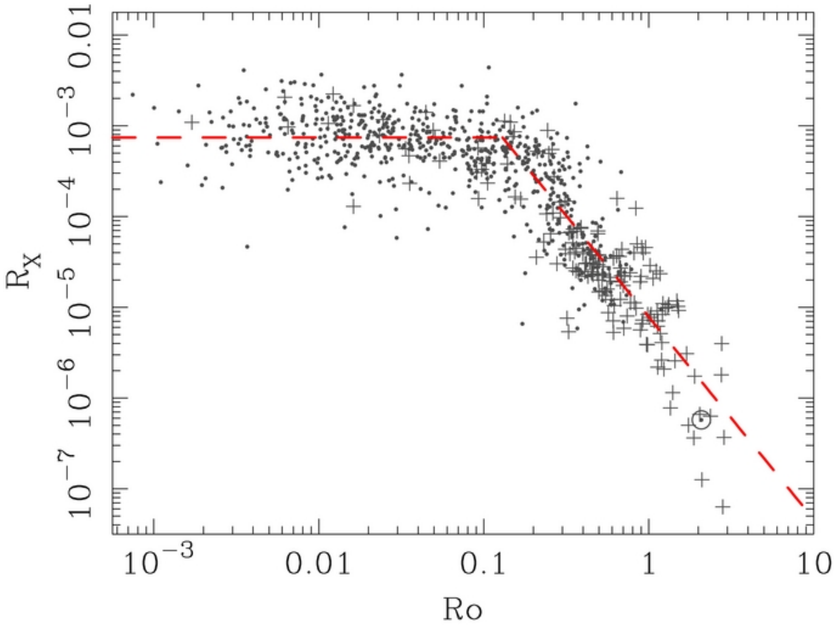

Figure 1.8: Plot of Rossby number *Ro* against X-ray activity R_X from Wright et al. [2011]. The red dashed lines indicate their fits to the saturated and unsaturated regimes of the rotation-activity relation.

1.4.2 The rotation-activity relation

Kraft [1967] first noted that F & G field stars with a higher chromospheric Ca II emission also had a higher rotational velocity. Using observations from the *Einstein* observatory, Pallavicini et al. [1981] also found a link between the X-ray luminosities of main sequence late-type stars and their projected rotation rate $v \sin i$, where v is the rotational velocity of the star and i is the stellar inclination relative to Earth. In this relation, X-ray luminosity increases with rotation rate as $L_x \sim (v \sin i)^{1.9 \pm 0.5}$.

This was consistent with the dynamo theory for stellar interiors [Tassoul, 1978; Parker, 1979], wherein stellar magnetic fields are powered by a magnetic dynamo mechanism. Plasma inside stars, which acts as a conducting fluid, is in motion due to convection powered by nuclear fusion in the star's core as well as stellar rotation. This motion results in a differential rotation within stellar interiors; rotation also induces Coriolis forces on the plasma.

Together, differential rotation and Coriolis forces cause rising convective cells to expand and rotate, twisting magnetic field lines into loops. These loops drive plasma (and thus electric current) into circular motions, which wind up the stellar dynamo and generate the magnetic field [e.g. Brandenburg and Subramanian, 2005; Browning et al., 2006; Guerrero et al., 2016].

A region of particular importance in this process is the interface between the radiative and convective zones within stars, the tachocline, where the stark difference between the rotation rates of the two layers creates a region of strong shear. It is only in this region that the plasma loops remain stable. In the radiative zone there is no differential rotation to maintain them, and in the convective zone they would rise, expand, and dissipate [Browning et al., 2006].

Further studies [e.g. Walter, 1982; Noyes, 1983] tightened the rotation-activity relation by expressing coronal activity as the ratio between X-ray and bolometric luminosities (L_X/L_{bol}), and Noyes et al. [1984] linked it to the *Rossby number*. The Rossby number is defined as the ratio between the stellar rotation period P_{rot} and the convective turnover time τ_{conv}, which measures the time it takes for a convective cell to rise to the surface of the star and is a function of spectral type. Compared to the rotation rate alone, the Rossby number better characterises the degree of differential rotation as a function of radius and thus the strength of the dynamo. In fluid mechanics, a fluid with a small Rossby number is strongly affected by Coriolis forces, whereas at large Rossby numbers the effects of rotation become negligible.

Vilhu [1984] also found that the rotation-activity relation breaks down for fast rotators with Rossby numbers below 0.1, where the X-ray activity reaches a constant value of $L_{\mathrm{X}}/L_{\mathrm{bol}} \sim 10^{-3}$ and the corona is said to *saturate*.

Pizzolato et al. [2003] extended this analysis to 259 late-type stars with X-ray observations from ROSAT. They determined that the spin periods at which stars saturate is dependent on mass, from ~ 1.5 days for solar-mass stars to ~ 10 days for early M-dwarfs. Saturation, however, occurs at a fixed Rossby number of $\mathrm{Ro} < 0.1$ for all stars regardless of mass. They additionally confirmed that the rotation-activity relation holds up even for the lowest mass stars with fully-convective interiors ($< 0.3\,\mathrm{M}_{\odot}$).

Wright et al. [2011] presented an extensive sample of 824 late-type stars with measured spin periods and X-ray observations from ROSAT. They thus refined the power-law fit to the unsaturated regime with a slope of -2.7, which I plotted in Figure 1.8. They further determined empirical thresholds for saturation as a function of stellar mass. They found that late-type M dwarfs may remain saturated for several Gyr, whilst, on the other end of the main sequence, early-type F dwarfs may skip the saturated regime altogether. Wright and Drake [2016] and later Wright et al. [2018] extended this analysis to fully convective M-dwarfs, which they found also follow this relation. Late M-dwarfs, however, are fully convective and thus have no tachocline, which is thought to be required to generate coronal activity under traditional dynamo theory. These observations suggest fully convective stars require an alternative dynamo mechanism powered with no tachocline.

Several possible mechanisms have been proposed for the origin of coronal saturation; these include dynamo saturation, coronal filling, and coronal stripping.

Dynamo saturation posits saturation is originated within the stellar interior in the generation of the dynamo itself [Gilman, 1983; Vilhu and Walter, 1987]. This would mean that other activity indicators, such as chromospheric indicators, should also saturate. Observations of the chromospheric activities of saturated stars, however, have failed to find a clear saturation threshold in Rossby number that agrees with that from X-ray observations [Cardini and Cassatella, 2007; Mamajek and Hillenbrand, 2008].

Under the coronal filling hypothesis [Vilhu, 1984], the surfaces of saturated stars are fully covered in active regions, hindering their growth and the formation of new ones. This is evidenced by a strong correlation between X-ray luminosity and surface area. On the other hand, low-amplitude activity cycles have been detected in saturated stars [e.g. Wargelin et al., 2017], and the mechanism requires enhanced stellar densities that may be unphysical [Vilhu, 1984]. Moreover, solar activity scaled to a filled corona falls one order of magnitude short of the observed saturation level of $L_{\rm X}/L_{\rm bol} \sim 10^{-3}$.

As for the coronal stripping hypothesis, Jardine and Unruh [1999] argued the coronas of very fast rotators experience centrifugal forces that can overcome gravity, causing large coronal loops to break apart into coronal holes. Wright et al. [2011], however, found that the co-rotation radius at which this phenomenon would affect the corona differs significantly from the observed saturation Rossby number, and instead argued that saturation in the empirical sense originates from a change in the dynamo configuration that does no longer depend on spin but rather on bolometric luminosity alone. The dynamo of a *saturated* star would instead originate in turbulent convection, which may also be able to produce large-scale magnetic fields [Brun et al., 2004]. This dynamo type would also explain magnetic activity on saturated M-dwarfs, which are fully convective and thus have no tachocline to power a rotationally-induced dynamo.

1.4.3 The age-activity relation

Accounting for age in studies of stellar spin and X-ray emission is essential in understanding how stellar activity evolves and thus its impact in the evaporation history of close-in exoplanets.

Skumanich [1972] first studied Ca^{+} emission and rotation in open clusters and noted that both chromospheric activity as well as spin period decayed with age. This suggested that age and rotation were predicted to be linked by the phenomenon of spin-down, wherein stars would decelerate throughout their lives by the loss of angular momentum through stellar wind. This process also creates a negative feedback loop: stellar rotation powers magnetic activity, which also drives stellar wind, which results in faster spin-down [Cranmer and Saar, 2011] As a result, fast rotators will spin down at a greater rate than slow rotators, causing their spins to converge over time. This occurs mostly within the first Gyr of age, after which the past activity of a star (whether it was a fast or a slow rotator in its youth) is erased, as seen in Figure 1.9.

In the X-rays, stars will thus start off as fast rotators and X-ray saturated. Initially, their X-ray emission remains constant even though they are spinning down. Once the saturation threshold is crossed, X-ray emission begins declining

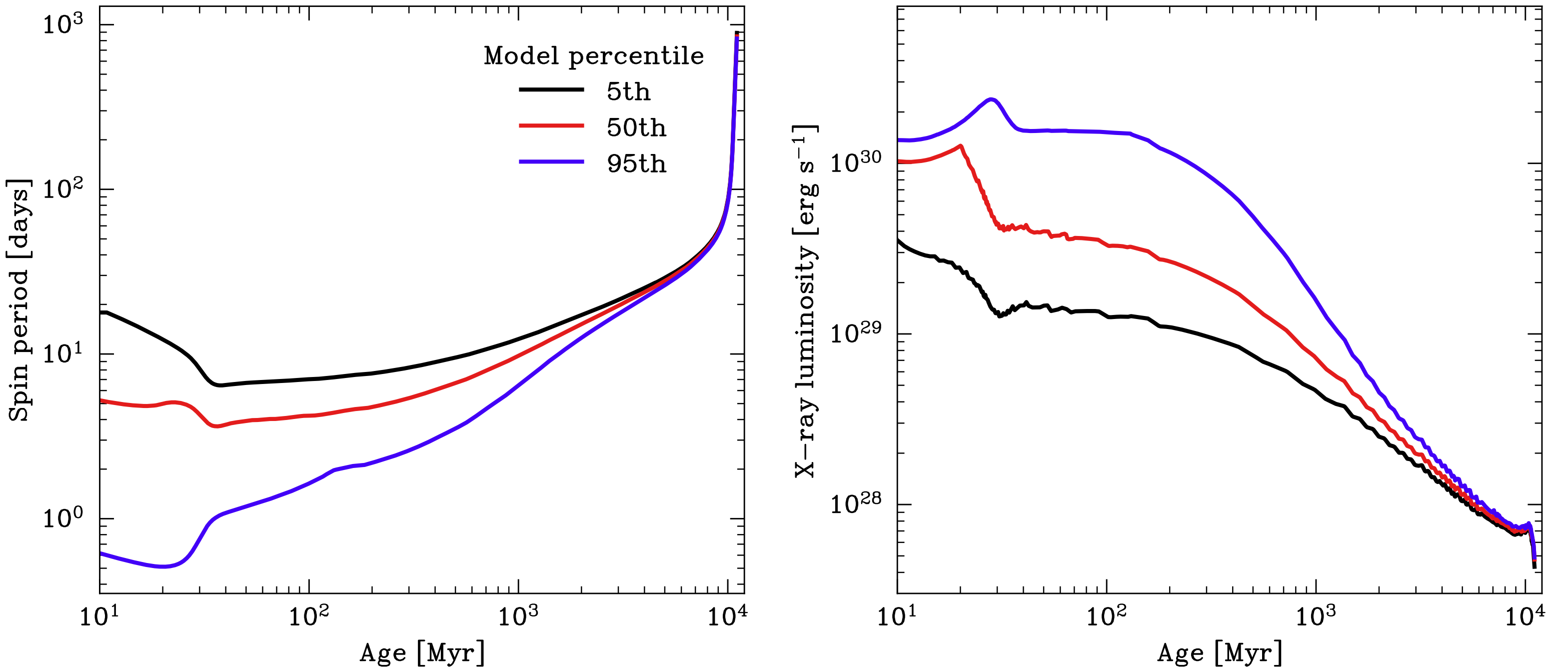

Figure 1.9: **Left panel**: stellar spin period plotted against age showing the spin evolution models by Johnstone et al. [2021] for a Sun-like star. The lines represent spin evolution of the 5th, 50th, and 95th percentiles of the distribution of spin periods observed in open clusters. **Right panel**: X-ray luminosity plotted against age showing the X-ray evolution models by Johnstone et al. [2021], following the left panel.

in par with spin-down.

Jackson et al. [2012] collected X-ray observations of 13 open clusters with ages ranging 5–740 Myr and built an *age-activity* relation as a function of spectral type, parametrised as $(B{-}V)_0$ colour. They found that the X-ray activity of cluster stars remains constant (saturated) up to the age of ∼100 Myr, after which it begins declining following a power law with index 1.2, which indicates that by the age of 1 Gyr, X-ray emission has declined two orders of magnitude below the saturation level. They also noted a dependence of the saturation X-ray activity to the $(B{-}V)_0$ colour, ranging from $\log_{10} L_X/L_{\mathrm{bol}} = 4.3$ for F-dwarfs to $\log_{10} L_X/L_{\mathrm{bol}} = 3.1$ for M-dwarfs.

More recently, Johnstone et al. [2021], building on the work by Tu et al. [2015] and Johnstone et al. [2015a], presented spin and X-ray evolution models that track how X-ray emission evolves as a function of spin, age, and spectral type for late-type stars. They introduced models of angular momentum evolution of stars, and anchored these models to spin period distributions from open clusters with ages spanning 5 Myr to 5 Gyr, such that the starting rotation rate of a star (or its percentile in the observed distributions) serves as an additional input to their models. In practice, this supports modelling the spin histories of both fast and slow rotators at young ages before they spins decrease and converge at more advanced ages. Additionally, Johnstone et al. [2021] fitted a rotation-activity relation to the data presented by Wright et al. [2011] and used it to translate their rotational sequences to X-ray evolution tracks. In Figure 1.9 I plotted the spin and X-ray evolution models by Johnstone et al. [2021] for a $1\,\mathrm{M}_\odot$ star. These show the spin evolution tracks for a star that started out as a fast rotator (5th percentile track), a median rotator (50th percentile track), and a slow rotator (95th percentile track). The corresponding X-ray emission histories show that a fast rotator will be one order of magnitude more active in the X-rays than a slow rotator for the first ~ 500 Myr of age.

In recent years, accurate astrometry and photometry from the *Gaia* mission has permitted refining cluster membership lists by screening for non-members that do not match the cluster kinematics. Núñez et al. [2022] presented membership lists curated with *Gaia* of the Praesepe and Hyades open clusters, as well as spin periods and X-ray luminosities for hundreds of their members. They found all dwarfs later than M3 type are still saturated at the age 700 Myr, whilst most FGK stars have spun down to X-ray activities $\sim 1 - 5 \times 10^{-5}$. They additionally noted a tentative link between rotation and coronal metallicity, where fast rotators have

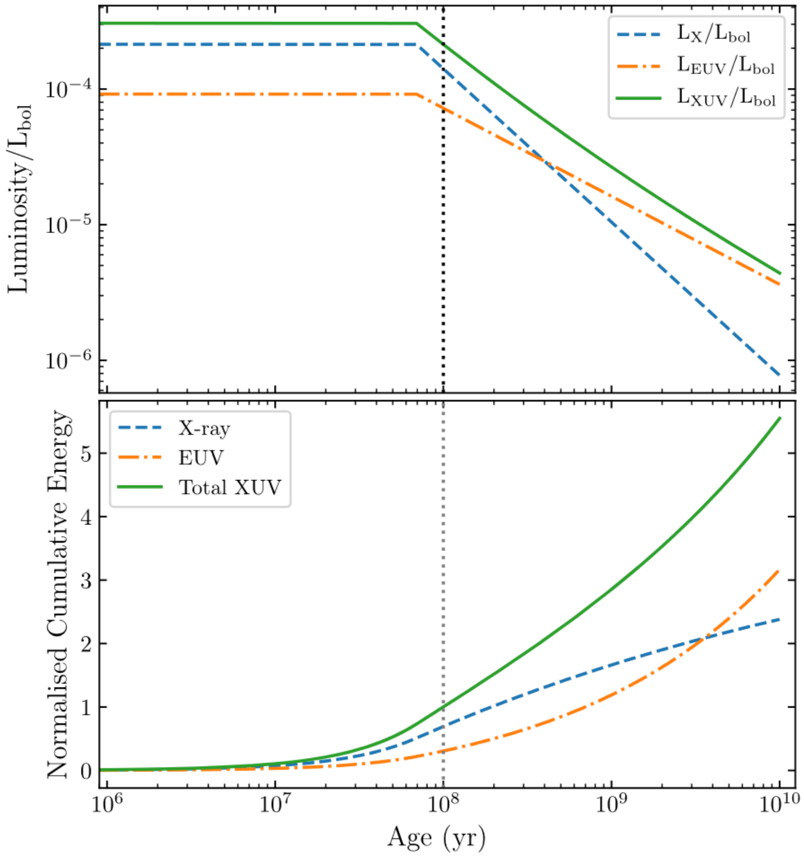

Figure 1.10: Figure from King and Wheatley [2021] showing the predicted evolution of stellar emission in X-ray (blue line) and EUV (orange line) wavelengths (top panel), and their cumulative energy across time (bottom panel).

lower coronal abundances of ~ 0.1 relative to solar whilst slow rotators (Ro> 0.3) have higher metallicities of ~ 0.4 but also a much larger spread of $0.1 - 0.5$.

Moreover, stellar evolution models predict that metal-rich stars should be more magnetically active and spin down more effectively, resulting in slower spin periods at later ages [e.g. van Saders and Pinsonneault, 2013; Karoff et al., 2018; Amard and Matt, 2020]. This relation between photospheric metallicity and magnetic activity arises from physics of stellar interiors: metal-rich stars have deeper convective layers and thus longer convective turnover times that reduce the Rossby number, strengthening the dynamo, and increasing magnetic activity. In line with their predictions, Amard et al. [2020]; See et al. [2024] found that old stars in the Kepler field with higher photospheric metallicities have slower rotation periods.

1.4.4 The extreme ultraviolet

So far, I have discussed stellar emission in the context of X-ray astronomy, which spans energies between 0.1 keV and 4 keV, since it offers ample observational constraints, benefiting from multiple observatories that have surveyed the sky for the last thirty years. Stars that are older and slowly rotating, however, have cooler coronae that emit the bulk of their high energy emission below X-ray wavelengths [Ribas et al., 2005], between 13.6 and 100 eV, which comprises the extreme ultraviolet. EUV photons are also responsible for populating the metastable helium triplet, one of the most prominent signatures of atmospheric escape, as I discussed in Section 1.3.1. EUV radiation may also be the main driver of atmospheric escape if the X-ray heated planetary wind is still sub-sonic when it crosses the ionisation front, where it becomes EUV-heated.

Stellar EUV emission, however, is unobserved – there is currently no observatory that surveys the sky in EUV wavelengths. Moreover, EUV photons suffer from significant absorption from atomic hydrogen in the ISM, completely obscuring coronal emission from stars beyond only 50-60 pc [Barstow et al., 2014].

The Extreme Ultraviolet Explorer (EUVE) surveyed the solar neighbourhood in the EUV, operating between 1992 and 2001, and compiled an atlas of 22 late-type main sequence stars from F-type to M dwarfs [Craig et al., 1997]. Moreover, the Sun also benefits from extensive EUV observations as well as precise spectral characterisation, which is often extrapolated to other stars.

In order to estimate the EUV component of stellar high energy emission, several studies have built empirical relations between X-rays and EUV using observations of both the Sun and of other stars. Chadney et al. [2015] used observations of the Sun across one full solar cycle (2002–2013) from the *TIMED/SEE* instrument to link X-ray and EUV surface fluxes, and later King et al. [2018] expanded the relation to improve uncertainties and include newer data. They found that such relation followed a power law, such that:

$$\frac{F_{\rm EUV}}{F_X} = 425 F_X^{-0.42}, \tag{1.8}$$

where F_X and $F_{\rm EUV}$ are the X-ray and EUV fluxes at the surface of the Sun, respectively. Such relation implies that EUV emission overtakes X-rays for low X-ray activities below $L_X/L_{\rm bol} < 2 \times 10^{-5}$ on Sun-like stars. Moreover, Johnstone et al. [2021] used data from EUVE satellite combined with X-ray observations from ROSAT to build empirical surface flux relations, which they found to be in agreement with solar data from Chadney et al. [2015] and King et al. [2018].

Alternatively, it is also possible to reconstruct the full EUV spectrum of a star from a synthetic spectral energy distribution (SED) using observational constraints of its UV and X-ray emissions [Ehrenreich et al., 2015]. Sanz-Forcada et al. [2011] and later Sanz-Forcada [2022] estimated EUV emission by constructing synthetic spectra instead, using coronal emission models and an atomic database of emission lines. They further tested their models against observed UV, EUV, and X-ray spectra of the Sun and other stars, finding excellent agreement with observations. Along the same lines, France et al. [2016] developed the *MUSCLES* survey, a library of stellar SEDs constrained with optical and UV spectra from HST and X-ray observations from Chandra & XMM-Newton, for a range of stellar activities and spectral types. Similarly, Louden et al. [2017] reconstructed the high energy spectrum of planet-hosting star HD 209458 using UV line strengths from HST/COS together with X-ray spectra from *XMM-Newton*. These UV lines are produced by highly ionised species that dominate line emission at EUV wavelengths, making them ideal lines to use when reconstructing the EUV spectrum.

Since stellar activity is linked to coronal temperature, X-ray active stars will have the peak of their high energy emission at shorter wavelengths. For the same reason, inactive stars with cooler coronae will peak at longer wavelengths. As I discussed in Section 1.4.3, stars spin down with age, and as a result their emission weakens with time. Ribas et al. [2005] argued that this spin down causes the peak of the emission to move towards EUV wavelengths, and thus EUV emission decays more slowly than X-ray emission.

King and Wheatley [2021] and Johnstone et al. [2021] confirmed this using their respective empirical relations between X-ray and EUV emission. King and Wheatley [2021] further assessed the impact on atmospheric evaporation, concluding that EUV-driven escape can continue to be significant in Gyr timescales, extending the effects of photoevaporation to much longer timescales than previously thought. This would be particularly impactful on planetary systems around F, G, and K dwarfs, since these stars become unsaturated earlier in their lives with their high energy emission turning EUV-dominated, as opposed to M-dwarfs which remain saturated for longer and whose emission will thus remain X-ray dominated for longer as well. In Figure 1.10 I display a figure from King and Wheatley [2021] showing the expected X-ray and EUV evolution of a Sun-like star across its lifetime. As seen, EUV emission becomes stronger than X-ray emission after the

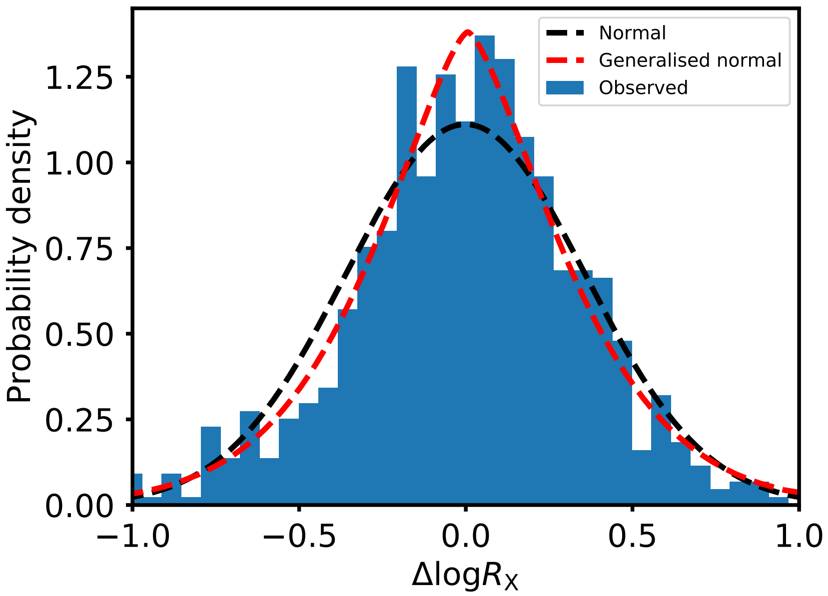

Figure 1.11: Figure 7 from Johnstone et al. [2021] showing a histogram of the scatter in the rotation-activity relation as the difference in $\log_{10} L_X/L_{\rm bol}$ between their fit and the data. The histogram is overlaid with the best fitting gaussian (black line) and generalised gaussian (red line) distributions.

first 400 Myr of age, reinforcing the total XUV emission at later ages. [King and Wheatley, 2021] also reported that most of the integrated XUV emission of a star lies after the first 100 Myr of age.

1.4.5 X-ray variability

The X-ray emission of stars undergoes short-term variability caused by different processes in the corona acting on different timescales. Flares temporarily increase coronal activity on timescales of minutes to hours; stellar rotation induces variability on timescales matching the spin period (days to weeks) as active regions rotate out of view; active regions evolve over several months; and, finally, activity cycles vary coronal emission over years and decades.

X-ray flares

Flares originate in the corona from the release of large amounts of energy stored in the magnetic field through the mechanism of magnetic reconnection. These events result in an increased brightness lasting minutes to hours across a wide range of wavelengths, from radio waves to gamma rays.

Flares have been observed in the Sun. The first solar flare to be observed was the so-called "Carrington Event", which took place in 1859 and was studied by Carrington [1859] and Hodgson [1859]. This event was later estimated to have released around $5.8 \times 10^{32}\,\mathrm{erg}$ of energy in 5 minutes [Hayakawa et al., 2023], making it one of the most powerful solar flares observed to date, even when it released the equivalent to only 0.05% of the total energy released by the Sun in the same amount of time. Flares have also been widely observed in other stars beyond the Sun. These have in some cases reached energies upwards of $10^{38}\,\mathrm{erg}$ [Schaefer et al., 2000], much greater than the Carrington Event in the Sun.

Flares are also observed regularly in the X-rays. Pye et al. [2015] published a survey of X-ray flares from XMM-Newton data from ~ 70 stars. They found X-ray flares tend to last 0.25 to 2 hours and have luminosities of 10^{29} to $10^{32}\,\mathrm{erg\,s^{-1}}$ with peak plasma temperatures reaching $kT = 3\,\mathrm{keV}$.

X-ray activity cycles

The Sun has an 11-year activity cycle, which presents itself as a variation in the number of sunspots on its surface [e.g. Hathaway, 2010]. Sunspots are cooler regions in the photosphere originated by magnetic fields inhibiting convection. As such, their presence is modulated by magnetic activity, and thus this solar cycle can be understood as a *magnetic* activity cycle. During a solar maximum, the Sun presents a greater number of sunspots, flares, and coronal loops, whilst, during a solar minimum, the frequency and magnitude of such phenomena reach a low point. In the X-rays, coronal emission can become ×100 stronger during solar maxima relative to solar minima [Domingo et al., 2009]. The magnetic activity cycle arises from a flip in the magnetic field of the Sun oscillating between a toroidal field and a polar field in a full 22-year cycle [e.g. Simon, 1983].

Beyond the Sun, activity cycles have been identified via activity indicators across many wavelengths, including the S-index for chromospheric activity and X-ray emission for coronal activity. In the X-rays, Sanz-Forcada et al. [2019] identified a 1.6 yr X-ray activity cycle in the nearby G0 dwarf ι Horologii, closely following the same cyclic variation observed in chromospheric activity. Other studies have also identified X-ray activity cycles in other stars with periodic observations of their chromospheric and coronal emission; e.g. ϵ Eri [2.9 yr, Coffaro et al., 2020], HD 81809 [7.3 yr, Orlando et al., 2017], 61 Cyg A, α Cen A, α Cen B [7.3, 12-15, and

8-9 yr, respectively, Robrade et al., 2012] and Proxima Cen [7 yr Wargelin et al., 2017].

X-ray scatter in the rotation-activity relation

The rotation–activity relation presents a large scatter of one order of magnitude each way in the X-rays, as seen in Figure 1.8. Johnstone et al. [2021] characterised this scatter in data from Wright et al. [2011] and found it resembles a normal distribution in $\log_{10} L_X/L_{\mathrm{bol}}$ with standard deviation $\sigma = 0.36$ independent of Rossby number. Such spread corresponds to a factor of 2.3 at 1σ and 5.2 at 2σ. In Figure 1.11, I show Figure 7 from Johnstone et al. [2021], which shows a histogram of the residuals between the fit to their rotation-activity relation and the data from Wright et al. [2011] which shows this scatter, overlaid with the best-fit gaussian distribution.

Johnstone et al. [2021] argued this scatter could have three different origins. Firstly, sample contamination and inhomogeneities will induce some level of scatter, in which a blend of different instruments, methodologies, and biases are introduced by combining datasets from different sources. Secondly, stars may have intrinsic activity levels independent of rotation and thus their emission will consistently lie some factor above or below the rotation-activity relation. Lastly, random cyclic X-ray variability, which Johnstone et al. [2021] favour, comes about from a variation in coronal emission from flares and activity cycles of individual stars. X-ray observations capture the coronal emission from many individual stars at different points of their respective cycles, inducing a scatter. As such, a star's emission would fluctuate about the rotation-activity relation and would average-out at the mean of the distribution.

Whether the scatter is a product of X-ray variability or intrinsic activity levels, it will have a significant impact in atmospheric escape that is often ignored. Understanding the origin of this scatter will be essential in assessing the impact of photoevaporation in driving the evolution of close-in planets and, more generally, sculpting their populations.

1.5 Goals of this thesis

- Study the impact of atmospheric escape on both the evaporation histories of individual planets as well as exoplanet populations (Chapters 3 to 7).

- Assess the predictive power of atmospheric escape models using simulations of evaporation history. Compare predictions of X-ray driven photoevaporation as well as core-powered mass loss on multi-planetary systems, as they share the same high energy environment, and where the evaporation histories of the planets can be constrained against one another (Chapters 3, 4, and 6).

- Characterise the present-day X-ray emission of stars using observations from the XMM-Newton telescope, and use them improve our constraints on models of X-ray emission history of stars. Place these observations of individual stars in context with cluster stars whose memberships has been established with *Gaia* (Chapters 3 to 7).

- Address the origin scatter in the rotation-activity relation and the contribution of X-ray variability of late-type stars to it, as well as its impact on atmospheric escape in Myr timescales (Chapter 7).

Chapter 2

Methodology

2.1 X-ray astronomy

In the context of X-ray astronomy of stars, wavelengths of interest range from 0.1 keV, the boundary between X-rays and EUV, to 4 keV (12 nm to 0.3 nm), after which stellar emission dies out. These high energy photons, however, are strongly absorbed high in Earth's atmosphere due to its high density and molecular abundances, with none reaching the surface. As such, X-ray astronomy can only be carried out with space-based observatories.

In the early days of X-ray astronomy, observations were carried out with sounding rockets and high altitude balloons. Indeed, X-ray radiation of cosmic origin was not measured until the advent of space exploration, when the first rockets left Earth's atmosphere and were exposed to the high energy environment of space [e.g. Burnight, 1949; Byram et al., 1956]. These were later followed in the 1970s by dedicated X-ray missions such as Uhuru [Jagoda et al., 1972], HEAO-1 [Matteson et al., 1974], and ANS [Gursky et al., 1975], which targeted a few select bright X-ray emitters.

These were followed by the Einstein observatory, launched by NASA in 1978, which revolutionised the field of X-ray astronomy as the first X-ray imaging telescope [Giacconi et al., 1979]. It performed the first population-level study of the X-ray emission of stars across the hertzsprung-russell (HR) diagram [Vaiana et al., 1981]. Its survey of 126 stars classified most FGKM stars as soft X-ray sources with luminosities $10^{26} - 10^{31}\,\mathrm{erg\,s^{-1}}$.

The *ROSAT* X-ray telescope, which operated from 1990 to 1999, later performed a much deeper survey of the sky which benefited from an increased resolution and collecting area, as well as sensitivity to softer energies down to 0.1 keV. The *ROSAT* All Sky Survey (*RASS*), presented by Agüeros et al. [2009], identified X-ray emission from 707 stars brighter than $V = 15$, including many late-type X-ray faint stars which emit the bulk of their high energy output at soft energies. Currently, there are four main X-ray imaging telescopes in operation: *XMM-Newton* [Jansen et al., 2001], *Chandra* [Weisskopf et al., 2000], *Swift* [Gehrels et al., 2004], and *eROSITA* [Predehl et al., 2021]. In short, *XMM-Newton* benefits from greater sensitivity and effective area, *Chandra* provides a better spatial resolution, and *Swift* offers a larger sky coverage.

Most stars are very faint X-ray sources, 4 to 6 orders of magnitude fainter than their optical brightness. As such, they require much longer exposure times. For instance, a star with the X-ray output of the Sun ($\sim 10^{27}\,\mathrm{erg\,s^{-1}}$) at a distance of 50 pc would produce a count rate of $3 \times 10^{-3}\,\mathrm{s^{-1}}$ in the EPIC-pn instrument onboard *XMM-Newton.* In order to obtain 200 counts, enough for a basic spectral characterisation and an estimate of the X-ray flux, this star would require an observation 18 hours long. These low count rates, on the other hand, allow for quick readout times, allowing X-ray telescope to discriminate each X-ray photon and obtain both its spatial and spectral information individually. Such quick readout times, where each pixel picks up no more than one X-ray photon during each short exposure, allows for the individual energies (and locations) of each photon to be determined.

2.1.1 The interstellar medium

The interstellar medium (ISM) refers to the matter and radiation in the space between stars. It is populated by primarily neutral hydrogen with very low densities of 0.1 atoms per cm^3 in the solar neighbourhood.

As X-ray photons emitted by stars travel through the ISM, they interact and ionise hydrogen and helium atoms in their path. Since their ionisation energies are 13.6 eV and 24.6 eV, respectively, interstellar atomic H and He readily absorb X-ray photons to produce photoelectrons. As a result, X-ray photons are completely absorbed and lost in the way. This effect is particularly strong for EUV photons, which are typically completely absorbed after only 50 pc, as I discussed in Section 1.4.4.

As such, the muting effect of the ISM in X-ray spectra can be corrected and accounted for, provided enough flux has reached the telescope in the first place.

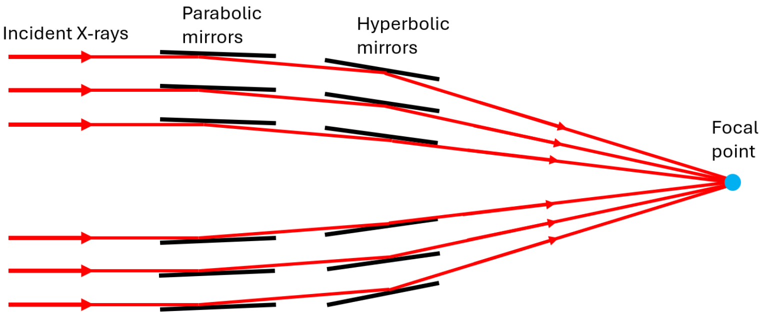

Figure 2.1: Diagram of a Wolter Type I telescope showing the paths of incident X-ray photons as they are reflected by parabolic and hyperbolic mirrors towards a focal point.

This correction requires the computation of the energy-dependent photoionisation cross-section σ_{ISM} of ISM matter, which must take into account its atomic and molecular abundances [Wilms et al., 2000a]. One such model is the Tuebingen-Boulder ISM absorption model [TBABS, Wilms et al., 2000b], often used together with plasma models when fitting X-ray spectra. The TBABS model calculates the total cross-section for X-ray absorption in the ISM, accounting for absorption by atomic gases, grains, and the H_2 molecule (the ISM abundances can also be manually specified), and computes the wavelength-dependent depletion of X-ray photons for a given X-ray spectrum.

For individual stars, the total hydrogen column density n_H along the line of sight is also necessary. This can be obtained from stars neighbouring our target from which line absorption has been used to estimate the column density. This is done with space-based spectrographs which measure line absorption at specific wavelengths that are associated with gas/dust in the Local Interstellar Cloud (LIC). The wavelengths of these absorption lines are correlated for nearby stars, consistent with the velocity vector of the LIC. Such observations have also allowed to map the 3D structure of the local interstellar medium [Redfield and Linsky, 2001]. The ISM only absorbs a few percent of X-ray photons for column densities of $n_H = 10^{19} - 10^{21}\,\mathrm{cm}^{-2}$, but quickly rises beyond 30% for $n_H > 10^{22}\,\mathrm{cm}^{-2}$; it also targets softer photons first, moving into higher energies as n_H increases.

2.1.2 X-ray telescopes

Traditional optical telescopes make use of lenses or mirrors to divert the path of light towards a detector. Due to their short wavelengths, however, X-ray photons that are incident on a medium will instead be scattered or absorbed by the material since at these energies most materials have indices of refraction only slightly smaller than one. As a result, X-ray photons can only be reflected at grazing angles of incidence under the phenomenon of total external reflection. Indeed, X-ray telescopes exploit this phenomenon, where the trajectory of X-ray photons can be veered and focused using grazing angles of incidence.

Wolter [1952] described three such configurations for X-ray telescopes. The most common one in X-ray astronomy, the Wolter Type I configuration, consists on a parabolic primary mirror followed by a hyperbolic secondary mirror, which I sketch in Figure 2.1. This setup reflects incoming X-ray photons twice at grazing angles below $\sim 1^\circ$. These mirrors can also be nested to maximise the effective light-collecting area, and are often coated with a highly reflective material such as gold or iridium.

Space-based observatories are typically diffraction-limited, such that their angular resolution is limited by the Rayleigh criterion. The Rayleigh criterion quantifies the minimum angular resolution θ of a telescope with circular aperture of diameter D for light of wavelength λ,

$$\theta = 1.22\frac{\lambda}{D}, \tag{2.1}$$

which suggests X-rays at 0.5 keV should have a resolution 200 times greater than optical (500 nm). In practice, the true resolution is limited by the alignment of the mirror system and the quality of the mirrors.

Instead, the angular resolution of X-ray telescopes is commonly quantified with the half energy width (HEW), the angular diameter that collects 50% of the photons of a point source. In Wolter Type I telescopes, the HEW degrades with off-axis angle. For instance, in the *XMM-Newton* observatory, the EPIC-pn instrument has an on-axis HEW of 15", but degrades to 19" at the edge of the detector. This is because the use of grazing incidence mirrors inherently results in very small collection areas. Telescopes like *XMM-Newton* account for this limitation by nesting many parabolic and hyperbolic mirrors in a coaxial and confocal configuration to increase the collection area. The geometry of this configuration results in a focal plane that is bowl-shaped. However, CCDs are flat with their centre lying on the focal point. As such, on-axis sources will have the best focus whilst off-axis sources are unfocused.

2.1.3 X-ray detectors: CCDs

Charge-coupled devices (CCDs) are a type of detector widely used in astronomy, including X-ray telescopes such as *XMM-Newton*, *Chandra*, and *Swift*. CCDs, like other detectors, are placed in the focal plane of the telescope to be illuminated by the incident photons, capturing an image of the sky.

In short, a CCD sensor consists on a silicon wafer divided into a grid of light-sensitive cells, each representing one pixel of the detector, arranged into rows and columns [Strüder et al., 2001]. Incident light on each cell releases electrons and holes from the silicon atom in equal numbers, due to the photoelectric effect, proportional to the energy of the absorbed photon. The electrons and holes are separated by an electric field, and the electrons are then guided towards a positively-charged capacitor where they are stored. On readout, a varying electrical current is run through each row, producing an electric potential which moves the charge stored on each capacitor to its neighbour along the row. The last capacitor on the row them dumps its charge into an amplifier, converting it into electric voltage, which is digitised and processed by the onboard computer.

If too many photons enter a cell (from bright sources or long exposure times), the electrons produced may not fit in the potential well of the capacitor, spilling over to neighbouring cells. During readout, this will create a "saturation trail" as the contents of a saturated cell are poured along the row, partially or fully erasing the genuine photon detections on that row. This phenomenon is a consequence of the readout operation on CCDs, where an anomaly on a cell (e.g. saturation, dead pixels, diffraction) may affect other cells across the image along its row.

In the context of X-ray telescopes, individual detections, called events (which are often photons but may be particles as well), are identified by reading out frequently; this is possible thanks to the low count rates in X-ray wavelengths. In this setup, "pile-up" may occur when multiple photons are captured by the same pixel, misrepresenting the energy of the event as the sum of the energies of the photons. CCDs in X-ray telescopes can also be affected by optical photons, where optical sources that are bright enough might trigger a detection in the CCD and be mistaken as an X-ray photon. Optical loading can be predicted by identifying likely culprits from optical surveys of the region of the pointing.

The high readout frequency of X-ray telescopes requires observations to be shutterless. As a consequence, photon detection events can occur during readout; in which case, the electronics will not be able to determine its true location on the CCD. For instance, in the CCD of the EPIC-pn instrument onboard *XMM-Newton* (which I describe further in depth in Section 2.2.1), one frame (in full-frame mode) lasts 73.3 ms, 4.6 ms of which is dedicated to readout (6.3% of the total time) whilst the remaining is used for the integration time of the image [Strüder et al., 2001]. Since *XMM-Newton* is shutterless, for any given observation under that setup, 6.3% of the photons will occur during readout and will be classed as "out-of-time" (OOT) events. The frequency of such events can be reduced by tuning the observation mode. Longer exposures, for instance, will reduce the relative number of OOT events at the risk of an increased chance of pile-up. Smaller windows will reduce readout times as well as the frequency of OOT events and pile-up, at the cost of reduced sky coverage. This is detrimental for observations of extended sources, and limits sky area available for background estimation, but has minimal effect for point sources. The associated shorter exposures also reduce the impact of optical loading.

2.2 The XMM-Newton observatory

In this section, I describe the setup and instruments of the *XMM-Newton* observatory, which I have used throughout my work (Chapters 3 to 7) to characterise X-ray emission from planet-hosting stars.

The X-ray Multi Mirror (XMM) mission, later renamed *XMM-Newton*, is a space-based observatory currently operational and launched by the European Space Agency in 1999. A schematic view of the spacecraft is shown in Figure 2.2. Its main objective is to improve sensitivity and provide high quality X-ray spectroscopy of faint sources. The observatory sits on a highly eccentric orbit 48 hours long to allow for long observations (up to 120 ks) unobstructed by Earth's shadow and avoiding particle noise from the radiation belts.

XMM-Newton benefits from three X-ray telescopes, each follow a Wolter Type I configuration with 58 nested mirrors, in a coaxial (parabolic mirrors) and confocal (hyperbolic mirrors) configuration, akin to the diagram shown in Figure 2.1. The grazing optics of 17 to 42 arcmin (0.3 to 0.7 degrees) provides poor collecting area per mirror, but this is mitigated by the large number of nested mir-

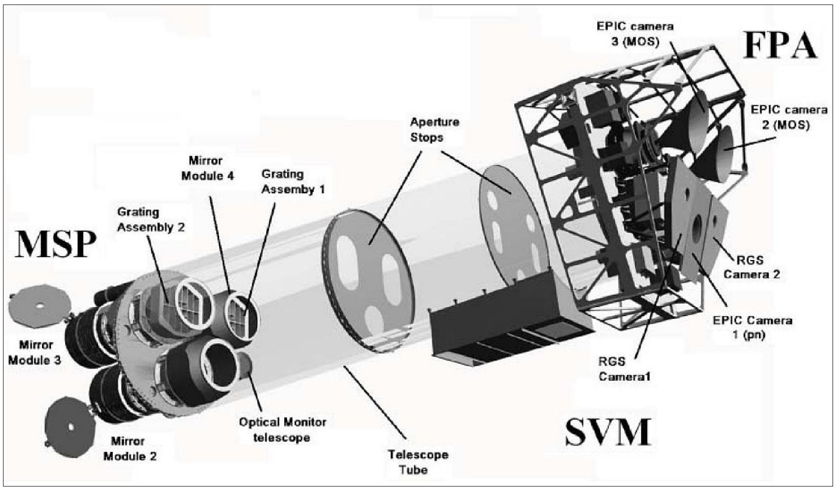

Figure 2.2: Schematic view of the XMM-Newton spacecraft showing the interiors of the Mirror Support Platform (MSP), the Service Module (SVM), and the Focal Plane Assembly (FPA). Credit: ESA/XMM-Newton.

rors in *XMM-Newton*. These instruments include three European Photon Imaging Cameras (EPIC), namely one EPIC-pn imaging detector [Strüder et al., 2001] and two Metal Oxide Semi-conductor (MOS) detectors [Turner et al., 2001].

XMM-Newton also includes two Reflection Grating Spectrometers (RGS), which perform high resolution X-ray spectroscopy with light intercepted from each EPIC-MOS. Another instrument, the Optical Monitor (OM), is mounted alongside the three X-ray mirror models at the front of the spacecraft, which provides optical and NUV imaging concurrent with the X-ray observations. I do not use observations with RGS or OM in the work presented in this thesis.

2.2.1 EPIC-pn

The EPIC-pn imaging detector is the principal instrument onboard *XMM-Newton* with the highest sensitivity and quantum efficiency out of the six instruments. The detector is subdivided into 12 CCD units fabricated from a single silicon wafer, each with a size of $3 \times 1\,\mathrm{cm}^2$. In total, it has a collecting area of $36\,\mathrm{cm}^2$ and 400×384 pixels with a pixel size of 150 microns (4.1 arcsec). The detector is sensitive to photons between 0.15 and 12 keV, with a half energy width (HEW) of 16 arcsec at 1.5 keV and 8 keV.

EPIC-pn can be operated in six observation modes. In the chapters where

I present EPIC-pn observations, I always used the “full frame” mode, which is the default for the instrument, in order to maximise the background collection area and to improve estimations of the overall quality of the observation; in the case of the binary companions of TOI-451 and TOI-1098 in Chapter 6, I also chose full-frame mode to ensure both stars are present in the field of view. In full frame, the full area of the detector is used with a time resolution of 73 ms (OOT fraction of 6.3%). In contrast, the extended full frame mode, apt for extended sources, adopts an integration time ×2.7 longer, reducing the frequency of OOT events by the same amount. The other modes (small window, large window, timing, and burst) reduce pile-up and the OOT frequency by reducing the collecting area instead.

EPIC-pn also has choice between three blocking filters which reduce optical loading to different degrees but also block a certain fraction of soft X-ray photons as well. These are the thin, medium, and thick filters, and are effective at preventing contamination for optical sources with magnitudes up to $m_V = 12$, 9, and 1, respectively. Compared to the thin filter, the medium and thick filters block 9% and 42% of the X-ray photons in the band 0.2-1.0 keV, respectively. In the *XMM-Newton* observations presented in this thesis, I always used the thin blocking filters as there were no bright optical sources in my observations that required accounting for optical loading.

2.2.2 EPIC-MOS

The other two X-ray telescopes onboard *XMM-Newton* direct their light towards the two identical EPIC-MOS imaging detectors.

Each of the two EPIC-MOS detectors consist in seven CCD units: one central one at the focal point and six others around it. Unlike EPIC-pn, these chips are not monolithic and were fabricated separately. In fact the outer six CCDs are placed 4.5 mm higher than the central one following the curvature of the focal plane in order to improve their focus for off-axis sources.

Each EPIC-MOS has a total collecting area of 2.5×2.5 cm and 600×600 pixels with a pixel size of 40 microns (1.1 arcsec). The detectors are sensitive to photons between 0.2 and 10 keV with a HEW of 17 arcsec at 1.5 keV. They are also less sensitive than EPIC-pn, particularly for soft X-rays (with an effective area a factor of ×1.5 at 1 keV and ×2.3 at 0.5 keV lower than EPIC-pn), but they are also less affected by background noise and have a spatial resolution ×4 higher. Their lower sensitivity is in part due to 58% of their respective incident light being diverted towards the two Reflection Grating Spectrometers (RGS).

EPIC-MOS have four observation modes. The default mode is full frame, where the full collecting area of the instruments is used and has a time resolution of 2.6 s. Like EPIC-pn, the EPIC-MOS can also be operated in large window, small window, and timing modes, which reduces the collecting area of the central CCD to gain in time resolution and reduce pile-up. The outer six CCDs always operate in full frame, whilst the central CCD can be operated in any of the modes. In this thesis, I have used EPIC-MOS observations in Chapters 4 and 6, always in full frame mode.

2.3 Analysis of X-ray observations

In this section, I describe the process I use for analysing *XMM-Newton* observations to extract light curves, spectra, and X-ray fluxes for a given target in the observation.

I use the Science Analysis System (`SAS`)[1] software developed explicitly for reducing and analysing *XMM-Newton* observations. Together with it, I use some software from the package `HEASoft`[2], developed by NASA for analysing data from a variety of X-ray observatories.

The *XMM-Newton* telescope, after carrying out a number of observations, sends the telemetry back to monitoring stations on Earth. This raw telemetry is packaged in the form of FITS files named Observation Data Files (ODF). The ODFs are also automatically reduced by a data pipeline, producing Pipeline Processing System (PPS) files, which contain validated scientific products. In my analyses in this thesis I do not use PPS products for science, as I reduce the data myself. Although in most cases the PPS products would be suitable, I find it is good practice to carry out the analysis myself to ensure the source has been correctly identified and to fine-tune the reduction beyond the steps taken by the pipeline (i.e. binning, X-ray spectral model, upper limits). Start-up of `SAS` for reducing an *XMM-Newton* observation also requires Current Calibration Files (CCF), which contains information necessary to calibrate the instruments in the telescope for science.

The ODFs of an observation can be translated into a more practical format, an event list, which contains a record of every photon detection event during an

---

[1] See `https://www.cosmos.esa.int/web/xmm-newton/sas-threads`

[2] See `https://heasarc.gsfc.nasa.gov/docs/software/heasoft/`

observation, as well as its timestamp, location in the detector, and energy (in the form of a *channel*). To process the ODFs into event files, I use the `SAS` commands `epproc` for EPIC-pn data and `emproc` for EPIC-MOS data. These commands collect the ODFs of an observation, concatenate them into a single file (the event list), and calibrate the data for telescope and instrument degradation as well as changes in the orbit of the telescope using the CCFs that are closest to the date of the observation.

The next step is to assess the level of flaring particle noise in the observation and, if necessary, remove it. The flaring particle background is attributed to soft protons from the Sun, which the detector incorrectly interprets as hard X-ray photons, which can extend beyond 10 keV. These soft protons, which reach the CCD window by scattering off the mirrors and skipping the particle shield, can ionise silicon atoms in the semiconductor, producing an electric charge that is indistinguishable from that of hard X-ray photons. Periods of high flaring background can thus be identified by querying the event list for high energy events (> 10 keV) and plotting them as a lightcurve. Querying the event list for events with specific timestamps, energies, flags, and positions can be done with the `SAS` command `evselect`. This high-energy lightcurve will be flat and close to zero during low background periods, but may increase significantly during periods of high flaring noise. This can be seen in Figure 2.3, where I plotted the high energy lightcurve of an *XMM-Newton* observation of the star K2-136 (which I present in Chapter 3). The recommended method for correct for these noisy intervals is to remove the periods of high noise entirely from the analysis. This is done by inspecting the lightcurve for a baseline “low background” level and removing the time intervals with background over this limit. This is done with the command `tabgtigen`, which generates a file that specifies the Good Time Intervals (GTI) of the observation, which can then be used to filter the event list. In practice the impact of high noise time intervals is limited to increasing the uncertainties in the count rates in the lightcurves, although they can reduce the signal-to-noise of the spectrum significantly when the background levels are very high. The downside of removing the noise intervals, on the other hand, is discarding significant portions of the observation. As such, one must strike a balance between having less data or having more data that is noisier. In my work, however, I have often chosen not to remove these noisy intervals as the background levels were never too high.

The reduced data is now in a state where science can be carried out and lightcurves and spectra can be extracted and analysed. The first step is to identify

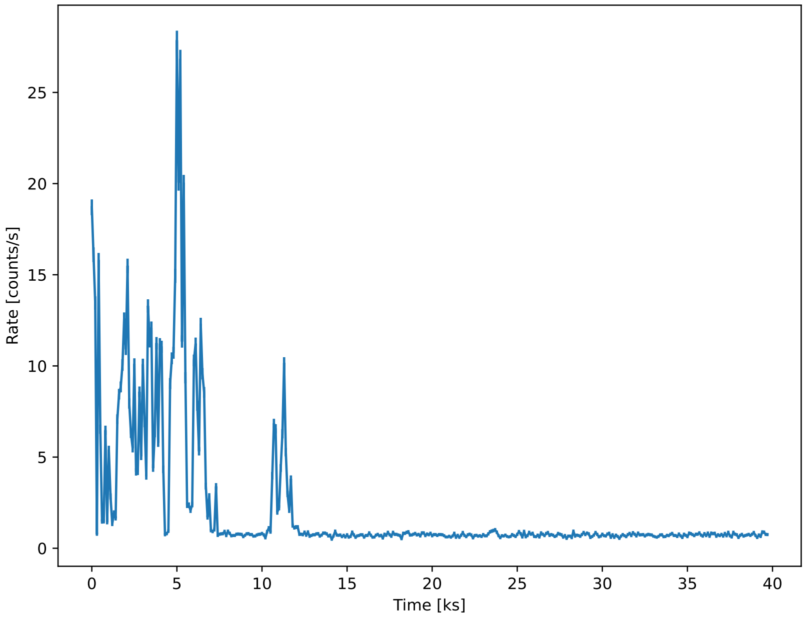

Figure 2.3: Plot of the count rate from the EPIC-pn instrument against time for high energy events ($> 10\,\mathrm{keV}$) during an *XMM-Newton* observation of the star K2-136 (which I present in Chapter 3). The high count rate intervals are caused by soft solar protons being funneled into the detector and mistaken as hard X-ray photons.

the source of interest in the observation. This is often first done via visual inspection by extracting an image from the event list with the command `evselect`, opening it with a FITS viewer such as DS9, and identifying the source at its expected sky coordinates (RA, Dec). Alternatively, one may inspect the pipeline outputs (PPS), which lists sources detected in the frame.

The lightcurve of the target can be extracted again with `evselect`. One must choose a circular aperture around the source which encompasses the PSF, as well as another aperture for estimating the background level close to the source. Lightcurves can thus be extracted for both the source and background regions, and the source lightcurve is then background-corrected with the command `epiclcorr`, which also corrects for other effects including vignetting, quantum efficiency, and bad pixels.

Spectra can also be extracted with `evselect` using the same method as for lightcurves, in which a source and background regions are chosen. In order to convert the instrument-specific energy channels into energies, information about the response of the detectors as a function of energy is needed. This is encoded in a set of response files, namely a redistribution matrix file (`rmf`) obtained with the command `rmfgen` and an ancillary file (`arf`) obtained with `arfgen`. These two files, together with the source and background spectra, can be provided to a spectral analysis software, such as `XSPEC`, to fit a spectral model and obtain the X-ray flux of the target.

2.3.1 Fitting X-ray spectra

In order to obtain the X-ray flux of a target, one must first fit a spectral model to the data and integrate it in the desired energy band. To do so, I employ the software `XSPEC` included in the `HEASoft` package. `XSPEC` is able to read spectrum files from `SAS`, and produce a source spectrum that is corrected for the background, as well as converted into physical units using knowledge of the response of the detector. `XSPEC` can also fit multiple spectra from different instruments and epochs simultaneously.

Once the spectral files have been loaded, a spectral model can be fitted. The model I chose throughout my work is a combination of ISM absorption and coronal emission. I account for ISM absorption with the Tuebingen-Boulder ISM absorption model [`TBABS`, Wilms et al., 2000b], which takes in a hydrogen column density n_H along the line of sight between the observer and the target. In my

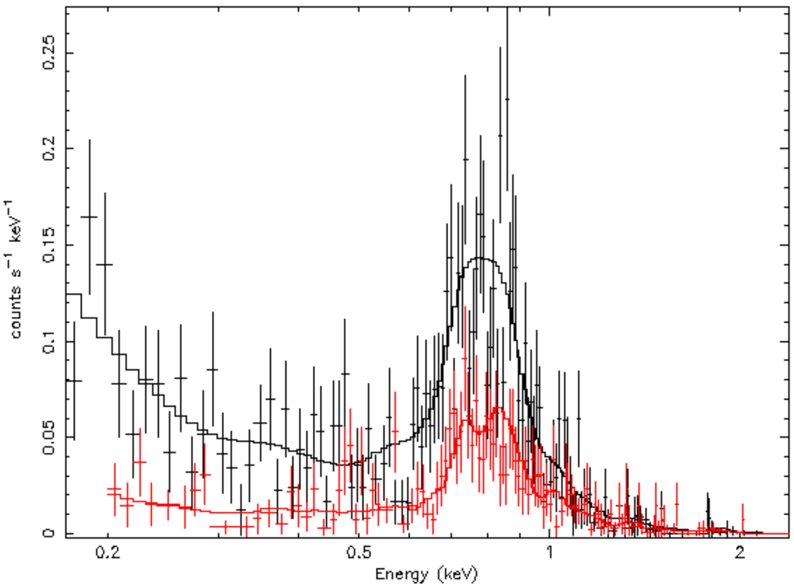

Figure 2.4: Plot of the X-ray spectrum of TOI-1098 produced with `XSPEC` as detailed in Chapter 6. The data points correspond to spectral counts from the EPIC-pn (black points) and the two EPIC-MOS instruments combined (red points). The lines show the spectral model fitted simultaneously to the data from the three instruments (black and red lines for EPIC-pn and EPIC-MOS, respectively), with a two-temperature `APEC` model as well as a `TBABS` model for ISM absorption.

work, I have estimated n_H using the distance to the star together with an estimated hydrogen density of $0.1\,\mathrm{cm}^{-3}$ in the local neighbourhood as determined by Redfield and Linsky [2001]. As for the coronal emission, I use the Astrophysical Plasma Emission Code [`APEC`, Smith et al., 2001], which models the corona of a star as collisionally-ionised optically-thin plasma. It offers the following free parameters: the temperature, redshift, coronal abundances relative to solar, and a normalisation constant that scales the model to match the observed count rate. In my work, I leave the temperature and normalisation as free parameters, whilst I fix the redshift to zero (since my sources of interest are nearby stars) and abundances to solar. The abundances in the model serve to account for emission lines of metals, which are set to solar abundances by default and can only be set globally to all elements, although the individual abundance of each element can be fine-tuned using the `VAPEC` and `VVAPEC` models instead. I use the `VAPEC` model in Chapter 3 to fit the abundances of N, O, Ne, and Fe individually and compare them to photospheric abundances. Moreover, I always use the solar abundances provided by Asplund et al. [2009]. Since the corona does not have a single temperature, but a distribution of temperatures, multiple `APEC` models can be fitted together for multi-temperature fits. Alternatively, one may use a multi-temperature model such as `CEMEKL` [Singh et al., 1996], which I used together with `APEC` in Chapter 3. `CEMEKL` models plasma emission using a continuous emission measure distribution, where a power law dictates the emission at a given temperature.

In Figure 2.4, I plot an example of an X-ray spectrum as seen in `XSPEC` fitted with a two-temperature `APEC` model.

For fitting the spectral model, I use the C-statistic [Cash, 1979], which assumes a Poisson distribution for the data rather than a Gaussian, since Cash [1979] showed that using bins with less than 10-20 counts (which is often the case in X-rays), the χ^2 statistic becomes unreliable as a fit statistic. I determine the best-fit parameters and their uncertainties using the Markov chain Monte Carlo (MCMC) method, which performs a number of random walks across parameter space seeking to minimise the fit statistic.

Finally, I integrate the spectral model in the desired energy band using the `XSPEC` command `flux`, which yields an X-ray flux in units of $\mathrm{erg\,s^{-1}\,cm^{-1}}$. For EPIC-pn, one can integrate across the energy band of choice, which for stars this is often $0.15 - 2.4\,\mathrm{keV}$. The lower bound of this energy range corresponds to the minimum operative energy of the EPIC-pn instrument, whilst the upper bound is motivated by the number of counts dropping very low for soft stellar sources. It is also common to extrapolate the model down to the full *ROSAT* band (0.1−2.4 keV) in order to capture the softer component of the X-rays. Extrapolation to softer wavelengths, though, is highly sensitive to the choice of model and the fitted parameters.

2.4 Archival datasets

Observatories that carry out surveys of the sky typically release their results in the form of catalogues and data releases. In my work, I have made use of public catalogues from two missions: *XMM-Newton*, which observes X-ray wavelengths, and *Gaia*, which observes optical wavelengths. These catalogues are the *4XMM* catalogue and *Gaia* Data Release 3 (*Gaia* DR3), respectively. In Chapter 5, I cross-match X-ray sources from the *4XMM* catalog with a list of Pleiades stars published by Godoy-Rivera et al. [2021] curated with *Gaia*; and in Chapter 7, I present a cross-match between all 4XMM sources and main sequence stars in *Gaia* DR3 within 200 pc. In both cases, my objective was to obtain the measured X-ray fluxes from a number of *Gaia* stars in order to characterise their coronal activity levels. In this section, I briefly discuss how these two catalogues are assembled and what information they offer.

2.4.1 The 4XMM catalogue

The fourth *XMM-Newton* Serendipitous Source Catalogue [*4XMM* Webb et al., 2020] offers count rates and fluxes of sources identified on archival *XMM-Newton* pointings. *XMM-Newton* pointings are originally obtained through guest observation requested with proposals in order to make targeted observations. These pointings will additionally contain many more sources in the frame, whose X-ray emission has been characterised by chance, hence why *4XMM* is known as a “serendipitous” catalogue. The *4XMM* catalogue is assembled by the *XMM-Newton* Survey Science Centre (SSC) and, its latest data release (*4XMM*-DR13) includes 983,948 X-ray detections compiled from 13,243 observations taken with *XMM-Newton* in the last 24 years.

Each *XMM-Newton* observation is processed following the standard pipeline to produce event lists, as described in Section 2.3. Source detection is run on the three X-ray cameras and all bands simultaneously. First, a search box of size 20” × 20” is slid through the image, identifying and removing sources from it; the result is normalised by the exposure map of the detector to compute a background map. A second pass with a search box again of size 20" × 20" is done, this time comparing the counts from the detected sources with the expected background level from the background map, which increases detection sensitivity [Webb et al., 2020]. Finally, source parameters are fitted on the distribution of source counts with a maximum-likelihood method over a circular aperture with radius 60". Using the background map, a set of flags are provided for each detection which report on the quality of the observation as well as the detection likelihood. Spectra and lightcurves are also extracted for the brightest sources. Then, count rates are extracted in eight standard energy bands: $0.2-0.5$, $0.5-1.0$, $1.0-2.0$, $2.0-4.5$, and $4.5-12\,\mathrm{keV}$. Finally, X-ray fluxes are calculated from the count rates using standard energy conversion factors (ECFs). ECFs are provided for each standard band, instrument, and filter, and are based on an absorbed power law model with a column density $n_H = 3 \times 10^{20}\,\mathrm{cm}^{-2}$ and a photon index $\Gamma = 1.7$. These model parameters were obtained by fitting said model to the best quality spectra in the archive and calculating the average of the best-fit parameters.

Each X-ray detection is labelled with an unique detection ID `DETID`. X-ray detections from different epochs that are close in the sky are cross-matched to identify if they correspond to the same astrophysical X-ray source observed at different times. These sources are assigned an unique source ID `SRCID`. A secondary catalogue is also assembled, the *stacked* catalogue, which provides information only on each unique X-ray source, where the provided X-ray fluxes on each band correspond to the average across all of its detections. In Chapter 7, where I make use of the *4XMM* catalogue, I do not use the stacked catalogue as the main aim of that chapter is to study X-ray variability, which requires examining all detections of a given X-ray source.

2.4.2 The *Gaia* archive

In my work, I have also benefited from the extensive survey that the *Gaia* spacecraft has carried out, which has measured accurate photometry and astrometry for billions of stars [Gaia Collaboration et al., 2016]. In Chapter 7, I cross-match the *Gaia* DR3 archive with the *4XMM* catalogue of *XMM-Newton* observations and obtain X-ray luminosities for thousands of *Gaia* stars. *Gaia* has also been instrumental in refining membership lists for open clusters [e.g. Freund et al., 2020; Godoy-Rivera et al., 2021; Núñez et al., 2022], as stars born from the same cluster share similar kinematics, which can be precisely measured with *Gaia*. Indeed, in Chapter 5 I obtain X-ray luminosities for a sample of Pleiades members compiled by Godoy-Rivera et al. [2021] using *Gaia* data.

Gaia is a space-based observatory launched by the European Space Agency in 2013. *Gaia* observes the sky by scanning it as the telescope spins with a period of 6 hours. Moreover, its focal plane is covered by 106 CCDs and a total of 1 billion pixels across three science instruments. These instruments, which operate in optical wavelengths, are the astrometric instrument, the Red and Blue Photometer (`BP/RP`), and the radial velocity spectrometer (`RVS`).

The astrometric instrument, with 62 CCDs, measures broadband photometry (G band) and identifies sources in the sky. Its main objective is to measure their sky positions as it orbits the Sun in order to characterise their parallaxes and proper motions. The red and blue photometer corresponds to two strips of 7 CCDs each, to measure low-resolution spectra of sky sources. The two strips measure two passbands, BP and RP, which roughly correspond to the blue (330-680 nm) and red (640-1050 nm) parts of the broader G passband. Finally, the `RVS` collects high resolution spectra using a diffraction grating in order to measure the radial velocities of its targets.

Gaia has so far published three data releases [*Gaia* DR1, DR2, and DR3; Gaia Collaboration et al., 2020], which contain science products from its observations, including an unique *Gaia* ID for each source as well as its photometry (G, G_{BP}, and G_{RP} magnitudes), sky position, parallax, and proper motion. Additional data are provided for each source which assess the quality of its observations. This includes the Renormalised Unit Weight Error (RUWE), which characterises the goodness of fit for a single-object astrometric solution. It is often used to single out unresolved binaries; an unseen stellar mass companion would induce a periodic motion in the source that is picked up by the astrometric fitting algorithm.

Photometry of stellar sources with $G \leq 19$ is also fitted with stellar models to determine certain physical parameters, such as the stellar mass, bolometric luminosity, effective temperature, and metallicity. The latest release, *Gaia* DR3, which contains 1.8 billion sources, also includes data from the RVS instrument, such as radial velocity, RV amplitude, and line broadening. In Chapter 5, I use RV measurements from *Gaia* DR3 to identify tidally-synchronised binaries, which are spun-up by their close stellar companions and as a result present high RV amplitudes.

2.5 photoevolver

`photoevolver` is a Python module I developed that simulates the evaporation histories of exoplanets. I use this code extensively for my work, in Chapters 3 to 7. The code is publicly available on GitHub at `github.com/jorgefz/photoevolver`.

`photoevolver` is highly modular, allowing the user to provide their own models for each aspect of the simulation, including the planet's internal structure, the stellar emission history, and the mass loss formulation for the planetary atmosphere. More generally, `photoevolver` acts as the *glue* between these models, such that each model provides one of the pieces required to simulate the evolution of a planet under atmospheric escape.

2.5.1 Determining the internal structures of planets

Before evolving a planet's atmosphere under evaporation, `photoevolver` must first know about the internal structure of the planet, e.g. how much of its mass corresponds to the gaseous envelope and how thick it is.

`photoevolver` describes the interiors of planets with two layers: a solid core surrounded by a gaseous envelope. This model can thus be described with four parameters: the core radius $\mathrm{R_{core}}$ and core mass $\mathrm{M_{core}}$, and the envelope thickness $\mathrm{R_{env}}$ and envelope mass $\mathrm{M_{env}}$. The envelope mass is most commonly expressed as an envelope mass *fraction*, defined as ratio of envelope mass to total planet mass ($\mathrm{f_{env}} = \mathrm{M_{env}}/\mathrm{M_{pl}}$), which is the definition `photoevolver` adopts. Other studies adopt an alternative definition corresponding to the ratio of envelope mass to core mass ($X_{\mathrm{env}} = \mathrm{M_{env}}/\mathrm{M_{core}}$), which is related to the first definition as follows: $\mathrm{f_{env}} = X_{\mathrm{env}}/(1 + X_{\mathrm{env}})$.

These four parameters are related to one another with four equations. The first two are trivial and follow the definitions of the planet's radius and mass. Planet radius is defined as the combination of core radius and envelope thickness $\mathrm{R_{pl}} = \mathrm{R_{core}} + \mathrm{R_{env}}$, whilst planet mass is the combination of envelope and core masses $\mathrm{M_{pl}} = \mathrm{M_{core}} + \mathrm{M_{env}}$. The envelope mass fraction can thus be rewritten as $\mathrm{f_{env}} = (\mathrm{M_{pl}} - \mathrm{M_{core}})/\mathrm{M_{pl}}$.

The other two equations pertain to relations between mass and radius for the core and the envelope. For the core, we can adopt theoretical mass radius relations that assume a certain composition, such as an Earth-like core with 2/3 silicates and 1/3 iron [e.g. Fortney et al., 2007], commonly assumed for exoplanet populations [Owen and Campos Estrada, 2020b]; whilst other alternate formulations include some fraction of water/ice [e.g. Zeng et al., 2019]. Alternatively, we can also use empirical fits to exoplanet populations, such as the mass-radius relation provided by Otegi et al. [2020], which was based on planets with densities greater than water.

For the envelope, we can again use such relations, although on this occasion between envelope thickness and envelope mass fraction, which I refer as envelope structure models. These often require further information to calculate the envelope thickness, such as the bolometric flux incident on the planet and the amount of thermal energy in the planet's core, both of which warm up the envelope and cause it to expand. One may use empirical fits to a grid produced with expensive simulations [e.g. Lopez and Fortney, 2014; Chen and Rogers, 2016]. Alternatively, Owen and Wu [2017] provided a fully analytical model suitable for super-Earths and sub-Neptunes. I compare these models in-depth in Section 3.4.3.

We can thus obtain the internal structure of a planet starting off from two sets of parameters. On one hand, we can provide the planet's core radius and envelope mass fraction. We can first use the mass-radius relation for the core to obtain the core mass, and then combine the core mass with the input envelope mass fraction to obtain the total planet mass. Finally, we can use the envelope structure model to calculate the envelope thickness from these parameters and thus the total planet radius.

Alternatively, we can start with a planet's total mass and radius. We can then make an initial guess for the envelope mass fraction, solve for the remaining parameters using the method described above, and see if the corresponding radius matches the input one. If it does not, we can adjust the envelope mass fraction and repeat until it matches. Essentially, the code is finding roots for the equation $R_{pl,guess}(f_{env,guess}, M_{pl}) - R_{pl,input} = 0$. To carry out this iterative calculation, `photoevolver` uses the function `fsolve` from the Python package `scipy` [Virtanen et al., 2020]. This is most useful to determine the internal structure of a real planet, whose mass and radius have been measured.

2.5.2 Simulating atmospheric evolution

Evolving a planet's atmosphere under photoevaporation requires knowledge of the XUV emission history of its host star and a model for the atmospheric escape. The XUV emission history of the host star is required to obtain the X-ray irradiation on the planet at each point in time. As stellar activity is linked to the stellar rotation

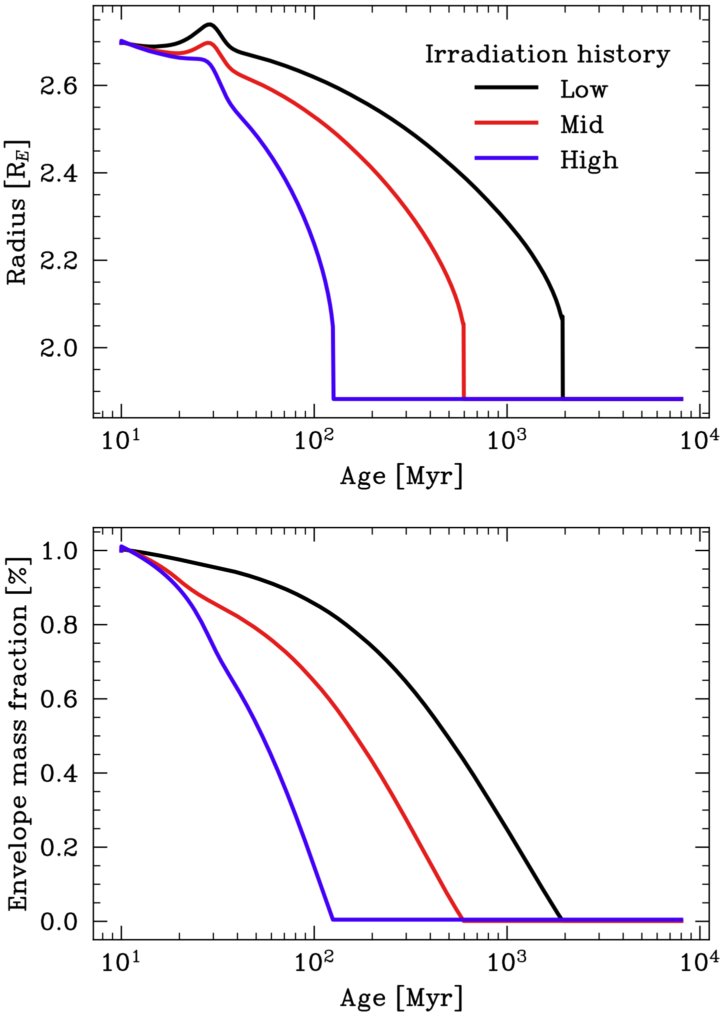

Figure 2.5: Simulations with `photoevolver` of the evaporation history of a sub-Neptune orbiting a Sun-like star with an orbital period of 6 days, a mass of 8 M_E, and an initial envelope mass fraction of 1%. I adopted three X-ray irradiation histories from the models by Johnstone et al. [2021] as shown in Figure 1.9: 5th percentile for low irradiation (black line), 50th percentile for medium irradiation (red line), and 95th percentile for high irradiation (blue line). The top panel shows evolution of the planet radius with age, and the bottom panel, evolution of the envelope mass fraction. The following models were adopted: stellar emission models from Johnstone et al. [2021], envelope structure model by Chen and Rogers [2016], core mass-radius relation by Otegi et al. [2020], and the energy-limited mass loss model [Watson et al., 1981; Erkaev et al., 2007]. The planet's atmosphere was evolved from the age of 10 Myr to 8 Gyr with a fixed time step of 1 Myr.

period (see Section 1.4.2), a model of the spin evolution of a star can be used to estimate its XUV emission history (see Section 1.4.3). One such example is the spin and X-ray evolution models by Johnstone et al. [2021] – in Figure 1.9 I show their models for a Sun-like star. Regarding the atmospheric escape model, it is required to translate the incident XUV radiation into a mass loss rate. In Section 1.3.2 I discuss the different mechanisms of atmospheric escape and in Chapter 3, I compare four different mass loss models in simulations of atmospheric evolution.

For each step of the simulation: (1) the stellar X-ray luminosity is obtained for the current age of the simulation and (2) fed to the mass loss model to obtain the atmospheric escape rate. Then, (3) the mass lost is removed from the envelope, and (4) the envelop thickness is recalculated using the envelope structure model.

`photoevolver` continues evolving the planet's atmosphere until either the end age is reached, or the atmosphere is fully stripped from the planet. The envelope is considered to be stripped if it falls under a certain minimum envelope mass fraction, which by default is $f_{\mathrm{env}} = 10^{-5}$, which corresponds to an envelope of negligible size. This limit exists because envelope structure models become unphysical at an envelope mass fraction of zero.

Moreover, `photoevolver` provides two integration methods to evolve planetary atmospheres. The first is the Euler method, which uses a fixed step size and evaluates the function once per step. The second method is the 4th order Runge-Kutta method (RK45), which uses an adaptive step size and is more stable than the Euler method but more computationally expensive, as it evaluates the function six times every step. In `photoevolver`, I adopted the implementation of the RK45 method provided by the Python package `scipy` [Virtanen et al., 2020].

In Figure 2.5, I show an example of the evolution of a sub-Neptune into a super-Earth with `photoevolver`, which highlights the importance of the stellar emission history in simulations of atmospheric escape. This test planet orbits a Sun-like star with a period of 6 days, a core mass of $8\,\mathrm{M_E}$, and an initial envelope mass fraction of 1%. I simulated the planet's evaporation history using three stellar emission histories from the models by Johnstone et al. [2021], as shown in Figure 1.9. These correspond to the 5th, 50th, and 95th percentiles of the spin period distribution in their models, which translate to a "low", "mid", and "high" irradiation histories. In all scenarios, the planet is fully stripped of its atmosphere. However, this occurs on timescales of 2 Gyr, 600 Myr, and 100 Myr, respectively, with the "high" irradiation history stripping the atmosphere 20 times earlier than the "low" irradiation history.

Chapter 3

The shared evaporation history of three planets around K2-136

3.1 Introduction

As discussed in Chapter 1, modelling the evaporation histories of exoplanets requires knowledge of the past X-ray emission of their host stars. X-ray observations of stars, however, only provide a snapshot of the high energy environment of its planetary system. One can attempt to model the current physical properties of a planet but its history can be hard to constrain. A straightforward solution to break the degeneracy is to study multiplanetary systems, where all the planets in the system have shared the same the irradiation history. Their current states can then be used to constrain each other's pasts, especially if the planets are found on both sides of the radius valley [Owen and Campos Estrada, 2020b].

This is particularly useful if one planet is evaporated whilst another retains an atmosphere. This is a common arrangement for Kepler systems, where a small barren rocky world is interior to a puffy mini-Neptune. These planetary systems are "size-ordered". The predicted integrated X-ray output of their host star can therefore be fine tuned: high enough to strip the interior planet of its atmosphere but low enough to maintain the atmosphere on the outer one.

Of particular interest are therefore planetary systems that are not size-ordered, i.e. a gaseous mini-Neptune interior to a barren rocky world. Such systems raise the question of the survival of the atmosphere of the inner planet. How could the inner planet have received a greater X-ray dose than the outer planet and yet maintained its gaseous envelope?

In this chapter I study the evaporation history of one such planetary system with three transiting planets: an Earth-size rocky planet, a low density mini-Neptune, and a dense super-Earth. K2-136 (EPIC 247589423, LP 358-348) is a K5V dwarf at a distance of 59 pc that hosts three transiting planets. The star, whose parameters are shown in Table 3.1, is a member of the Hyades cluster, which makes it about 700 Myr in age [Brandt and Huang, 2015; Martín et al., 2018]. The three planets (K2-136 b, c, and d) have radii 1.0, 3.0, and 1.5 $\mathrm{R_E}$, respectively, as reported by Ciardi et al. [2018], Livingston et al. [2018], and Mann et al. [2018], and their orbital and physical properties are shown in Table 3.2. Given that the planets straddle the radius valley, this system provides an excellent opportunity to study the evaporation history of exoplanets in a shared X-ray environment.

The chapter is structured as follows: Section 3.2 introduces the planets in the system and their physical properties, Section 3.3 concerns my X-ray observations of K2-136, in Sects. 3.4 & 3.5 I model the evaporation histories of the three planets, and in Sects. 3.6 & 3.7 I discuss and summarise the results.

3.2 Planetary system

The planetary radii, orbital periods, and mass measurements of the three planets around K2-136 are shown in Table 3.2. The radius measurements from the different studies all agree within 1σ, and the orbital periods all agree within minutes.

The precision of these original radius measurements were limited by the precision of the stellar radius, which in turn was limited by knowledge of the distance to K2-136. Since the publication of the discovery papers, we now have improved precision on the stellar radius from Gaia, and I was able to recalculate the planet radii using the R_p/R_* values from the discovery papers together with the stellar radius of $0.6854 \pm 0.0010\,\mathrm{R_\odot}$ from Gaia DR3 [Gaia Collaboration et al., 2022]. This resulted in reduced uncertainties as well as closer consistency between the radii from Mann et al. [2018] and Livingston et al. [2018] (see Table 3.2).

The mass measurements in Table 3.2 are from HARPS-N observations. Mayo et al. [2021] published an abstract summarising these HARPS-N measurements for K2-136, where they report a mass of $15.9 \pm 2.4\,M_\mathrm{E}$ for K2-136 c. However, during the preparation of this chapter I became aware of revised HARPS-N masses and limits for all three planets by Mayo et al. [2023], which are shown in Table 3.2.

Despite the relatively high mass of K2-136 c of $18.1 \pm 1.9\,\mathrm{M_E}$, the planet still has a relatively low density of $\sim 3.8\,\mathrm{g\,cm^{-3}}$ (using $R_\mathrm{p} = 3.0\,\mathrm{R_E}$) strongly suggesting

Table 3.1: Stellar parameters of K2-136

Parameter	Units	Value	Reference
		Spatial	
RA (J2000)	hh:mm:ss	$04:29:38.99$	Gaia DR3[b]
Dec (J2000)	dd:mm:ss	$+22:52:57.78$	Gaia DR3[b]
$\mu_{\rm RA}$	mas yr^{-1}	82.778 ± 0.021	Gaia DR3[b]
$\mu_{\rm Dec}$	mas yr^{-1}	-35.541 ± 0.015	Gaia DR3[b]
Parallax	mas	16.982 ± 0.019	Gaia DR3[b]
Distance	pc	58.89 ± 0.065	Gaia DR3[b]
		Photometric	
B	mag	12.48 ± 0.01	UCAC4[a]
V	mag	11.20 ± 0.01	UCAC4[a]
G	mag	10.8537 ± 0.0005	Gaia DR3[b]
BP	mag	11.5398 ± 0.001	Gaia DR3[b]
RP	mag	10.0527 ± 0.001	Gaia DR3[b]
J	mag	9.096 ± 0.022	2MASS[d]
H	mag	8.496 ± 0.020	2MASS[d]
Ks	mag	8.368 ± 0.019	2MASS[d]
		Physical	
Spectral type	—	$K5V$	L18[e]
$T_{\rm eff}$	K	4359 ± 50	L18[e]
M_*	$M_\odot$	0.686 ± 0.028	L18[e]
R_*	$R_\odot$	0.723 ± 0.072	L18[e]
L_*	$L_\odot$	0.171 ± 0.036	L18[e]
[Fe/H]	dex	0.17 ± 0.12	L18[e]
$P_{\rm rot}$	days	$13.6^{+2.2}_{-1.5}$	L18[e]
$P_{\rm rot}$	days	13.8 ± 1.0	Ciardi et al. [2018]
$P_{\rm rot}$	days	15.0 ± 1.0	Mann et al. [2018]
Age	Myr	625±50	Perryman et al. [1998]
Age	Myr	750±100	Brandt and Huang [2015]
Age	Myr	650±70	Martín et al. [2018]

[a] UCAC4: Zacharias et al. [2012]

[b] Gaia DR3: Gaia Collaboration et al. [2022]

[d] 2MASS: Cutri et al. [2003]

[e] L18: Livingston et al. [2018]

Table 3.2: Properties of the transiting exoplanets orbiting K2-136. Radius estimates are divided in three columns, following the source studies, from left to right: Livingston et al. [2018, L18], Mann et al. [2018, M18], and Ciardi et al. [2018, C18]. The radii quoted on the discovery papers are shown on the three leftmost columns. The radii I calculated using R_p/R_* values from these papers together with the Gaia DR3 estimated stellar radius are shown on the three middle columns. The last three columns are orbital periods and separations from Mann et al. [2018] and planet masses from Mayo et al. [2023, M23].

Planet	Radius (R_E)			Radius (R_E) updated using Gaia DR3			Orbital Period (days)	Semi-major axis (au)	Mass (M_E)
	L18	M18	C18	L18	M18	C18	M18	M18	M23
b	1.05 ± 0.16	$0.99^{+0.06}_{-0.04}$		1.00 ± 0.05	1.02 ± 0.04		7.97520 ± 0.00079	$0.071^{+0.008}_{-0.004}$	$<2.9^{a}$ $<4.3^{b}$
c	3.14 ± 0.36	$2.91^{+0.11}_{-0.10}$	$3.03^{+0.53}_{-0.47}$	2.98 ± 0.05	3.00 ± 0.07	2.88 ± 0.01	17.30713 ± 0.00027	$0.120^{+0.022}_{-0.006}$	18.1 ± 1.9
d	$1.55^{+0.21}_{-0.24}$	$1.45^{+0.11}_{-0.08}$		1.47 ± 0.07	1.50 ± 0.07		25.5750 ± 0.0024	$0.156^{+0.017}_{-0.015}$	$<1.3^{a}$ $<3.0^{b}$

[a] 1σ upper limit

[b] 2σ upper limit

the presence of a gaseous envelope. Since envelopes tend to make up a small percentage of the mass of small planets [typically 1-2%, Rogers and Owen, 2021], we can assume that the total mass is approximately equal to the core mass. I then used the mass-radius relations by Otegi et al. [2020] for rocky planets to estimate a core radius for K2-136 c of $2.38 \pm 0.11\,\mathrm{R_E}$, making its envelope $0.58 \pm 0.18\,\mathrm{R_E}$ in thickness.

K2-136 d, with a radius of $1.48{\pm}0.11\,\mathrm{R_E}$, has mass upper limits of $1.3\,\mathrm{M_E}$ (1σ) and $3.0\,\mathrm{M_E}$ (2σ). Assuming no envelope, the mass-radius relation by Otegi et al. [2020] suggests a planet mass of $3.49 \pm 0.94\,\mathrm{M_E}$, which is consistent with the 2σ mass upper limit. The 1σ limit, however, results in a density of $2.1\,\mathrm{g\,cm^{-3}}$, which suggests the presence of an envelope. For this case, using the analysis above, I estimated a core radius of $1.10\,\mathrm{R_E}$ and thus an envelope size of $0.4\,\mathrm{R_E}$. I therefore choose to explore the evaporation past of K2-136 d using a range of core masses between these two scenarios.

Finally, the small size of K2-136 b, placing it well below the radius valley, and its close proximity to the host star indicates that it lacks an envelope. I adopted a mass of $0.95\,\mathrm{M_E}$, estimated with the mass-radius relations by Otegi et al. [2020], which is well within the 1σ and 2σ upper limits of 2.9 and $4.3\,\mathrm{M_E}$, respectively.

3.3 X-ray observations & analysis

K2-136 was observed with the *XMM-Newton* telescope on 2018 November 9, from 11:14:01 to 23:10:41 (observation ID 0824850201), [1] with a total exposure time of 41 ks, using the European Photon Imaging Camera (EPIC). A preliminary inspection of the data revealed some contamination by particle background flares in the early part of the observation, which are common in *XMM-Newton* observations [Walsh et al., 2014]. However, the signal to noise ratio of the spectrum was not improved by rejecting these events and so I chose not to filter out these time intervals.

The data were reduced using the Science Data Analysis System (SAS)[2], a collection of digital procedures and libraries designed to analyse the *XMM-Newton* telescope outputs. Since the target is expected to be a soft X-ray source, I used the data from the EPIC-pn detector, which has an operative range of 0.15 to

---

[1] The *XMM-Newton* data used in this work is publicly available at the *XMM-Newton* Science Archive (`https://www.cosmos.esa.int/web/xmm-newton/xsa`), under the observation ID 0824850201 (target: LP 358–348, PI: Wheatley)

[2] `https://www.cosmos.esa.int/web/xmm-newton/sas-threads`

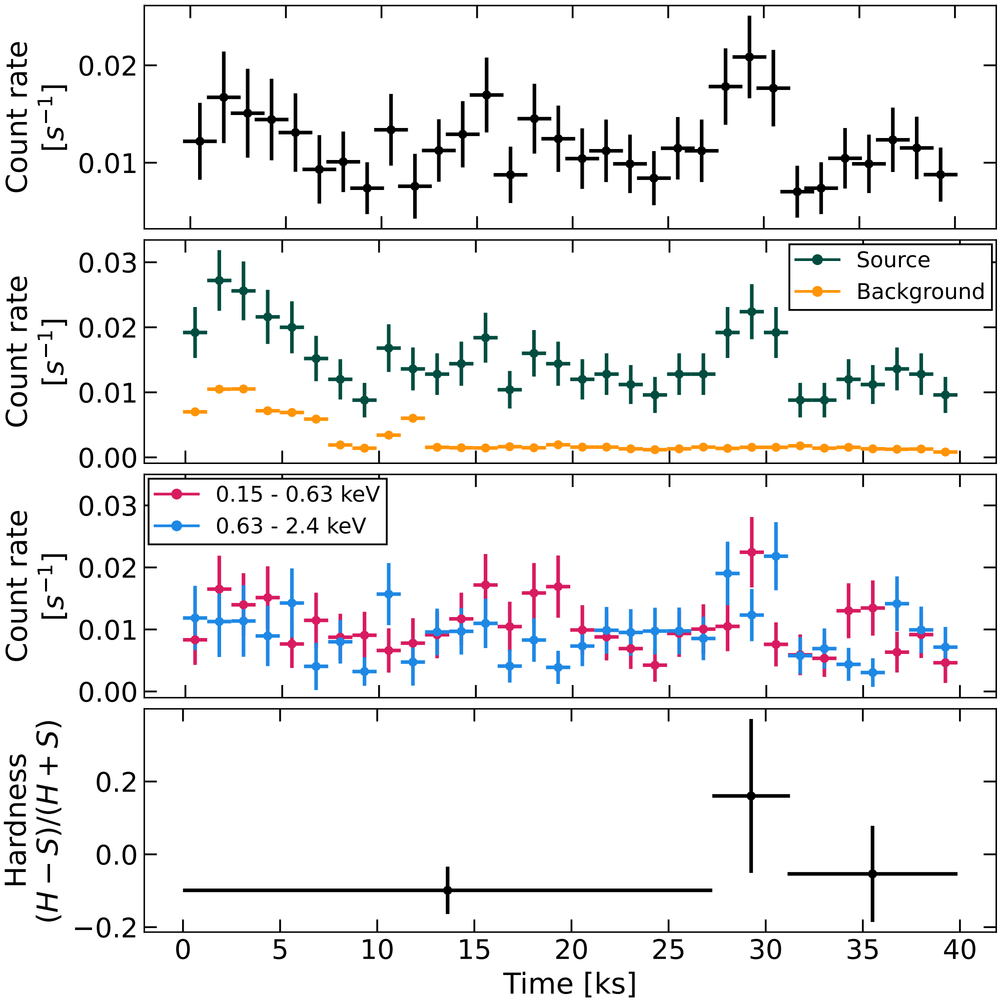

Figure 3.1: **Top panel**: background-subtracted lightcurve of K2-136. **Middle-top panel**: X-ray lightcurve of K2-136, with background count rates in yellow and source count rates in dark green. **Middle-bottom panel**: background-corrected count rate for soft (0.15-0.63 keV) and hard (0.63-2.4 keV) X-ray counts in red and blue, respectively. **Bottom panel**: hardness $(H - S)/(H + S)$ between the soft (S) and hard (H) lightcurves.

12 keV and is the most sensitive to soft X-rays [Strüder et al., 2001]. I extracted the source counts using a circular region 15 arcsec in radius centred on the proper-motion corrected coordinates of the star, and estimated the background using a circular aperture of radius 148 arcsec on a nearby source-free region. A search of Gaia DR3 [Gaia Collaboration et al., 2022] reveals no other sources within a 30 arcsecond radius.

3.3.1 Light curve

The background-subtracted lightcurve is plotted in Figure 3.1 (topmost panel). I found an average background-subtracted count rate of 0.012 s^{-1} for counts in the energy band 0.15 – 2.4 keV. The first 12 ks of the observation has elevated background counts. However, there is no increase in the background count rate at the time of the source brightening 30 ks into the observation, which is likely caused by an X-ray flare from the star.

I calculated the energy at which half the photon counts are found at lower (softer) energies and the other half at higher (harder) energies, which I found to be 0.63 keV. I plotted the soft (0.15–0.63 keV) and hard (0.63-2.40 keV) X-ray lightcurves separately in Figure 3.1, as well as the hardness ratio, defined as $(H - S)/(H + S)$, which is binned to isolate the potential flare at around 30 ks. I thus found marginal evidence that the source is harder at the time of this event, which would be expected for a stellar flare.

3.3.2 Spectral analysis

The X-ray spectrum of K2-136, plotted in Figure 3.2, is dominated by soft X-rays (< 1 keV). I fitted the spectrum using `XSPEC` [Arnaud, 1996], employing the `VAPEC` model [Smith et al., 2001], which describes the emission spectrum of collisionally-ionized diffuse gas. I allowed the abundances of common elements with strong lines in the soft X-ray range to vary (N, O, Ne, and Fe) while keeping the abundances of other elements fixed at Solar values [Asplund et al., 2009]. These elements allow us to characterize the first ionization potential (FIP) bias on the star [following e.g. Brinkman et al., 2001; Nordon et al., 2013].

To account for interstellar absorption I used the TBABS model [Wilms et al., 2000b] with a fixed hydrogen column density of $n_{\mathrm{H}} \approx 10^{18}\,\mathrm{cm}^{-2}$, as estimated for the Hyades by Redfield and Linsky [2001]. Given the relatively low number of counts, I binned the spectrum to a minimum of one count per bin and fitted using the Cash statistic [Cash, 1979]. I estimated parameter uncertainties using a Markov chain Monte Carlo (MCMC) method with 20 walkers, 10^4 steps and a burn-in of 2000 steps using the algorithm of Goodman and Weare [2010].

I found that at least three temperature components were required for the model to account for the main features and shape of the spectrum, particularly the rise in flux at softer energies. This three-temperature model is simply an approximation to a plasma with a continuous range of temperatures, which is typically found for the coronae FGK stars [Bourrier et al., 2020]. The three temperatures components had best fit energies $kT_1 = 0.11^{+0.03}_{-0.02}$ keV, $kT_2 = 0.22^{+0.02}_{-0.06}$ keV, and $kT_3 = 0.80^{+0.04}_{-0.01}$ keV. Best fitting abundances were: $2.50^{+0.48}_{-0.16}$ for N; $1.01^{+0.80}_{-0.32}$ for O; $2.28^{+0.26}_{-1.32}$ for Ne; and $0.53^{+0.13}_{-0.06}$ for Fe (relative to Solar). The resulting X-ray flux is $F_\mathrm{X} = 2.56^{+0.32}_{-0.21} \times 10^{-14}\,\mathrm{erg\,cm^{-2}\,s^{-1}}$ in the range 0.15 to 2.4 keV.

The flux at energies down to 0.1 keV was estimated by extrapolating my three-temperature model, resulting in a flux $F_\mathrm{X} = 2.80^{+0.43}_{-0.23} \times 10^{-14}\,\mathrm{erg\,cm^{-2}\,s^{-1}}$ in the range 0.1–2.4 keV.

The integrated X-ray fluxes in different energy ranges are presented in Table 3.3 and the three-temperature model is overlaid in Figure 3.2. The corresponding X-ray luminosity is $L_\mathrm{X} = 1.16^{+0.18}_{-0.10} \times 10^{28}$ erg s^{-1} in the band 0.1 – 2.4 keV, and thus the X-ray activity is $L_\mathrm{X}/L_\mathrm{bol} = 1.77^{+0.40}_{-0.46} \times 10^{-5}$. Furthermore, using the empirical relations by King et al. [2018], I estimated an EUV luminosity $L_\mathrm{EUV} = 2.31^{+0.28}_{-0.23} \times 10^{28}$ erg s^{-1} at energies 0.0136 to 0.1 keV.

FIP bias

Stellar coronal abundances have been observed to be biased according to first ionization potential [FIP; Feldman, 1992; Laming, 2015]. For solar-type stars, elements with higher FIP (e.g. O, Ne) are typically present in the corona with lower abundances than lower FIP elements (e.g. Fe) in comparison to photospheric abundances. This is caused by plasma waves in the chromosphere inducing motion in ions whilst leaving neutral atoms untouched. The geometry and type of these waves determines whether the abundances of ions are augmented or depleted in the corona [Laming, 2015]. The FIP bias is quantified as $F_\mathrm{bias} = \log_{10}(\mathrm{X/Fe})_\mathrm{cor} - \log_{10}(\mathrm{X/Fe})_\mathrm{phot}$ for an element X in comparison to iron, which as a low FIP of 7 eV [Wood and Linsky, 2010; Wood et al., 2012]. I found a coronal Ne/Fe value of $4.30^{+1.16}_{-2.54}$, and hence a positive FIP bias $F_\mathrm{bias} = 0.63^{+0.07}_{-0.27}$ for Ne, which suggests a strong *inverse* FIP effect, which is characteristic of young active stars [Audard

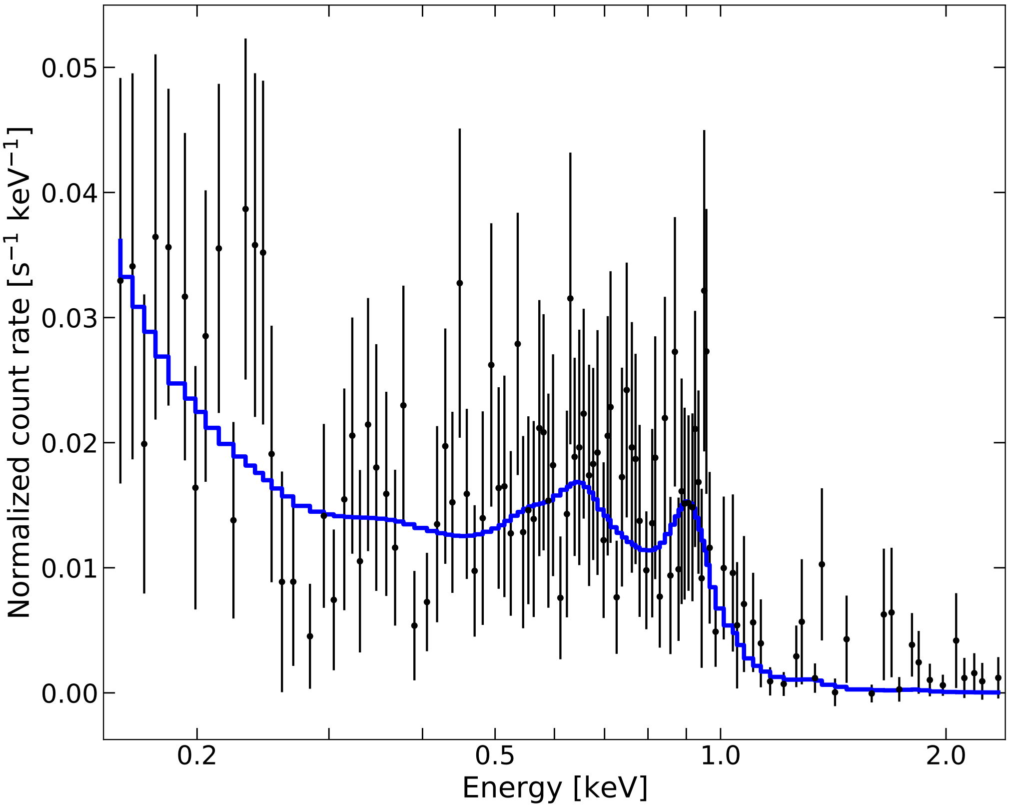

Figure 3.2: Plot of the best fit for the X-ray spectrum of K2-136 (blue line) binned to 3 counts per bin alongside my *XMM-Newton* measurements (black data points).

Table 3.3: X-ray fluxes integrated from my three-temperature VAPEC model binned to 1 count per bin.

Energy range (keV)	X-ray flux (10^{-14} erg cm^{-2} s^{-1})	Label / telescope
0.15 - 2.40	$2.56^{+0.32}_{-0.21}$	X-ray, *XMM-Newton*
0.10 - 2.40[a]	$2.80^{+0.43}_{-0.23}$	X-ray, *ROSAT*
0.0136 - 0.10[b]	$5.56^{+0.68}_{-0.55}$	EUV

[a] Extrapolated from *XMM-Newton* range.

[b] Calculated from the scaling relation of King et al. [2018].

et al., 2003; Telleschi et al., 2005a] as well as late K-dwarfs and M-type stars [Güdel et al., 2007; Wood et al., 2012; Laming, 2015].

3.3.3 Stellar companion

Ciardi et al. [2018] reported the presence of a stellar-mass companion 0.7 arcsec away from the main star using high contrast imaging at the Keck Observatory. Assuming the same distance, this translates to a projected separation of about 40 au. Since the spatial resolution (half energy width) of the *XMM-Newton* telescope EPIC-pn detector is 15 arcsec [Strüder et al., 2001]s, the candidate companion is unresolved from the primary star in my observations. Ciardi et al. [2018] provided measured magnitudes $J = 14.1 \pm 0.1$, $H = 13.47 \pm 0.04$, and $K_\mathrm{s} = 13.03 \pm 0.03$, and estimated it to be a M7/8V dwarf. Based on its colour index $\mathrm{J} - \mathrm{H} = 0.63 \pm 0.11$, I interpolated with the stellar parameter sequences by Pecaut and Mamajek [2013] and obtained a bolometric luminosity of $L_\mathrm{bol} = (1.77 \pm 0.70) \times 10^{30}$ erg s^{-1}.

Assuming that this object is indeed an M-dwarf close to K2-136 and a Hyades member, and considering that very low mass stars can remain X-ray saturated for several Gyr [Johnstone et al., 2021], I estimated its maximum contribution to the measured flux using the saturated X-ray activity of $\log_{10} L_\mathrm{X}/L_\mathrm{bol} = -3.13 \pm 0.08$ determined by Wright et al. [2011]. Its estimated X-ray luminosity is thus $L_\mathrm{X} = (1.3 \pm 0.6) \times 10^{27}$ erg s^{-1} in the band $0.1 - 2.4$ keV, with a flux that would contribute roughly 5–15% of the flux in the X-ray measurement. Since this estimated flux from the companion is comparable to the 1σ uncertainty in the XMM-Newton measurement, I chose not to account for the X-ray flux from the stellar companion in my analysis.

3.4 Evolution modelling

In order to simulate the evaporation histories of the planets, I evolved their current states back and forward in time, for which I introduce the `photoevolver` [3] code. This simulation is built upon three main components: (1) a description of the stellar XUV emission history, which provides the X-ray luminosity of the star at each point in time (Section 3.4.1); (2) a formulation for the atmospheric mass loss, which will take the incident XUV flux at the planet and translate it into mass lost (Section 3.4.2); and (3) an envelope structure formulation, which links the envelope mass to its size and describes how the envelope radius responds to mass loss (Section 3.4.3). For each of these three components I explored a range of published models. I adopted and compared three envelope structure models from Lopez and Fortney [2014], Chen and Rogers [2016] and Owen and Wu [2017], as well as four mass loss models from Erkaev et al. [2007], Salz et al. [2016], Gupta and Schlichting [2019], and Kubyshkina et al. [2018]. In some cases I took equations from those models, in others I used code provided by the authors, and in one case I translated the code into the C programming language to reduce computation time.

At each simulation time step, the XUV flux is drawn from stellar tracks (Section 3.4.1) and used to calculate the mass loss rate (Section 3.4.2) and update the envelope mass fraction. Then, the radius is recalculated using the structure formulation (Section 3.4.3).

I first solved for the current internal structure of each planet in the system, calculating what fractions of the planetary mass and radius correspond to the core and the gaseous envelope. I then evolved planets that retain a present-day envelope backwards in time from their current age of 700 Myr to 10 Myr with 0.1 Myr time steps. Ten million years is the age at which the protoplanetary disc is fully dissipated [Fedele et al., 2010] and any boil-off phase has completed [Lammer et al., 2016; Fossati et al., 2017; Owen and Wu, 2016], and I refer to this as the planet's initial state for my simulations. I also evolve these planets forward to 5 Gyr with 1 Myr time steps. Finally, in order to ensure these evaporation histories are consistent across all planets in the system, I evolved the planets with no present-day envelope forward in time from 10 Myr using a range of initial envelope mass fractions, ensuring that the envelopes are fully stripped within 700 Myr. I considered the envelope lost if the envelope mass fraction $X_{\mathrm{env}} = M_{\mathrm{env}}/M_{\mathrm{core}}$ fell below 0.01%.

---

[3] The code is available on GitHub at `https://github.com/jorgefz/photoevolver`

I choose this limit because, although such a planet might be stable [Misener and Schlichting, 2021], my chosen envelope models are not rated below this limit, and the envelope would contribute only a small fraction of the planet's radius. Furthermore, I found that the evolution code removes such envelopes within a few time steps in any case.

3.4.1 Stellar XUV history

I adopted the stellar rotation description of Johnstone et al. [2021], who modeled stellar rotational evolution by describing the convective and radiative regions as two solid shells that rotate independently, taking into account different angular momentum transport mechanisms. They combine this description with distributions of rotation periods as a function of stellar mass and age estimated from observations of nearby open clusters. The rotational evolution models for a star of the mass of K2-136 are shown in Figure 3.3.

The age of the Hyades cluster (and thus of K2-136) is well constrained (see Table 3.1) and I adopted a value of 700 Myr. In addition, Livingston et al. [2018] measured a rotation period of $13.6^{+2.2}_{-1.5}$ days, in agreement with Mann et al. [2018], who measured 15.0±1.0 days, and Ciardi et al. [2018] who identified a spin period of 13.8±1.0 days based on the periodogram of the K2 lightcurve. This period matches the median (50th percentile) of the model's distribution (Figure 3.3), although a range of rotational pasts are possible based on the error on the period, with early-age periods at 10 Myr spanning 1.7 to 9.2 days. Nevertheless, I adopted the stellar tracks that fit the star's current mass, age, and rotation period.

The X-ray activity $L_{\mathrm{X}}/L_{\mathrm{bol}}$ predicted by this model is about 3.5 times higher than my measured value (Figure 3.3 and Section 3.3). This is mainly due to the predicted X-ray luminosity, which is 2.7 times stronger than the *XMM-Newton* measurement [the predicted bolometric luminosity is only 22% greater and close to the 20% uncertainty estimated by Livingston et al., 2018]. This discrepancy is not surprising, given the spread in X-ray emission of about one order of magnitude on the rotation-activity relation [e.g. Wright et al., 2011]. The origin of this spread is not clear, although short timescale X-ray variability has been proposed as a explanation [e.g. Johnstone et al., 2021]. If this were the case, we would expect these variations to average out over time and thus the current X-ray luminosity of K2-136 might be explained by a temporary low-activity season. However, if stars follow intrinsic X-ray evolution tracks and hence the X-

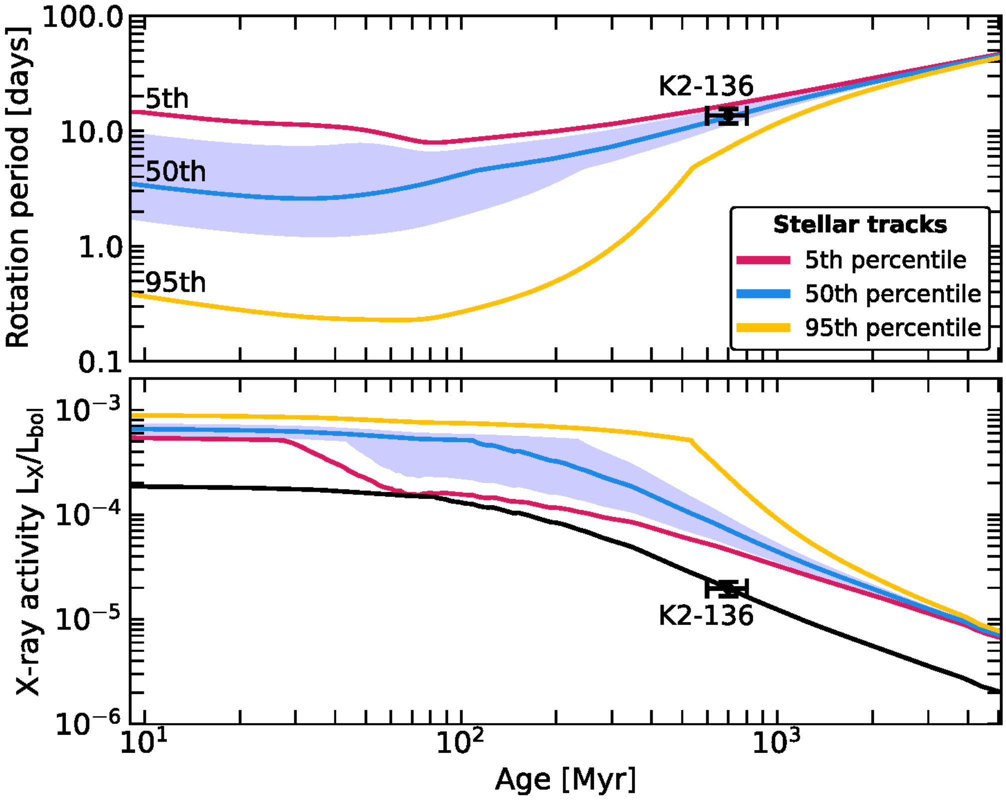

Figure 3.3: Simulated time evolution of the rotation period (top panel) and the corresponding X-ray activity (bottom panel) of a star of mass 0.69 $M_\odot$ following the models by Johnstone et al. [2021]. The diversity of rotation periods with which a star of this mass starts out is represented with three rotational evolution tracks at the 5th (red), 50th (blue), and 95th (yellow) percentiles. The measured values for the period and X-ray activity of K2-136 are plotted as black points with error bars. The area shaded in blue represents the possible rotational pasts of K2-136 given the uncertainty in its measured period. The black line on the bottom panel corresponds to the model tracks that fit the star based on its mass, period, and age, but scaled to match the X-ray measurement.

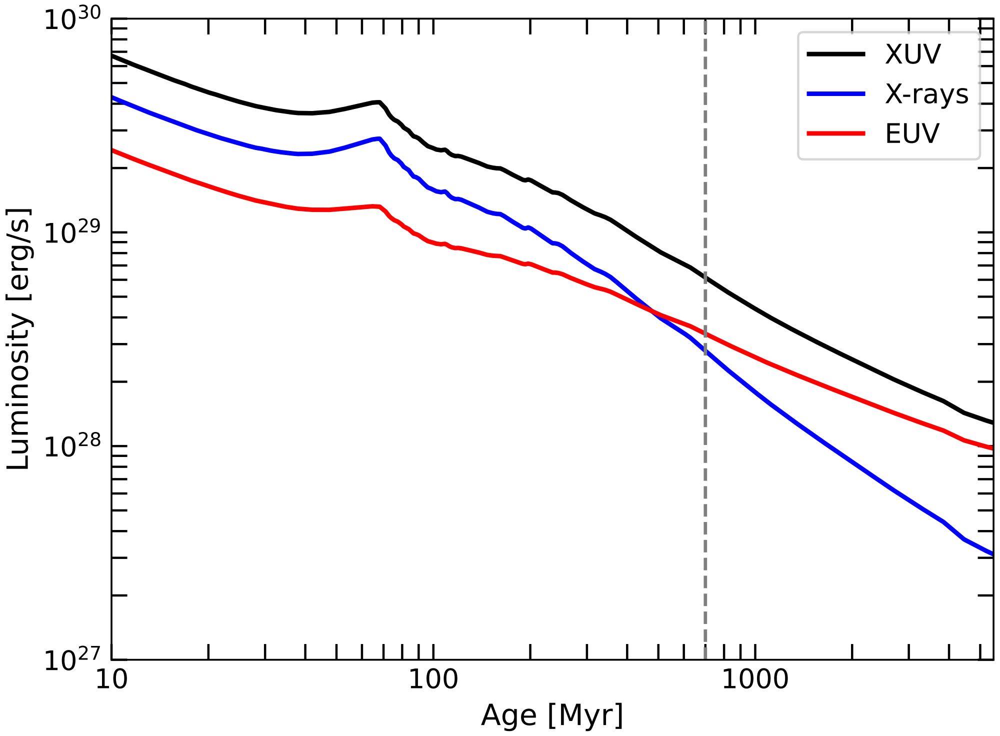

Figure 3.4: X-ray (blue), EUV (red), and the combined XUV (black) luminosity evolution tracks of K2-136 following the rotational models by Johnstone et al. [2021] for X-rays and the scaling relations by King et al. [2018] for EUV. The current age of the system, 700 Myr, is plotted as a dashed grey line.

ray activity of K2-136 is consistently lower than the model, this would result in lower mass loss rates on its planets. I thus implemented two parallel analyses: one with the predicted X-ray luminosity track for K2-136, and another with a low-luminosity track 2.7 times fainter that fits the X-ray measurements of K2-136 at its current age of 700 Myr. In Section 3.6.1 I compared the X-ray emission of K2-136 with similar Hyades members in order to assess whether the measured or modelled XUV fluxes are the most typical.

I estimated the corresponding EUV emission for the two X-ray histories using the scaling relations by King et al. [2018], who derive empirical relations between X-ray (0.1–2.4 keV) and EUV (0.036–0.1 keV) fluxes using Solar *TIMED/SEE* data. Furthermore, King and Wheatley [2021] find that the EUV luminosity of a star declines more slowly than X-rays, with EUV irradiation dominating in later ages, which may affect the evolution of planets in Gyr timescales. In Figure 3.4, I plotted both the X-ray and EUV luminosity evolution of K2-136 following this prescription, together with the combined XUV track. Indeed, the X-rays start out twice as strong as EUV at 10 Myr, then become equal at around 480 Myr, and by the age of 5 Gyr the EUV emission ends up three times stronger than X-rays (Figure 3.4).

3.4.2 Atmospheric mass loss

Atmospheric loss models estimate the mass loss rate from a planet's atmosphere. A commonly used X-ray based approximation is the energy-limited approach, in which high-energy radiation incident on the planet is converted to the work needed to bring an atom from the upper atmosphere to the Roche lobe, where it escapes the planet's gravity [Watson et al., 1981; Lecavelier Des Etangs, 2007; Erkaev et al., 2007]. The energy-limited mass loss rate is given by

$$\dot{M} = \frac{\pi \eta \beta^2 F_{\mathrm{XUV}} R_{\mathrm{p}}^3}{G K M_{\mathrm{p}}}, \tag{3.1}$$

where M_{p} and R_{p} are the mass and radius of the planet, respectively, F_{XUV} is the incident X-ray and EUV flux onto the planet, η is the energy efficiency of the process, $\beta = R_{\mathrm{XUV}}/R_{\mathrm{p}}$ where R_{XUV} is the radius at which the atmosphere becomes optically thick for XUV wavelengths; and K is the factor that accounts for the potential difference between the surface for the planet and the Roche lobe,

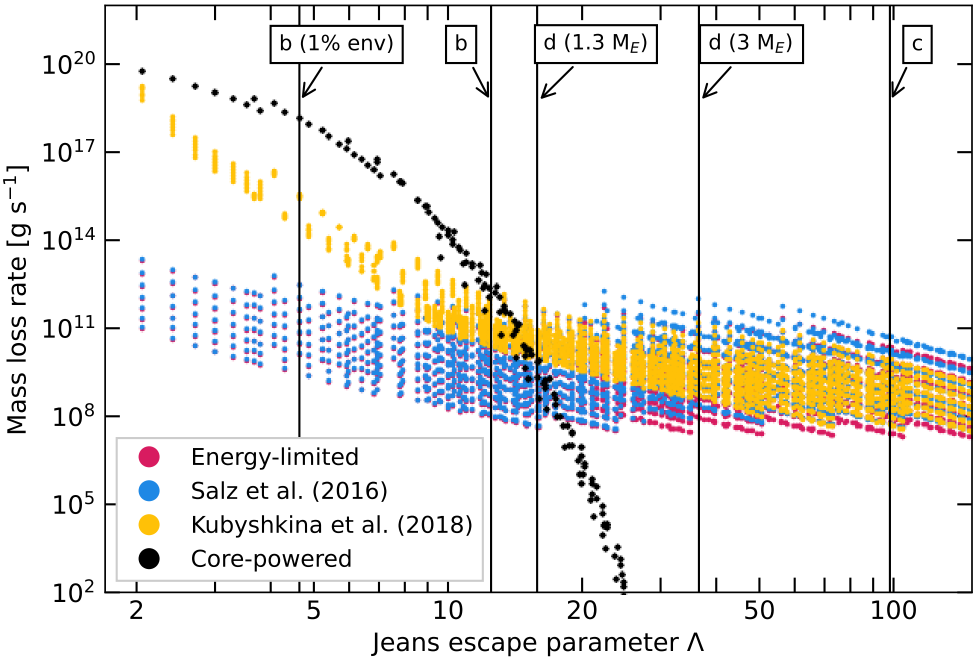

Figure 3.5: Mass loss rates from the formulations described in Section 3.4.2 as a function of the Jeans escape parameter, following Kubyshkina and Fossati [2021]. The mass loss rates are calculated from a grid of parameters that cover the expected incident XUV fluxes as well as masses and radii of the three planets across their evaporation history. The Jeans parameters of the K2-136 planets are shown as vertical lines. For planet b, I show it at its current position, and with a 1% envelope added (representative of its possible past). For planet d, I show its position for the two possible masses I consider (at 1.3 M_E with envelope mass fraction of 0.2%, and at 3 M_E with 0.05%).

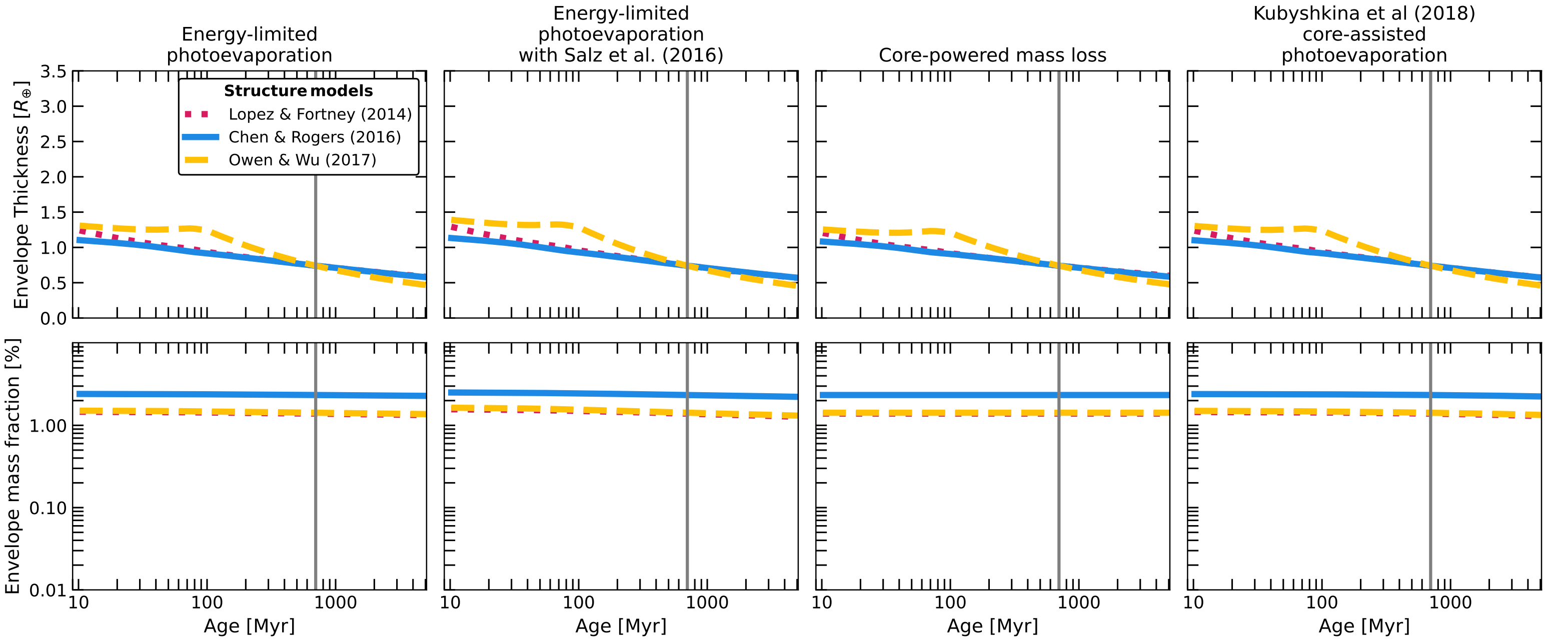

Figure 3.6: Past and future structure evolution of the planet K2-136 c, for both its thickness R_{env} (top panels) and its envelope mass fraction M_{env}/M_{core} (bottom panels). Each column uses a different mass loss formulation which are explained in detail in Section 3.4.2; from left to right: (1) standard energy-limited photoevaporation, (2) energy-limited photoevaporation enhanced by Salz et al. [2016], (3) the core-powered mass loss model by Ginzburg et al. [2016], and (4) the hydrodynamic core-assisted photoevaporation model by Kubyshkina et al. [2018]. The different coloured lines indicate each of the structure models used in the simulation: Lopez and Fortney [2014] as a red dotted line, Chen and Rogers [2016] as a blue solid line, and Owen and Wu [2017] as a yellow dashed line. The grey vertical line indicates the planet's current age. The axes are the same as for K2-136 d in Figure 3.7.

which is given by

$$K = 1 - \frac{3}{2\xi} + \frac{1}{2\xi^3}, \tag{3.2}$$

where ξ is given by

$$\xi = \frac{R_{\text{Roche}}}{R_{\text{p}}} \approx \frac{a}{R_{\text{p}}} \left(\frac{M_{\text{p}}}{3M_*} \right)^{1/3}, \tag{3.3}$$

and R_{Roche} is the Roche radius, a is the semi-major axis of the planet's orbit, and M_* is the mass of the host star [Erkaev et al., 2007].

This approach is attractively simple, although it does mask more complex physics behind the efficiency (η) and XUV radius (β) parameters, which are difficult to determine. In the first instance, I have assumed an efficiency of 15% [Lammer et al., 2009; Jackson et al., 2012; Shematovich et al., 2014; King et al., 2019] as well as an XUV radius $R_{\text{XUV}} = R_{\text{p}}$ ($\beta = 1$), which is a physical lower limit. However, observations of high-energy transits have found XUV radii to be larger than optical radii [Linsky et al., 2010b; Poppenhaeger et al., 2013; Bourrier et al., 2016], and hence I also adopted the formulation by Salz et al. [2016], who provide estimates for XUV radii using a grid of planetary gravitational potentials and incident XUV fluxes generated using hydrodynamic simulations.

Kubyshkina et al. [2018] introduced an upper atmosphere hydrodynamic model based on the work by Johnstone et al. [2015b]. They compute radial profiles for atmospheric velocity, temperature, and density, and hence estimate the atmospheric escape rate at the Roche lobe by taking into account high energy radiation at two wavelengths (EUV at 60 nm and X-rays at 5 nm) as well as internal core heating. The model deviates from the energy-limited approach for highly-irradiated low-gravity planets, where it predicts greater mass loss rates. I adopted the updated model grid and interpolation routine provided by Kubyshkina and Fossati [2021].

Alternative formulations that do not rely on XUV irradiation have also been suggested. One such example is core-powered mass loss [Ginzburg et al., 2016], which draws the energy to evaporate envelopes from the core's internal thermal luminosity. This formulation has also been shown to replicate the observed exoplanet radius-period distribution [Ginzburg et al., 2018; Gupta and Schlichting, 2019], and operates on timescales of Gyr. King and Wheatley [2021], however, have shown that significant EUV irradiation also continues on Gyr timescales, and thus the timescale of mass loss alone cannot easily be used to distinguish between the photoevaporative and core-powered mechanisms.

I ran a set of simulations that combine each structure formulation described in Section 3.4.3 with the following mass loss descriptions: (1) energy-limited with 15% efficiency and $R_{\mathrm{XUV}} = R_{\mathrm{p}}$, which I refer as 'standard' hereafter, (2) energy-limited with 15% efficiency and R_{XUV} described by Salz et al. [2016], (3) core-powered mass loss [Ginzburg et al., 2016], and (4) hydrodynamic simulations of Kubyshkina et al. [2018], which reproduce the core-powered and photoevaporative mass loss regimes.

In Figure 3.5 I compared these mass loss formulations as a function of the Jeans escape parameter, which quantifies how vulnerable a gaseous atmosphere is to escape due to thermal escape mechanisms. This parameter is defined as

$$\Lambda = \frac{G M_{\mathrm{p}} m_{\mathrm{H}}}{k_{\mathrm{B}} R_{\mathrm{p}} T_{\mathrm{eq}}}, \tag{3.4}$$

where M_{p} and R_{p} are the planet's mass and radius, respectively, T_{eq} is the equilibrium temperature, m_{H} is the mass of a hydrogen atom, and k_{B} is the Boltzmann constant. Following Kubyshkina and Fossati [2021], two mass loss regimes can be identified. Atmospheres in the low-Λ regime are loosely bound and are more susceptible to mass loss; this regime contains planets that are highly irradiated and/or low gravity. The high-Λ regime, on the other hand, applies to massive planets with tightly bound envelopes. In practice, individual planets will tend to evolve towards higher Λ (right) and lower mass loss rates (down) as envelopes cool and shrink, and as the stellar XUV emission declines.

As expected, the energy-limited formulation is not a strong function of Jeans parameter (Figure 3.5), with most points lying on the same range of mass loss rates across Λ, as mass loss scales linearly with flux and inversely with potential. Furthermore, both the Kubyshkina et al. [2018] and the core-powered formulations predict mass loss rates several orders of magnitude greater than energy-limited on planets with low Jeans parameter, but differ the most on the high-Λ regime, where Kubyshkina et al. [2018] tends to maintain levels similar to energy-limited in most cases whereas core-powered drops steeply and the escape rate becomes negligible for $\Lambda > 20$.

3.4.3 Envelope structure models

Models typically describe the gaseous planetary envelope as having two layers: an inner adiabatic and convective layer, and an outer radiative layer that is isothermal at the equilibrium temperature. Sources of heat act to inflate the envelope, and heat loss causes it to shrink. In my simulations, I considered three envelope structure models from the studies of Lopez and Fortney [2014], Chen and Rogers [2016], and Owen and Wu [2017]. The envelope structure model by Lopez and Fortney [2014] provides the envelope thickness as a function of planet mass, envelope mass fraction, bolometric flux, and age. It considers the core entropy and radioactive elements within the planet as well as the stellar bolometric flux as sources of heat, and heat loss occurs through wavelength-dependent radiative cooling. The optical radius of the planet is defined by a fixed atmospheric pressure of 20 mbar. Additionally, they also use hot-start models, which imply a high starting core entropy on newly formed planets. This energy comes from the gravitational potential energy of accreted matter being turned into thermal energy during planet formation. This assumption can result in particularly large initial radii, although it also leads to rapid cooling and envelope shrinking at early ages, making the choice of initial entropy unimportant by the age of 100 Myr [Lopez et al., 2012]. I adopted the polynomial fit they provided in Lopez and Fortney [2014, equation 4], which is an empirical characterisation of a precalculated grid of models covering envelope mass fractions between 0.01% and 20%.

The envelope model from Chen and Rogers [2016] follows a similar description to Lopez and Fortney [2014] but they make use of the 1D stellar evolution code MESA (Modules for Experiments in Stellar Astrophysics) adapted to H/He planetary envelopes. This model also defines the planet radius as the height at a fixed optical depth, in order to avoid issues that arise with small planets with puffy initial states contracting rapidly. In my simulations, I adopted the quadratic fit to a precalculated model grid provided by Chen and Rogers [2016, equation 5], which is also valid for envelope mass fractions between 0.01% and 20%.

Finally, Owen and Wu [2017] introduced a fully analytical approach for calculating the envelope thickness considers the heat transport through the convective-radiative boundary in the atmosphere as well. In their model, the temperature profile of the atmosphere is adiabatic in the convective interior, but it's anchored to the equilibrium temperature at the radiative-convective boundary, as the radiative layer above is isothermal due to heating from stellar insolation. and used it to recreate the radius valley adopting envelope mass fractions from 0.01% to 60% and ages from 1 Myr to 3 Gyr. Owen and Campos Estrada [2020a] later provided a Python implementation of this envelope structure model[4] which I adopted for

---

[4] The envelope structure model by Owen [2019] is available on GitHub at `https://github.`

this work. In this case, I translated their Python code into the C programming language to shorten the computation time. This code is included in `photoevolver`, and I have ensured that it produces identical results to the original Python code.

3.5 Simulation results

3.5.1 Current planet structures and mass loss rates

For K2-136 c, I estimated the current envelope mass fraction $M_{\text{env}}/M_{\text{core}}$ to be 1.1% with the models of Lopez and Fortney [2014] and Owen and Wu [2017], and 1.7% with Chen and Rogers [2016], where M_{env} is the mass of the gaseous envelope and M_{core} is the mass of the rocky core. For K2-136 d, using the 1σ upper limit on the mass ($< 1.3\,\mathrm{M_E}$; Table 3.2), I estimated an envelope mass fraction of 0.2% for all three models. As noted in Section 3.2, the 2σ upper limit on the mass of K2-136 d is consistent with a bare rocky core, with no significant gaseous envelope surviving to the present day. The mass constraints for K2-136 b are less precise and allow a gaseous envelope, but due to its small radius and proximity to its host star I assumed it is a rocky core at the present day.

The current mass loss rates for planets c and d are shown in Table 3.4 for each of the mass-loss prescriptions described in Section 3.4.2. Due to its lower gravitational potential, K2-136 d has higher predicted mass loss rates overall than K2-136 c, despite being more distant from its host star. Furthermore, in the case of K2-136 d, standard energy-limited predicts lower escape rates in comparison to other formulations, whereas for K2-136 c the energy-limited formulations predict similar escape rates to Kubyshkina et al. [2018]. Those authors argue that the energy-limited formulation underestimates mass loss on very low gravity planets, as it does not account for the contribution of the planet's internal thermal energy in assisting atmospheric escape. Finally, in the case of planet c, core-powered mass loss predicts a negligible escape rate due to the deeper gravitational potential.

3.5.2 Evaporation histories

K2-136 c

Firstly, I found that K2-136 c has remained relatively unchanged during its lifetime, as shown in Figure 3.6, regardless of the choice of envelope and mass loss prescrip-

---

`com/jo276/EvapMass`

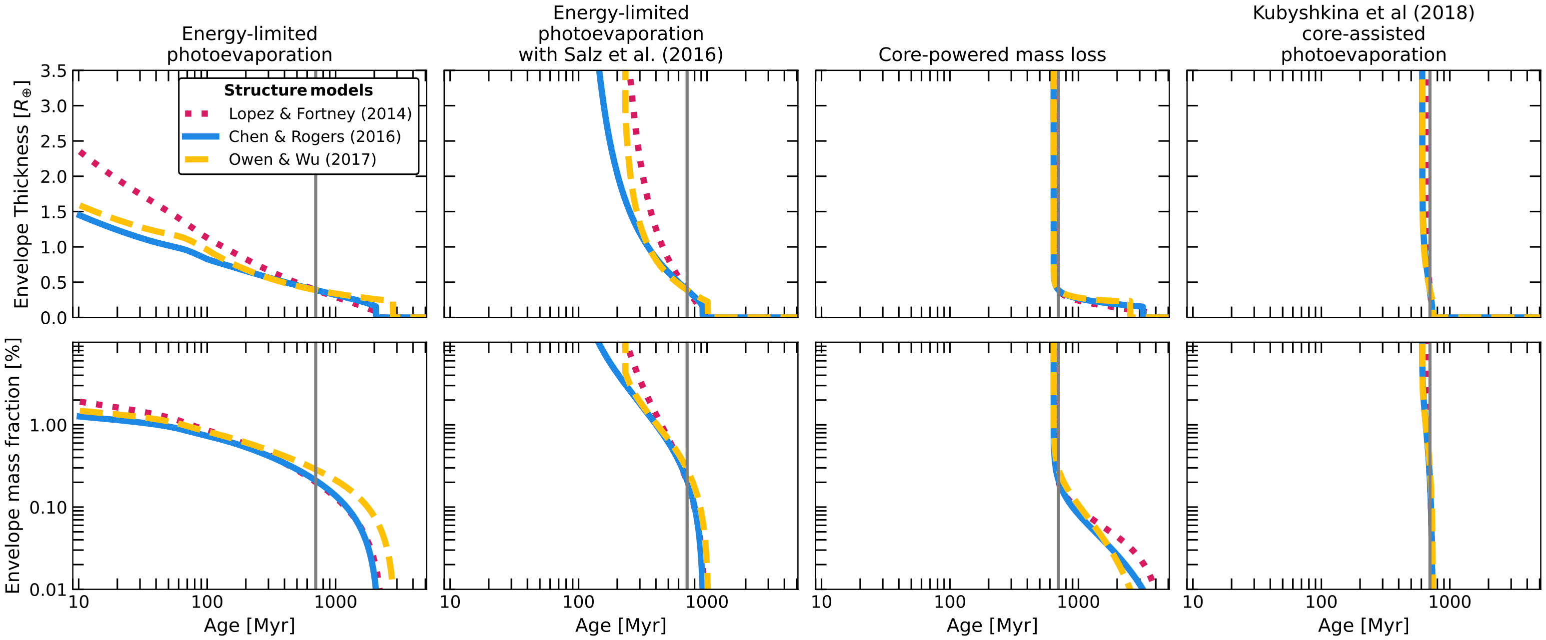

Figure 3.7: Past and future structure evolution of the planet K2-136 d with a core mass of 1.3 $\mathrm{M_E}$, akin to Figure 3.6.

Table 3.4: Current mass loss rates for planets c and d using the mass loss prescriptions described in Section 3.4.2. From left to right: standard energy-limited (EL), enhanced energy-limited according to Salz et al. [2016, S16], core-powered mass loss by Gupta and Schlichting [2019, GS20], and the hydrodynamic simulations of Kubyshkina et al. [2018, K18].

Planet	Mass loss rate (10^8 g s^{-1})			
	EL	S16	GS20	K18
K2-136 c	8.7	18.3	0.0[b]	10.4
K2-136 d[a]	7.7	32.2	36.5	237

[a] Using core mass $M_{\rm core} = 1.3\,{\rm M_E}$.
[b] Mass loss rate below 10^3 g s $^{-1}$ (negligible).

tions. This is due to its high mass of $18.1 \pm 1.9\,{\rm M_E}$ and thus deep gravitational potential which inhibits atmospheric loss. All scenarios predict an initial planet size at 10 Myr of $R_{\rm p} = 3.5\,{\rm R_E}$, following any boil-off phase [e.g. Owen and Wu, 2016]. Subsequently, the planet shrinks primarily due to the thermal cooling and contraction of its envelope. Mass loss is minimal, with an almost constant envelope mass fraction throughout its lifetime. I also found that this planet will not lose its envelope in the next several Gyr. The bump apparent in the envelope model by Owen and Wu [2017] model in Figure 3.6 is a feature of their formulation. They argue that boil-off early in the planet's evolution leads to a rapid cooling and loss of the primordial gaseous envelope, affecting the thermal evolution of the envelope for the first 100 Myr. They address this phenomenon by halting age-dependent thermal evolution for this period of time.

K2-136 d

The evolution of K2-136 d is shown in Figure 3.7, in which a core mass of $M_{\rm core} = 1.3\,{\rm M_E}$ was used (see Sections 3.2 & 3.5.1). The planet's envelope experiences significant evolution in both its past and its future. The standard energy-limited model predicts an initial planet radius of 2.6 to $3.3\,{\rm R_E}$, with initial envelope mass fractions of 1 to 2%, and complete envelope loss within the next 1 to 2 Gyr. All other mass loss formulations, however, predict an apparent runaway enlargement during backwards evolution. This difference is consistent with the argument by Kubyshkina et al. [2018] that energy-limited formulations underestimate mass loss for low-gravity planets.

Apart from standard energy-limited escape, the models in Figure 3.7 indi-

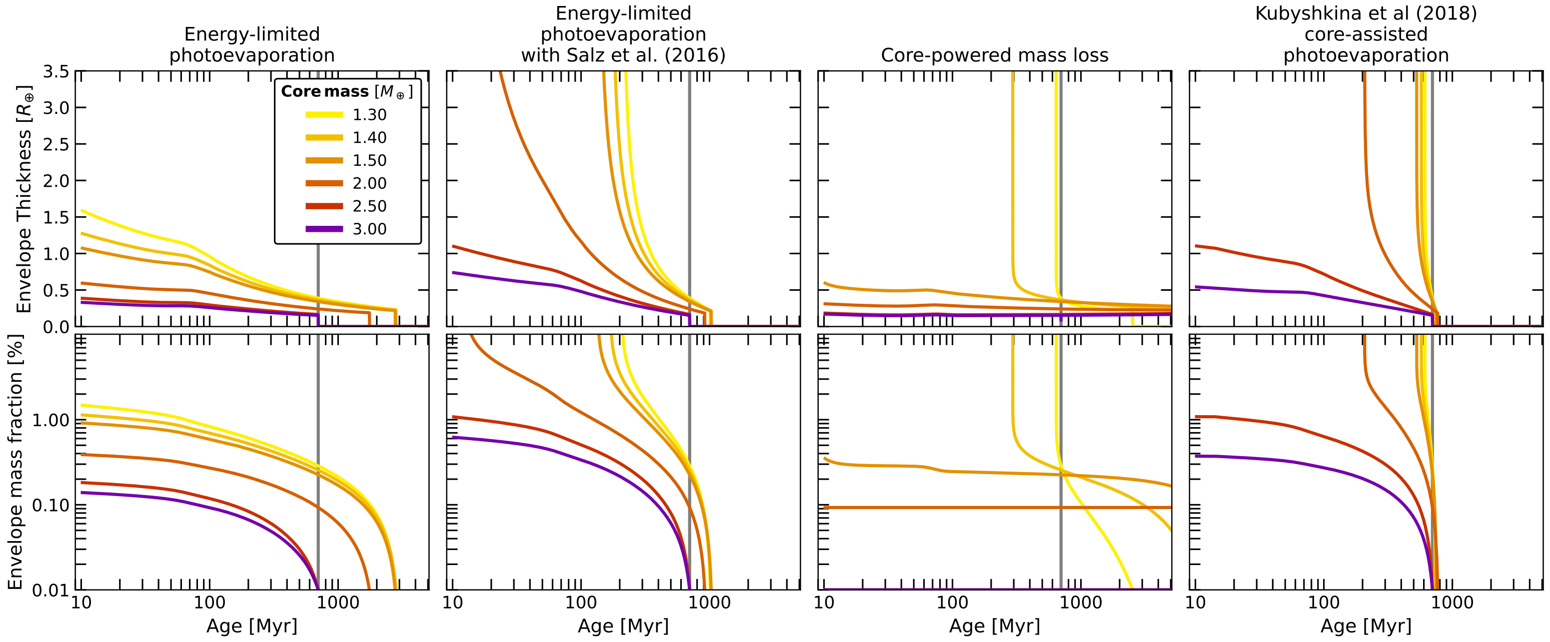

Figure 3.8: Past and future evolution of the planet K2-136 d with a range core masses (and radii) from lightest (yellow) to heaviest (purple): 1.3 $\mathrm{M_E}$ (1.11 $\mathrm{R_E}$), 1.4 $\mathrm{M_E}$ (1.14 $\mathrm{R_E}$), 1.5 $\mathrm{M_E}$ (1.16 $\mathrm{R_E}$), 2.0 $\mathrm{M_E}$ (1.26 $\mathrm{R_E}$), 2.5 $\mathrm{M_E}$ (1.34 $\mathrm{R_E}$), and 3.0 $\mathrm{M_E}$ (1.42 $\mathrm{R_E}$). The corresponding solid core radii are calculated using the mass radius relations by Otegi et al. [2020]. The evolution of the envelope thickness $\mathrm{R_{env}}$ is shown on the top panels and the corresponding mass fraction on the bottom panels. All tracks make use of the structure formulation by Owen and Wu [2017]. A different mass loss model is used for each column, which are described on Section 3.4.2; from left to right: (1) standard energy-limited photoevaporation, (2) energy-limited photoevaporation enhanced by Salz et al. [2016], (3) the core-powered mass loss model by Ginzburg et al. [2016], and (4) the hydrodynamic photoevaporation model by Kubyshkina et al. [2018].

cate that the planet, with a core mass of $1.3\,\mathrm{M_E}$, requires an very large initial envelope fraction (more akin to a gas giant with $M_{\mathrm{env}} \gg M_{\mathrm{core}}$) in order to still retain part of its envelope by the age of 700 Myr. However, the steepness of the evolution around the current time shows that models with very large initial envelope fractions would require very fine tuning to reproduce the state of K2-136 d at its current age. Instead, I concluded that K2-136 d is more likely to have a mass significantly in excess of $1.3\,\mathrm{M_E}$ (which is the $1\,\sigma$ upper limit from HARPS-N, see Section 3.2).

I then proceeded to find a lower limit to the mass of K2-136 d, such that the presence of a small envelope (to explain its size and density) is consistent with my simulated evaporation histories. The upper limit of the mass, on the other hand, comes from assuming that K2-136 d is entirely rocky with a mass of $3.6\,\mathrm{M_E}$.

In order to constrain the minimum viable mass of K2-136 d, I studied its evaporation history as a function of mass. I applied the same analysis with a range of core masses between $M_{\mathrm{p}} = 1.3\,\mathrm{M_E}$ (corresponding to $R_{\mathrm{core}} = 1.1\,\mathrm{R_E}$) to $M_{\mathrm{p}} = 3.0\,\mathrm{M_E}$ (with $R_{\mathrm{core}} = 1.4\,\mathrm{R_E}$). I adopted a single structure model for my analysis, Owen and Wu [2017], which predicts intermediate planet sizes in comparison to Lopez and Fortney [2014] and Chen and Rogers [2016], and is applicable to ages younger than 100 Myr. My results in Figure 3.8 show that the energy-limited model is consistent with the full range of masses and predicts initial planet radii ranging from 1.8 to $2.7\,\mathrm{R_E}$, with envelope mass fractions of 0.15 to 1.5%, for the heaviest and lightest cases, respectively. For the other mass-loss formulations, I defined a threshold core mass above which the planet does not grow exponentially in size to earlier times.

I thus estimated minimum core masses of $1.5\,\mathrm{M_E}$ with core-powered mass loss [Gupta and Schlichting, 2019], $2.0\,\mathrm{M_E}$ with enhanced energy-limited escape [Salz et al., 2016] and $2.5\,\mathrm{M_E}$ for the model of Kubyshkina et al. [2018].

Salz et al. [2016] and Kubyshkina et al. [2018] generally agree in their results for the 3.0 and $2.5\,\mathrm{M_E}$ cores, predicting initial radii of 2.0 and $2.4\,\mathrm{R_E}$ and corresponding envelope mass fractions of 0.5% and 1.0% for the two core masses, respectively (Figure 3.8). These results would classify K2-136 d as a sub-Neptune for at least 100 Myr after formation. These two formulations, however, diverge on their assessment of the $2.0\,\mathrm{M_E}$ case. Whilst Kubyshkina et al. [2018] predicts runaway enlargement during backward evolution, Salz et al. [2016] predicts an inflated Saturn-sized planet with radius $9.9\,\mathrm{R_E}$ and mass fraction 11% as the initial state.

In contrast, core-powered mass-loss [Gupta and Schlichting, 2019] predicts much lower mass loss rates for the higher mass cores, and thus only discards the 1.3 and 1.4 $\mathrm{M_E}$ core mass scenarios. For its minimum viable mass case of 1.5 $\mathrm{M_E}$, it predicts a smaller initial planet size of 1.7 $\mathrm{R_E}$ (mass fraction 0.3%), which would place the planet at the centre of the radius valley after formation.

Looking at the future evolution of planet d in Figure 3.8, complete envelope loss occurs fairly rapidly with the Salz et al. [2016] and Kubyshkina et al. [2018] models, with both mass-loss prescriptions stripping the envelopes within tens to 200 Myr into the future. Standard energy-limited escape is slower, but still results in complete loss of the envelope within 2 Gyr. Core-powered mass loss predicts complete envelope loss only for the lightest core of 1.3 $\mathrm{M_E}$ within 2 Gyr.

Finally, I explored the case where K2-136 d is entirely rocky, with a mass of 3.6 $\mathrm{M_E}$. For this planet, we can find an upper limit on the mass of its primordial atmosphere, which should be completely removed by its current age in order to be consistent with photoevaporation. To do so, I first added an envelope consisting of 0.01% of its mass (which would be stripped within one simulation time step), and evolved the planet backwards in time using the Kubyshkina et al. [2018] model. This led to a relatively low upper limit on the initial envelope mass fraction of such a planet of just 0.2%. This scenario is also in tension with constraints on the total mass of the planet (Section 3.2).

K2-136 b

For K2-136 b, the smallest and most close-in of the three planets, I ran my evolution code forward from 10 Myr using initial envelope mass fractions ranging from 0.1% to 5% and assuming a core mass of 1 $\mathrm{M_E}$. I found all of these initial envelopes are lost within 5 to 30 Myr even with the standard energy-limited model. All the other mass loss prescriptions are even faster, with envelope loss timescales of 1-2 Myr. These results were expected, given the planet's small size and close proximity to the star, and confirm that any primordial envelope will have been lost early in its evolution.

The initial radius of K2-136 b can be estimated by mirroring the initial states of the other two planets. An initial envelope mass fraction of about 1.5%, emulating K2-136 c, would translate to an initial radius of 2.8 $\mathrm{R_E}$, using the Owen and Wu [2017] structure formulation. Likewise, an initial mass fraction of 0.6%, following the higher mass scenarios for K2-136 d, results in an initial radius of

$2.1\,\mathrm{R_E}$. Both cases would qualify the planet as a sub-Neptune at disk dispersal.

3.5.3 Alternative low-level XUV history

I repeated my analysis from Section 3.5.2 using an alternative low-luminosity XUV track that scales the Johnstone et al. [2021] model to the X-ray flux measured with *XMM-Newton* in Section 3.3.2. This flux is a factor 2.7 lower than used in Section 3.5.2, and it is a better match to the X-ray fluxes of similar stars in the Hyades cluster (see Section 3.6.1).

As expected, my results for K2-136 c are essentially identical, with negligible mass loss and the evolution progressing as a gradual thermal contraction of its envelope. Results for K2-136 b are also essentially unchanged, with complete loss of any primordial envelope occurring early in the lifetime of the system.

My results for K2-136 d are plotted in Figure 3.9, excluding core-powered mass loss, which does not depend on high energy irradiation (and is hence unchanged from Figure 3.8). As expected, the lower XUV flux results in reduced mass loss for all of the other three models. For standard energy-limited mass loss, the predicted initial radii are roughly 50% smaller. Similarly, the Salz et al. [2016] and Kubyshkina et al. [2018] models predict lower initial radii for tracks that do not lead to very rapid evaporation. For the Kubyshkina et al. [2018] model, only the 2.5 and $3.0\,\mathrm{R_E}$ tracks are consistent with formation as a sub-Neptune, as before, but for the Salz et al. [2016] enhanced energy-limited model, the $1.5\,\mathrm{M_E}$ core mass scenario becomes viable, bringing the model closer to consistency with the 1σ upper limit on the measured mass (Table 3.2). This $1.5\,\mathrm{M_E}$ track has an initial envelope mass fraction of 5% and planet radius of $5.6\,\mathrm{R_E}$. A core mass between 1.5 and $2.0\,\mathrm{M_E}$ would now mirror the initial envelope mass fraction of K2-136 c of approximately 1.5%.

3.6 Discussion

Based purely on the radii and orbital periods of the planets orbiting K2-136, the system presents a challenge to photoevaporation as an explanation of the radius-period valley. The innermost planet, K2-136 b, lies below the radius valley, and can easily be explained as the stripped core of a sub-Neptune. The next planet, K2-136 c, is above the valley and can be understood as having survived the strongest XUV irradiation from the young star. However, the planet farthest from the

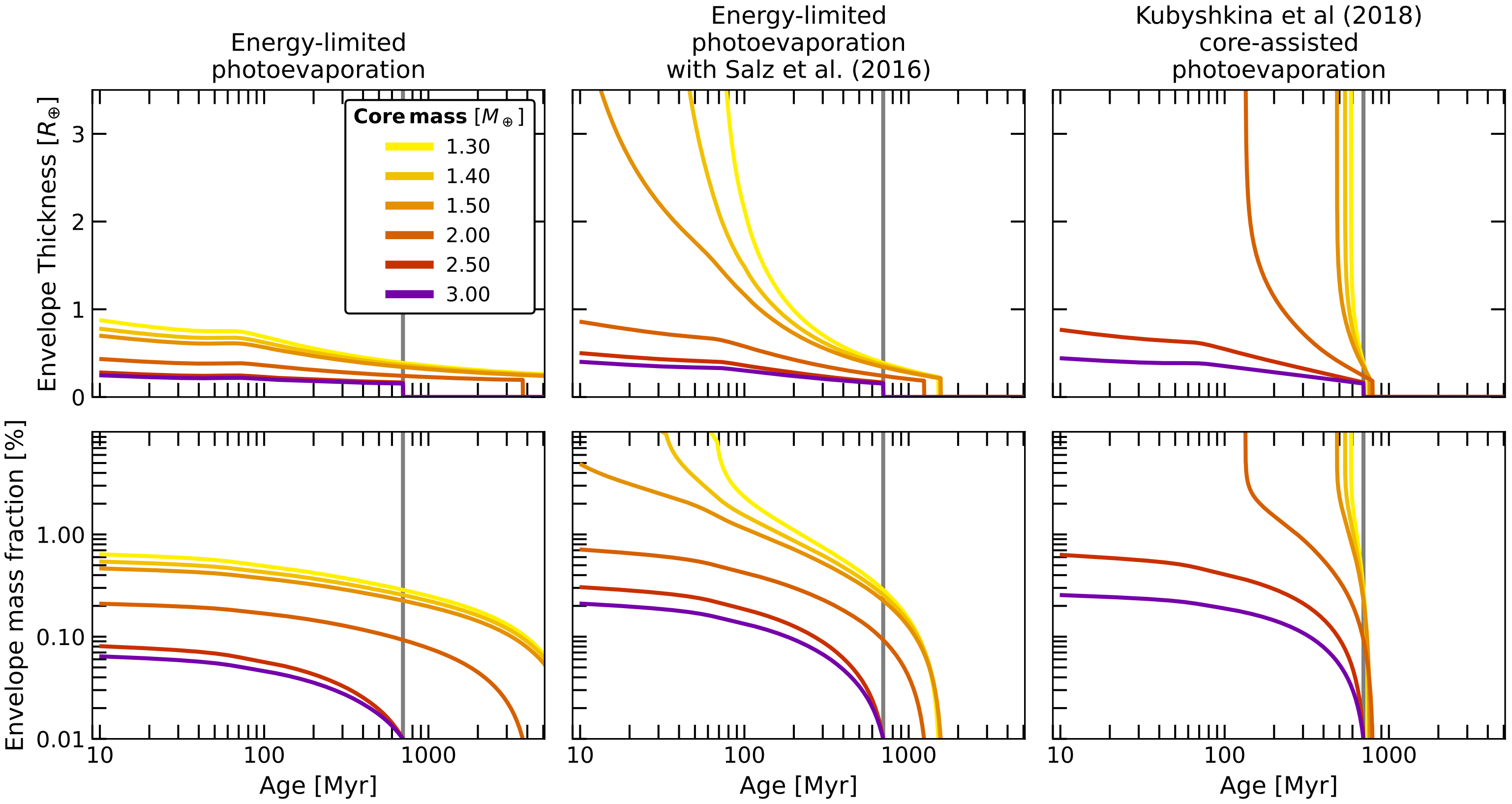

Figure 3.9: Past and future evolution of the planet K2-136 d presented in a similar manner to Figure 3.8 but with stellar XUV tracks that fit the measured X-ray luminosity of K2-136. Core-powered mass loss is omitted as it is unaffected by changes in X-ray irradiation.

star, K2-136 d, lies below the radius valley, suggesting it has lost any primordial envelope. The simultaneous presence of planets c and d in the same system, having experienced the same XUV flux history, presents useful constraints on the process of photoevaporative mass loss on multi-planet systems.

The two key factors controlling photoevaporative mass loss from exoplanets are the XUV radiation environment (and its history) and the response of the planetary envelope to irradiation as a function of core mass. I discuss the XUV radiation environment of the K2-136 planets in Section 3.6.1, in context with its membership of the Hyades cluster. I then discuss the response of the K2-136 planetary envelopes to that irradiation in Section 3.6.2.

3.6.1 K2-136 in context within the Hyades

Freund et al. [2020] compiled a Hyades membership list using Gaia DR2 [Gaia Collaboration et al., 2018b] and collected X-ray flux measurements from 281 Hyades members, 103 of which also have measured rotation periods (from TESS and K2), and estimated X-ray upper limits for the undetected ones. In Figure 3.10 (left hand panel), I plotted the rotation dependence on Gaia BP-RP colour index (the difference between blue and red Gaia magnitudes) for the Hyades, which is indicative of the stellar spectral class. FGK and early M stars present a tight relation between temperature and period that has been observed in other open clusters [e.g. Hartman et al., 2009; Agüeros et al., 2011; Gillen et al., 2020]. The outliers in the FGK range with shorter periods are likely to be close binaries that have been spun up by tidal interactions [Zahn, 1977; Simonian et al., 2019]. Later type M-dwarfs, on the other hand, present a wide range of rotation periods. I found that K2-136, which is a K-dwarf with a period of $13.6^{+2.2}_{-1.5}$ days, fits well within this tight relation, and thus has a rotation period that is typical for a Hyades member of this spectral type. The model by Johnstone et al. [2021] is also in good agreement with the star's rotation period.

In Figure 3.10 (right hand panel) I also plotted X-ray activity $L_{\mathrm{X}}/L_{\mathrm{bol}}$ against BP-RP colour for these Hyades stars. The stars I identified as spun-up binaries are generally more X-ray active than other FGK stars, which is expected as faster rotators are more X-ray active [Walter et al., 1978; Dempsey et al., 1993, 1997]. The measured X-ray activity of K2-136 from Section 3.3.2 is also plotted in Figure 3.10, as is the predicted X-ray activity from the Johnstone et al. [2021] model. It can be seen that the measured X-ray activity of 1.77×10^{-5} is a much

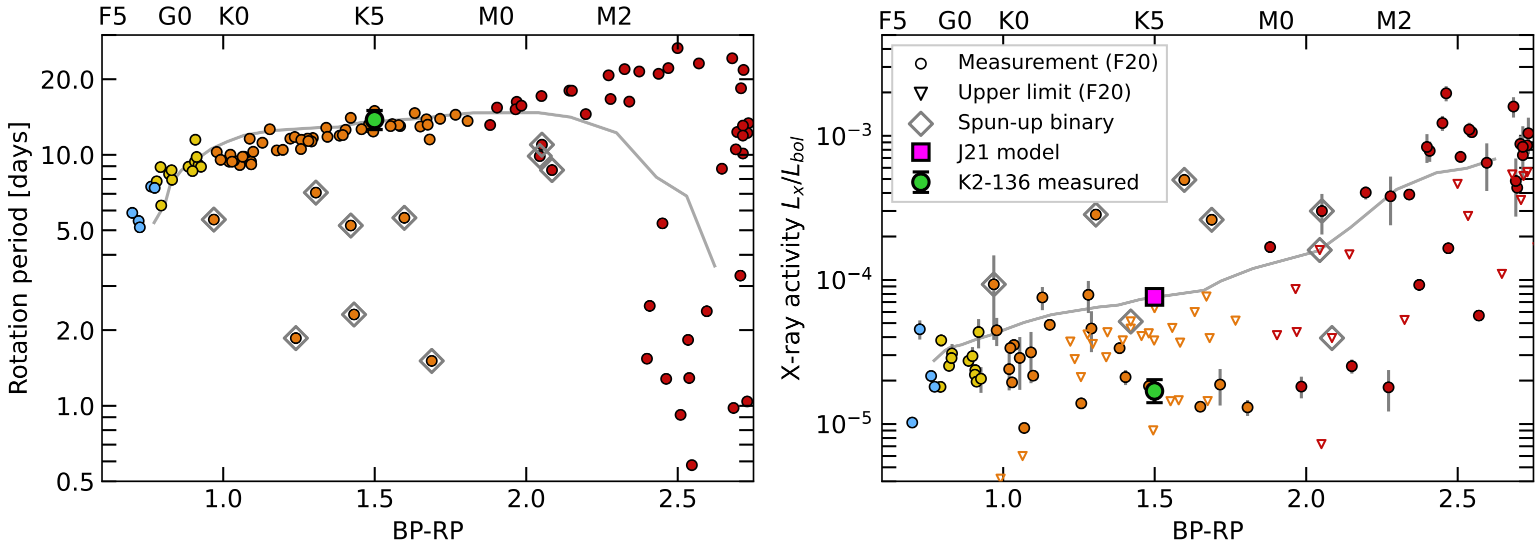

Figure 3.10: **Left panel:** Hyades stars from Freund et al. [2020, F20] plotted on a Gaia BP-RP colour index against rotation period plot. The stars are also colour-coded to spectral type (F stars light blue, G stars yellow, K dwarfs orange, and M dwarfs red). K2-136 is shown as a green circle, and the outliers I identified as spun-up close binaries are marked with diamonds. The grey line represents the mean rotation period as a function of stellar mass for Hyades stars predicted by the model of Johnstone et al. [2021, J21]. **Right panel:** Hyades stars from Freund et al. [2020, F20] plotted on a Gaia BP-RP colour index against measured X-ray activity $L_{\mathrm{X}}/L_{\mathrm{bol}}$ in the energy band $0.1 - 2.4\,\mathrm{keV}$, with markers and symbols similar to the panel on the left. X-ray upper limits (2σ) are shown as triangles. The X-ray activity I determined for K2-136 is shown as a green circle, and the activity predicted by the model of J21 is shown as a magenta square. It can be seen that the measured X-ray flux for K2-136 is a better match to the other Hyades K stars than the flux predicted by J21.

better match to the X-ray detections and upper limits of similar Hyades K-dwarfs (with detections around $\sim 2 \times 10^{-5}$) than it is to the model prediction, which lies between the measured single stars and close binaries at 6.6×10^{-5}.

For this reason, I favoured the analysis of photoevaporation I carried out in Section 3.5.3, where I scaled the Johnstone et al. [2021] model to the observed X-ray luminosity.

More generally, Figure 3.10 shows that the rotation-activity relation employed by Johnstone et al. [2021] is systematically over-predicting the X-ray luminosities of single G and K stars in the Hyades. This may be due to contamination by close binaries of the sample of stars used to determine the rotation-activity relation.

3.6.2 Evaporation history of the three planets

In Figure 3.11 I presented a period-radius plot with the locations of the three planets as observed at the present time, together with their evaporative pasts and futures as modelled in Section 3.5.

K2-136 b

I found that K2-136 b is most consistent with an Earth-sized rocky world: an apparently typical member of the large population of small dense planets below the radius-period valley. My simulations show that its primordial envelope, if any, was lost shortly after the dispersal of the protoplanetary disc. Assuming this primordial envelope made up 1% of its mass (mirroring its sibling K2-136 c) I found that K2-136 b would have formed with a radius of $2.8\,\mathrm{R_E}$ adopting the envelope model by Owen and Wu [2017], making it a sub-Neptune above the radius valley (Figure 3.11).

K2-136 c

In contrast, K2-136 c remains a sub-Neptune above the radius valley, with a thick envelope making up of 1–2% of its mass. All my evaporation models suggest that this planet is stable against evaporation. In large part, this is due to its relatively high mass of $18\,\mathrm{M_E}$ measured with HARPS-N (Section 3.2).

Interestingly, this high mass implies a core radius of $2.4\,\mathrm{R_E}$ (see Section 3.2), which would place K2-136 c above the radius valley even if its envelope were entirely stripped (Figure 3.11). In such a case, without a mass measurement, the planet might be misidentified as a lower-mass planet with a thick envelope, leading to erroneous conclusions about the efficiency of envelope evaporation. This underlines the importance of mass measurements. It also illustrates that a location above the radius valley does not in itself require a planet to have a gaseous envelope.

Unfortunately, most Kepler planets do not have mass measurements, and it is informative to consider how K2-136 c would have interpreted in the absence of a mass measurement. In that case I would have turned to a mass-radius relation such as that by Otegi et al. [2020], which would point to a mass between 5 and 20 $\mathrm{M_E}$. As an experiment, I explored the photoevaporation history of K2-136 c as a function of its core mass, as I did for K2-136 d in Section 3.5.2. The results of such an analysis using the Kubyshkina et al. [2018] model are plotted in Figure 3.12, which shows that the low end of the mass range implies unrealistically rapid evaporation at early times (see Section 3.6.2). Photoevaporation models are therefore capable of placing a lower limit on the mass of a planet that is tighter than can be determined from a mass-radius relation alone. Similarly, my photoevaporation model would also rule out a scenario in which the planet was already a stripped core, since the implied higher core mass is shown to be stable to atmospheric escape.

K2-136 d

As seen in Figure 3.11, K2-136 d currently lies just below the valley, and its uncertain mass leads to a variety of possible internal structures, ranging from a 1.3 $\mathrm{M_E}$ planet with a tenuous atmosphere (motivated by the mass upper limits; Section 3.2) to a completely rocky world with a mass of 3.6 $\mathrm{M_E}$ (which is in tension with the HARPS-N upper limit).

According to my favoured evolution scenario, where I scale the XUV track to match the X-ray observations (Sects. 3.5.3 & 3.6.1), photoevaporation suggests the planet mass must be at least 2.0–2.5 $\mathrm{M_E}$ in order to maintain a gaseous envelope to the present day (Figure 3.9). Backwards evolution of these models suggest an initial state between a super-Earth with envelope mass fraction $\sim 0.2\%$ in the middle of radius valley, to a sub-Neptune with a sizeable envelope of 1% mass fraction, more akin to K2-136 c.

For the lower-mass models, evolution backwards in time requires rapidly growing envelopes, with the mass of the envelope quickly becoming greater than the core mass (e.g. Figure 3.9). I have deemed these scenarios to be unphysical because in forward evolution they require unrealistic fine-tuning to their starting parameters to match the planet at the present time — with a precise starting envelope only marginally lighter than the self-gravitating envelopes on gas giants, which are stable against evaporation [Murray-Clay et al., 2009b].

Alternative composition

All of the models in Sects. 3.4 & 3.5 assume a planet with a rocky core, with Earth-like composition, and a gaseous envelope dominated by hydrogen and helium. However, the low density of K2-136 d implied by the 1-σ mass upper limit of $1.3\,\mathrm{M_E}$ (Section 3.2) could also be explained by a composition that included a significant proportion of water [e.g. Zeng et al., 2019; Venturini et al., 2020]. Indeed, the mass-radius relations by Owen and Wu [2013], which allow for varying water, iron, and silicate mass fractions within the core, show that a composition of 50% ice and 50% rock would reproduce a mass of $1.3\,\mathrm{M_E}$ without any gaseous envelope. This scenario would also be compatible with a primordial gaseous envelope that has already been completely removed. Of course, a significant water content is also possible for K2-136 c.

The presence of considerable water compositions in close-in exoplanets, though, is contested. Rogers and Owen [2021] produced an ensemble of synthetic planets using distributions of core masses, core compositions, and envelope mass fractions fitted to the observed CKS sample of planets, and evolved them under photoevaporation. They found that the Kepler planets are most consistent as rock-iron cores that are either bare or surrounded by gaseous envelopes. Their results also indicate little evidence of the widespread presence of water-rich worlds, as these planets would produce a radius-valley at greater radii than observed under photoevaporation, or no valley at all in the absence of mass loss.

Multi-planet systems

The presence of the Earth-sized K2-136 b and the sub-Neptune K2-136 c alone would be consistent with the picture that the architectures of multi-planet systems tend towards size ordering, with inner planets below the valley that are stripped, and less-irradiated outer planets above the valley that maintain a gaseous envelope [Ciardi et al., 2013; Millholland et al., 2017; Weiss et al., 2022]. The additional presence of the super-Earth K2-136 d below the valley as the outermost planet is intriguing.

Based on my modelling, I have plotted the likely past, present and future architectures of the K2-136 planetary system in Figure 3.11. Overall, I found that all three planets are consistent with starting out as sub-Neptunes above the radius valley with envelope mass fractions of $\sim$1%. I found that planet d is now below the radius valley because it lost most of its envelope due to a low core mass. This makes it more susceptible to photoevaporation than planet c, despite experiencing weaker XUV irradiation.

Data from the NASA Exoplanet Archive [5] reveals that about 30 multi-planet systems ($\sim$ 3% of those discovered to date) host a planet above the valley ($R_\mathrm{p} \geq 2.0\,\mathrm{R_E}$) interior to a another planet below the valley ($R_\mathrm{p} \leq 1.6\,\mathrm{R_E}$), 13 of which are three-planet systems, akin to K2-136. This suggests that the architecture of the K2-136 system is relatively rare, but by no means unique. In such systems we need to understand how the outer planet formed with a lower mass core, when both planet radii and masses tend to increase with separation within the protoplanetary disc [Millholland et al., 2017; Weiss et al., 2018].

My results also illustrate how photoevaporation is able to produce a diverse set of architectures, since it is sensitive both core masses and XUV irradiation history. My results are also sensitive to the choice of atmospheric escape model, suggesting that observations of multi-planet systems can distinguish between these models. I found that the choice of envelope structure model is less important as the models are largely consistent with one another in both the higher mass regime, as seen with K2-136 c in Figure 3.6, and the low mass regime, with K2-136 d in Figure 3.7.

As pointed out by Owen and Campos Estrada [2020b], multi-planet systems provide the most sensitive tests of photoevaporation-driven evolution, especially when the planets straddle the radius-period valley. Studies of multi-planet systems in open clusters, such as this one, have the added advantages of known ages and a set of sibling stars to assess the average XUV activity of the host star. Future studies of additional systems at a range of ages, including very young planets [e.g. Poppenhaeger et al., 2021], and planets with measured masses, have the potential to distinguish between evaporation models and directly determine the efficiency of the mass loss.

---

[5] The NASA Exoplanet Archive can be accessed on `https://exoplanetarchive.ipac.caltech.edu/`

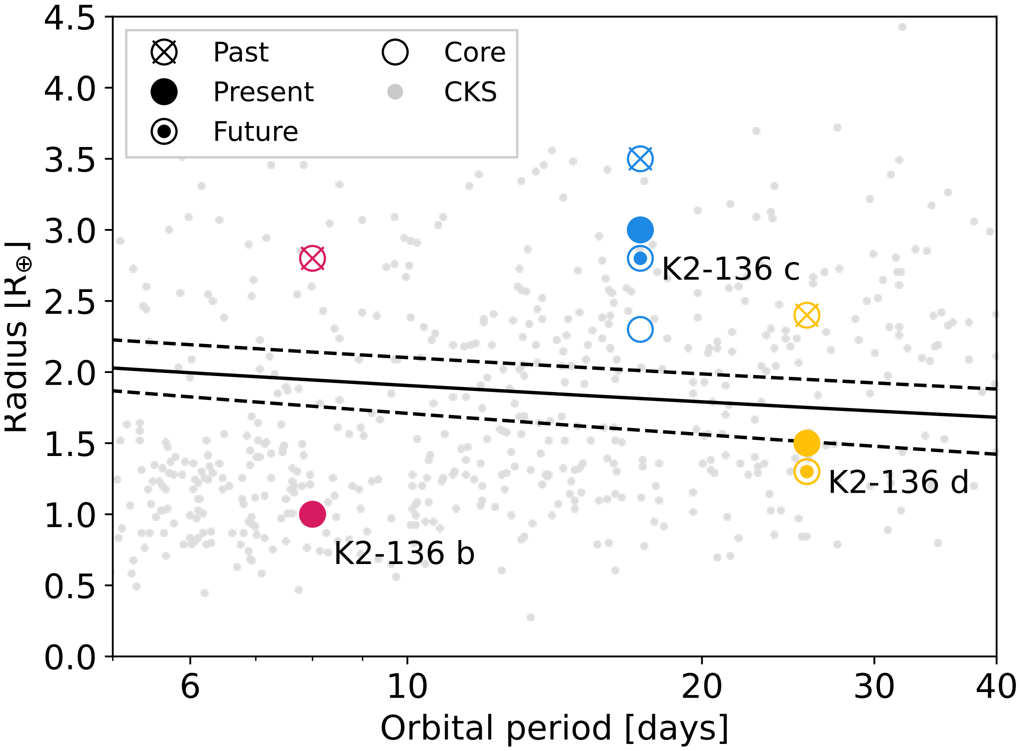

Figure 3.11: Plot of orbital period against planetary radius. The radii of the K2-136 planets at different points throughout their history are plotted as circles in red (K2-136 b), blue (K2-136 c), and yellow (K2-136 d). The circles with a cross, a solid colour, and a dot represent the past, present, and future states, respectively. The circles with no filling represent the planets' core alone. The initial size of K2-136 d was calculated using a core mass of $2.5\,\mathrm{M_E}$, following my results in Section 3.5.3. The past radius of K2-136 b was estimated from an envelope mass fraction of 1.5%, mirroring K2-136 c and d. The California-*Kepler* Survey (CKS) planets [Fulton et al., 2017] are plotted as grey points, and the radius-period valley as defined by Van Eylen et al. [2018] is marked with a black line (with the 1σ errors as the dashed lines).

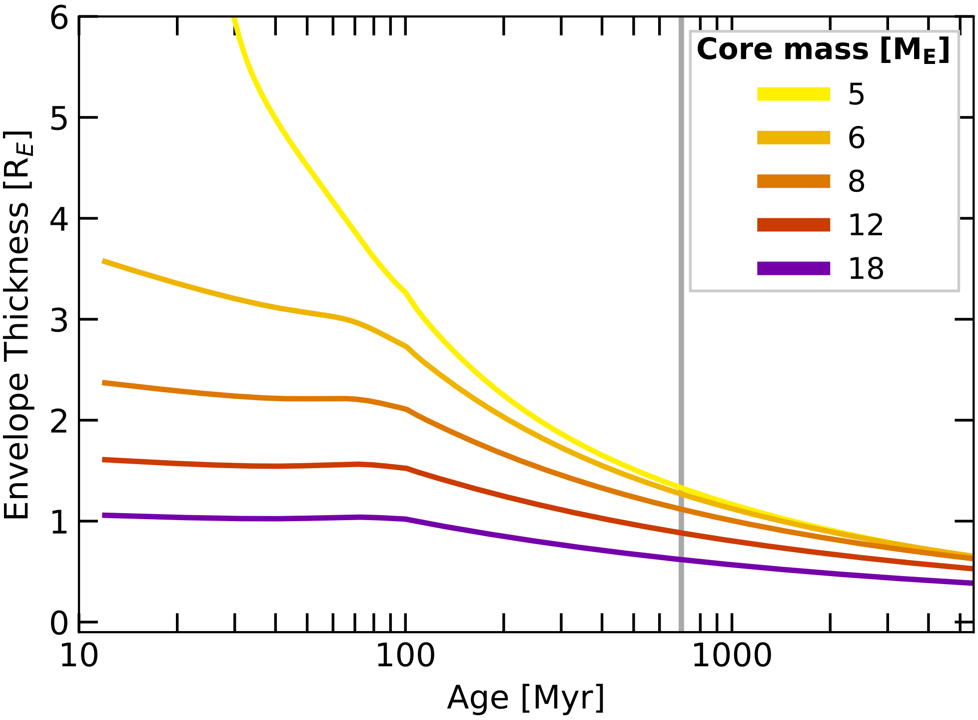

Figure 3.12: Plot of planet radius against age showing evolution of K2-136 c with a radius of 3 $\mathrm{R_E}$ and a range of planet masses between 5 and 18 $\mathrm{M_E}$, motivated by the variety of masses observed on exoplanet populations for planets of this size.

3.7 Conclusion

I have investigated the past and future evolution of the planetary system around K2-136, which is a Hyades cluster member hosting three transiting exoplanets spanning the radius-period valley. The system is intriguing because the innermost and outermost planets lie below the radius valley, whereas the middle planet lies above the valley. Its presence in the Hyades open cluster provides both a known age of 700 Myr and a set of similar stars with which to compare its XUV emission.

I employed an *XMM-Newton* observation to measure the X-ray luminosity K2-136, which I found to be typical of similar single stars in the Hyades cluster. This X-ray luminosity is a factor of 2.7 lower than predicted by the model of Johnstone et al. [2021], suggesting that existing rotation-activity relations may be biased by close binaries.

Using both the measured (Section 3.3.2) and predicted (Section 3.4.1) X-ray activity of the star, I modeled the photoevaporative evolution of all three planets forwards and backwards in time from their present age.

I employed a range of planet structure models, and a range of mass-loss prescriptions, including core-powered mass loss. Overall, I found that all three planets are consistent with having formed as sub-Neptunes above the radius-period valley, with envelope mass fractions of around 1%.

I found that the innermost planet, K2-136 b, will have lost any primordial gaseous envelope early in its evolution, regardless of choice of structure model or mass-loss prescription. In contrast, the relatively high measured mass of the middle planet, K2-136 c, results in an envelope that is stable to mass loss, again regardless of structure model or mass-loss prescription.

The outer planet, however, K2-136 d, has a history and future that is sensitive to the XUV irradiation and the choice of mass-loss prescription. Using the measured X-ray luminosity to scale the XUV irradiation history, I found that some core-powered and energy-limited photoevaporative mass loss prescriptions are both consistent with formation as a sub-Neptune with a core mass that conforms to upper limits from HARPS-N observations. The models of Kubyshkina et al. [2018] and Salz et al. [2016], however, are only consistent with core masses at the upper end of the allowed range from HARPS-N, greater than $2.5\,\mathrm{M_E}$, and favour a fully-stripped massive core at the present time (which is in tension with the HARPS-N data). A more precise mass measurement (or limit) for this planet would tightly constrain the allowed sets of photoevaporation models.

This work has shown that studies of multi-planet systems spanning the radius-period valley can provide meaningful constraints on the physical processes controlling mass loss from planetary envelopes. This is especially true where masses can be measured for the planets and where the age of the system is tightly constrained. As I have shown, membership of an open cluster is also valuable in testing whether the X-ray emission of a host star is typical for its age and mass — marginalising over variability of the X-ray emission.

Chapter 4

Survival in the Neptunian desert. LTT 9779 b survived thanks to an unusually X-ray faint star

4.1 Introduction

In Chapter 1, I presented the existence of the Neptunian desert, a feature of exoplanet populations where very few Neptune-sized planets (2-5 $\mathrm{R_E}$) exist at short orbital periods ($P < 2$ d).

This feature is linked to atmospheric escape, where Neptune-sized planets that formed in the desert, or migrated there in their youth, would be stripped of their H/He envelopes joining the more abundant population of hot rocky worlds with smaller radii. Hot Jupiters ($> 10\,\mathrm{R_E}$), on the other hand, are thought to be stable against significant atmospheric loss thanks to their deep gravitational potentials [Yelle, 2004; Murray-Clay et al., 2009b; Vissapragada et al., 2022].

In Figure 4.1, I plotted all validated exoplanets from the NASA Exoplanet Archive[1] as of July 2023. The Neptune desert is delimited by the boundaries proposed by Mazeh et al. [2016], who defined the lower and upper edges by finding the boundaries of maximum contrast of planet number density.

In the past few years, a handful of ultra-short period Neptunes have been

---

[1] The NASA Exoplanet Archive can be accessed at `https://exoplanetarchive.ipac.caltech.edu/`.

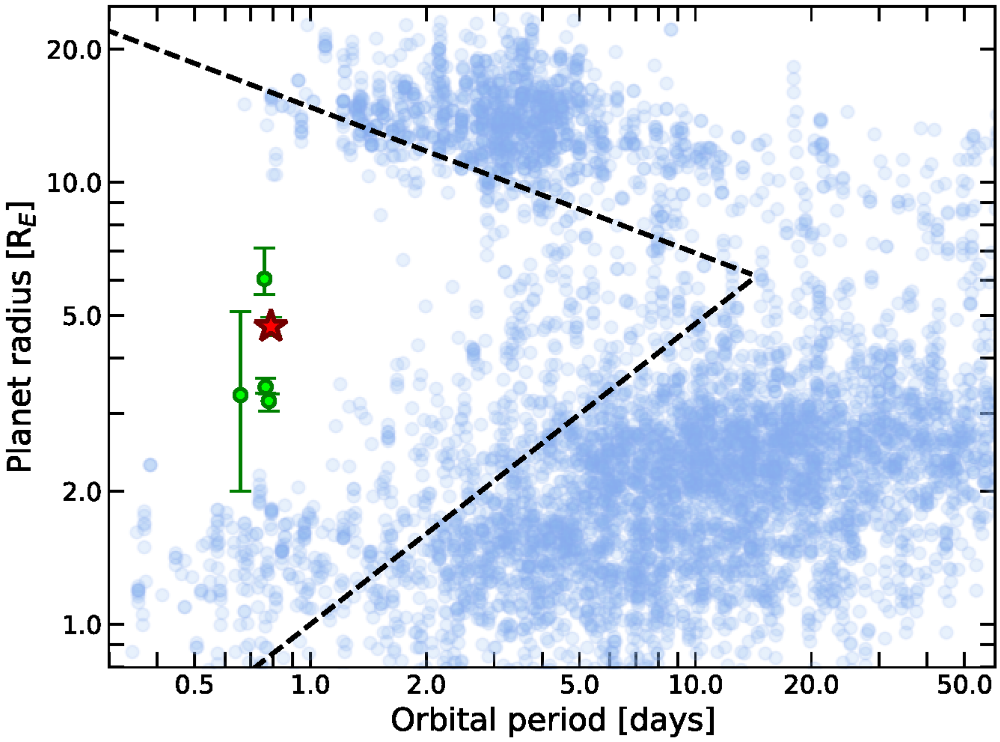

Figure 4.1: Plot of orbital period against planet radius, with LTT 9779 b marked as a red star. The upper and lower bounds of the Neptune desert are shown as black dashed lines, following Mazeh et al. [2016]. Data points represent confirmed exoplanets source from the *NASA Exoplanet Archive*, with ultra-short period Neptunes shown as green circles.

discovered, a group of planets distinct from the larger exoplanet population, plotted as green points in Figure 4.1. Some of these ultra-short period Neptune-sized planets are consistent with a rocky density and hence a high-mass core (TOI-849 b, Armstrong et al. [2020]; TOI-332 b, Osborn et al. [2023]) and whose origins are still unknown; others lack mass measurements [K2-399 b, Christiansen et al., 2022] or the necessary precision in mass measurement to constrain their densities and internal structures [K2-266 b, Rodriguez et al., 2018]. There is also a growing population of low density sub-Neptunes in the desert at periods of 1–3 days, such as NGTS-4 b [West et al., 2019] and GJ 1214 b [Cloutier et al., 2021].

Finally, LTT 9779 b (marked in red in Figure 4.1) is a hot Neptune in an extremely short orbit around a G7V star with a period of just 0.79 days [about 19 hours, Jenkins et al., 2020]. Its measured mass ($29.30^{+0.78}_{-0.81}\,\mathrm{M_E}$) and radius ($4.72 \pm 0.23\,\mathrm{R_E}$) require a very low density ($1.53 \pm 0.23\,\mathrm{g\,cm^{-3}}$) characteristic of a volatile-rich planet.

The presence of a large gaseous atmosphere on LTT 9779 b has already been determined not only by the low density of the planet, which can only be explained with a substantial H/He envelope, but also by observations of the planet with multiple facilities. Dragomir et al. [2020] observed a secondary transit of LTT 9779 b with Spitzer in the infrared at 3.6 and 4.5 microns and detected an offset between the two wavelengths, indicative of CO absorption and thus the presence of an atmosphere. These results were later supported by Edwards et al. [2023], who performed transmission spectroscopy on the planet with HST/WFC3 in the near infrared and detected a gradual increase in transit depth towards longer wavelengths, which is also indicative of an atmosphere, as opposed to a flat featureless transmission spectrum, expected from a barren planet. Moreover, observations of phase curves of LTT 9779 b with Spitzer presented by Crossfield et al. [2020] showed a large amplitude and a small phase offset, which hinted at a high-metallicity atmosphere. This was also later supported by Hoyer et al. [2023], who detected a 115 pm deep secondary transit of the planet with CHEOPS, suggesting the planet's atmosphere has a very high albedo and a metal-rich atmosphere.

The existence of a substantial H/He-rich atmosphere makes LTT 9779 b a one-of-a-kind planet and its survival deep in the Neptune desert puzzling. If the Neptune desert is the result of X-ray driven evaporation, one would expect that a highly irradiated Neptune-sized planet, such as LTT 9779 b, should have already been stripped of its envelope.

I listed the stellar parameters of LTT 9779 in Table 4.1 and note that the star has very low measured rotational broadening ($v \sin i$). Assuming the rotation axis of the star is not pointing towards the Earth, this implies a spin period of around 45 d, which is unusually long for a star of its type and age [Johnstone et al., 2021]. Since stellar activity and X-ray emission are strongly correlated with spin period [e.g Wright et al., 2011] the slow spin of LTT 9779 suggests diminished XUV emission that might have failed to remove the planet's atmosphere.

In this chapter, we test this scenario for the survival of LTT 9779 b. We observed LTT 9779 with *XMM-Newton* and placed a limit on its X-ray luminosity (Section 4.2). We then modelled the rotation and X-ray emission history of the star (Section 4.3) and the possible evaporation histories of LTT 9779 b (Sections 4.4 & 4.5). In Section 4.6, we conclude that the survival of LTT 9779 b in the Neptunian can indeed be explained by an unusually low X-ray emission history of its host star, adding weight to the suggestion that the wider Neptunian desert originates from photoevaporation.

4.2 X-ray observations & analysis

LTT 9779 was observed with the *XMM-Newton* spacecraft on May 27th and 28th 2021 for a continuous exposure of 52 ks (ObsID: 0884250101, PI: Wheatley)[2]. The star, however, was not detected in the standard pipeline outputs. We inspected the data from the the EPIC pn [Strüder et al., 2001] and MOS [Turner et al., 2001] detectors using the proper-motion corrected coordinates of the star on the pipeline-processed event list, adopting both wide and narrow standard energy bands. Nevertheless, we found no evidence of a detection of our target.

We also found that the particle background in the detectors increased significantly towards the end of the observation, and hence we decided to remove these noisy sections by dropping the time intervals with count rates higher than $0.5\,\mathrm{s}^{-1}$ for pn and $0.35\,\mathrm{s}^{-1}$ for MOS in the band 10-12 keV across the full area of the detector. The remaining data amounted to 31.7 ks for pn and 42.3 ks for each MOS. The target star, however, remained undetected after this removal of noisy data.

In the absence of a detection, we estimated an upper limit X-ray flux from LTT 9779 using the method described by Farihi et al. [2018]. This analysis is

---

[2] The *XMM-Newton* data used in this work is publicly available at the *XMM-Newton* Science Archive (`https://www.cosmos.esa.int/web/xmm-newton/xsa`), under the observation ID 0884250101 (target: LTT 9779, PI: Wheatley)

Table 4.1: Stellar parameters of LTT 9779.

Parameter	Units	Value	Reference
		Astrometric	
RA (J2000)	hh:mm:ss	23 : 54 : 40.21	Gaia DR3[c]
Dec (J2000)	dd:mm:ss	−37 : 37 : 40.52	Gaia DR3[c]
μ_{RA}	mas yr^{-1}	247.634 ± 0.013	Gaia DR3[c]
μ_{Dec}	mas yr^{-1}	-69.752 ± 0.014	Gaia DR3[c]
Parallax	mas	12.338 ± 0.017	Gaia DR3[c]
Distance	pc	81.050 ± 0.011	Gaia DR3[c]
		Physical	
Spectral type	—	G7V	J20[a]
V	mag	9.76 ± 0.03	UCAC4[b]
T_{eff}	K	5480 ± 42	J20[a]
M_*	$M_\odot$	$1.02^{+0.02}_{-0.03}$	J20[a]
R_*	$R_\odot$	0.949 ± 0.006	J20[a]
L_*	$L_\odot$	0.708 ± 0.016	J20[a]
[Fe/H]	dex	0.25 ± 0.04	J20[a]
$v \sin i$	km s^{-1}	1.06 ± 0.37	J20[a]
P_{rot}	days	< 45	J20[a]
Age	Gyr	$2.0^{+1.3}_{-0.9}$	J20[a]
$\log R'_{\mathrm{HK}}$	dex	-5.10 ± 0.04	J20[a]

[a] J20: Jenkins et al. [2020]

[b] UCAC4: Zacharias et al. [2012]

[c] Gaia DR3: Gaia Collaboration et al. [2022]

[d] 2MASS: Cutri et al. [2003]

Table 4.2: Upper limit count rates for the PN and MOS1+2 instruments.

Instrument	pn	MOS1+2
Energy range (keV)	0.15 – 2.0	0.20 – 2.0
Exposure (ks)	31.7	42.3
Source counts	91	32
Expected background counts	69.6	34.3
90% upper limit source counts	37.3	9.64
Upper limit rate (counts ks^{-1})	1.177	0.228

Table 4.3: Upper limit X-ray fluxes and luminosities predicted by the APEC model from pn and MOS count rates.

Energy range (keV)	Instrument	X-ray flux (10^{-15} erg cm^{-2} s^{-1})	Luminosity (10^{27} erg s^{-1})
0.1 – 2.4	pn	2.87	2.26
	MOS1+2	2.83	2.23
0.2 – 2.4	pn	2.07	1.63
	MOS1+2	2.04	1.60

also based on the standard data analysis threads using the XMM Science Analysis Software (SAS)[3] version 19.

We first applied an extraction area around the proper motion corrected coordinates of the source with a circular aperture of radius 16 arcseconds, as well as a secondary aperture of radius 80 arcseconds for the background in a nearby region that contained no X-ray sources. We collected the detected counts in these regions using the energy ranges 0.15 – 2.0 keV for pn and 0.2 – 2.0 keV for MOS. We discarded counts over 2 keV as coronal emission from stellar activity is relatively soft [Güdel, 2004]. We then scaled the background counts to the aperture area used for the source region. In the case of the two MOS detectors, we combined the count rates from both instruments by making use of common Good Time Intervals (GTI) and adding up the detected counts.

We then applied the method by Kraft et al. [1991] to estimate 90% confidence upper limit count rates. They model noise using a Poisson distribution and adopt a Bayesian approach with the prior that the source count rate cannot be negative. The results, shown in Table 4.2, indicate upper limit count rates of 1.18 ks^{-1} for pn and 0.23 ks^{-1} for the combined MOS1 and MOS2 detectors (hereafter MOS1+2).

In order to convert the count rates to X-ray fluxes, we built model spectra using the software `XSPEC` version 12.12.1 [Arnaud, 1996], which we then scaled to match the upper limit count rates in Table 4.2. In the case of MOS, we loaded the response and ancillary files for MOS1 only, and scaled the model to half the combined MOS1+2 count rate. We adopted solar abundances from Asplund et al. [2009] and accounted for interstellar absorption with the TBABS model by Wilms et al. [2000b]. We estimated an interstellar hydrogen column density of

---

[3] Users Guide to the XMM-Newton Science Analysis System, Issue 17.0, 2022 (ESA: XMM-Newton SOC), `https://www.cosmos.esa.int/web/xmm-newton/sas-threads`

$2.5 \times 10^{19}\,\mathrm{cm}^{-2}$ following Redfield and Linsky [2001], who determined a hydrogen density of $0.1\,\mathrm{cm}^{-3}$ for the local interstellar medium. We used a single-temperature APEC model to simulate the spectrum [Smith et al., 2001], which models the emission spectrum of collisionally-ionized diffuse gas. In order to determine a plasma temperature for our spectral model, we adopted the luminosity-temperature relation by Güdel [2004], which shows that average coronal temperatures increase with X-ray luminosity on Sun-like stars. We found that their relation is consistent with our choice of model for plasma temperatures between 0.15 and 0.3 keV. For our upper limit calculation we selected a temperature of 0.15 keV, since this results in the most conservative (higher) limit.

Finally, we scaled and integrated the spectral model, and estimated X-ray fluxes and luminosities for both the pn and MOS1+2 instruments, as shown on Table 4.3. The pn and MOS limits are very similar, corresponding to upper limit X-ray luminosities of $2.2 \times 10^{27}\,\mathrm{erg\ s}^{-1}$ in the 0.1–2.4 keV energy range, and $1.6 \times 10^{27}\,\mathrm{erg\ s}^{-1}$ in the 0.2–2.4 keV band.

The measured rotational velocity $v \sin i$ of LTT 9779 implies a spin period of 45 d, assuming its spin axis is aligned with the planet's orbit. Using rotation-activity relations [e.g. Wright et al., 2011], we estimated an X-ray luminosity of $3.9 \times 10^{27}\,\mathrm{erg\ s}^{-1}$ in the band 0.1–2.4 keV, which is within a factor of two of our upper limit – consistent with the 1σ uncertainty on the measured $v \sin i$.

We also verified that the exact value for the hydrogen column density did not have a strong effect on the spectral model for values of $N_H \leq 10^{21}\,\mathrm{cm}^{-2}$. A change of a factor of two in this quantity resulted in only a difference of a few percent in the output fluxes.

4.3 Stellar rotation and XUV history

In order to model the XUV emission history of LTT 9779, we adopted the rotation evolution models by Johnstone et al. [2021]. Those authors model the spin evolution of stars of different masses by combining angular momentum transfer mechanisms within the star (core-envelope coupling) as well as interactions with its environment (stellar wind and disc-locking), and constrain the distribution of stellar rotation rates to observations of clusters of ages 12 Myr to 2.5 Gyr. Their models predict that the average rotation period for Solar-mass star of 2 Gyr age, such as LTT 9779, is 14 days, with a 2σ spread from 12 to 16 days. The spin and X-ray luminosity evolution of a $1\,\mathrm{M}_\odot$ star according to this model are shown in

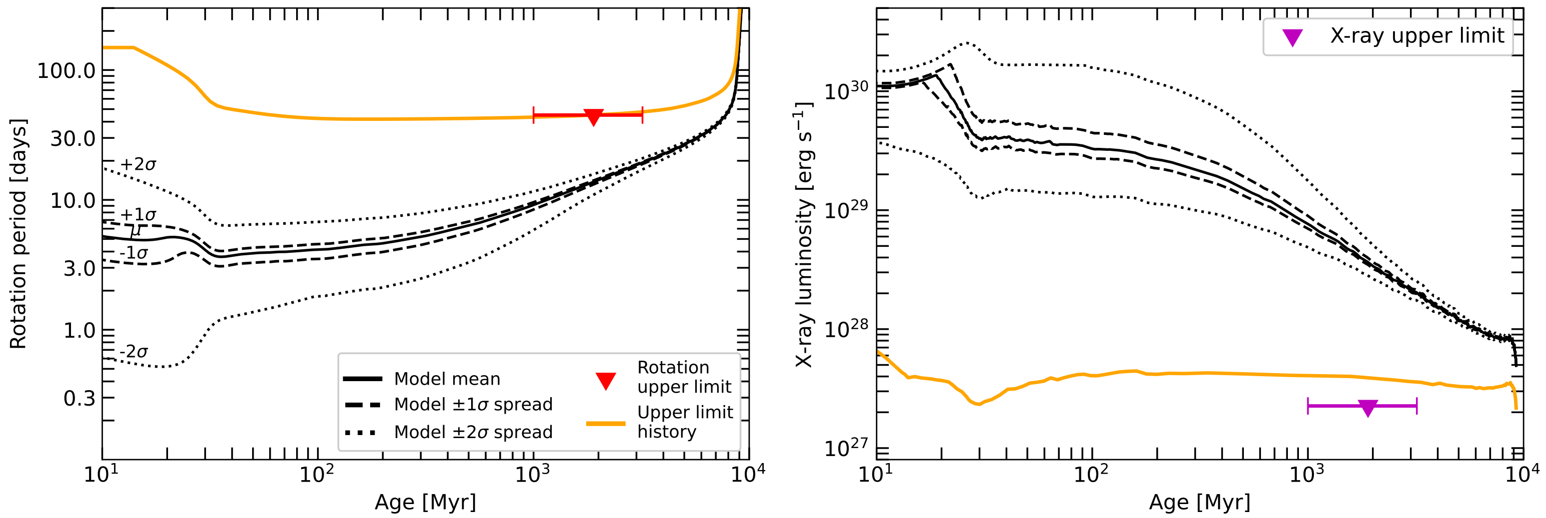

Figure 4.2: **Left panel**: spin histories for a 1 $\mathrm{M}_\odot$ star predicted by Johnstone et al. [2021], including the population mean, 1σ, and 2σ spreads, as well as the spin history fitted to the 45-day upper limit spin of LTT 9779. **Right panel**: X-ray emission histories in the 0.1–2.4 keV band corresponding to the spin histories on the left panel. Our X-ray upper limit measured from *XMM-Newton* observations is shown as a magenta triangle.

black in Figure 4.2, with the the X-ray emission determined from the spin evolution using rotation-activity relations [Pizzolato et al., 2003; Wright et al., 2011, 2018].

Even though the rotation period of LTT 9779 is unknown, Jenkins et al. [2020] were able to place an upper limit on the period of 45 days based on a HARPS $v \sin i$ of $1.06 \pm 0.37\,\mathrm{km\ s^{-1}}$. This 45 d period will correspond to the true rotation period of the star if its spin axis is aligned with the orbit of the planet (i.e. $i = 90°$). The implied period remains well above 14 d for stellar inclinations greater than 20 deg, and the probability of an inclination of 20 deg or less is only 6%, even if the stellar inclination is randomly misaligned with the planet's orbit. Furthermore, Jenkins et al. [2020] also measured the strength of the Ca II HK lines and found a $\log R'_{HK}$ value of -5.10 ± 0.04 dex, which is indicative of a very low activity and also supports the star having an unusually slow rotation period.

In order to model a plausible low XUV emission history, we choose to adopt the 45-day limit as the current rotation period of the star and use the models by Johnstone et al. [2021] to extrapolate to earlier and later times. The spin and X-ray luminosity evolution in this scenario are shown in orange in Figure 4.2.

Our results for a typical star in Figure 4.2 show a predicted X-ray luminosity of $3.4 \times 10^{28}\ \mathrm{erg\ s^{-1}}$ for LTT 9779 at the present time, which is a factor of 15 brighter than our *XMM-Newton* upper limit from Section 4.2. In contrast, our X-ray upper limit is within a factor of 2 of the predicted X-ray luminosity for the 45 d spin period corresponding to the measured $v \sin i$ and an aligned system. Our *XMM-Newton* upper limit is clearly more consistent with the anomalously slow rotation scenario.

4.4 Evolution modelling

We used the X-ray luminosity evolution for the different scenarios shown in Figure 4.2 to model the evaporation history of the LTT 9779 b in order to determine the conditions under which the planetary atmosphere will be stripped.

We used the `photoevolver` [4] code [Fernández Fernández et al., 2023a], which combines three ingredients: (1) a description of the stellar X-ray history, using the model by Johnstone et al. [2021] described in Section 4.3, (2) the envelope structure model by Chen and Rogers [2016, Eqn. 5] based on MESA hydrodynamic simulations, which links the atmospheric mass to its size, and (3) the mass loss

---

[4] The code is available on GitHub at `https://github.com/jorgefz/photoevolver`

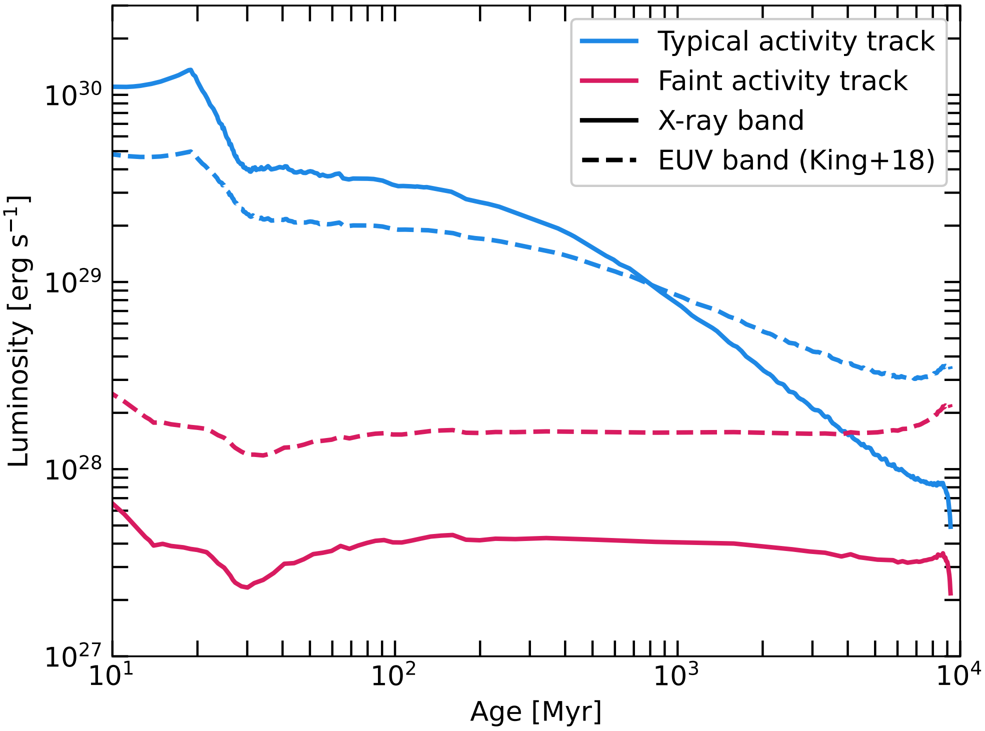

Figure 4.3: Emission histories for the X-ray band (solid lines) and EUV band (dashed lines) for the two stellar models discussed in Section 4.3: the predicted history for a solar mass star (blue) and the fainter history motivated by spin and X-ray measurements (red). The EUV band was estimated from the X-rays using the scaling law by King et al. [2018].

Table 4.4: Planetary parameters and internal structure of LTT 9779 b.

Parameter		Value	Source
Orbital period	P_{orb} (days)	$0.792 \pm (9.3 \times 10^{-6})$	J20[a]
Semi-major axis	a (au)	0.01679 ± 0.00014	J20[a]
Equilibrium temperature	T_{eq} (K)	1978 ± 19	J20[a]
Mass	M_{p} (M_{E})	$29.30^{+0.78}_{-0.81}$	J20[a]
Radius	R_{p} (R_{E})	4.72 ± 0.23	J20[a]
Core radius	R_{core} (R_{E})	2.69 ± 0.11	This work
Core mass	M_{core} (M_{E})	27.30 ± 1.10	This work
Envelope radius	R_{env} (R_{E})	2.03 ± 0.26	This work
Envelope mass fraction	f_{env}	0.067 ± 0.029	This work

[a] J20: Jenkins et al. [2020]

model by Kubyshkina et al. [2018], which translates incident X-ray irradiation into atmospheric mass loss rate.

At each simulation time step, the XUV flux incident on the planet is drawn from the stellar tracks in Figure 4.2 and then used to remove some mass from the atmosphere, calculated using the mass loss model. The envelope size is then recalculated with the new mass, and the age advances one time step forward. We evolved the planet from the age of 10 Myr, the time at which the protoplanetary disc has fully dissipated [Fedele et al., 2010] and any boil-off processes have completed [Lammer et al., 2016; Owen and Wu, 2016], to 5 Gyr, with a fixed time step of 0.1 Myr. We considered the envelope stripped when its mass reached a value below 0.01% of the planet's mass, as it is the lower limit for which the envelope model by Chen and Rogers [2016] is rated.

We adopted two spin period histories from Figure 4.2 to find feasible evaporation pasts for LTT 9779 b: one matching the typical spin period distribution for a solar-mass star, and another matching the star's measured rotation upper limit of 45 days at its current age. We also estimated the extreme ultraviolet (EUV) stellar emission in the band 0.0136–0.1 keV using the empirical relations by King et al. [2018], which are based on Solar *TIMED/SEE* data. We plot the relative contributions of the X-ray and EUV bands in Figure 4.3.

4.4.1 Internal structure

We modelled the internal structure of LTT 9779 b assuming a silicate-iron (rocky) core surrounded by a large H/He-rich atmosphere, following Rogers and Owen

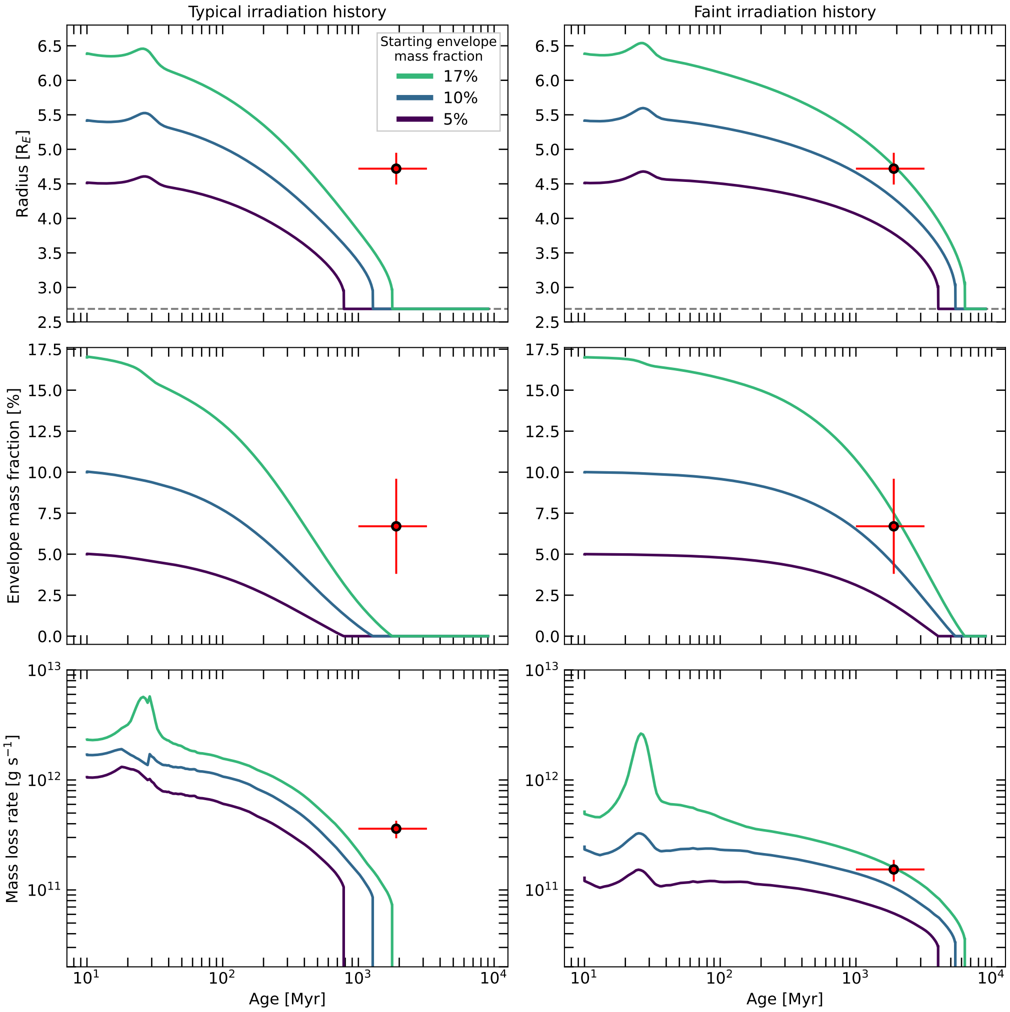

Figure 4.4: Evaporation histories of a range of simulated scenarios for LTT 9779 b, with initial envelope mass fractions from 5% to 17%. The panels present the evolution of the planet radius (top), envelope mass fraction (middle), and mass loss rate (bottom) under two XUV irradiation histories: (1) the expected stellar emission history of a solar mass star (left column), and (2) a fainter emission history consistent with the measured stellar rotation velocity and our X-ray upper limit from our *XMM-Newton* observation (right column). The dashed grey line on the top panels represents the rocky core radius of LTT 9779 b.

[2021]. This description entails a total of four model parameters: the core radius $\mathrm{R_{core}}$, core mass $\mathrm{M_{core}}$, envelope radius $\mathrm{R_{env}}$, and envelope mass fraction $\mathrm{f_{env}}$ (see Table 4.4). With knowledge of the planet's mass and radius alone (together with orbital and host star parameters), we can deduce values for these quantities by combining four equations. First we defined planet radius as $\mathrm{R_p = R_{core} + R_{env}}$, and envelope mass fraction as the ratio of envelope and planet masses $\mathrm{f_{env} = M_{env}/M_p = (M_p - M_{core})/M_p}$. Additionally, we adopted the empirical mass-radius relation for rocky planets by Otegi et al. [2020, Eqn. 1] to link the core mass $\mathrm{M_{core}}$ to the core radius $\mathrm{R_{core}}$. Finally, we adopt the envelope structure model by Chen and Rogers [2016, Eqn. 5], which links the mass fraction of the envelope $\mathrm{f_{env}}$ to its thickness $\mathrm{R_{env}}$. We found that LTT 9779 b is consistent with a rocky core of radius $2.69 \pm 0.11\ \mathrm{R_E}$ and a gaseous envelope of mass fraction $6.7 \pm 2.9\%$ (see Table 4.4), in good agreement with the mass fraction of 9% estimated by Jenkins et al. [2020].

Moreover, we estimated that the predicted XUV emission for LTT 9779 induces a present-day mass loss rate of $3.5 \times 10^{11}\ \mathrm{g\ s^{-1}}$ using the model by Kubyshkina et al. [2018]. Energy-limited photoevaporation, a simpler model that accounts only for the energy from incident X-ray photons [Watson et al., 1981; Lecavelier Des Etangs, 2007], predicts a lower present-day mass loss rate of $2.8 \times 10^{11}\ \mathrm{g\ s^{-1}}$ using an evaporation efficiency of 15%, a value commonly adopted in literature [Lammer et al., 2009; Jackson et al., 2012; Shematovich et al., 2014; King et al., 2019]. On the other hand, the fainter XUV emission motivated by our *XMM-Newton* observations yields a present-day mass loss rate of $1.5 \times 10^{11}\ \mathrm{g\ s^{-1}}$ using the model by Kubyshkina et al. [2018], and $0.6 \times 10^{11}\ \mathrm{g\ s^{-1}}$ with the energy-limited formulation.

4.5 Evaporation history

We simulated a range of evolutionary scenarios for LTT 9779 b, all using the rocky core determined in Table 4.4, but each starting off at an age of 10 Myr with a different envelope mass fraction. We used envelope mass fractions of 5%, 10%, and 17%, with the lowest of these values being motivated by the uncertainty on the planet's current envelope mass fraction.

The maximum initial envelope is motivated by the maximum radius the planet could have following its formation. This is set by the radius of its Roche lobe which we calculate using the expression by Owen and Lai [2018, Eqn. 3] for low density gaseous planets. This gives a maximum envelope mass fraction of 17% for LTT 9779 b at the beginning of our simulation. Finally, the choice of initial envelope mass fraction of 10% serves as a mid-point between the two values above.

4.5.1 Expected XUV history

Firstly, we adopt the XUV luminosity tracks that are expected for a typical solar-mass star following the model by Johnstone et al. [2021], as shown in Figure 4.2 (right hand panel), and evolve LTT 9779 b under photoevaporation for the three initial envelope mass fractions. The results, shown in Figure 4.4 (left column) show that none of these scenarios match the mass and radius of LTT 9779 b at the present time, as they are all stripped of their envelopes before now. This confirms that a planet of this nature orbiting LTT 9779 with the expected X-ray emission history would already be a hot rocky world of radius 2.7 R_E, joining the population of planets that define the lower edge of the Neptune desert. We thus rule out this scenario as a description of the evaporation history of LTT 9779 b.

4.5.2 Faint XUV history

We repeat the analysis in Section 4.5.1 but adopting a stellar XUV history that respects both the measured stellar rotation velocity and our X-ray upper limit, as determined with our *XMM-Newton* observation (Section 4.2). This emission history, shown in Figure 4.2 (right hand panel), matches a star that has a rotation period of 45 days at the age of 2 Gyr.

We find that the planetary atmosphere survives evaporation to the present day for all three initial envelope fractions, as shown in Figure 4.4 (right column). Furthermore, we find that, under these conditions, LTT 9779 b is consistent with an evaporation history where it started out with an envelope mass fraction of 10% to 17%. This would make the planet a 6–7 R_E puffy super-Neptune after disc dispersal.

We find that continued exposure to these low XUV fluxes does end up stripping the planet of its envelope by the age of 6–7 Gyr (Figure 4.4). As can be seen in Figure 4.2, this is because the low activity track is flat in comparison to the high activity track, and so the X-ray emission in both histories become comparable at later ages. This behaviour can be attributed to faster rotators spinning down more rapidly than slow rotators, leading to the tracks converging [Johnstone et al., 2021].

In principle, our conclusion that the low activity track is consistent with the planet retaining its envelope to the present day is sensitive to our choice of

EUV scaling law. This is illustrated in Figure 4.3, where it is clear that the EUV emission is expected to be higher than X-rays throughout the lifetime of the star. Maggio et al. [2023] compared different X-ray/EUV scaling laws and confirmed the that the King et al. [2018] relation used here is in good agreement with available EUV observations. Some other EUV scaling laws, however, such as that from Sanz-Forcada et al. [2011] predict somewhat higher EUV emission up to a factor 2 [revised down to 1.5 by Sanz-Forcada et al., 2022]. In order to test whether the choice of scaling relation affects our conclusions, we re-ran our model with both the Sanz-Forcada et al. [2011] and Sanz-Forcada et al. [2022] relations. We found that the gaseous envelope of the planet is still expected survive to the present day for both scaling relations, demonstrating that our results in practice are not sensitive to this choice.

4.6 Discussion & Conclusions

We have presented an analysis of X-ray driven photoevaporation of the ultra-short period Neptune LTT 9779 b: the only known planet deep in the Neptune desert with a significant gaseous envelope. Since the Neptune desert is thought to be cleared out by X-ray photoevaporation [e.g. Owen and Lai, 2018], the existence of this planet at such a short period is puzzling.

Specifically, we have considered the possibility that LTT 9779 b has survived at its present orbital separation due to anomalously low X-ray emission from its host star, as suggested by its unusually low rotational velocity (Table 4.1) and lack of Ca II HK emission lines [Jenkins et al., 2020].

We made an *XMM-Newton* observation of the host star and measured an upper-limit to the X-ray luminosity that is a factor of fifteen lower than the expected X-ray luminosity for a star of this type and age (Sections 4.2 & 4.3). In contrast, our X-ray upper limit is within a factor of 2 of the luminosity expected for a star rotating with the much slower 45 d period suggested by the rotational velocity and an assumed alignment between the stellar spin and planetary orbital axes.

We also simulated the possible evaporation history of the planet using a range of initial envelope mass fractions. As expected, we confirm that the planetary atmosphere would not survive to the present day under the expected X-ray emission history of a solar mass star like LTT 9779 (Section 4.5.1). However, we find that a dimmer X-ray past, motivated by the upper limits on the X-ray luminosity and spin period, allows the planetary atmosphere to survive to the present day (Section 4.5.2).

We conclude that LTT 9779 most-likely formed as an anomalously slowly rotating star, and that its close-in Neptune-sized planet LTT 9779 b was thus able to survive in the Neptune desert to the present day due to unusually low X-ray irradiation. This scenario is consistent with the planet forming in situ and/or migrating within the protoplanetary disc, offering an alternative to the scenario suggested by Jenkins et al. [2020], in which LTT 9779 b started out as a Jupiter-sized planet that migrated inward to its current orbit later in its life, avoiding any XUV irradiation from its host star during its youth. As a result of its migration, the planet would have approached its star within its Roche-lobe, such that the planet's atmosphere would have been stripped off by the host star's gravitational forces (in a process known as Roche-lobe overflow), leaving a smaller Neptune-sized planet behind.

Moreover, the super-solar (400×) metallicity of its atmosphere together with its very high albedo, determined by Hoyer et al. [2023], would make the planet more resistant to evaporation as heavier species require more energy to remove [Wilson et al., 2022; Owen and Jackson, 2012].

Even though the implied slow 45-day spin of LTT 9779 may be unusual, examples of long-period (30-45 d) solar-mass stars have been found in the 950 Myr-old cluster NGC 6811, hinting towards a rare mechanism that yields extremely slow rotators [Godoy-Rivera et al., 2021].

This unusual feature of the host star is consistent with our interpretation because of the unique nature of LTT 9779 b within the Neptunian desert. The strong selection bias in favour of large close-in transiting exoplanets means that planets like LTT 9779 b must be extremely rare. In contrast, finding similarly anomalous stars without a hot Neptune is extremely difficult. This is because their low stellar activity results in low amplitude photometric modulation that is difficult to detect. Their long periods are also beyond the reach of most photometric surveys, and we cannot use $v \sin i$ because of contamination by pole-on faster rotators. Nevertheless, it is known that stars are formed with a wide range of initial spin periods, at least in part due to interactions with long-lived protoplanetary discs (~10 Myr), which can prevent them from spinning-up during the pre-main sequence stage of their evolution and allowing slow rotators to maintain their initial spin into the main sequence [e.g. Moraux et al., 2013; Ribas et al., 2015; Richert et al., 2018].

Finally, our conclusion that the only known planet deep in the Neptunian desert with a gasesous envelope is also unusual in having an X-ray faint star, strongly supports the suggestion that the primary origin of the Neptunian desert is X-ray driven photoeveporation.

Chapter 5

Reassessing the X-ray irradiation of young exoplanets around FGK stars

5.1 Introduction

As I demonstrated in Chapter 3 with the planetary system around K2-136 & Chapter 4 with the hot Neptune LTT 9779 b, testing and calibrating models of stellar XUV emission is essential in predicting the outcome of exoplanet atmosphere evolution under photoevaporation and thus the origins of the radius valley and the Neptunian desert. This is particularly true for young stars, which are the most X-ray active. A key example is LTT 9779 b, the only ultra-hot Neptune deep in the Neptunian desert that retains a gaseous atmosphere [Jenkins et al., 2020]. In Chapter 4 I presented *XMM-Newton* observations of the host star, a 2 Gyr old G dwarf, and found that its X-ray activity was at least 15 times fainter than model predictions. My models showed that this anomalously low X-ray emission has allowed the planet's envelope to survive to the present day.

In order to characterise how the X-ray emission of planet-hosting stars evolves over time, it is necessary to determine their ages, spin periods, and X-ray luminosities accurately. This can be done by studying open clusters where all stars share a common age and origin, providing a snapshot of their evolution. To do so, one must build accurate membership lists to filter out non-members, and this field has advanced rapidly with the advent of the *Gaia* mission, which has measured kinematics and parallaxes for more than a billion stars. The precision of such measurements has allowed discerning between the kinematics of cluster members and field stars, allowing membership of list for many star clusters to be refined [e.g. Freund et al., 2020; Godoy-Rivera et al., 2021; Núñez et al., 2022].

Another source of contamination in X-ray and spin period surveys of open clusters is the presence of tidally-synchronized binary stars. Close binaries can interact with one another and become tidally-locked by spinning each other up to match their orbital period [Simonian et al., 2019; Avallone et al., 2022], leading to a stronger X-ray emission [Dempsey et al., 1993, 1997]. Moreover, these binaries are close enough to one another to have disrupted their protoplanetary disks, preventing the formation of close-in planets [Kraus et al., 2016], and since their spin and X-ray activity have been altered, they are not useful in constraining the X-ray evolution of planet-hosting stars. They appear as unusually fast rotators and, if the spectral types of the two components are similar, they will be located above the locus of the main sequence by up to 0.75 mag [Simonian et al., 2019]. These tight binaries also produce strong radial velocity signals due to their orbital motion. These binaries can be identified with *Gaia*, which measured radial velocities of a subset of its targets [Katz et al., 2023].

In Chapter 3, I studied the Hyades open cluster using the *Gaia* membership list from Freund et al. [2020], and found that, when accounting for binaries, the X-ray activity of single FGK dwarfs was a factor of two fainter than model predictions. Exoplanet atmospheres tend to evolve more rapidly during the first 100 Myr of age, when their host stars are the brightest in the X-rays. The Hyades, however, has an age of 650 Myr [Martín et al., 2018], and so its stars have spun down significantly and are less X-ray active, and their close-in planets are for the most part already evolved.

In this Chapter, I aim to study the X-ray activity of younger stars in order to compare them to the X-ray evolution models by Johnstone et al. [2021]. I studied the Pleiades open cluster, which has an age of 125 Myr [Godoy-Rivera et al., 2021]. At this stage of their evolution, Pleiades stars are still rotating rapidly and are active in the X-rays, and thus close-in planets are still actively evolving under atmospheric escape.

This chapter is structured as follows: in Section 5.2 I identify tidally-synchronised binaries in the Pleiades and compare its population of single FGK stars to rotational evolution models. In Section 5.3, I obtain X-ray activities for Pleiades stars from archival *XMM-Newton* observations, and in Sections 5.4 and 5.5 I compare them to X-ray evolution models and assess the impact on simulations of the evap-

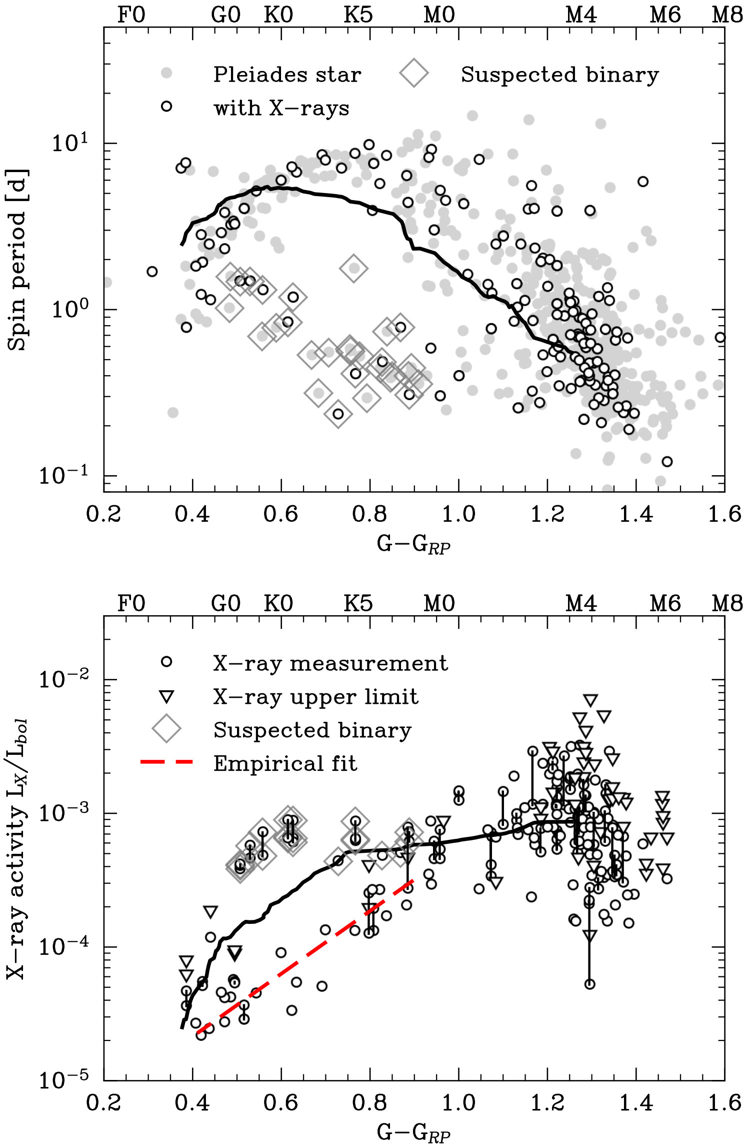

Figure 5.1: **Top panel:** spin period against *Gaia* G-G$_{\mathrm{RP}}$ colour of Pleiades stars. The rotational evolution model by J21 is shown as a black line. Stars which I identified as spun-up close binaries are highlighted with diamonds. White circles with black borders represent stars with X-ray detections from *XMM-Newton*, whereas the grey circles are stars with no X-ray detections. **Bottom panel:** X-ray activity against *Gaia* G-G$_{\mathrm{RP}}$ colour of Pleiades stars, following the top panel. X-ray detections are shown as circles and upper limits as triangles. The data points linked by black lines represent multiple X-ray detections of the same stars.

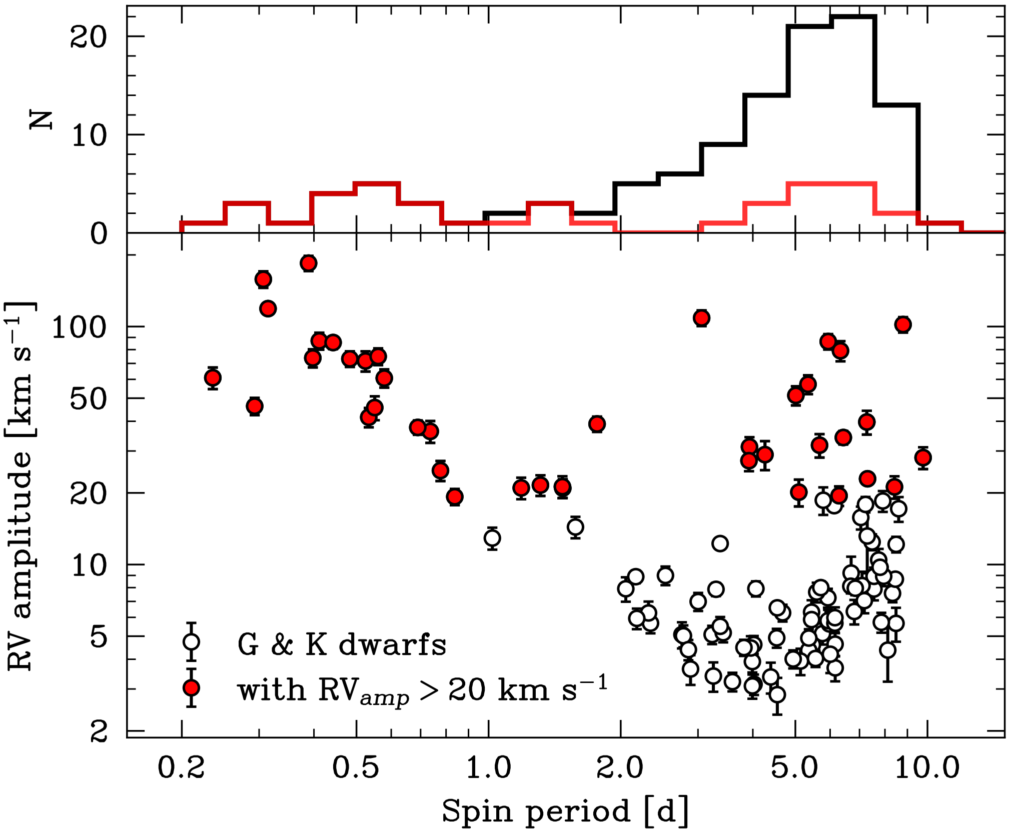

Figure 5.2: **Top panel:** Distribution of the spin periods of G & K dwarfs in the Pleiades (black) and those with high RV amplitudes (red). The distribution is bimodal, with two populations: fast rotators ($P_{\rm rot} = 0.2 - 1\,\rm d$) and slow rotators ($P_{\rm rot} = 3 - 10\,\rm d$). **Bottom panel:** Spin period against *Gaia* RV amplitude for Pleiades G & K dwarfs (white circles), with those with a high RV amplitude ($RV_{\rm amp} > 20\,\rm km\,s^{-1}$) highlighted in red. The fast rotators all have high RV amplitudes.

oration history of exoplanets.

5.2 Rotation in the Pleiades

Godoy-Rivera et al. [2021] reassessed the memberships of stars in seven open clusters, including the Pleiades, using astrometry from *Gaia* DR2. They also obtained rotation periods for 759 stars in their Pleiades sample using archival observations from both ground and space-based photometric monitoring.

In Figure 5.1 (top panel) I plotted the spin periods of the Pleiades stars in their sample and identified a tight correlation between rotation and spectral type for the FGK stars ($0.4 \geq G - BP \geq 0.9$). This tight relation, which has also been observed in other clusters [e.g. Gillen et al., 2020; Freund et al., 2020], is caused by stars bunching up as the evolve to longer periods, with more rapidly rotating stars slowing faster as they lose angular momentum to the stellar wind [Johnstone et al., 2015a]. Faster rotators spin down at a greater pace than slow rotators, leading to their spin periods converging over time in a tight rotation-mass relation [Tu et al., 2015]. This occurs because faster rotators are more magnetically active and thus experience grater mass loss from stellar wind, which carries angular momentum away from the star. This in turn results in an increased spin down rate compared to slow rotators. Moreover, it can be seen that, whilst FGK Pleiads follow this tight relation, M-dwarfs present a much larger scatter in their spin periods (see Figure 5.1, top panel). This is explained by the fact that populations higher mass stars converge in their spin periods earlier than low mass stars, as the mass loss (and thus spin down) from stellar wind is also a strong function of stellar mass [Johnstone et al., 2021], which suggests M-dwarfs in the Pleiades are yet to converge.

Figure 5.1 also shows a population of rapidly-spinning G & K stars at $P_{\mathrm{rot}} > 1.5\,\mathrm{d}$ that do not follow this tight relation, which I highlighted with diamond markers. In Figure 5.2 (top panel) I plotted the distribution of spin periods of Pleiades G & K dwarfs and found a clear bimodal distribution which separates two populations: the slow rotators, which peak at $\mathrm{P}_{\mathrm{rot}} = 7\,\mathrm{d}$, and fast rotators, which peak at $\mathrm{P}_{\mathrm{rot}} = 0.5\,\mathrm{d}$. These two populations are separated by a dearth of stars at $\mathrm{P}_{\mathrm{rot}} = 1.5\,\mathrm{d}$. This bimodality is a known feature of the rotational distribution of FGK and M stars [e.g. McQuillan et al., 2013; Davenport and Covey, 2018], and has been attributed to the presence of tidally-synchronised binaries, which produce a population of fast rotators that are tidally spun-up by their companions

[Simonian et al., 2019]. These fast rotators all have high radial velocity amplitudes was well, with $\mathrm{RV}_{\mathrm{amp}} > 20\,\mathrm{km\,s^{-1}}$, as seen in Figure 5.2 (bottom panel), which suggest the presence of close-in stellar-mass companions, distinguishing them as tidally-synchronised binaries. On the other hand, the slow rotators with large RV amplitudes could be explained by unresolved binaries with greater separations that are not tidally interacting. For that reason, I identified all G & K dwarfs with spin periods faster than 1.5 days as close binary systems.

Johnstone et al. [2021] introduced a series of models of the spin period evolution of FGKM stars. These models are built upon semi-empirical descriptions of the evolution of the angular momentum of stars, both within stellar interiors and through the emission of stellar wind. The also anchored their rotation models to the measured spin periods of open clusters spanning ages between 10 Myr and 5 Gyr.

I compared the spin periods predicted by their model with measured spin periods of FGK stars in the Pleiades. In Figure 5.1 (top panel) I plotted the median (50th percentile) rotation periods for FGKM stars aged 125 Myr predicted by the model as a black line. As seen, this rotational evolution model overestimates the spin periods of F & G stars in the Pleiades by a factor of 1.5 and underestimates the rotation of K dwarfs by the same amount on average.

5.3 X-ray observations

The Pleiades has been observed extensively by *XMM-Newton* [e.g. Briggs and Pye, 2003; Guarcello et al., 2019]. In order to determine X-ray activities for Pleiades members, I cross-matched their *Gaia* DR2 sky positions with the *XMM-Newton* archive [4XMM-DR13, Webb et al., 2020] using the software `TOPCAT`[1] [Taylor, 2005] and selected all matches within 5 arcseconds of separation. From the sample of Pleiades stars with spin periods from Godoy-Rivera et al. [2021], I obtained 156 Pleiades stars with X-ray detections, with 40 of them detected multiple times.

For those stars that were observed with *XMM-Newton* but not detected, I determined X-ray upper limits. I retrieved background and source counts for these stars using the software `PFLIX`[2] [Carrera et al., 2007] with a circular aperture of

---

[1] TOPCAT documentation is accessible via the link `http://www.starlink.ac.uk/topcat/`

[2] PFLIX documentation is accessible via the link `https://www.ledas.ac.uk/flix/pflix_description.html`

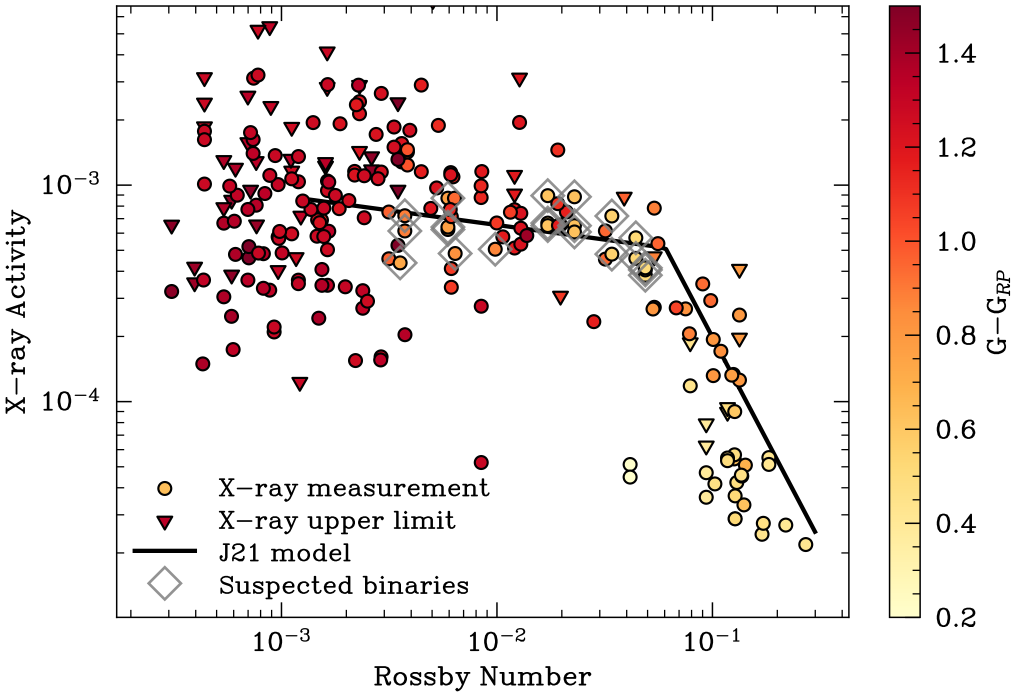

Figure 5.3: Rotation-activity relation for Pleiades stars with Rossby number plotted against X-ray activity. *XMM-Newton* detections of Pleiades stars are marked as circles, and upper limits as triangles. Stars which I identified as spun-up close binaries are highlighted with diamonds. The rotation-activity relation by J21 is shown as a black line. Marker colour indicates the *Gaia* $G - G_{\mathrm{RP}}$ colour of stars, ranging from late M dwarfs in red to F dwarfs in yellow.

radius 30 arcseconds. I then adopted the method by Kraft et al. [1991] to determine 90% confidence (2σ) upper limit count rates. I determined the X-ray fluxes for both detections and upper limits from the EPIC-pn count rates using PIMMS version 4.12d[3]. For the X-ray spectrum, I assumed an APEC model [Smith et al., 2001] of temperature 0.27 keV, which is typical for young active stars [Güdel, 2004], and a hydrogen column density assuming a density of $0.1\,\mathrm{cm}^{-3}$ [Redfield and Linsky, 2001]. I chose the energy band $0.1 - 2.4\,\mathrm{keV}$ for the output X-ray fluxes, following Johnstone et al. [2021]. Lastly, I converted the X-ray fluxes to luminosities using *Gaia* DR2 parallactic distances.

In Figure 5.1, I plotted the spin periods of Pleiades stars (top panel) and their corresponding X-ray activities (bottom panel), and in Figure 5.3, I plotted the resulting rotation-activity relation. I compared these observations with the rotational and X-ray evolution model by Johnstone et al. [2021], which I plotted as a black line. Following Johnstone et al. [2021], I determined Rossby numbers and bolometric luminosities using the stellar models by Spada et al. [2013] together with the stellar masses determined by Godoy-Rivera et al. [2021].

5.4 Discussion

5.4.1 Tidally spun-up binaries

As seen in Figure 5.1 (top panel), tidally-synchronised binaries appear as a population of fast rotators that deviate from the tight relation between spin period and spectral type for FGK dwarfs. I highlighted the X-ray activities of these fast rotators in Figure 5.1 (bottom panel) and found they create a bimodal distribution of X-ray activities, akin to the distribution of spin periods of FGK stars. I also determined these binaries are, on average, a factor of 3.7 more X-ray active than the single G & K stars. Moreover, in the rotation-activity relation (see Figure 5.3), they also lie in the saturated regime thanks to their strong X-ray activity, unlike the slowly rotating FGK dwarfs, which are predominantly found in the unsaturated regime.

---

[3] PIMMS documentation is accessible via the link `https://heasarc.gsfc.nasa.gov/docs/software/tools/pimms.html`

5.4.2 Comparison to spin & X-ray evolution models

In addition to the rotational evolution models, Johnstone et al. [2021] also fitted a rotation-activity relation to archival X-ray observations of cluster stars, which they combined with their rotation models to produce equivalent X-ray evolution models.

As discussed in Sections 5.2 & 5.4.1, when taking into account spun-up binaries, I found the rotational model by Johnstone et al. [2021] overestimates the rotation periods of single F & G dwarfs by a factor of 1.5, and underestimates the rotation of single K-dwarfs by the same amount (see Figure 5.1, top panel). Moreover, as seen in Figure 5.3, their rotation-activity relation fits K-dwarfs well but overpredicts the X-ray activities of F & G stars by a factor of 2.5. Together, these two effects result in predictions for the X-ray activity a factor of 2.5–3.5 higher than observed for FGK stars in the Pleiades open cluster (see Figure 5.1, bottom panel).

In Chapter 3, I performed a similar analysis where I compared the model by Johnstone et al. [2021] to stars in the Hyades open cluster, which are 600–800 Myr old [Brandt and Huang, 2015; Martín et al., 2018]. I arrived at a similar conclusion where I favoured an X-ray emission for K-dwarfs fainter by a factor of two compared to the model by Johnstone et al. [2021]. Our results therefore suggest that the overall X-ray emission history of FGK dwarfs younger than 1 Gyr is fainter than model predictions by a factor of 2 to 3.

These disagreements could be caused by sample contamination from a number of sources. Regarding the predicted spin periods, the differences could arise from the cluster samples they adopted to calibrate their models. Johnstone et al. [2021] anchored their rotation models to the spin period distributions of four different clusters: Pleiades [125 Myr Rebull et al., 2004; Hartman et al., 2010], M50 [130 Myr Irwin et al., 2009a], M35 [150 Myr Meibom et al., 2009], and NGC 2516 [150 Myr Irwin et al., 2007]; which they combined into a common age bin of 150 Myr. They then simulated the rotational evolution of this combined sample to determine the distributions at other age bins in order to compare them with other clusters spanning ages between 10 Myr and 5 Gyr. Since these four clusters have different ages, combining them into a single age bin could have contaminated the rotational sample they adopted to normalise their models, introducing a scatter that is greater than what is observed in each cluster individually. This would result in their rotational models predicting a greater diversity of spin periods than cluster stars actually have at a given age.

More recently, Godoy-Rivera et al. [2021] revised membership lists for a number of these clusters: Pleiades, M50, and NGC 2516 using astrometry from *Gaia* DR2. Their analysis found low contamination rates for the Pleiades and NGC 2516 (4% and 3%, respectively), but substantial non-member contamination for M50, up to 36%, compared to pre-*Gaia* literature. By removing the non-members from M50, they were able to uncover the tight relation between spin period and spectral type for FGK stars, also seen in the Pleiades (see Figure 5.1, top panel).

In this chapter, I also identified and removed tidally-synchronised binaries which were contaminating the spin period distributions of G & K dwarfs which the rotation models use. As discussed in Sections 5.1 & 5.2, these binaries induce a bimodal distribution in spin periods and cannot host close-in planetary systems, so they are not useful in constraining the X-ray irradiation histories of close-in exoplanets.

Regarding the predicted X-ray activities, Johnstone et al. [2021] built a rotation-activity relation by fitting a broken power law to the sample of stars by Wright et al. [2011], who combined archival X-ray observations of several clusters from different X-ray observatories (e.g. *XMM-Newton*, ROSAT, Einstein). These observatories are sensitive to different energy bands and the derived X-ray fluxes were determined with different assumptions for the spectral model, which can add to the scatter in the rotation-activity relation.

Finally, I performed an empirical fit to the X-ray activities of single FGK stars in the Pleiades as a function of their *Gaia* $G - RP$ colour, which is valid for $0.4 \geq G - RP \geq 0.9$:

$$\log_{10} L_{\mathrm{X}}/L_{\mathrm{bol}} = (2.35 \pm 0.25)(G - RP) - (5.61 \pm 0.16) \tag{5.1}$$

which is plotted in Figure 5.1 (bottom panel). I also performed an additional fit as a function of the stellar masses determined by Godoy-Rivera et al. [2021], valid for $1.2 \geq M_* \geq 0.6$:

$$\log_{10} L_{\mathrm{X}}/L_{\mathrm{bol}} = (-1.93 \pm 0.21)M_* - (2.40 \pm 0.20), \tag{5.2}$$

The fits were performed using the least squares approximation with the Python module `SciPy`.

5.4.3 Effects on atmospheric escape

I then studied the effects of choosing a faint X-ray history on the atmospheric evolution of exoplanets orbiting a typical K-dwarf ($\mathrm{M}_* = 0.75\,\mathrm{M}_\odot$). I simulated the evaporation history of a typical sub-Neptune in the radius valley, with a mass of $5\,\mathrm{M}_\mathrm{E}$ and an orbital period of 8 days, starting with a gaseous atmosphere consisting of 1% of its mass. I adopted two X-ray irradiation histories: (1) the one predicted by the model of Johnstone et al. [2021], and (2) the same model scaled down by a factor of three to fit X-ray observations of Pleiades FGK dwarfs. To evolve the planet, I adopted the `photoevolver`[4] code [Fernández Fernández et al., 2023b]. I assumed a two layer internal structure with a rocky core and a pure H/He atmosphere, adopting the envelope structure model by Owen and Wu [2017] and the empirical mass-radius relations by Otegi et al. [2020] for the rocky core. To calculate the escape rates, I used the evaporation model by Kubyshkina and Fossati [2021]. I evolved the planet's atmosphere from the age of 10 Myr to 1 Gyr using the 4th order Runge-Kutta algorithm as the integration method.

The results of the simulations are shown in Figure 5.4. I found the planet is fully stripped of its gaseous envelope within 1 Gyr in both cases. Under the predicted X-ray history, this occurs at the age of 200 Myr, whilst under the fainter X-ray history, the planet does not lose its envelope for another 475 Myr, until the age of 675 Myr. Our results suggest that X-ray driven photoevaporation acts in timescales of 600–700 Myr, much longer than the canonical value of 100–200 Myr. I also showed that the choice of X-ray irradiation history has a significant impact in the timescales in which photoevaporation acts to sculpt exoplanet atmospheres.

King and Wheatley [2021] already showed that the EUV component of stellar emission remains active for Gyr timescales. Our findings therefore support the picture that XUV photoevaporation acts in longer timescales spanning several Gyr, which further blurs the line between photoevaporation and core-powered mass loss, which also acts in Gyr timescales [Gupta and Schlichting, 2020].

5.5 Conclusions

The atmospheres of close-in exoplanets are sculpted by stellar high energy radiation, particularly during the first few 100 Myr of their life when their host stars are the most active at X-ray wavelengths. In this Chapter, I assessed the X-ray

---

[4] The `photoevolver` code is available on GitHub at `https://github.com/jorgefz/photoevolver`

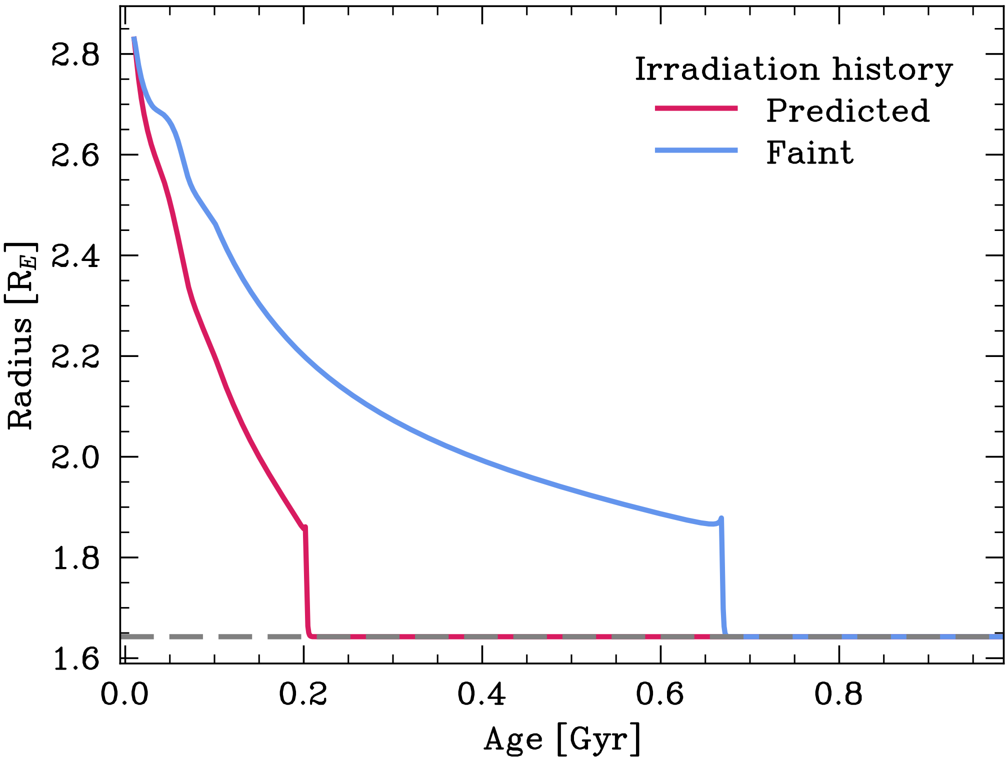

Figure 5.4: Evolution of the radius of a mini-Neptune under two X-ray irradiation histories, one predicted by models (red) and one scaled down to match observations (blue). The radius of the rocky core is shown as a dashed grey line.

activities of young FGK dwarfs in the Pleiades open cluster, which is 125 Myr of age, and compared them to predictions from the spin & X-ray evolution models by Johnstone et al. [2021].

I adopted the sample of Pleiades stars with measured spin periods by Godoy-Rivera et al. [2021], which they filtered for non-members. I then cross-matched their *Gaia* DR2 sky positions with the *XMM-Newton* archive (4XMM DR13) and obtained a sample of 156 Pleiads with both measured X-ray fluxes and spin periods. Finally, I identified and filtered out tidally-interacting binaries in the sample using radial velocities from *Gaia* DR3, which are spun-up and appear as X-ray bright sources.

I found that the X-ray activities of single Pleiades FGK dwarfs are a factor of three fainter than model predictions. I also found that a fainter X-ray history results in X-ray driven photoevaporation acting in timescales 3 to 4 times longer than expected, extending the lifetime of the simulated envelope from 200 Myr to 675 Myr, challenging the view that this occurs within the first 100-200 Myr.

This work highlights the importance of building accurate models for the X-ray emission history of stars, which in turn will inform simulations of atmospheric escape. These models can be constrained more accurately with X-ray observations of cluster stars, which requires refined cluster membership lists and filtering for binaries. This is particularly true in the *Gaia* era, where cluster sequences can be vetted against non-members using the precise astrometric monitoring offered by the *Gaia* mission. More generally, accurate X-ray emission models are essential to constrain the extent to which photoevaporation influences the evolution of close-in super-Earths and mini-Neptunes and thus uncover the origin of the period-radius valley and the Neptunian desert.

Chapter 6

The evaporation histories of four young sub-Neptunes

6.1 Introduction

Whilst an X-ray observation of a star provides its emission at the present time, its past emission history remains uncertain. On single-planet systems, one can only use present-day observations to constrain models for the emission history. Owen and Campos Estrada [2020b] argued that on multi-planetary systems, however, all planets around the same star must have shared the same irradiation history, and so their evaporation pasts can be constrained against one another. This is particularly true for systems with planets that straddle the valley, with one rocky world and volatile-rich planet, where the integrated past X-ray output of the host star must have been high enough to strip the rocky world but low enough to maintain the atmosphere of the gaseous planet.

In Chapter 3, I studied the evaporation histories of three planets around the K-dwarf K2-136, which is part of the Hyades open cluster. The Hyades, however, is around 700 Myr old, and thus its stars may no longer be X-ray active as their spin periods have slowed. Indeed, in Chapter 3 I found that K2-136 has already been spinning down for several hundred Myr and its X-ray activity has consequently diminished by an order of magnitude from its prime. My simulations of atmospheric escape also showed that its planets have already undergone the bulk of their evolution.

On the other hand, younger stars (with only a few hundred Myr of age) are still active in the X-rays and any small close-in planets in orbit are likely still undergoing atmospheric escape. Moreover, these young stars still maintain the diversity of spin periods they started out with, and thus their individual past X-ray history has not yet been erased. Older stars, in contrast, have spun down and converged into a single mass-dependent rotation period, and as a result we are unable to distinguish between those that were active and inactive during their youth [Johnstone et al., 2021].

If the star is too young (only a few tens of Myr), however, its planets have just begun evolving and are thus still likely to have large gaseous atmospheres whose survival is still uncertain. As such, rather than showing us the final outcomes of planet evolution or its initial conditions, "adolescent" stars aged $100-300$ Myr are caught red-handed removing the gaseous envelopes from their planets. Planets around such young stars are thus the ideal laboratory for studies of evaporation.

In this chapter, I present *XMM-Newton* observations of two young stars, TOI-451 and TOI-1098, aged just 120 Myr and 250 Myr, respectively, both of which also host planetary systems. TOI-451 is a G7V star with three transiting planets, one super-Earth and two mini-Neptunes [Tofflemire et al., 2021]; and TOI-1098 is a F8V star with one transiting sub-Neptune [Newton et al., 2021]. The two stars also host wide-orbit M dwarf companions whose X-ray emissions are also detected with *XMM-Newton*. Given their young ages, it is expected these planets are still actively evolving under atmospheric escape.

In this chapter, I aim to constrain the current X-ray irradiation of these four sub-Neptunes with observations from *XMM-Newton* and model their past and future evaporation histories in order to test the origin of the radius valley. In Section 6.2, I introduce the planets and determine their internal structures. In Section 6.3, I analyse my *XMM-Newton* observations and determine the X-ray activities of the stars. In Sections 6.4 & 6.5, I model the evaporation histories of the planets, and in Sections 6.7 & 6.8, I discuss and summarise the results of my simulations.

6.2 The planetary systems

The parameters of TOI-1098 and TOI-451 are shown on Table 6.1. The radii, masses, and orbital periods of their transiting planets are shown on Table 6.2, and their positions on the radius-period diagram are shown in Figure 6.1.

TOI-1098 is a late F-dwarf 105 pc away. It is a member of the young stellar association MELANGE-1, which is 250 Myr old [Tofflemire et al., 2021]. It

Table 6.1: Stellar parameters of TOI-1098 and TOI-451

Parameter	Units	TOI-1098	TOI-451
Photometry & astrometry			
RA	hh:mm:ss	$12:50:22.020$	$04:11:51.947$
Dec	hh:mm:ss	$-88:07:15.72$	$-37:56:23.219$
Parallax	mas	9.51 ± 0.01	8.10 ± 0.01
Distance	pc	105.15 ± 0.11	123.46 ± 0.15
V	mag	9.23 ± 0.03	11.02 ± 0.06
Physical properties			
Spt	–	F8V	G7V
M_*	$M_\oplus$	1.21 ± 0.06	0.95 ± 0.02
R_*	$R_\oplus$	1.19 ± 0.06	0.88 ± 0.03
L_*	$L_\oplus$	1.91 ± 0.04	0.65 ± 0.03
$T_{\rm eff}$	K	6200 ± 100	5550 ± 56
[Fe/H]	dex	0.08 ± 0.05	-0.02 ± 0.08
$P_{\rm rot}$	days	2.34 ± 0.07	5.1 ± 0.1
Age	Myr	250^{+50}_{-70}	134 ± 6.5

hosts one transiting sub-Neptune above the radius valley, TOI-1098 b, with radius $3.2\,R_E$.

TOI-451 is a young late G-type star at a distance of 123 pc. It is part of the Pisces-Eridanus stream, with an age of 120 Myr [Newton et al., 2021]. It hosts three transiting planets; the closest one, TOI-451 b (radius $1.9\,R_E$) is a super-Earth lying below the valley as well as in the Neptune desert, whilst the other two, TOI-451 c and d (radii $3.1\,R_E$ and $4.1\,R_E$, respectively), are sub-Neptunes above the radius valley. I adopted radii and periods reported by Barragán et al. [2021], who re-analysised the TESS lightcurves to obtain more accurate ephemerides. Additionally, Barragán et al. (in prep.) collected radial velocity observations of TOI-451 with ESPRESSO and measured the masses of its three transiting planets, providing 2σ detections for TOI-451 b and c, and an upper limit for TOI-451 d (see Table 6.2).

Both stars also have wide-orbit companions, TOI-1098 B and TOI-451 B, as suggested by their Gaia DR2 astrometry and kinematics. Their Gaia $G_{\rm BP} - G_{\rm RP}$ colour indices suggest an M3 spectral type for both, although TOI-451 B lies +0.65 mag above the main sequence, hinting towards multiplicity [Newton et al., 2021].

I estimated the internal structures of the four planets assuming a two-layer model consisting on a rocky core surrounded by a pure H/He envelope. This model

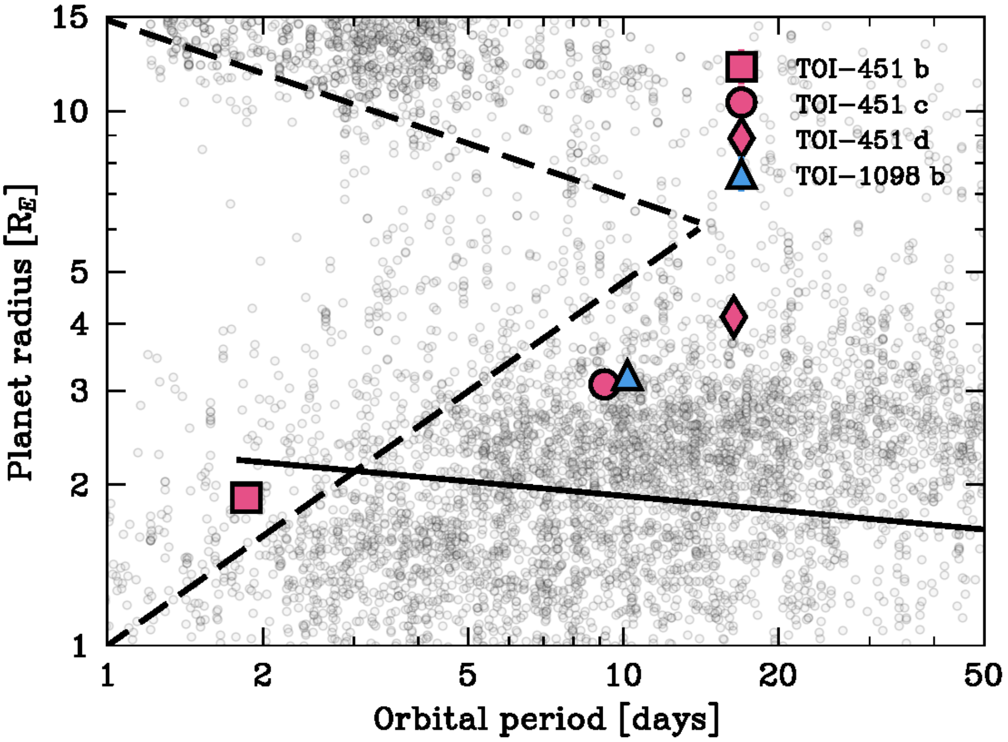

Figure 6.1: Period-radius plot with the planets around TOI-451 (red markers) and TOI-1098 (blue marker) together with the confirmed planets on the NASA Exoplanet Archive (grey circles). The errors on the planets' radii and periods are smaller than the symbols. The edges of the Neptune desert as defined by Mazeh et al. [2016] are plotted as dashed lines, and the boundary of the radius valley as defined by Van Eylen et al. [2018] is plotted as a solid line.

Table 6.2: Planetary parameters of the planets around TOI-1098 and TOI-451

Planet	Radius	Orbital period[b]	Semi-major axis	Mass	Equilibrium temperature[a]
	R_E	days	au	M_E	K
TOI-1098 b	3.2 ± 0.1	10.18	0.11 ± 0.01	—	933 ± 43
TOI-451 b	1.9 ± 0.1	1.86	0.0291 ± 0.0002	$3.8^{+3.4c}_{-2.6}$	1439 ± 82
TOI-451 c	3.08 ± 0.14	9.19	0.0844 ± 0.0006	$9.2^{+5.5c}_{-5.0}$	852 ± 45
TOI-451 d	4.12 ± 0.17	16.36	0.1240 ± 0.0009	$< 16.8^{d}$	666 ± 18

[a] Assuming a bond albedo of 0.2

[b] The errors on the orbital periods are all less than four seconds.

[c] Mass measurement from Barragán et al. (in prep.) with 1σ errors.

[d] 3σ mass upper limit from Barragán et al. (in prep.)

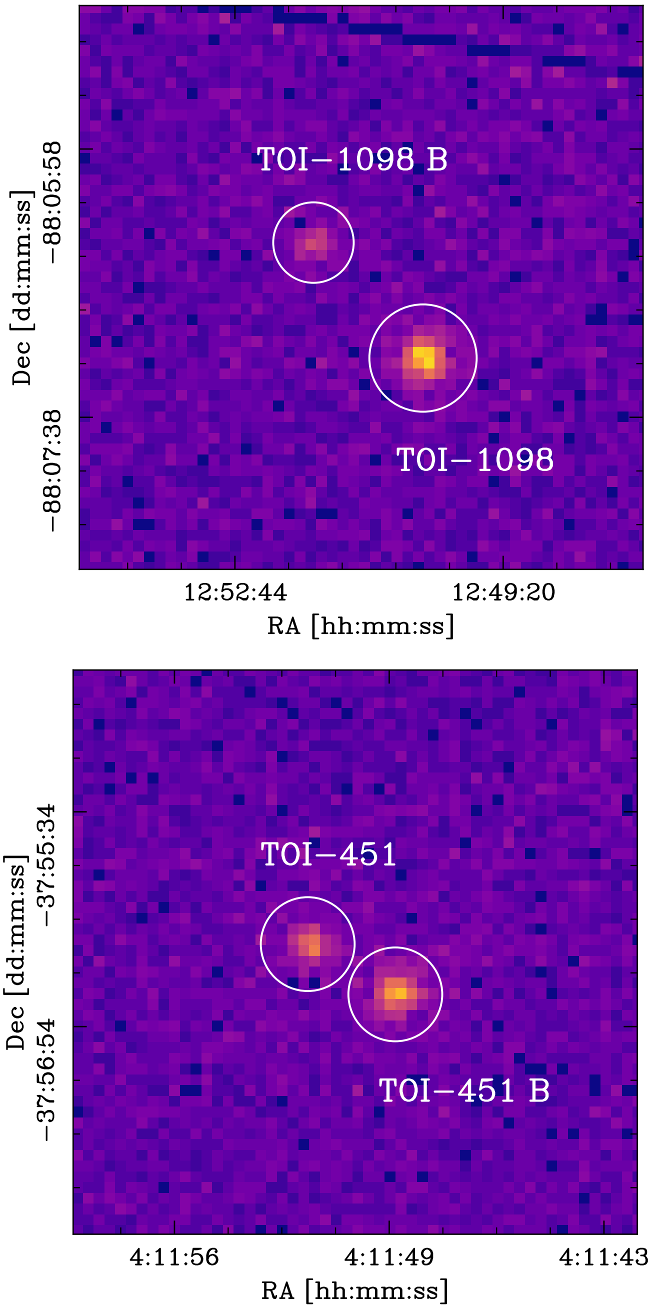

Figure 6.2: EPIC-pn images of the TOI-1098 (left) and TOI-451 (right) observations, with both stars and their companions labelled. The circles represent the apertures used to extract the X-ray counts from each star.

consist on four quantities: the core mass $\mathrm{M_{core}}$ and radius $\mathrm{R_{core}}$, the envelope thickness $\mathrm{R_{env}}$, and the envelope mass fraction $\mathrm{f_{env}}$, defined as the ratio between envelope and planet masses $\mathrm{M_{env}/M_p = (M_p - M_{core})/M_p}$.

I determined these quantities by combining the planet mass $\mathrm{M_p}$ and radius $\mathrm{R_p}$ with two models: a mass-radius relation for the rocky core, and an envelope structure formulation, which relates the thickness of an envelope (and its temperature) to its mass. For the rocky core, I adopted the empirical mass-radius relation by Otegi et al. [2020], which they determined by fitting to exoplanet populations with masses less than $25\,\mathrm{M_E}$ and densities higher than predicted for a pure water composition. For the gaseous envelope, I adopted the structure model by Chen and Rogers [2016], which consists on a polynomial fit to the results of MESA simulations, and is valid for envelope mass fractions $\mathrm{f_{env}} \leq 20\,\%$.

TOI-451 b is a super-Earth of $1.9\,\mathrm{R_E}$ that orbits very close to its star with a period of 1.9 days. Its measured mass of $3.8^{+3.4}_{-2.6}\,\mathrm{M_E}$, however, implies a low density of $3.1 \pm 2.5\,\mathrm{g\,cm^{-3}}$, which is puzzling, since its short period and small size places it inside the Neptunian desert (see Figure 6.1), where any gaseous envelope would be most susceptible to evaporation [Owen and Lai, 2018]. In fact, the interior structure models suggest the planet is only consistent with a pure rocky composition and no gaseous atmosphere, predicting a mass of $8.3 \pm 1.3\,\mathrm{M_E}$ and so a density of $6.7 \pm 1.5\,\mathrm{g\,cm^{-3}}$. Due to the short distance to its star, the planet receives a high bolometric flux, which would make any gaseous envelope puff up beyond the measured radius of the planet.

TOI-451 c is a mini-Neptune above the radius valley. Its radius of $3.1\,\mathrm{R_E}$ and mass of $9.2^{+5.0}_{-5.5}\,\mathrm{M_E}$ result in a very low density of $1.7 \pm 1.0\,\mathrm{g\,cm^{-3}}$, strongly suggesting the presence of volatiles. I determined an internal structure consisting on a sizeable gaseous atmosphere of mass fraction $2.7 \pm 0.8\,\%$ and thickness $1.1 \pm 0.4\,\mathrm{R_E}$.

TOI-451 d is a Neptune-sized planet well above the radius valley, with a radius of $4.1\,\mathrm{R_E}$. Its 3σ mass upper limit of $16.8\,\mathrm{M_E}$ suggests a very low density no greater than $1.3 \pm 0.2\,\mathrm{g\,cm^{-3}}$, which requires the presence of a hydrogen-rich envelope. Adopting this upper limit as the mass of the planet, I found the planet is consistent with an envelope of mass fraction $7.9 \pm 1.2\,\%$ and thickness $1.8 \pm 0.2\,\mathrm{R_E}$.

Finally, TOI-1098 b is a sub-Neptune above the valley with radius $3.1\,\mathrm{R_E}$. Its mass has not yet been measured at the time of writing, and so I explored a range of possible internal structures constrained by its past evaporation history.

In my simulations, I explored the past and future evaporation histories of the four planets. I adopted a range of masses for each planet motivated by

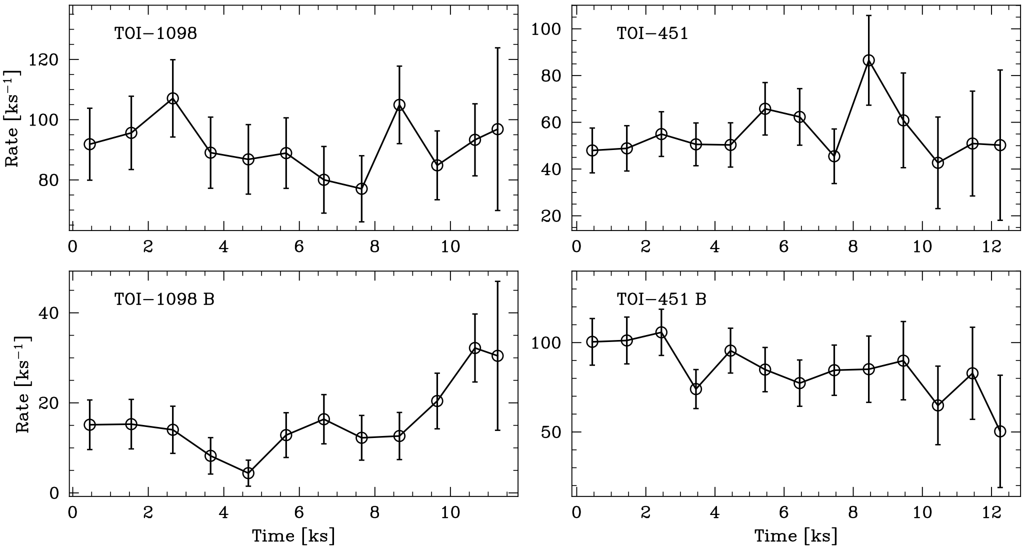

Figure 6.3: EPIC-pn lightcurves of the four stars.

the uncertainties in their measured masses (TOI-451 b and c) and mass upper limits (TOI-451 d), as well as the measured mass distributions of mini-Neptune populations [Otegi et al., 2020]. I chose a range of 5 to 15 $\mathrm{M_E}$, which covers the spread observed in sub-Neptunes with radii 2–4 $\mathrm{R_E}$ [Otegi et al., 2020] as well as the mass measurements of the three planets around TOI-451.

6.3 X-ray observations & analysis

I used `SAS v19` to reduce and analyse the *XMM-Newton* observations, following the SAS Data Analysis Threads[1].

6.3.1 TOI-1098

TOI-1098 was observed by the *XMM-Newton* telescope on March 25th 2023 for a duration of 15.5 ks (observation ID `0904310601`).[2] I identified both TOI-1098 and its fainter wide-orbit companion, TOI-1098 B, in both EPIC-pn and EPIC-MOS using their Gaia DR3 coordinates, which I corrected for proper motion, and plotted them in Figure 6.2 (left panel). I found the two stars are separated by

---

[1] https://www.cosmos.esa.int/web/xmm-newton/sas-threads

[2] The *XMM-Newton* data used in this work is publicly available at the *XMM-Newton*Science Archive (XSA) (`https://www.cosmos.esa.int/web/xmm-newton/xsa`), under observation IDs 0904310201 (target: TOI-451, PI: Wheatley) and 0904310601 (target: TOI-1098, PI: Wheatley).

60 arcseconds in the X-ray image, consistent with the value of 59.3 arcseconds determined by Tofflemire et al. [2021].

I removed time intervals with high flaring particle noise, which is significant on the last 5 ks of the observation. I adopted a count rate cutoff of $1\,\mathrm{s}^{-1}$ on EPIC-pn and $0.5\,\mathrm{s}^{-1}$ on EPIC-MOS, reducing the length of the observation to 11.9 ks and 13 ks, respectively.

The X-ray counts from the sources were extracted using a circular aperture at their proper-motion corrected coordinates, with a radius of 20 arcseconds for TOI-1098 and 15 arcseconds for TOI-1098 B. The X-ray background was estimated by collecting the counts on a circular aperture in a region adjacent to the sources within the same CCD and containing no X-ray detections, with radius of 80 arcseconds on EPIC-pn and 90 arcseconds on EPIC-MOS.

I plotted the EPIC-pn lightcurves of the two stars in Figure 6.3 (left panels). I only found marginal evidence for flaring on the lightcurve of TOI-1098 B at 11 ks, simultaneous with the increase in the flaring particle noise.

I then extracted pn and MOS spectra for both sources and analysed them with the software `XSPEC v12.12.1` [Arnaud, 1996]. I combined the spectra from the MOS1 and MOS2 cameras (MOS1+2, hereafter) using the `SAS` task `epicspeccombine`. I then fitted the pn and MOS1+2 spectra simultaneously with `XSPEC`.

I limited the energy band to 0.15–2.4 keV for pn and 0.2–2.4 keV for MOS, and adopted the C-statistic [Cash, 1979] as the fit statistic. I modelled the hydrogen absorption on the ISM with a `TBABS` model [Wilms et al., 2000b], assuming a hydrogen density of $0.1\,\mathrm{cm}^{-3}$ [Redfield and Linsky, 2001].

To extract the X-ray flux, I fitted a two-temperature `APEC` model [Smith et al., 2001] to the spectrum of TOI-1098, and a single temperature in the case of TOI-1098 B due to the low number of spectral counts. Finally, I computed the parameter uncertainties with the MCMC method via the `chain` command in `XSPEC` and using the Goodman-Weare algorithm [Goodman and Weare, 2010]. I adopted 10 random walkers and a total chain length of 20,000 steps with a burn-in of 5,000 steps. The spectra, together with the fitted models, are plotted in Figure 6.4, and the best fit parameters and X-ray fluxes are presented on Table 6.3.

I thus determined an X-ray luminosity for TOI-1098 of $\mathrm{L_X} = (1.80 \pm 0.13) \times 10^{29}\,\mathrm{erg\,s^{-1}}$ in the energy band $0.1 - 2.4\,\mathrm{keV}$, and a corresponding X-ray activity $\mathrm{L_X/L_{bol}} = (2.46 \pm 0.19) \times 10^{-5}$. I further estimated the EUV component from the scaling relations by King et al. [2018], which predicted an EUV luminosity of $\mathrm{L_{EUV}} = (1.71 \pm 0.1) \times 10^{28}\,\mathrm{erg\,s^{-1}}$ in the energy band $0.0136 - 0.1\,\mathrm{keV}$.

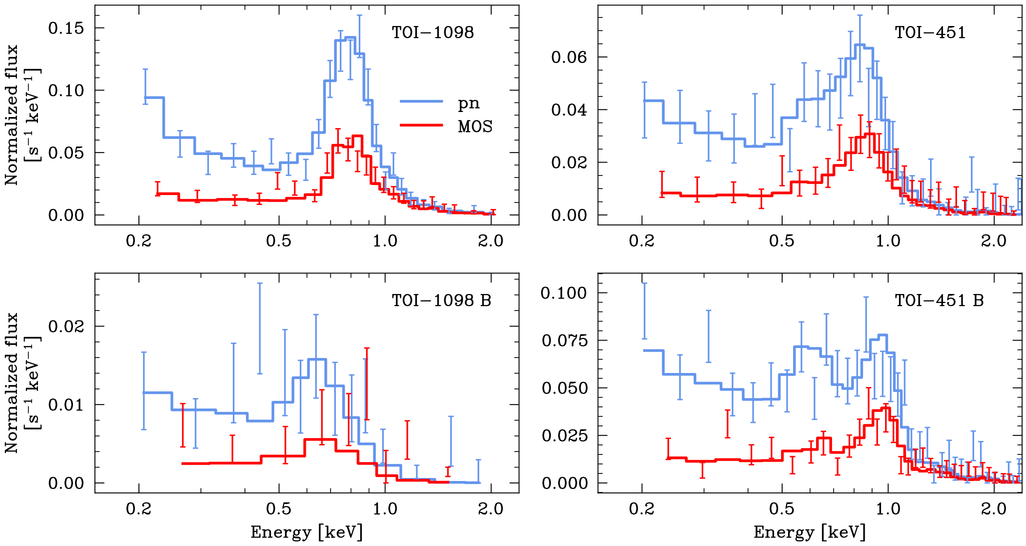

Figure 6.4: X-ray spectra of the four stars from the pn and MOS1+2 cameras (data points) together with the fitted models (solid lines).

Regarding TOI-1098 B, I determined an X-ray luminosity of $L_X = (1.79 \pm 0.18) \times 10^{28}\,\mathrm{erg\,s^{-1}}$ in the energy band $0.1 - 2.4\,\mathrm{keV}$, a factor of 10 fainter than its F8V companion. Together with the bolometric luminosity provided by Tofflemire et al. [2021] of $L_{\mathrm{bol}} = (6.28 \pm 0.29) \times 10^{-3}\,L_{\odot}$, I found an X-ray activity of $L_X/L_{\mathrm{bol}} = (7.46 \pm 0.84) \times 10^{-4}$.

6.3.2 TOI-451

TOI-451 was observed by the *XMM-Newton* telescope on March 17th 2023 for a duration of 13 ks (observation ID `0904310201`). I identified both TOI-451 and its wide-orbit companion, TOI-451 B, in the X-ray observation at their proper motion corrected coordinates, as shown in Figure 6.2 (right panel) . I determined a sky separation of 37 arcseconds, agreeing with Newton et al. [2021].

The majority of the observation has an increased level of flaring particle noise; past 5 ks for pn and past 7.5 ks for MOS. As seen in their X-ray lightcurves, which I plotted in Figure 6.3 (right panels), the noisy time intervals do not have a significant impact in the errors of the count rates. I thus chose not to remove these noisy intervals.

In order to determine the X-ray fluxes, I repeated the analysis I carried out for TOI-1098 in Section 6.3.1. I adopted circular apertures of radius 17.5

Table 6.3: X-ray fluxes at Earth and fitted coronal temperatures of the spectral models. The models were fitted to the pn and MOS1+2 spectra simultaneously.

Star	kT_1	kT_2	X-ray flux[a]	X-ray flux[b]
	keV	keV	$10^{-14}\,\mathrm{erg\,cm^{-2}\,s^{-1}}$	$10^{-14}\,\mathrm{erg\,cm^{-2}\,s^{-1}}$
TOI-1098	$0.10^{+0.02}_{-0.01}$	$0.59^{+0.03}_{-0.02}$	$12.6^{+0.1}_{-0.4}$	$13.6^{+1.4}_{-0.7}$
TOI-1098 B	$0.25^{+0.02}_{-0.02}$	—	$1.3^{+0.1}_{-0.1}$	$1.4^{+0.2}_{-0.1}$
TOI-451	$0.20^{+0.09}_{-0.02}$	$0.78^{+0.15}_{-0.02}$	$7.1^{+0.3}_{-0.5}$	$7.3^{+0.4}_{-0.6}$
TOI-451 B	$0.21^{+0.02}_{-0.02}$	$1.05^{+0.07}_{-0.05}$	$11.0^{+0.5}_{-0.4}$	$11.2^{+0.5}_{-0.4}$

[a] Energy band 0.15 – 2.4 keV

[b] Energy band 0.1 – 2.4 keV

arcseconds for both stars on their proper-motion corrected coordinates, as well as a circular aperture for the background with a radius of 60 arcseconds on EPIC-pn and 95 arcseconds on EPIC-MOS. In this case, since the two stars appear closer in the sky, I picked smaller extraction radii to avoid overlap.

Both targets were bright in the X-rays and so I were able to extract and fit their X-ray spectra with two-temperature APEC models. The spectra, together with the fitted models, are plotted in Figure 6.4, and the best fit parameters are presented on Table 6.3.

For TOI-451, I determined an X-ray luminosity of $L_X = (1.34 \pm 0.08) \times 10^{29}\,\mathrm{erg\,s^{-1}}$ in the energy band $0.1 - 2.4\,\mathrm{keV}$, and so an activity of $L_X/L_{bol} = (5.38 \pm 0.41) \times 10^{-5}$. Applying the scaling relations by King et al. [2018], I further estimated an EUV luminosity of $L_{EUV} = (1.11 \pm 0.05) \times 10^{29}\,\mathrm{erg\,s^{-1}}$.

Regarding TOI-451 B, I found an X-ray luminosity of $L_X = (2.04 \pm 0.09) \times 10^{29}\,\mathrm{erg\,s^{-1}}$, making it 50% brighter in the X-rays than its G7V companion. I also found no evidence of flaring in the lightcurve during the observation that could explain its high luminosity (Figure 6.3, bottom right panel). It's unexpectedly bright X-ray emission supports the idea that TOI-451 B could be an unresolved M dwarf binary, as proposed by Newton et al. [2021], where the combined X-ray emission of the two stars gives the appearance of a brighter single source.

6.4 Stellar spin & emission histories

In order to study the evaporation histories of the four transiting planets, it is necessary to determine the XUV emission history of their host stars. Since the

X-ray activities of stars are related to their spin period, one can estimate their past and future XUV emission from rotational evolution models.

I adopted the rotational evolution models by Johnstone et al. [2021, hereafter J21], together with their rotation-activity relation, to model the X-ray emission histories of TOI-451 and TOI-1098. To use the models, I adopted their Python code `Mors`[3], which generates the X-ray emission history of a star given its mass and its spin period at a given age. I additionally estimated the EUV emission histories of the stars using the scaling relations by King et al. [2018], derived from Solar TIMED/SEE data.

6.4.1 TOI-1098

I fitted the measured mass, age, and spin period of TOI-1098 to the models of J21, and plotted them in Figure 6.5, both evolution of the spin period (left panel) and XUV emission (right panel).

The measured spin period of TOI-1098 of 2.34 ± 0.07 d is well predicted by the model of J21, which predicts a mean spin period of 2.57 d with a 2σ spread from 1.19 to 5.36 d. The predicted X-ray activity, plotted in Figure 6.5 (right panel), is also in good agreement with my *XMM-Newton* observations – within one standard deviation from my measured activity of $(2.46 \pm 0.19) \times 10^{-5}$.

Its M-dwarf companion, TOI-1098 B, is a M4V star with a mass of $0.26\,\mathrm{M}_\odot$ [Tofflemire et al., 2021]. Tofflemire et al. [2021] also extracted a spin period of 0.8 ± 0.01 d days from its TESS lightcurve, applying a systematics correction and a regression against the rotation period of TOI-1098. Following the rotation-activity relation of J21, this corresponds to an X-ray activity of 6.4×10^{-4}, within 2σ of the X-ray activity of $(7.46 \pm 0.84) \times 10^{-4}$ I determined from my *XMM-Newton* observations.

I additionally applied the activity–age relations by Engle [2024] for M-dwarfs, based on a curated sample of nearby M-dwarfs with well constrained ages. These relations predicted an X-ray activity of $8.84 \pm 2.56 \times 10^{-4}$, in good agreement with my observations.

6.4.2 TOI-451

In Figure 6.6, I plotted models of the evolution of the spin period (left panel) and XUV emission (right panel) of TOI-451.

---

[3] `https://github.com/ColinPhilipJohnstone/Mors`

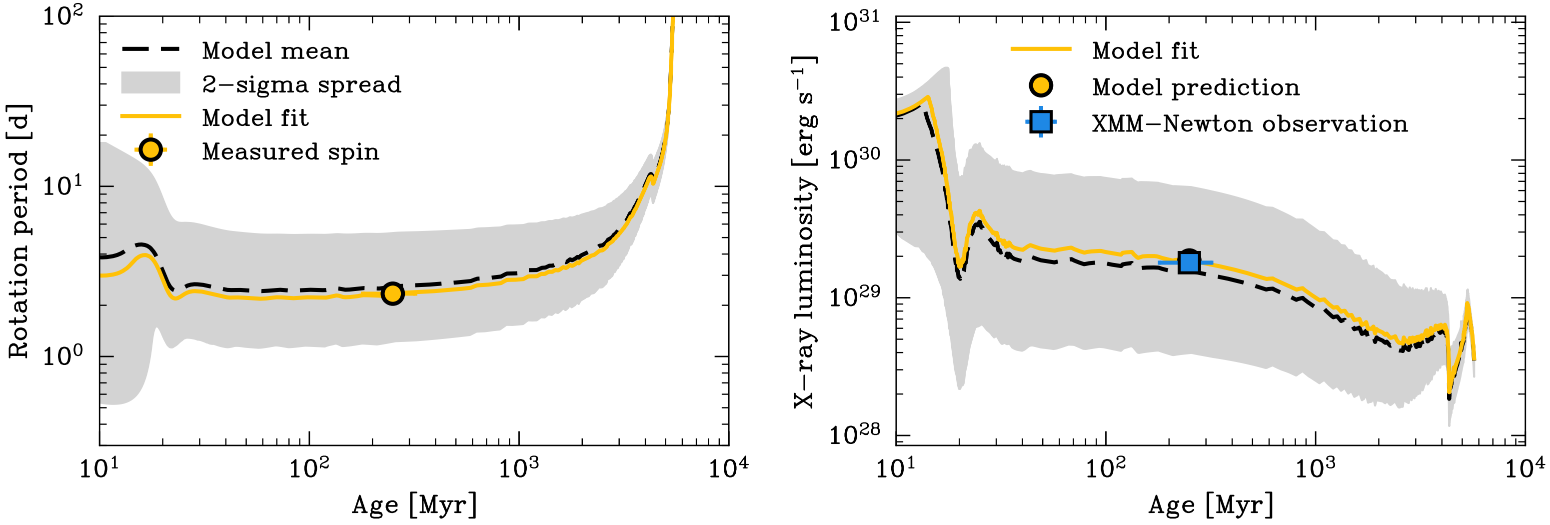

Figure 6.5: **Left panel:** spin evolution models by J21 for TOI-1098. The mean model is plotted as a dashed line, and the 2σ spread based on the initial spin period is plotted as a shaded region. The model fitted to the spin period and age of TOI-1098 is plotted as an orange line, and the star's measured rotation period is shown as a circle. **Right panel:** X-ray emission models by J21 akin to the left panel. The X-ray luminosities derived from my *XMM-Newton* observations are shown as a square, and the predicted value as a circle (behind the square).

The model by J21 predicted a mean rotation period of 4.8 d, with a 2σ spread between 1.2 and 7.1 d, in agreement with its measured spin period of 5.1 ± 0.1 d. The model also predicted an X-ray activity of 1.12×10^{-4}, which is a factor of two greater than my measured activity of $(5.40 \pm 0.33) \times 10^{-5}$.

Regarding TOI-451 B, Newton et al. [2021] found its Gaia DR2 astrometry and kinematics to be consistent with that of TOI-451, suggesting both stars are bound. The star has a Gaia DR3 colour of $\mathrm{G_{BP}} - \mathrm{G_{RP}} = 2.53$ mag, which I combined with the stellar sequences by Pecaut and Mamajek [2013] to determine an spectral type of M3V and a mass of $0.34\,\mathrm{M_\odot}$. Newton et al. [2021] also uncovered a signal at 1.64 d on the periodogram, which they attributed to the spin period. Fitting the mass and spin period to the models by J21, I obtained an X-ray luminosity of $4 \times 10^{28}\,\mathrm{erg\,s^{-1}}$, a factor of 5 fainter than suggested by my *XMM-Newton* observations.

Moreover, the X-ray luminosity I measured, $\mathrm{L_X} = 2 \times 10^{29}\,\mathrm{erg\,s^{-1}}$, is 50% brighter than that of its G-type companion. The X-ray lightcurve (see Figure 6.3, lower right) also shows no evidence of a flare that might explain its high luminosity.

Newton et al. [2021], however, found evidence that points towards TOI-451 B being an unresolved binary system. They found the source lies above the $\mathrm{G} - \mathrm{G_{RP}}$ colour-magnitude diagram by 0.65 mag, and has a Gaia DR2 renormalized unit weight error (RUWE) of 1.24, indicative of a poor astrometric fit for a single source [Fabricius et al., 2021a]. Newton et al. [2021] argued the rotational signal they detected corresponds to the spin period of one of the stars; the rotational signal of the second star would not have been detected if it had a smaller amplitude or if it was affected by the removal of systematics. The rotational signal that Newton et al. [2021] detected could also arise from the the orbit of the binary. However, if it were indeed the orbital period of the binary, then the two stars would likely be tidally-locked due to their small separation, and thus they would also have spin periods of the same value. An unresolved M-dwarf binary would have a higher luminosity, as the X-ray output from each star would combine to give the appearance of a brighter single source. I assumed TOI-451 B is comprised of two equal mass stars, which implies both have the same colour index and so each a mass of $0.34\,\mathrm{M_\odot}$.

Using the knowledge that one of the stars has a spin period of 1.64 d, and assuming the other M-dwarf is X-ray saturated (with $\mathrm{L_X}/\mathrm{L_{bol}} = 10^{-3}$, as is common for young M-dwarfs, J21), I found their combined X-ray luminosity to be $1 \times 10^{29}\,\mathrm{erg\,s^{-1}}$, more consistent with my *XMM-Newton* measurement of

$2 \times 10^{29}\,\mathrm{erg\,s^{-1}}$.

Alternatively, the activity–age relations by Engle [2024] predict an X-ray luminosity of $6.0 \pm 2.2 \times 10^{28}\,\mathrm{erg\,s^{-1}}$ for a $0.34\,\mathrm{M_\odot}$. Assuming again that the other M-dwarf is X-ray saturated, this results in a combined luminosity of $1.2 \pm 0.2 \times 10^{29}\,\mathrm{erg\,s^{-1}}$, which is also consistent with my *XMM-Newton* measurements.

6.5 Modelling the evaporation histories

To model the evaporation histories of the four planets, I followed the method I outlined in Chapter 2.5 using the code `photoevolver`[4]. I adopted the mass loss formulation by Kubyshkina et al. [2018] with the planet grid and interpolation routine provided by Kubyshkina and Fossati [2021]. I simulated the past and future evaporation histories of the planets back to 10 Myr, after which disk dispersal [Fedele et al., 2010] and boil-off mechanisms [Owen and Wu, 2016] should have completed, and forward to the approximate end of the main sequence stage in stellar evolution – this corresponds to 10 Gyr for the G-type TOI-451 and 6 Gyr for the F-type TOI-1098 [Choi et al., 2016]. As for the integration method, I adopted the 4th order Runge-Kutta algorithm provided by the Python package `scipy` [Virtanen et al., 2020] with a variable step size no larger than 1 Myr.

I considered two scenarios for the X-ray emission history of TOI-451, (1) the one predicted by the J21 model, (2) and the same model adjusted to my *XMM-Newton* observations of TOI-451, which are fainter by a factor of two (see Figure 6.6, right panel).

6.6 Simulation results

6.6.1 Current mass loss rates

On Table 6.4, I show the incident X-ray flux on the planets and the subsequent mass loss rates. I found the super-Earth TOI-451 b would experience high mass loss rates of about $10^{11} - 10^{12}\,\mathrm{g\,s^{-1}}$. The large errors, which originate in the large uncertainty in its mass, allow for escape rates an order of magnitude greater, which suggests that the presence of a gaseous envelope at the present time is not realistic. As for the sub-Neptunes TOI-451 c and d, these mini-Neptunes experience moderate mass loss rates at least 10–30 times lower than TOI-451 b, around $10^{10} - 10^{11}$ g

---

[4] github.com/jorgefz/photoevolver

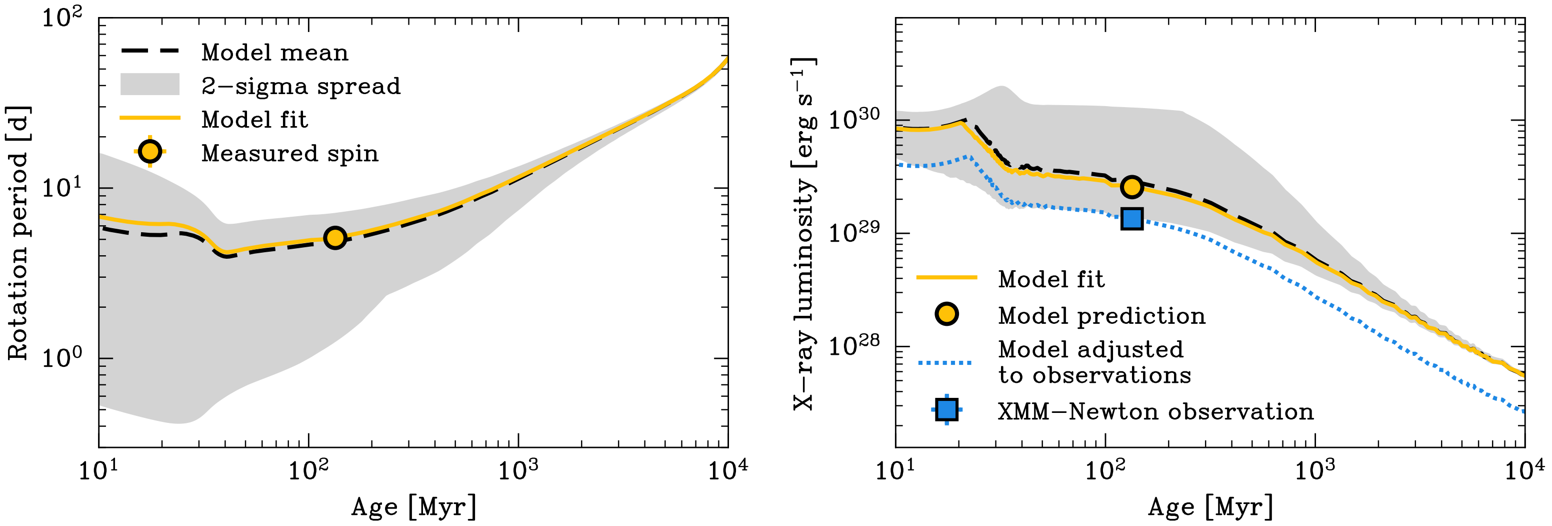

Figure 6.6: **Left panel:** spin evolution models for TOI-451, following Figure 6.5, with the solid line representing the model fitted to the current age and spin period of TOI-451. **Right panel:** X-ray emission models by J21 following Figure 6.5. The model fitted to the measured spin period has been offset to fit the measured X-ray luminosity of the star, shown as a dotted line.

Table 6.4: Incident X-ray irradiation and mass loss rates of the four planets.

Planet	Incident X-ray flux[a] $10^3\,\mathrm{erg\,cm^{-2}\,s^{-1}}$	Mass loss rate $10^{10}\,\mathrm{g\,s^{-1}}$
TOI-451 b	65.3 ± 15.3	81^{+332}_{-73}
TOI-451 c	8.0 ± 1.8	6.9 ± 2.1
TOI-451 d	3.0 ± 0.4	$> 3.0 \pm 0.5$[b]
TOI-1098 b ($5\,\mathrm{M_E}$)	5.3 ± 1.1	53 ± 12
TOI-1098 b ($15\,\mathrm{M_E}$)	5.3 ± 1.1	2.1 ± 0.3

[a] Energy band 0.1 – 2.4 keV
[b] 3σ lower limit

$\mathrm{s^{-1}}$. Their greater masses, which result in deeper gravitational potentials, and larger orbital separations, which result in lower X-ray fluxes, shield them from significant mass loss. Regarding TOI-1098 b, since its mass is only constrained by an upper limit, I chose to calculate its mass loss rate at two choices for the mass, 5 and 15 $\mathrm{M_E}$, informed by the span observed on sub-Neptune populations. These two escape rates differ by a factor of 26, from 2×10^{10} g $\mathrm{s^{-1}}$ at 15 $\mathrm{M_E}$ to 5×10^{11} g $\mathrm{s^{-1}}$at 5 $\mathrm{M_E}$, demonstrating the strong impact that the choice of mass has in models of atmospheric escape. The higher mass case resembles TOI-451 c & d in its escape rates, pointing towards a potentially stable atmosphere that will not stripped, whereas the lower mass case is more similar to TOI-451 b, suggesting a much more weakly bound atmosphere that is evaporated in relatively short timescales.

6.6.2 Evaporation histories

In Figure 6.7 I present the evaporation histories of TOI-1098 b (left panels), TOI-451 c (middle panels), and TOI-451 d (right panels).

Regarding their future evolution, I found the planets atmospheres end up fully evaporating in most scenarios. This occurs within 1 Gyr for both TOI-1098 b and TOI-451 c, except for the 15 $\mathrm{M_E}$ scenarios, where the envelope lasts till the age of 1-2 Gyr. TOI-451 d is further away from its star and so experiences lower evaporation rates. As a result, most scenarios end up being stripped after 1 Gyr, with only those over 10 $\mathrm{M_E}$ being stable against evaporation and maintaining significant amounts of H/He throughout their lives.

As for their past evaporation, I found the scenarios with the lowest masses

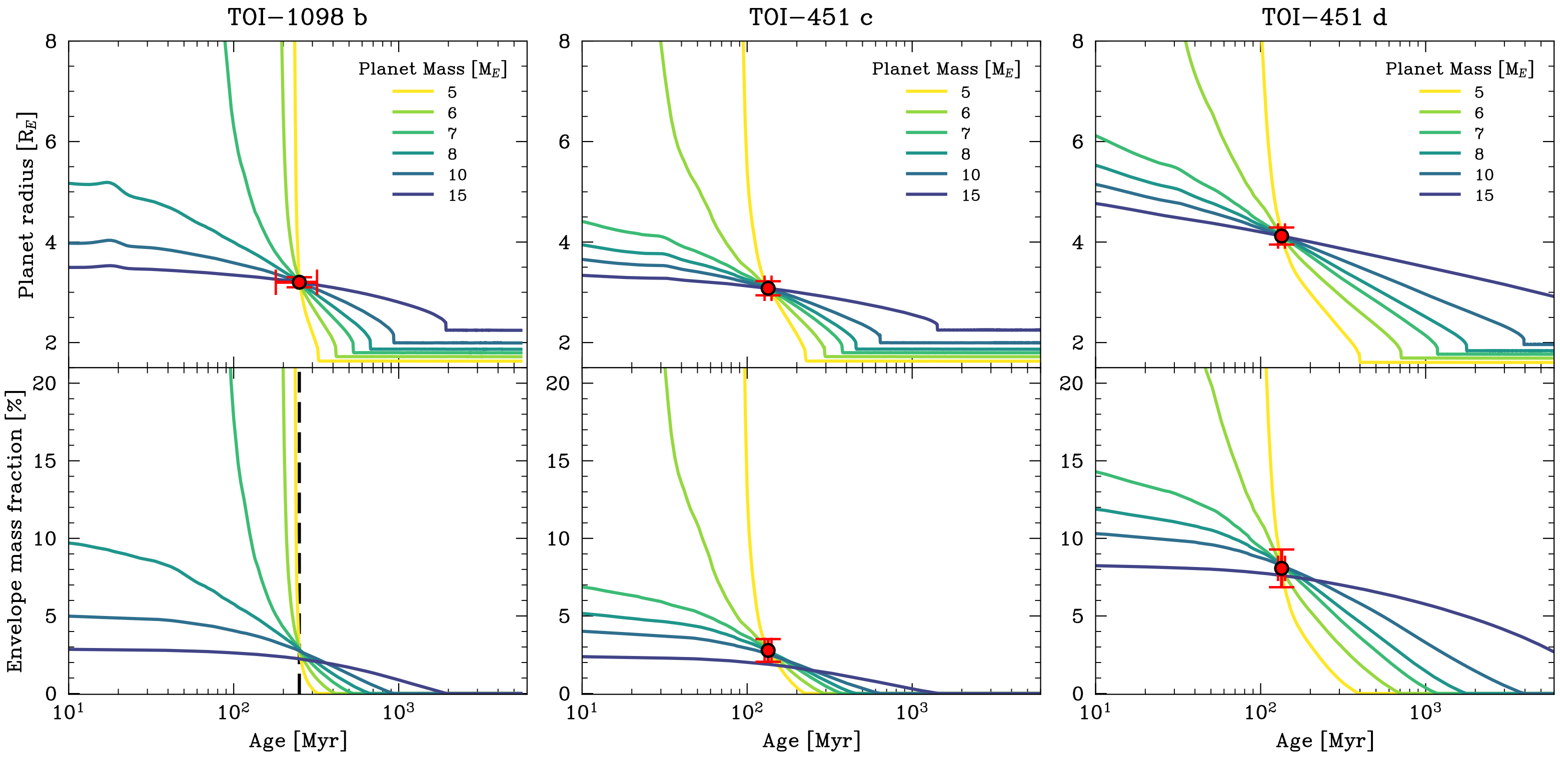

Figure 6.7: Simulation results for the past and future evaporation histories of TOI-1098 b (left column), TOI-451 c (middle column), and TOI-451 d (right column) assuming a range of planet masses between 5 and 15 M_E. The evolution of their radii is shown on the top row of panels, and the evolution of their envelope mass fractions on the bottom row of panels. The current radii of the planets and their envelope mass fractions are shown as a red circle on the top and bottom panels, respectively. In the case of TOI-1098 b, which has no mass measurement, its current age is shown on the bottom panel as a black dashed line.

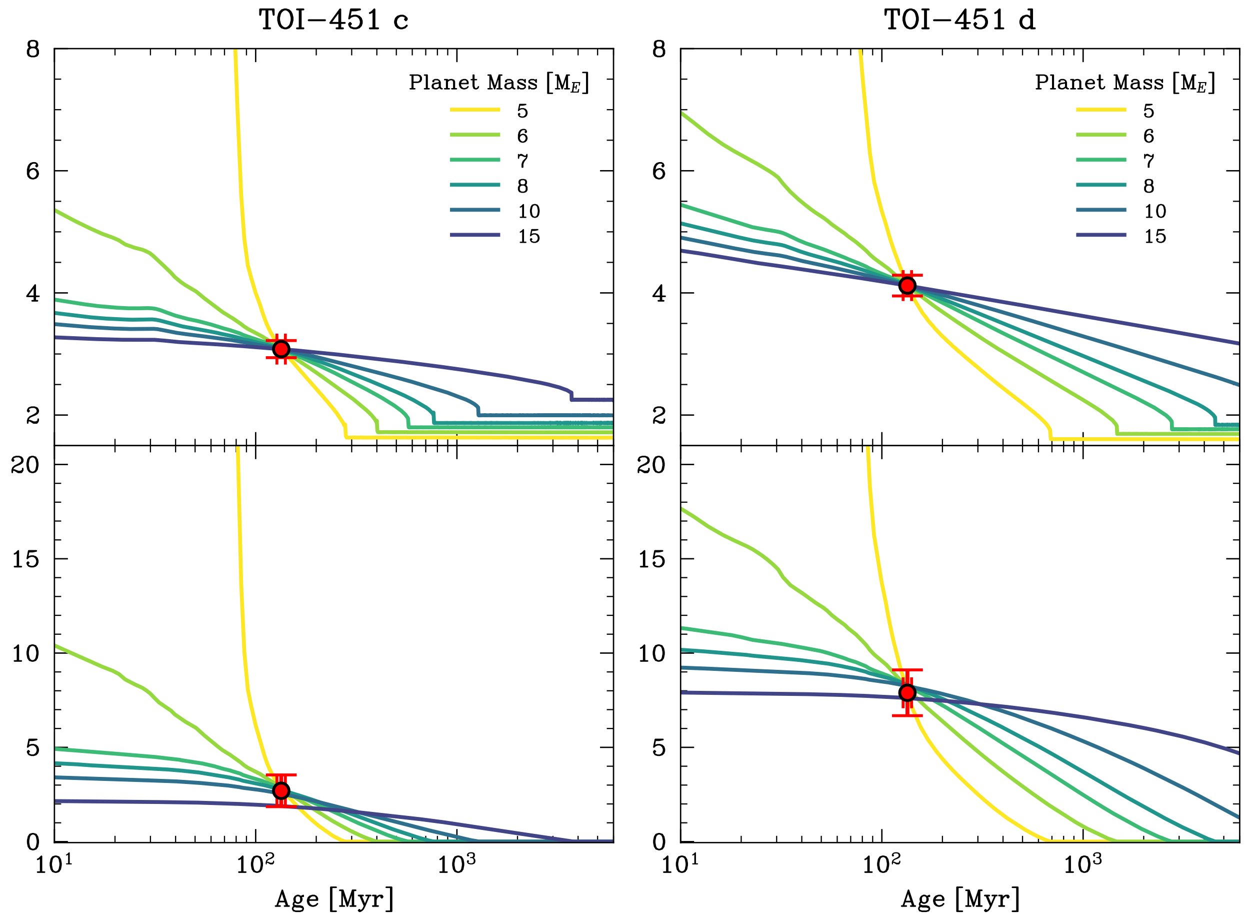

Figure 6.8: Following Figure 6.7, simulation results for the past and future evaporation histories of TOI-451 c and d, assuming a fainter X-ray irradiation history consistent with the *XMM-Newton* observations of their host star.

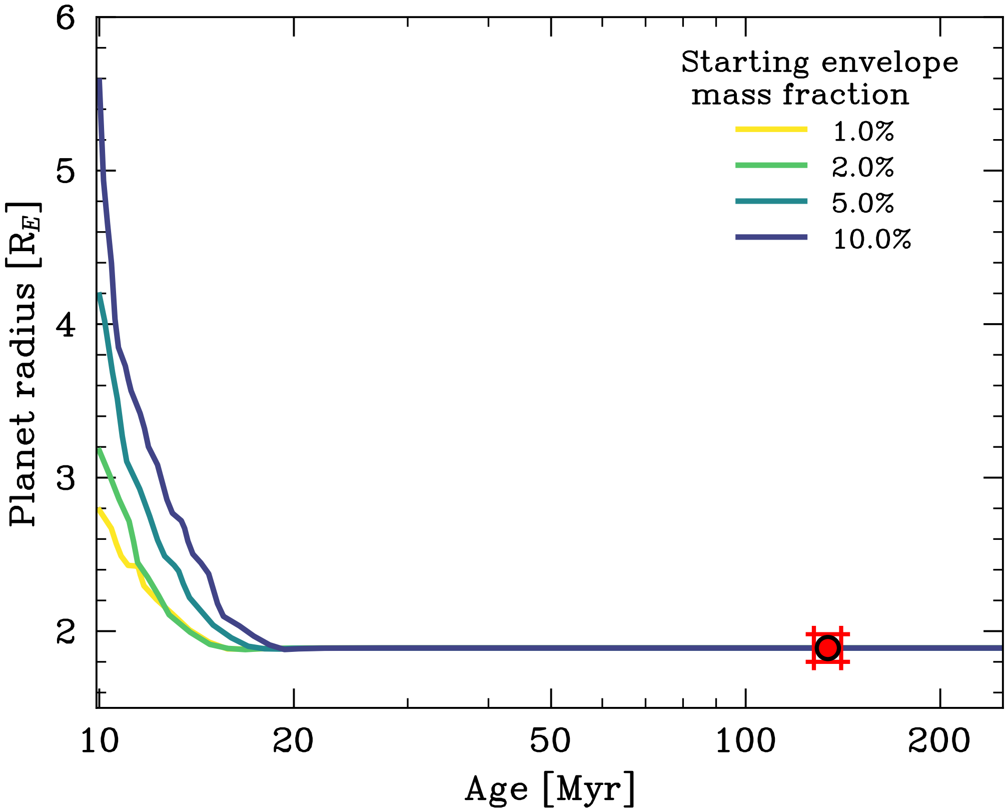

Figure 6.9: Evolution scenarios for the radius for TOI-451 b with a range of starting envelope mass fractions between 1% and 10%, and assuming a rocky core of mass 8 M_E. The current radius of the planet is shown as a red circle.

end up predicting unfeasibly large initial radii. These low mass planets experience extremely high evaporation rates that should have removed their atmospheres completely. And so, during backwards evolution, the simulation requires extremely large initial envelopes to account for such mass loss rates. This feature allows us to determine minimum masses for the planets, under which no envelope would have survived to the present day.

I thus determined a minimum mass of 7 $\mathrm{M_E}$ for both TOI-451 c and d, and 8,$\mathrm{M_E}$ for TOI-1098 b. At 10 Myr, the earliest age I consider in the simulations, the scenarios with "valid" masses result in initial radii of 3.8-4.5 $\mathrm{R_E}$ for TOI-451 c, 4.8-6.1 $\mathrm{R_E}$ for TOI-451 d, and 3.5-5.2 $\mathrm{R_E}$ for TOI-1098 b. At this age, the corresponding starting envelope mass fractions are thus 2-7% for TOI-451 c, 8-14% for TOI-451 d, and 4-10% for TOI-1098 b.

Regarding TOI-451 b, given the proximity to its star and thus the high bolometric flux it receives, my models predict a lack of a H/He atmosphere. This implies either its primordial envelope was evaporated at some point in its past, or the planet formed without one. I thus explored the evaporation history of a range of primordial envelopes. To do so, I adopted a mass of 8 $\mathrm{M_E}$, which the interior models predict for a purely rocky planet, and is consistent with the uncertainty of its mass. I then ran my simulations forward from the age of 10 Myr with initial envelope mass fractions ranging from 1% to 10% of the planet's mass. As shown in Figure 6.9, I found all primordial envelopes were fully removed within the first 20 Myr of evolution.

I repeated the simulations for the TOI-451 planets using the model for the X-ray emission history by J21 adjusted to my *XMM-Newton* observations, which are a factor of two fainter. As seen in Figure 6.8, I found TOI-451 c and d are able to retain an envelope to this day with masses of at least 6 $\mathrm{M_E}$, only lower by 1 $\mathrm{M_E}$ compared to predictions from the previous X-ray evolution model.

The predicted radii for the planets at 10 Myr, the earliest age I considered in the simulations, now cover a somewhat narrower range of 3.3-3.9 $\mathrm{R_E}$ (TOI-451 c) and 4.7-5.5 $\mathrm{R_E}$ (TOI-451 d) for masses of 7-15 $\mathrm{M_E}$. These correspond to starting envelope mass fractions of 2-5% for TOI-451 c and 8-11% for TOI-451 d.

In both planets, the scenarios with 6 $\mathrm{M_E}$ constitute an outlier, reaching much larger initial radii than the other more massive cases, with 5.4 $\mathrm{R_E}$ for TOI-451 c and 7 $\mathrm{R_E}$ for TOI-451 d. These initial radii correspond to starting envelope mass fractions of 10% and 17.5%, respectively.

I also find no considerable effect on the survival of any primordial envelope on TOI-451 b, with all scenarios being stripped before the age of 20 Myr.

6.7 Discussion

In general, the fates of the atmospheres of close-in planets are dictated by the XUV emission of their host stars (and is evolution), as well as the response of the upper atmosphere in face of this irradiation.

In Section 6.7.1 I will place the *XMM-Newton* observations of the two stars in context with cluster stars and the X-ray evolution model by Johnstone et al. [2021], assessing its predictive power against the observed X-ray luminosities of stellar populations. In Section 6.7.2, I will discuss the results from my simulations of evaporation history of the four planets, and the impact of the different assumptions for their internal structures.

6.7.1 Comparison with Psc-Eri and the Pleiades

Tofflemire et al. [2021], using Gaia kinematics, found that TOI-1098 is part of a newly discovered cluster, aged 250 Myr, which they named MELANGE-1. Similarly, Newton et al. [2021] determined TOI-451 is part of the Pisces-Eridanus stream, aged 120 Myr and recently discovered by Curtis et al. [2019]. Unfortunately, neither of these two clusters benefit from *XMM-Newton* observations, in part due to their recent discovery and, in the case of Psc-Eri, due to its large angular size, as it stretches over 120° across the sky.

Fortunately, Psc-Eri has a very age similar to the Pleiades open cluster, aged 125 Myr, and the rotational sequences of the two clusters closely match too [Curtis et al., 2019]. Moreover, the Pleiades has been extensively studied in the X-rays. I studied the X-ray emission from Pleiads in Chapter 5 using the membership list that Godoy-Rivera et al. [2021] filtered with Gaia. I obtained X-ray luminosities for 156 Pleiads in their sample by cross-matching their sky positions with the *4XMM* catalogue of X-ray detections from *XMM-Newton*. I also compared the spin periods and X-ray activities of these Pleiades stars with the predictions from the models by Johnstone et al. [2021], which I also used in this chapter to estimate the stellar emission histories of TOI-451 and TOI-1098.

In Figure 6.10, I plotted the spin periods of Psc-Eri and Pleiades (left panel) and the corresponding X-ray activities of Pleiades stars (right panel). I noticed that both the spin period and X-ray activity of TOI-451 are consistent with other

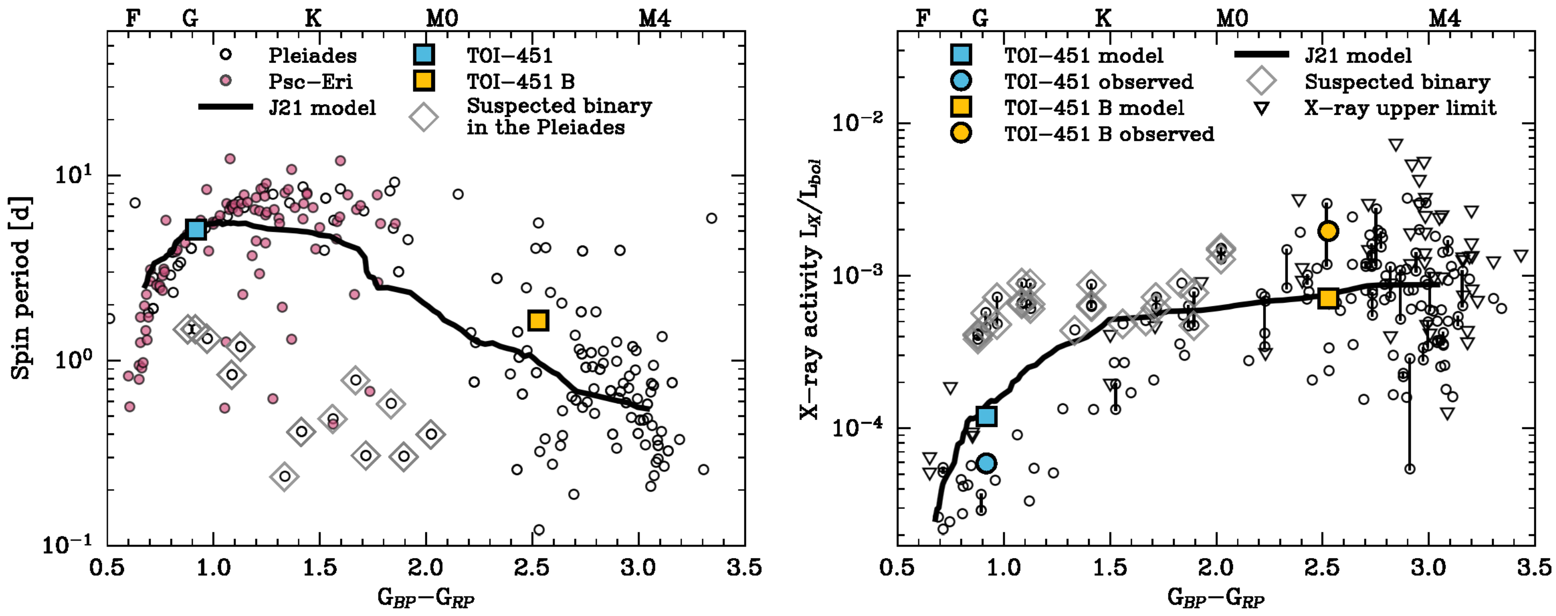

Figure 6.10: **Left panel:** Gaia BP-RP colour vs spin period for stars in Psc-Eri (red circles) and the Pleiades (white circles). Only the Pleiades stars with *XMM-Newton* observations are plotted. TOI-451 is plotted as a blue square, and TOI-451 B as a yellow square. The 50th percentile model by J21 is shown as a black line. I marked the fast rotating Pleiades FGK stars with diamonds. **Right panel:** Gaia BP-RP colour vs X-ray activity for Pleiades stars, both detections (white circles) and upper limits (white triangles). The *XMM-Newton* observations of TOI-451 are TOI-451 B are marked as a blue and yellow circles, respectively. The model by J21 is shown as a black line, and its predictions for the X-ray activity of TOI-451 and TOI-451 B are shown as blue and yellow squares, respectively. Multiple X-ray observations of the same star are linked with thin black lines.

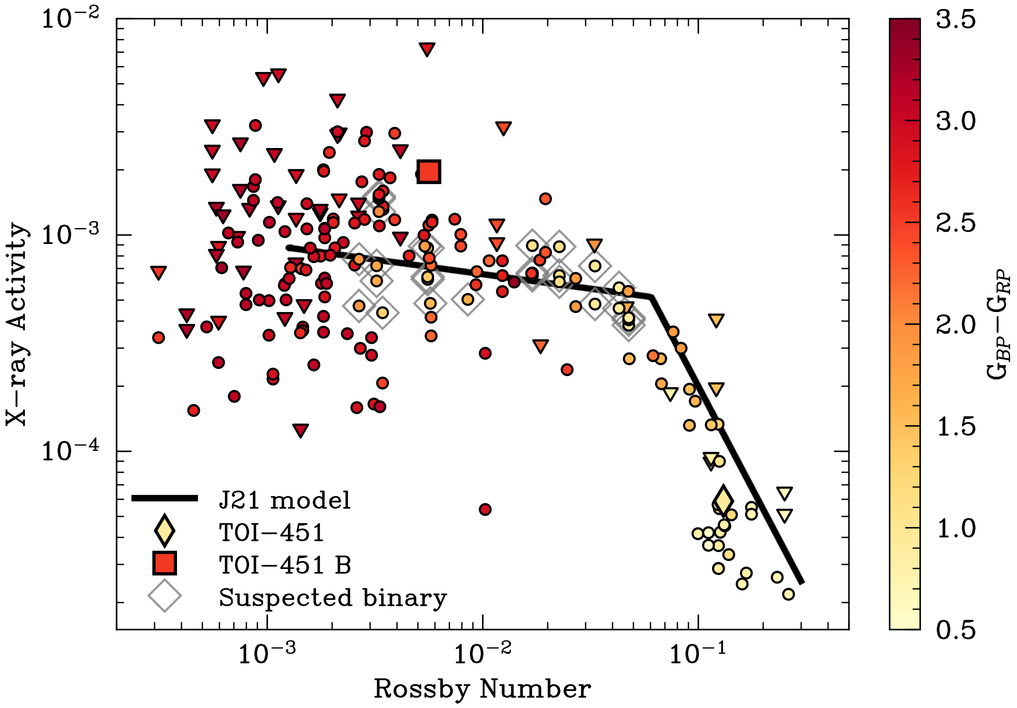

Figure 6.11: Rotation-activity relation for the Pleiades with Rossby number plotted against X-ray activity. *XMM-Newton* detections of Pleiades stars are marked as circles, and upper limits as triangles. TOI-451 is plotted as a diamond and TOI-451 B as a square. The rotation-activity relation by J21 is shown as a black line. Colour indicates the Gaia BP-RP colour index of stars.

G dwarfs in both Psc-Eri and the Pleiades. In fact, TOI-451 lies within a tight relation between spin period and spectral type that is present in both clusters, thought to be caused by spin periods converging over time [Tu et al., 2015]. There is also a population of rapidly-spinning stragglers that lie below this relation, which in Chapter 5 I identified as tidally-synchronised binaries that have been spun-up by a close companion.

Regarding TOI-451 B, I calculated its bolometric luminosity using the models by Spada et al. [2013] for a $0.34\,\mathrm{M}_{\odot}$ star and increased it by a factor of 1.85 to match its brightness of 0.65 mag above the main sequence [Newton et al., 2021]. As shown in Figure 6.11, TOI-451 B lies on the high end of the scatter of X-ray activities for M dwarfs, a factor of 2.9 more active than predicted by J21.

In Figure 6.11 I additionally plotted the rotation-activity relation between the spin periods of Pleiades stars and their corresponding *XMM-Newton* observations, together with the relation by Johnstone et al. [2021]. All in all, as I determined in Chapter 5, the rotation model by J21 overestimates the spin periods of F & G stars by a factor of 1.5 and underestimates the rotation of K-dwarfs by the same amount (see Figure 6.10, left panel). Moreover, their activity-relation (see Figure 6.11) fits K dwarfs well but over-predicts the X-ray activity of F & G stars by a factor of 3. Together, these two effects result in predictions for the X-ray activity a factor of three higher than observed for FGK stars (see Figure 6.10, right panel). For that reason, I favour a fainter X-ray emission history for TOI-451 that matches my *XMM-Newton* observations.

6.7.2 Evaporation histories

In the simulations, I considered two models for the X-ray emission history of TOI-451. The first is the predicted evolution for a $0.95\,\mathrm{M}_{\odot}$ star following the models by Johnstone et al. [2021]. The second model follow *XMM-Newton* observations of TOI-451 which suggest an X-ray luminosity fainter than predictions from the first model by a factor of two. This second model is constructed by taking the first model and scaling it down to match the observed X-ray luminosity of TOI-451 at the present time.

In this section, I will discuss the results from my simulations of the evaporation histories of the four planets. In the case of the planets around TOI-451, I will additionally address the differences that arise from considering either model for the X-ray irradiation.

TOI-451 b

TOI-451 b ($1.9\,\mathrm{R_E}$, 1.9 d) is a hot super-Earth remarkably close to its star, at a separation of only 0.03 au, placing it not only below the radius valley but also within the Neptunian desert. TOI-451 b is consistent with the large population of hot rocky worlds at the lower edge of the Neptunian desert that have been stripped of their gaseous envelopes [Owen and Lai, 2018].

My simulations predict that any primordial H/He envelope was rapidly evaporated within 20 Myr (see Figure 6.9). This result is also independent on the stellar X-ray emission history adopted.

Even without photoevaporation, such close-in super-Earths are susceptible to boil-off processes, where significant fractions of the primordial H/He envelopes accreted during formation rapidly escape when the external pressure from the protoplanetary disk is lifted [e.g. Owen and Wu, 2016; Fossati et al., 2017; Rogers and Owen, 2021]. As such, I find TOI-451 b is inconsistent with the presence of a hydrogen-rich atmosphere. Indeed, the mass radius relations by Otegi et al. [2020] predict a purely rocky composition with no H/He envelope, which requires a mass of $8.1\,\mathrm{M_E}$.

On the other hand, the planet's measured mass of $3.8^{+3.4}_{-2.6}\,\mathrm{M_E}$, whilst consistent with a barren rocky core within 2σ, also allows for much lower densities that require additional volatiles. Our simulations, however, rule out a hydrogen-dominated atmosphere, as any primordial H/He envelope would have been rapidly evaporated. Alternatively, compositions that include a high water content could permit such lower densities. For instance, the internal structure models by Zeng et al. [2019] predict that TOI-451 b is also consistent with a water-rich composition with 20%–30% of water by mass. These water-rich worlds, however, must have been born beyond the ice-line, where the water is allowed to condense, and later migrated within the protoplanetary disk to their current orbits. These would include TOI-451 c and d, both of which are further away and must therefore be water-rich too. Additional radial velocity observations are thus required to further constrain the planet's mass and density and discern between the predictions from the different interior models.

Regardless, TOI-451 b demonstrates that simulations of atmospheric escape can potentially be used to identify low density worlds that are inconsistent with a hydrogen-rich atmosphere, and thus differentiate between the two paradigms for the radius valley, i.e. whether it is the migration of water-rich worlds [e.g. Zeng et al., 2019; Luque and Pallé, 2022] or the evaporation of hydrogen-rich worlds [e.g. Owen, 2019] that gives rise to the radius valley.

TOI-451 c

TOI-451 c ($3.1\,\mathrm{R_E}$, $9.1\,\mathrm{d}$) is consistent with being a mini-Neptune above the radius valley with a sizeable gaseous atmosphere consisting of 2.8% of its total mass.

Regarding its past evaporation, where I favoured a faint X-ray emission history, I find that the planet must be at least $6\,\mathrm{M_E}$ in mass to be consistent with photoevaporation, which corresponds to an initial envelope mass fraction of 10% and radius of $5.4\,\mathrm{R_E}$. This scenario, however, may be unattainable due to the action of boil-off processes. Indeed, Owen and Wu [2016] showed that a $5\,\mathrm{M_E}$ core with equilibrium temperatures between 500 K and 1000 K would end up with an envelope mass fraction no greater than 5% after boil-off. If the planet's initial envelope mass fraction were to be lower, though, it would follow a different evolutionary track and no longer match the radius we see in the present day. For that reason, I favour a minimum mass of $7\,\mathrm{M_E}$, which results in an initial radius of $4\,\mathrm{R_E}$with an envelope mass fraction of 5%, consistent with both photoevaporation and boil-off.

My simulations also show the planet's envelope does not survive into the future, as I find the XUV radiation from its host star completely removes the planet's atmosphere within the next 1.5 Gyr, at least for masses below $15\,\mathrm{M_E}$, typical amongst sub-Neptunes. Interestingly, on all my scenarios for the mass of the planet (5–$15\,\mathrm{M_E}$), the evaporated rocky core would be at least $1.7\,\mathrm{R_E}$ in size, placing it either within or above the radius valley.

Regarding its internal structure, even thought its measured mass of $9.2^{+5.5}_{-5.0}\,\mathrm{M_E}$ allows for lower masses down to $4\,\mathrm{M_E}$, my simulations suggest the planet's envelope could only have survived to this day with a mass of at least $7\,\mathrm{M_E}$, consistent within 1σ.

Akin to TOI-451 b, the large uncertainties on the masses allow for a wide range of internal structures. In the case of TOI-451 c, however, most of the values allowed by these uncertainties, including the mean, lie above the minimum mass I predict with my simulations. This suggests that, even though the lower errors on the mass are ruled out by photoevaporation and thus would require water-rich compositions, such scenarios are less likely.

TOI-451 d

TOI-451 d ($4.1\,\mathrm{R_E}$, 16 d) is a Neptune-sized planet with the farthest separation of the three planets in the system. Its 3σ mass upper limit of $16.8\,\mathrm{M_E}$ suggests an envelope mass fraction no lower than 8%. It lies at the upper edge of the population of sub-Neptunes (see Figure 6.1), in a sparsely populated region that bridges the gap with the hot and warm Jupiters at $\geq 10\,\mathrm{R_E}$.

Given its large size and wide orbit, it is expected that the planet's envelope is resistant against evaporation and survives into the future. The simulations show that its sizeable atmosphere would evaporate within 2 Gyr in all scenarios save for the 10 and $15\,\mathrm{M_E}$ cases, consistent with the masses observed for other Neptunes and in agreement with predictions of photoevaporation. Moreover, in these two scenarios, the planet cools down and shrinks into a mini-Neptune with radius $\sim 3 - 3.5\,\mathrm{R_E}$ after the first Gyr.

Regarding its past evolution, where I favoured an X-ray faint irradiation history, the simulations predicted a minimum mass of $6\,\mathrm{M_E}$, which correspond to initial radius of $7\,\mathrm{R_E}$ and mass fraction of 17%. The same arguments for discarding a $6\,\mathrm{M_E}$ scenario on TOI-451 c can be used in this case: once one takes into account boil-off processes, an initial envelope mass fraction of 17% becomes unlikely. Instead, akin to TOI-451 c, I favour a minimum mass of $7\,\mathrm{M_E}$, which imply an initial radius of $5.5\,\mathrm{R_E}$with an envelope mass fraction of 11%. Even at this mass, however, the amount of mass lost via boil-off would not have been negligible, and thus it is more likely that the planet's true mass lies closer to the upper limit of $17\,\mathrm{M_E}$.

Regarding its internal structure, the 3σ mass upper limit of $16.8\,\mathrm{M_E}$ allows for a wide range of internal structures, as is the case for the other two planets in the system. Regardless of the composition of the core, planets of such sizes require hydrogen-dominated atmospheres, even when considering the case of a 100% water core. Indeed, the interior structure models by Zeng et al. [2019] predict a 100% water world with $17\,\mathrm{M_E}$ would have a radius of $3\,\mathrm{R_E}$, falling short of the radius of $4\,\mathrm{R_E}$ that TOI-451 d has. However, if the planet had a lower density core rich in water, its gaseous envelope would be thinner and easier to evaporate, and it might not have survived to the present day, which would rule out such internal structure.

TOI-1098 b

TOI-1098 b ($3.2\,\mathrm{R_E}$, 10.2 d) is a mini-Neptune above the radius valley. It is the only close-in transiting planet orbiting its F8V host star. The planet is similar to

TOI-451 c in size and orbital period, although TOI-1098 b receives a bolometric flux 70% greater, since it orbits a more massive star, which puffs up its atmosphere. On the other hand, TOI-1098 b is also somewhat older, with an age of 250 Myr, and thus the planet has had more time to cool down, shrinking the atmosphere. As a result, the two planets end up having very similar envelope mass fractions of 2-3% for the range of masses I considered in my simulations.

TOI-1098 b, however, lacks mass measurements. In my simulations, I used the same range of masses of 5 to 15 $\mathrm{M_E}$, although, unlike the TOI-451 planets, I am unable to compare my results to any observational constraints on the masses. My simulations suggest the planet requires a mass of at least 8 $\mathrm{M_E}$, and thus any mass below that limit would require a more massive envelope that should have already been evaporated. This limit is greater than the minimum mass of 7 $\mathrm{M_E}$ I determined for TOI-451 c, suggesting TOI-1098 b has experienced a stronger XUV irradiation in its past. Indeed, as revealed by my *XMM-Newton* observations, TOI-1098 is a factor of 1.4 more X-ray luminous than TOI-451 as well as a faster rotator, despite being twice its age. This is likely because TOI-1098 started out with a shorter spin period than TOI-451 (as seen in Figures 6.5 & 6.6) resulting in a stronger X-ray emission during its youth even at its current age of 250 Myr.

Such mass constraints imply initial states for the planet that range from an initial radius of 3.5 $\mathrm{R_E}$ and envelope mass fraction of 3% for a mass of 15 $\mathrm{M_E}$, to radius 5.2 $\mathrm{R_E}$ and envelope fraction 10% for a mass of 8 $\mathrm{M_E}$. Akin to TOI-451 c & d, however, the planet's true mass is likely to be higher than the minimum mass I determined with photoevaporation, given the effects of the boil-off mechanism, which diminish the range of allowed initial envelope mass fractions. As for its future, I find all scenarios are fully evaporated within 1 Gyr, save for the 15 $\mathrm{M_E}$ case, which is evaporated within 2 Gyr.

6.8 Conclusions

In this chapter, I studied the past and future evaporation histories of the atmospheres of four sub-Neptunes in the radius valley. The objective of this work is to assess the impact of the stellar X-ray emission history as well as X-ray driven atmospheric escape on the populations of small close-in exoplanets. TOI-1098 is a late F-dwarf that hosts one transiting super-Earth in the Neptunian desert, and TOI-451 is a late G-dwarf with three transiting planets that straddle the radius valley: a super-Earth followed by two Neptunes-sized planets.

I observed the two stars with the *XMM-Newton* telescope in order to determine their present-day X-ray luminosity and constrain models of their X-ray emission history. The two stars also have M-dwarf companions which are also detected in my *XMM-Newton* observations.

In short, the X-ray activity of TOI-1098 is consistent with predictions from the X-ray evolution models by Johnstone et al. [2021]. TOI-451, however, is a factor of two fainter than predicted. I additionally placed the observations of TOI-451 and its M-dwarf companion in context with cluster stars in the Pleiades, of very similar age. I found that TOI-451 is consistent with other Pleiades G-dwarfs, whilst the models by Johnstone et al. [2021] overpredict their X-ray emission by a factor of 2-3, in agreement with my results from Chapter 5. As such, I favoured an X-ray emission history for TOI-451 where I scaled down the models by Johnstone et al. [2021] by a factor of two to match its observed X-ray luminosity at the present day. As for its M-dwarf companion, I found TOI-451 B to be 5 times brighter than model predictions, and more luminous than most M-dwarfs in the Pleiades, supporting previous evidence that it is not a single star, but instead consists of an unresolved M-dwarf binary.

Using simulations of atmospheric escape, I used these constraints on the stellar X-ray emission to model the past and future evaporation histories of the four planets under a variety of planet masses between 5 and 15 $\mathrm{M_E}$.

I determined that TOI-451 b is most likely a barren rocky core, and any primordial H/He atmosphere would have been readily stripped by either boil-off or photoevaporation in timescales shorter than 20 Myr. I also determined that the other three planets host gaseous atmospheres, as indicated by their large radii and low densities. Using simulations of atmospheric escape, I determined minimum masses for these planets under which their envelopes should have already been stripped before the present day. These are 7 $\mathrm{M_E}$ for TOI-451 b & c, and 8 $\mathrm{M_E}$ for TOI-1098 b.

More generally, I show that photoevaporation is indeed consistent with the shaping the evolution of close-in sub-Neptunes and thus sculpting the radius valley. I have also highlighted the importance of adopting accurate models for the X-ray emission histories of the host stars, and doing so by constraining them with observations from X-ray telescopes.

Chapter 7

Characterising the X-ray variability of FGKM stars with Gaia and XMM-Newton

7.1 Introduction

In Chapter 1 I examined the origin and evolution of the X-ray and EUV emission of main sequence stars (Section 1.4) and discussed how these photons are absorbed in high doses by small close-in planets orbiting these stars (Section 1.3.2), heating up their gaseous atmospheres and driving mass loss which, in some cases, can ultimately strip them of their envelopes. Consequently, this mechanism can carve gaps in the distributions of the masses and radii of these planets, which can be identified in the observed populations of close-in exoplanets in features such as the radius valley and the Neptunian desert (see Section 1.2).

In Chapters 3, 4, and 6 I have presented simulations of the evaporation history of eight planets across four systems. These simulations can not only constrain the internal structures of these planets, but also tell us about their XUV irradiation history and the future fate of their atmospheres. A vital ingredient in these simulations is the X-ray emission history of the host star, i.e. the amount of X-rays the planet receives at each point in its life. As I discussed in Sections 1.4.2 & 1.4.3, the X-ray activities of stars are correlated to their spin period, where faster rotators are more X-ray active. Moreover, as stars spin down with age, their XUV emission also gets fainter.

These rotation-activity relations, however, also present a scatter in the X-ray activity of about an order of magnitude (see Section 1.4.5 and Figure 1.11). The origin of this scatter is still unclear; it has been proposed this scatter arises mainly due to random and/or cyclic X-ray variability [Johnstone et al., 2021], although it can also be explained by stars having intrinsic X-ray activity levels that are consistently higher or lower than predicted by their spin period.

Regardless of which mechanism gives rise to the scatter in the rotation-activity relation, their impact on the evaporation histories of their planetary systems has been seldom explored.

If the scatter originates in intrinsic coronal activity levels, stellar spin period alone is no longer enough to predict the X-ray emission history of a star, and thus models that rely on rotation-activity relations would be systematically overestimating or underestimating the irradiation history of the planets in the system. If for instance a star always lies above the model fit to the rotation-activity relation, then its X-ray emission would be underestimated by the model; however, if it lies below the model fit, then its emission would be overestimated. Indeed, Ho et al. [2024] argued that the shallow depth of the period-radius valley on M-dwarfs could be explained by intrinsic differences in coronal emission between stars.

If, on the other hand, the scatter originates in random variability, the evaporation histories of orbiting planets would instead be impacted by (1) the width of the distribution of the coronal emission of the host star, i.e. the *variability level*, and (2) the response of the planet's atmosphere to these varying activity levels in short (days) and long (years) timescales.

In order to determine the contribution of X-ray variability to the scatter it is necessary to characterise the level of X-ray variability of individual stars. This can be achieved by studying stars that benefit from multiple observations in X-ray wavelengths, and determine to what extent the measured X-ray emission has changed across the different epochs.

The *XMM-Newton* observatory, launched in 1999, has collected X-ray observations of the sky for the past 25 years [Jansen et al., 2001]. Fluxes from X-ray sources in these observations have been compiled into the *4XMM* catalogue, which provides X-ray fluxes for nearly one million sources [Webb et al., 2020]. These X-ray sources, however, may not be of stellar origin. More recently the *Gaia* mission has given us accurate parallaxes and photometry for billions of stars [Gaia Collaboration et al., 2016]. Combining archival observations of the two missions would allow us to identify which X-ray sources are indeed stars as well as their spectral types and their distances, necessary to convert X-ray fluxes to luminosities.

In this chapter, I characterised the X-ray variability of FGKM stars on timescales of days to decades in order to uncover the origin of the scatter in the rotation-activity relation. To do so, I sought stars with multiple X-ray observations by cross-matching the *4XMM* catalogue of *XMM-Newton* observations with the *Gaia* Data Release 3 (DR3) archive.

This chapter is structured as follows: in Section 7.2 I obtained a clean sample of *Gaia DR3* main sequence stars and cross-matched it with sources in the *4XMM* catalogue; in Sections 7.3 & 7.4 I identified the stars in this sample with multiple X-ray observations, characterised their X-ray variability, and assessed its impact on simulations of the evaporation histories of super-Earths and sub-Neptunes. Finally, I concluded with Section 7.5 where I summarise my main results.

7.2 Compilation of the sample

In this section, I lay out the steps for selecting the samples from the *Gaia DR3* and *4XMM* catalogues and how the two are cross-matched to produce a dataset of nearby main sequence stars with X-ray luminosities.

7.2.1 The Gaia archive

I queried a volume-limited sample of stars within 200 pc from the *Gaia DR3* archive. The sample selection I followed for filtering the *Gaia DR3* archive can be summarised in the following steps: (1) querying the Gaia database with a set of selection criteria to collect nearby stellar sources with high quality astrometry, (2) improving the accuracy and quality of the photometry by means of standard photometric corrections and galactic extinction maps, and (3) selecting single stars in the locus of the main sequence.

The selection criteria and quality cuts were aimed at obtaining a reduced sample of main sequence *Gaia* stars with accurate astrometry and photometry, as well as reducing the number of binaries in the sample. Binary stars that are unresolved by *XMM-Newton* will have their individual X-ray emissions combined into a single point source. Since the contributions of each component cannot be disentangled, their individual emission and variability level cannot be constrained. Moreover, close binaries can interact tidally, altering their spin periods and thus their coronal emission [Simonian et al., 2019]; since these binaries cannot host

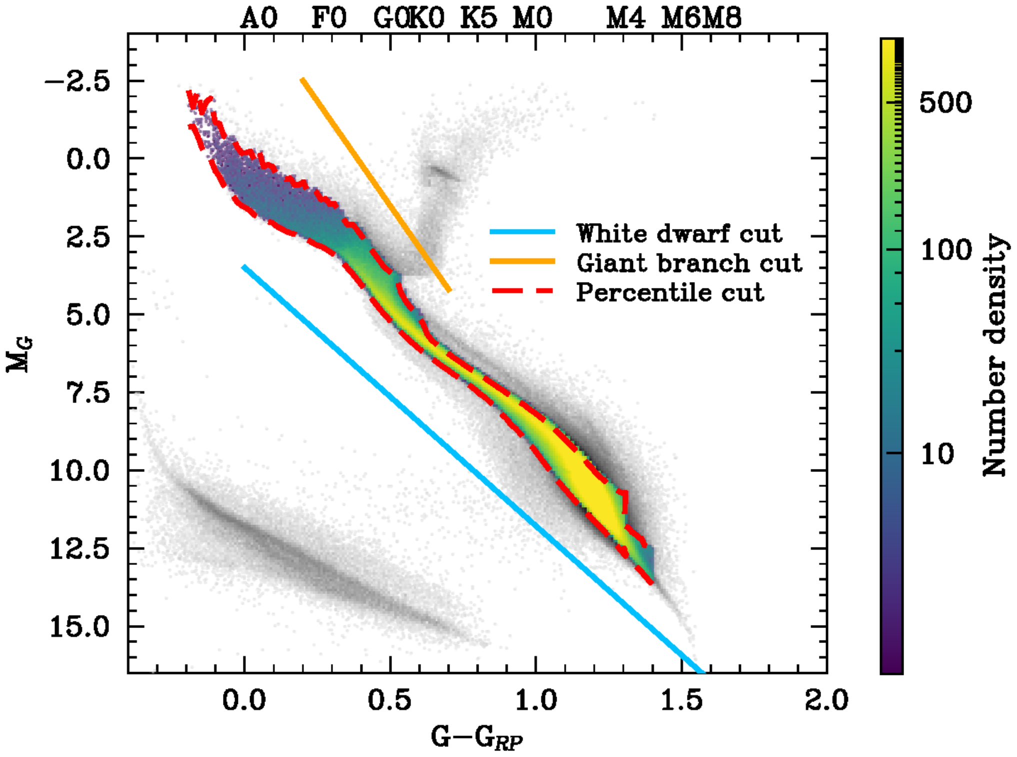

Figure 7.1: **Right panel**: Colour-magnitude diagram of $G - G_{\mathrm{RP}}$ colour against absolute green band magnitude M_{G} of my sample of *Gaia DR3* stars within 200 pc (grey points). I plotted the magnitude cuts I applied to the sample, including the broad cuts for white dwarfs (blue line) and the giant branch (orange line) as well as the cuts to trace the locus of the main sequence (red lines). The resulting main sequence sample is shown in coloured points (blue for low density regions to yellow for high density regions).

close-in planets, their anomalous X-ray emission cannot be used to characterise X-ray evolution histories of planet-hosting stars.

Regarding the distance cut-off of the sample, I chose a limit of 200 pc in order to reduce the number of spurious X-ray matches, since X-ray sources detected by *XMM-Newton* beyond this limit are likely to be too X-ray active to be single stellar sources. This also introduces a strong bias against M-dwarfs at large distances, as these stars, whilst they are typically more X-ray active than FGK dwarfs [e.g. Wright et al., 2018; Johnstone et al., 2021], their X-ray luminosities are also much fainter. This is because their bolometric luminosities are also much lower than that of FGK stars. For instance, an M0V star with an X-ray activity of $L_X/L_{\rm bol} = 10^{-4}$ at a distance of 200 pc would be observed at Earth with an X-ray flux of $5 \times 10^{-15}\,{\rm erg\,cm^{-2}\,s^{-1}}$ (neglecting ISM absorption), close to the detection limit of EPIC-pn of $\sim 10^{-15}\,{\rm erg\,cm^{-2}\,s^{-1}}$ [Webb et al., 2020]. On the other hand, observing an G-dwarf with the same X-ray activity at a distance of 200 pc would result in an X-ray flux at Earth sixteen times brighter. In Section 7.4.2, I characterised the impact of my choice of distance cut-off in the full sample of X-ray emitting stars.

Querying the *Gaia* database

I first queried the *Gaia DR3* database with the following `ADQL` query:

```
SELECT * FROM gaiadr3.gaia_source
WHERE (
    1000/parallax < 200
    AND ruwe < 1.4
    AND parallax_over_error > 20
    AND (
        astrometric_excess_noise_sig <= 2
        OR (astrometric_excess_noise_sig > 2
            AND astrometric_excess_noise <= 1.5)
    )
    AND astrometric_sigma5d_max < 1.5
    AND astrometric_params_solved = 31
)
ORDER BY source_id
```

I selected all sources within a distance of 200 pc, which I determined using inverse parallax. I also discarded sources with inaccurate or inconsistent astrometry, where the error in the parallax is greater than 5% ($p/\delta_p < 20$) and the Renormalised Unit Weight Error (`RUWE`) is high, over 1.4, following [Fabricius et al., 2021b]. `RUWE` encodes the quality of the fit of a single-star astrometric solution on a source, and thus applying a cut-off for high `RUWE` values also removes some unresolved binary systems whose orbital motion induces noise in the astrometric fit. Further quality cuts on the astrometry were achieved with the parameters `astrometric_excess_noise` and `astrometric_sigma5d_max`, following Gentile Fusillo et al. [2021]. The `astrometric_excess_noise` parameter quantifies the disagreement between observations of the location of a source and its best fitting astrometric model, and the `astrometric_sigma5d_max` parameter collects the maximum error in the position, parallax, or proper motion of a source. I also only considered stars with a 5-parameter astrometric solution (`astrometric_params_solved = 31`), where the proper motion has been constrained, and is the standard for stars with good quality photometry and astrometry [Lindegren et al., 2021]. We do not consider 6-parameter astrometric solutions as these are only computed for targets where high-quality colour information is not available. After applying the selection criteria, I arrived at a sample of 1,316,469 *Gaia* sources.

Photometric corrections

I then applied quality cuts to the photometry of the remaining sources, namely the *Gaia* G, $G_{\rm BP}$, and $G_{\rm RP}$ magnitudes. I calculated the error on the $G_{\rm BP} - G_{\rm RP}$ color with the method of Riello et al. [2021] and discarded sources with errors larger than 0.06 mag[1]. I additionally adopted the recipes by Riello et al. [2021] to calculate corrected $G_{\rm BP} - G_{\rm RP}$ excess factors as well as their expected 1σ scatter for well-behaved stars with standard photometry. Photometric excess factors measure the disagreement between the sum of integrated $G_{\rm BP}$ and $G_{\rm RP}$ fluxes with respect to the flux in the G band. Following Gentile Fusillo et al. [2021], I removed sources whose corrected excess factors exceeded the 1σ scatter by a factor greater than 5, hence arriving at a sample containing 1,227,085 Gaia sources.

I accounted for interstellar extinction by using the 3D extinction map by Edenhofer et al. [2024] available via the Python module `dustmaps`[2], which is valid

---

[1] I calculated the color corrections using the code by Anthony G.A. Brown available at `https://github.com/agabrown/gaiaedr3-flux-excess-correction`

[2] The `dustmaps` source code is available at `https://github.com/gregreen/dustmaps`

for sources between 69 pc and 1.2 kpc away from Earth. For sources closer than 69 pc, I applied no corrections. At this distance, the map predicts G-band extinction values under 0.05 mag and $G_{\rm BP} - G_{\rm RP}$ reddening under 0.025 mag, both of which lie under the magnitude uncertainty cut-off of 0.06 mag I adopted earlier.

The locus of the main sequence

I plotted the Hertzsprung-Russel (HR) diagram of the resulting sample of *Gaia* stars in Figure 7.1, which shows the main sequence along with populations of white dwarfs and evolved stars in the giant branch.

In order to further refine the sample of *Gaia* stars, I further limited the sample to stars in the locus of the main sequence. I first calculated the absolute magnitude on the Gaia band $\rm M_G$ of the stars using their parallaxes. I applied wide cuts on the HR diagram to remove white dwarfs and stars on the giant branch, as seen in Figure 7.1 (blue and orange lines). For white dwarfs, I filtered the sample with the expression $M_G < 8.29 \times (G - G_{\rm RP}) + 3.5$ applied to the entire range of $G - G_{\rm RP}$, and for evolved stars on the red giant branch with expression $(G - G_{\rm RP}) < 0.075 \times M_G - 0.39$ only for $-2.5 < M_G < 4.2$ whilst keeping all other stars outside this M_G range.

I then traced the locus of the main sequence by dividing up the resulting sample into fine $G - G_{\rm RP}$ bins, collecting the distribution of $\rm M_G$ on each bin, and shaving off points beyond the 5th and 95th (2σ) percentiles. For later-type stars with $G - G_{\rm RP} > 1.3$ (later than M4.5), due to the reduced number of points and broader M_G distribution, I adopted wider $G - G_{\rm RP}$ bins and cut-offs at the 32nd (1σ) and 95th (2σ) percentiles instead.

This method also removes the population of K & early M dwarfs that lie parallel to the main sequence in the HR diagram but above it, offset by $\Delta M_{\rm G} \sim 0.65$ mag [Simonian et al., 2019]. These stars are likely binaries that are unresolved by *Gaia*, whose individual luminosities combine to appear as brighter single stars [Gaia Collaboration et al., 2018a]. Since these binary systems are unresolved by *Gaia*, they will also be unresolved in *XMM-Newton* observations, as the latter has a lower angular resolution [Lindegren et al., 2021; Webb et al., 2020].

For that same reason, I additionally discarded *Gaia* stars from the sample that are close enough to one another to be unresolved in *XMM-Newton* observations, but still resolved by *Gaia*. To do so, I identified *Gaia* stars in my sample that were separated by less than 16 arcseconds, which corresponds to the half-

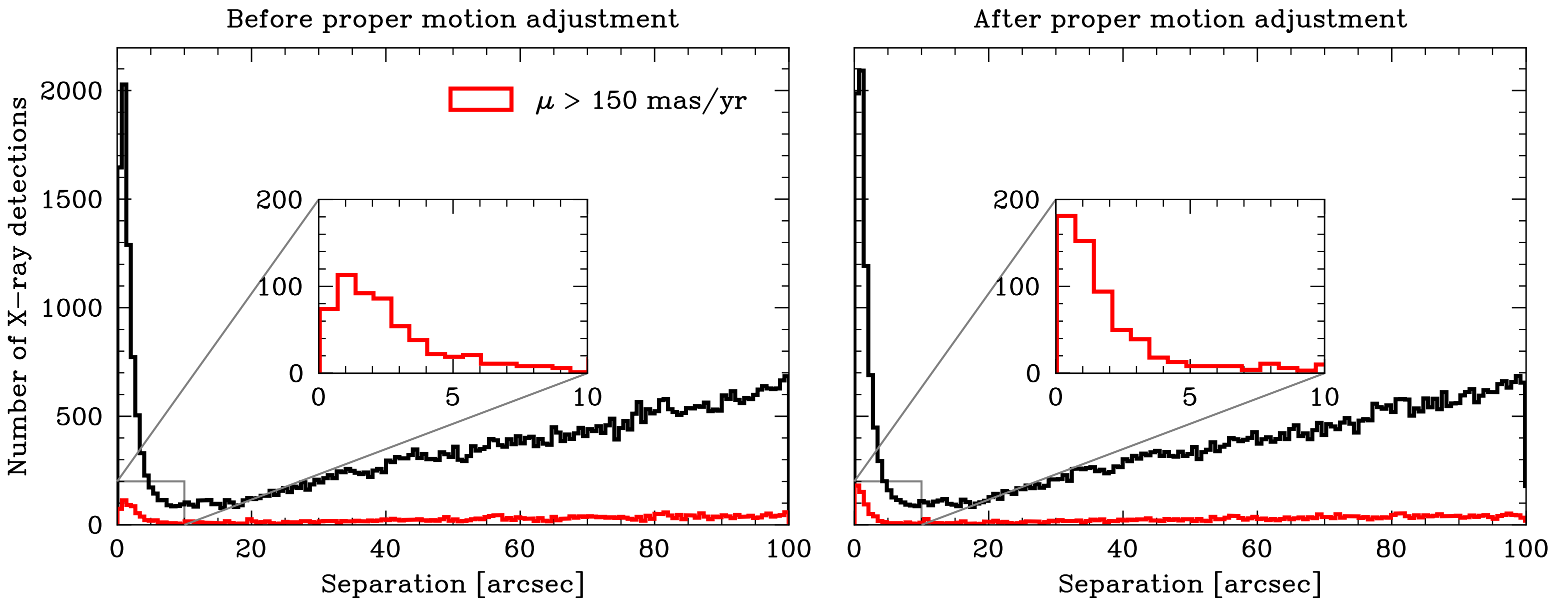

Figure 7.2: **Right panel**: Histogram of the separations between Gaia sources and their corresponding X-ray detections within 100 arcseconds. The Gaia sources with the highest proper motion ($\mu > 150\,\mathrm{mas\ yr^{-1}}$) are highlighted in red. **Left panel**: Following the right panel, histogram of separations between Gaia and 4XMM sources where the Gaia positions have been adjusted for the proper motion drift since the date of the X-ray observation.

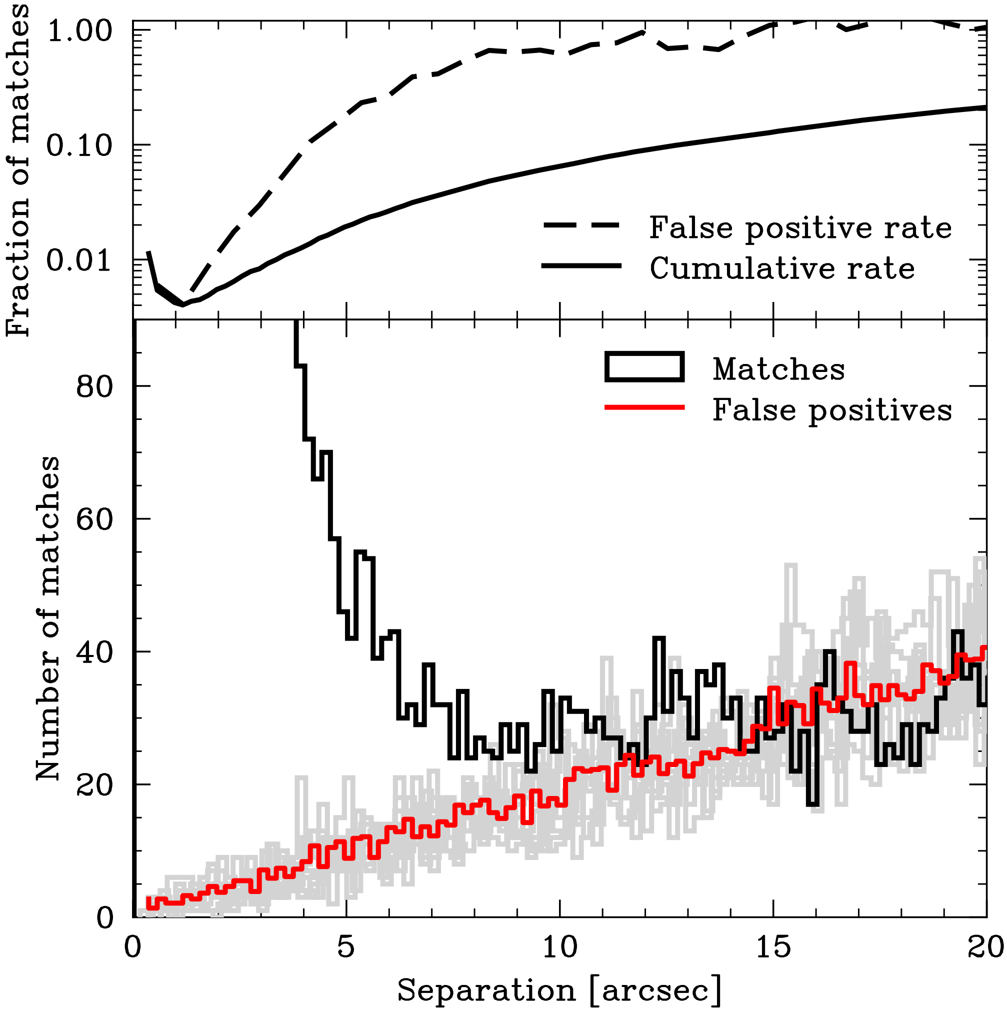

Figure 7.3: **Top**: False positive rate in the matches between Gaia sources and their 4XMM counterparts as a function of angular separation. The false positive rate on each bin is shown as a dashed line, and the cumulative rate as a solid line. **Bottom**: Histogram of angular separations between the positions of Gaia and 4XMM sources within 20 arcseconds (black). The same separations were plotted with Gaia sources shifted in position by ±1 degrees in right ascension and declination (grey lines), showing no peak at close-in separation and only a slope of false positives. The mean of these shifted datasets is shown as a red line.

energy width (HEW) of the EPIC-pn instrument onboard *XMM-Newton* [Strüder et al., 2001]. These close sources added up to 37,332 pairs and 114 triplets, which I removed. In principle, it may be possible to assign the X-ray flux to one of the blended sources on a probabilistic basis, and in future work this may be beneficial in particular for stars in crowded regions of clusters. Such objects are of particular value because stellar ages can be determined. After rejecting close objects, I arrived at a sample of 980,693 *bona-fide* main sequence single *Gaia* stars with accurate photometry and astrometry, which I plotted in Figure 7.1.

7.2.2 The *4XMM* catalogue

The *4XMM* DR13 catalogue [Webb et al., 2020] contains 983,948 rows, each representing a single X-ray detection of a point source in a given *XMM-Newton* observation. Detections in this catalogue were collected by identifying point sources on each *XMM-Newton* observation with a sliding box algorithm using search windows $20'' \times 20''$ in size, where a search box is slid across the image and a model is fitted to each source in the image comparing their counts with the expected background level. Moreover, the X-ray fluxes were calculated from the count rates using the standard energy conversion factors (ECFs), which assume a power-law spectral model at a constant hydrogen column density of $n_H = 3 \times 10^{20}\,\mathrm{cm}^{-2}$. I described the *4XMM* catalogue further in detail in Section 2.4.1.

I first removed X-ray detections from the *4XMM* catalogue whose EPIC-pn data was unavailable (count rates are `NaN` or zero), reducing the number of X-ray detections in the dataset to 819,444. The catalogue also contains information about the quality of each detection and the region within the pointing where it lies, including whether it lies close to the edge of the detector or close to another bright source. These flags are summarised in the column `PN_FLAG`. In Sections 7.3 and 7.4, I assess the impact of filtering *4XMM* detections using these flags.

7.2.3 The Gaia-XMM dataset

I cross-matched our selection of sources from *Gaia DR3* with the full *4XMM* DR13 catalogue using the software `STILTS/TOPCAT` [Taylor, 2005], initially adopting a separation cut-off of 100 arcseconds in order to capture all possible matches.

The positions of all sources in the *Gaia DR3* archive are provided in the J2016 epoch, whilst the positions of sources in the *4XMM* catalogue are in the epoch in which they were observed. As a result, stars that have undergone significant proper motion between the two epochs will present a mismatch between their locations as observed by *XMM-Newton* and *Gaia*. I accounted for this mismatch by computing the angular distance each *4XMM* source has travelled across the sky in the time passed between its X-ray observation and the *Gaia* epoch, and then comparing its *adjusted* position with the location of the closest *Gaia DR3* source.

I plotted the histogram of separations between Gaia and X-ray sources in Figure 7.2 before and after the proper motion adjustment on the left and right panels, respectively. I found that this adjustment resulted in an improved match rate, increasing the number of matches within 1" by 12%. This is especially impactful on the stars with the highest proper motions ($\mu > 250\,\mathrm{mas\,yr^{-1}}$), with an increase of 89% within 1".

Finally, in order to remove spurious matches, I applied a separation cutoff between *4XMM* and *Gaia* sources. In order to inform my choice of separation cutoff, I computed the false positive rate of the matches as a function of separation. The false positive matches are seen in Figure 7.2 as a constant increase in matches at separations over 20 arcseconds. This slope can also be reproduced by matching against a set of points placed randomly in the sky. I separated the peak of true positives (seen at small separations) from the slope of false positives by shifting the positions of the *Gaia* stars by one degree in both right ascension and declination, and cross-matching these shifted datasets with the *4XMM* dataset. I plotted the resulting histogram of the separations of false positive matches in Figure 7.3.

I adopted a separation cutoff of 5 arcseconds, which corresponds to a false positive rate of 20% at that separation and a total cumulative false positive rate of 2% within that limit. After applying this separation cutoff, the resulting cross-matched dataset amounted to 4,421 *Gaia* stars with X-ray detections and a total of 6,787 *XMM-Newton* detections, including 1,000 stars with multiple X-ray detections.

7.3 Characterising X-ray variability

In this section, I studied the dataset of *Gaia* stars with *XMM-Newton* observations I have assembled and their X-ray variability. This involves measuring how much the X-ray emission of individual stars changes over time, which requires stars with multiple X-ray detections.

In Figure 7.4, I plotted the X-ray activities all stars in the sample that benefit from multiple X-ray detections, highlighting those with at least 10 detections.

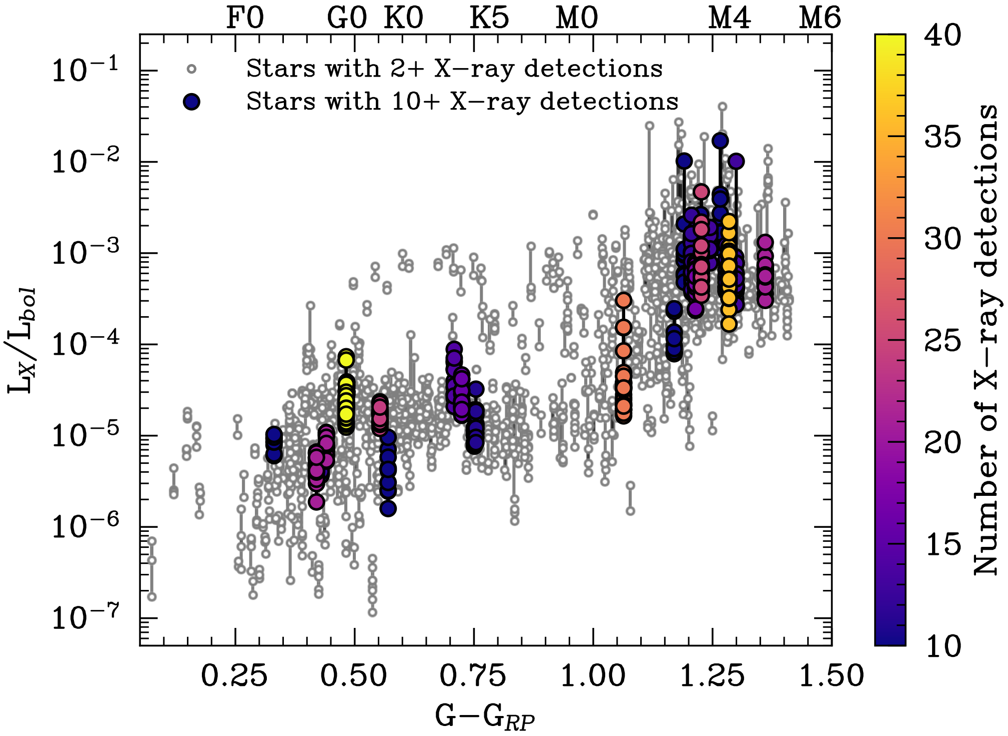

Figure 7.4: Gaia colour index G-G_{RP} against X-ray activity for stars in our sample with multiple X-ray observations. Those with at least 10 X-ray detections have been highlighted.

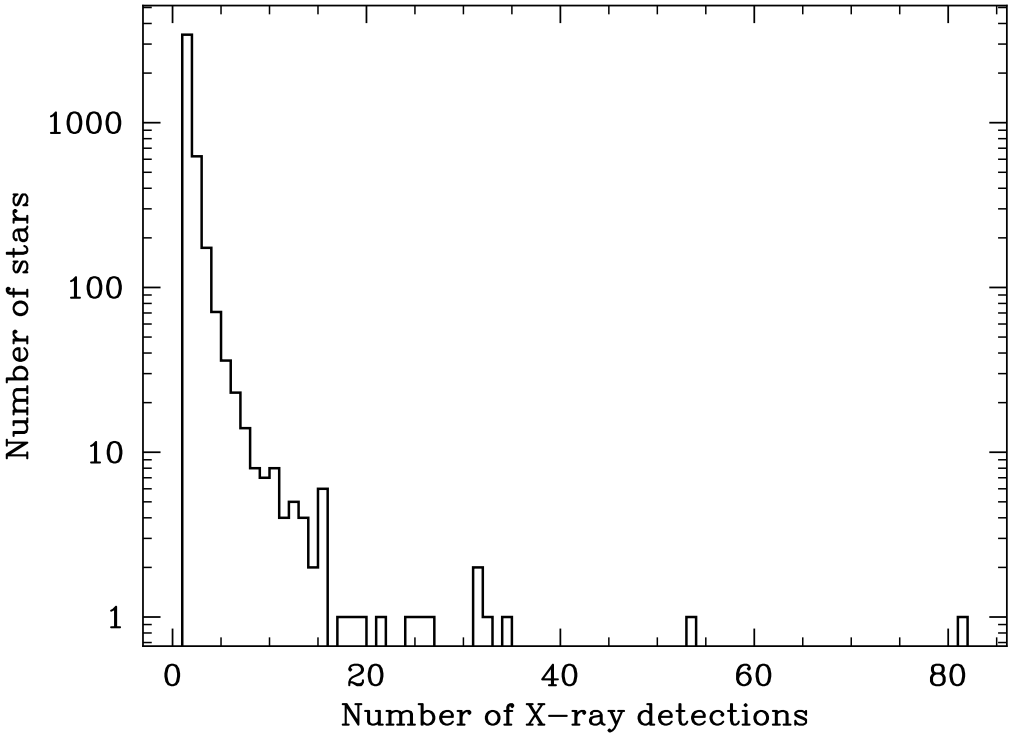

Figure 7.5: Distribution of the number of X-ray detections of individual stars.

This demonstrates that stars with both few and many X-ray detections are well sampled across spectral types ranging from early F to mid-late M. Moreover, Figure 7.4 shows that stars with the same spectral type have different overall activity levels, which is likely to be caused by different ages or spin periods: those stars that are young and spin rapidly will be on average more X-ray active than those that are older and spin more slowly, as I discussed in Sections 1.4.3 & 1.4.2. This also implies that the X-ray activities of stars cannot be directly compared to one another, as their ages and spin periods could be different.

I further plotted the distribution of the number of X-ray observations per star in Figure 7.5, which shows that the majority of stars only have a few detections in the X-rays, and only a handful have more than 20. The most populous bin consists of those stars that have only been detected in the X-rays once, consisting of 77% of all stars in the dataset. Amongst those with multiple X-ray detections, 90% (905 stars) have 5 X-ray detections or less and 62% (625 stars) have only two. In contrast, only 10 stars have at least 20 detections (1% of the sample) and only 34 stars have more than 10 detections (3.4% of the sample).

Figure 7.5 therefore highlights two populations of stars in the dataset: a group of few stars with many X-ray detections, which I define as those with at least 10 X-ray detections, and a group of many stars with few X-ray detections, which have fewer than 10.

These two populations require two separate analyses. Stars that have many detections across long timescales can be studied on their own, and their variability determined directly simply by computing the standard deviation of their X-ray emission, which I compute in Section 7.3.1 below.

For stars with less than 10 detections, however, X-ray variability cannot be directly computed on individual stars reliably, as they have too few detections, or by combining the X-ray luminosities of different stars, as they might have intrinsically different activity levels. Instead, we can compute how much the X-ray emission has changed between detections of the each star (by taking the ratios of X-ray measurements) and combine these instead across multiple stars (which I assumed have the same overall variability, even if their activity levels differ) to obtain an overall estimate of the X-ray variability at the population level. I carry out this analysis in Section 7.3.2 below.

7.3.1 X-ray variability of individual stars

In the dataset, there are 42 stars which benefit from at least 10 X-ray detections with *XMM-Newton*. In Figure 7.6 (top panels), I plotted the distribution of X-ray luminosities of the five FGK stars with most X-ray observations. These correspond to three late F dwarfs, one late G dwarf, and one K dwarf. Similarly, in Figure 7.7 (top panels), I plotted the same figures for the top five M-dwarfs with most X-ray observations, all early to mid M-dwarfs (M2–M5).

I then computed the individual variability levels of these stars by assuming stellar X-ray emission tends to follow a normal distribution in log X-ray luminosity space, akin to the distribution of the X-ray scatter observed in the rotation-activity relation, following [Johnstone et al., 2021] which determined its standard deviation to be $\sigma = 0.36$ from the sample of stars by Wright et al. [2011]. The X-ray variability of an individual star can thus be characterised by computing the standard deviation of its distribution of measured X-ray luminosities in log space.

I therefore found that the five FGK stars in Figure 7.6 present variability levels ranging from $\sigma = 0.06$ to 0.18, which correspond to a factor of 1.14 to 1.52 in X-ray luminosity, whereas the five M-dwarfs in Figure 7.7 range from $\sigma = 0.19$ to 0.34, which correspond to a factor of 1.54 to 2.18 in X-ray luminosity. Moreover, in Figure 7.8, I plotted the variability levels of all stars with 10+ X-ray observations against their weighted mean X-ray activities. As seen, two distinct stellar populations can be identified. Whilst all FGK stars have low X-ray activities below $L_X/L_{\text{bol}} < 4 \times 10^{-5}$ and present variability levels no greater than $\sigma = 0.25$, M-dwarfs are more active, with $L_X/L_{\text{bol}} > 10^{-4}$, and also present greater variability levels, spanning $\sigma = 0.2$ to 0.55. These figures therefore demonstrate a contrast between both stellar populations, with M-dwarfs being on average 40% more variable than FGK stars, although there is also evidence for stars with the same spectral types presenting moderately different variability levels.

In the same manner, I then computed the variability levels of all stars with at least 10 X-ray detections, arriving at $\sigma_{\text{FG}} = 0.13 \pm 0.06$ for F & G dwarfs, $\sigma_{\text{K}} = 0.20 \pm 0.08$ for K-dwarfs, and $\sigma_{\text{M}} = 0.35 \pm 0.12$ for M-dwarfs, which highlights a discrepancy between FG stars and M-dwarfs, where M-dwarfs are around 40% more variable. Moreover, I also noted a tentative increased variability level for K-dwarfs relative to F & G stars, hinting at a trend of increasing X-ray variability with decreasing stellar mass. I note that the observed effect is the opposite of that expected from the Malmquist bias, which would tend to make M-dwarfs appear less variable because they are inherently less luminous and hence tend to be undetectable when fainter than average.

7.3.2 X-ray variability of stellar populations

The dataset also contains 958 stars that have between two and nine X-ray detections. Since they have too few detections to compute their individual variability directly, only the overall variability at the population level can be computed.

For a given star, I took a pair of its X-ray detections; I then calculated the *variability level* from the ratio of the two X-ray luminosities, and the *variability timescale* from the time passed between the dates of the two observations. This provides an estimate of how much the coronal emission has changed between the two observations. I then repeated this procedure for all unique pairs of X-ray detections of the star, resulting in a set of *variability data points*, which yields information on how the star's coronal emission varies on both short and long timescales.

The number of such data points that a star can yield is equivalent to the binomial formula $\binom{n}{k}$ with $k = 2$, since we are counting all unique *pairs* of X-ray detections, and thus $n(n-1)/2$ variability data points, where n is the number of X-ray detections. Therefore, a star with two X-ray detections yields one variability point, and another with three detections yields three variability points. If we increase this to 10 X-ray detections, the number of variability points jumps to 45. Indeed, the number of variability points scales with n^2, and thus stars with many X-ray detections will offer much more information on their variability than stars with few detections.

Moreover, assuming the X-ray emission of a star follows a normal distribution in $\log_{10} \mathrm{L_X}$ space, then the variability level I defined earlier as the ratio between two X-ray measurements, would thus correspond to their difference in log space (since $\log_{10} a/b = \log_{10} a - \log_{10} b$). If we take many pairs of measurements of $\log_{10} \mathrm{L_X}$ of a star's X-ray emission, and calculate the differences in each pair, the resulting distribution will also be normally distributed but with two important properties: (1) the standard deviation will remain the same and (2) the mean will always be zero. If we then take a pair of measurements of the X-ray emission of many stars, each with a different mean X-ray emission but with the same X-ray variability level, and once again calculate the difference in each pair, the resulting distribution will also have mean zero and a standard deviation equal to the X-ray

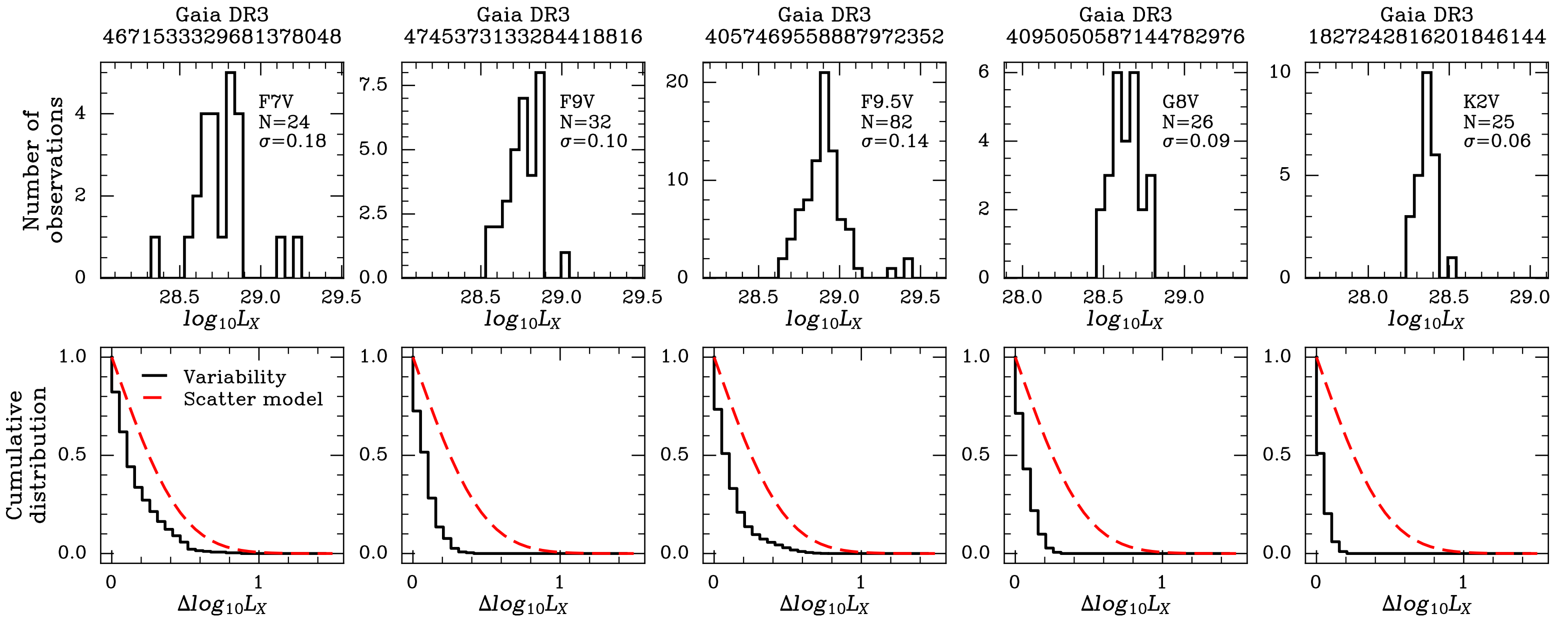

Figure 7.6: **Top panels:** distributions of the X-ray luminosities of the FGK stars with the largest number of X-ray observations in our sample. **Bottom panels:** cumulative distributions of the variability levels of the five stars in the top panels (black lines) compared to the scatter in the rotation-activity relation (red line).

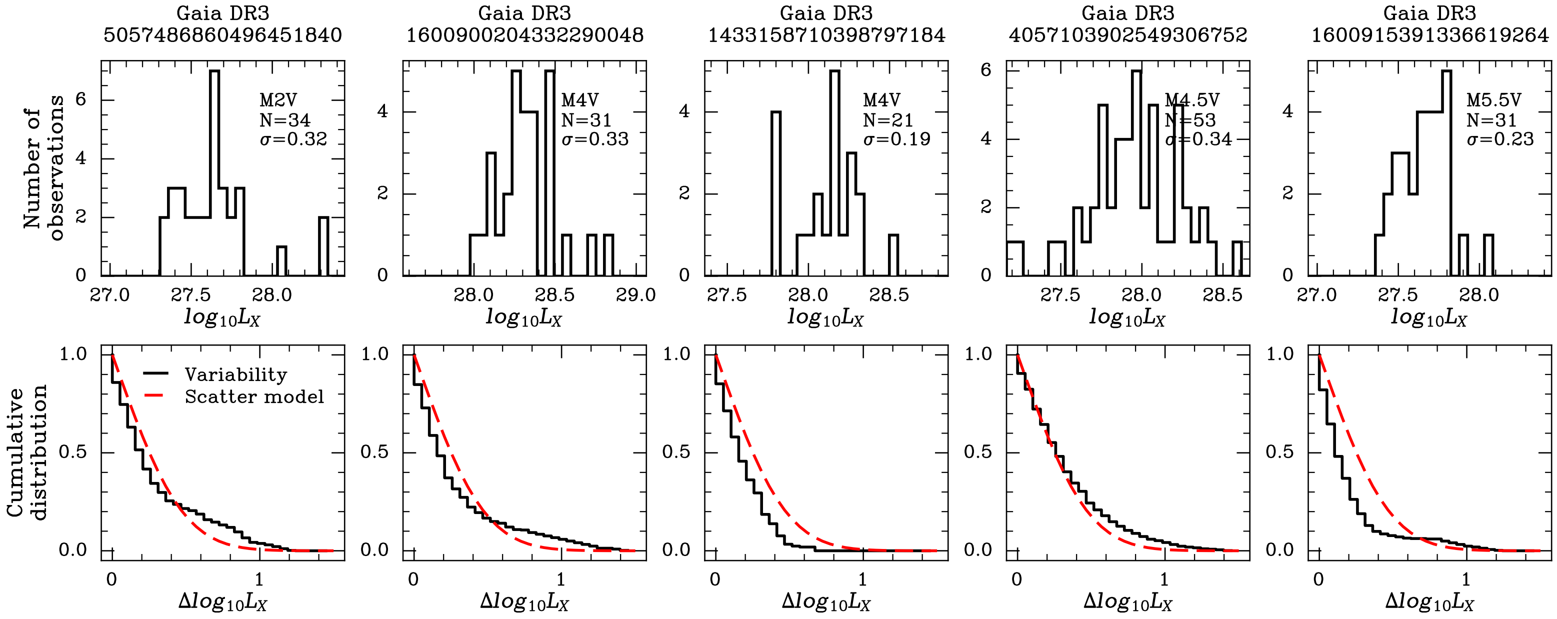

Figure 7.7: Following Figure 7.6, the distributions of the X-ray luminosities (top panels) and variability levels (bottom panels) of the five M-dwarfs in our sample with the most X-ray observations.

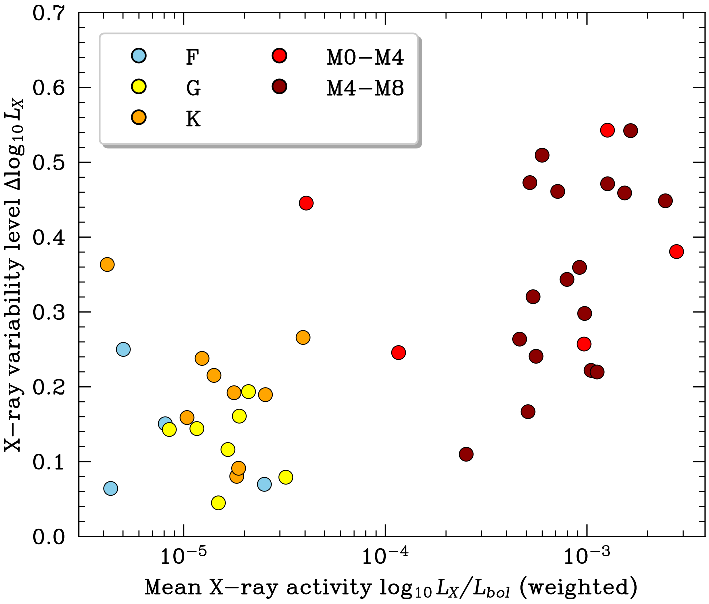

Figure 7.8: Weighted mean X-ray activity against X-ray variability level of stars in my sample with at least 10 X-ray observations, with colour indicating the spectral type.

variability of the population. This implies that we can study the X-ray variability of multiple stars together as long as they have the same X-ray variability (the same standard deviation in their X-ray emission), regardless of their individual average activities. In practice, for stars with few X-ray observations, we do not know *a priori* whether they share the same variability level, and thus we must make assumptions linking it to, for instance, spectral type or overall activity level.

I first applied this analysis to individual stars with many observations I introduced in Section 7.3.1. In Figures 7.6 and 7.6 (bottom panels), I plotted cumulative distributions of the variability levels of individual FGK and M stars with the largest number of detections in the dataset. The width of this distribution is a measure of the overall X-ray variability of the star. In comparison, I also plotted the scatter in the rotation-activity relation as measured by Johnstone et al. [2021] as a red line. Indeed, as I determined in Section 7.3.1, the distributions of the five FGK stars in Figure 7.6 (bottom panels) are much narrower than the X-ray scatter and thus less variable. On the other hand, the distributions of the five M-dwarfs in Figure 7.7 (bottom panels) are for the most part as wide as the X-ray scatter, and thus have an X-ray variability that matches this scatter.

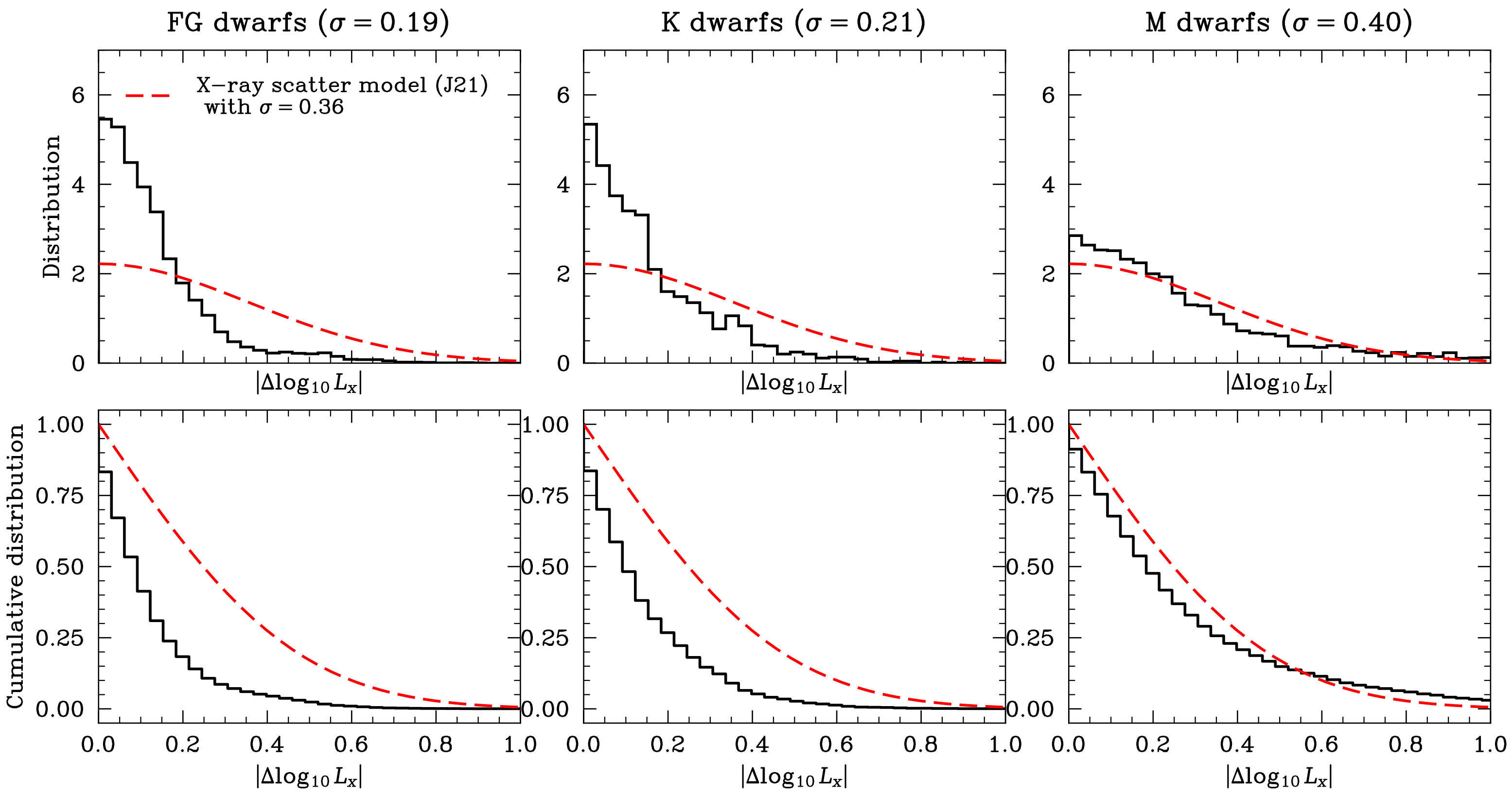

Figure 7.9: **Top panels:** distributions of the changes in X-ray luminosity across all observations of individual stars for FG dwarfs (left column), K-dwarfs (middle column), and M-dwarfs (right column). These changes are quantified as the difference of the log X-ray luminosities of pairs of X-ray detections of every star. **Bottom panels:** reverse cumulative distributions of the data in the top panels.

I then expanded this analysis to stars with fewer than 10 X-ray detections in order to reveal trends at the population level. In order to highlight differences across spectral types, I analysed F & G, K, and M-dwarfs separately. I combined F and G dwarfs into a single group to maximise the number of data points in comparison with the K and M dwarfs. I thus calculated variability data points for these stars individually and then combined them into histograms of $\Delta \log_{10} \mathrm{L_X}$, where the standard deviation reveals the overall X-ray variability of each population of stars. Figure 7.9 shows such histograms for F & G dwarfs, K-dwarfs, and M-dwarfs separately in comparison with the X-ray scatter of the rotation-activity relation by Johnstone et al. [2021]. I thus determined that, for stars with fewer than 10 X-ray detections, F & G stars present a variability level of $\sigma = 0.21$ (a factor of 1.62), K-dwarfs have $\sigma = 0.22$ (a factor of 1.66), and lastly M-dwarfs have $\sigma = 0.34$ (a factor of 2.19). These results indicate that FGK stars have similar overall variability levels that are 35% lower than M-dwarfs, in agreement with the X-ray variability of individual stars with at least 10 X-ray detections I determined in Section 7.3.1. Since both groups have similar variability levels, I repeated this analysis on the entire dataset, and thus determined variability levels of $\sigma = 0.19$ for F & G stars (a factor of 1.55), $\sigma = 0.21$ for K-dwarfs (a factor of 1.62), and $\sigma = 0.40$ for M-dwarfs (a factor of 2.50).

Finally, I repeated the variability analysis on a sample of stars where I required the `PN_FLAG` column to be zero in the *4XMM* catalogue, which removes the X-ray detections that may be more likely to be spurious, as described in Section 7.2.2. The results of the variability analysis are plotted in Figure 7.13, which is consistent with my previous results, showing that FGK stars are less X-ray variable than M-dwarfs as well, with variability levels of $\sigma = 0.18$, 0.22, and 0.34, for F & G, K, and M-dwarfs, respectively.

7.3.3 Timescales of variability

I further studied the dependence of X-ray variability on timescale – whether the overall variability originates in short-term (days and weeks) or long-term (months and years) variation in X-ray luminosity. Figure 7.10 shows the distribution of the timescales between pairs of X-ray observations for all stars in the dataset as well as stars with fewer X-ray detections. As seen, timescales between observations from days to decades are all well sampled in the dataset, with observations separated by one to ten years being more frequent than those separated by days to weeks.

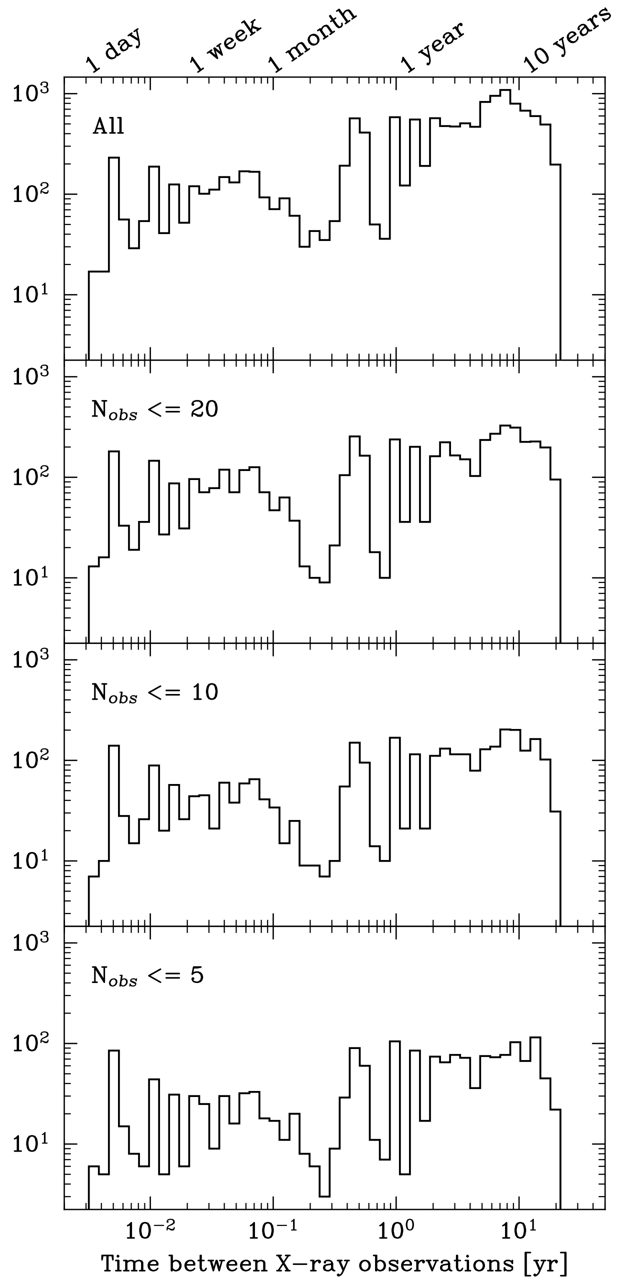

Figure 7.10: Histograms of the time passed between *XMM-Newton* detections of individual stars. The top panel shows such distribution including all stars in the sample, whereas the panels below show distributions including stars with no more than 20, 10, and 5 X-ray detections, from top to bottom, respectively.

Additionally, in Figure 7.11, I plotted the distribution of variability levels for pairs of X-ray observations separated by days, weeks, months, years, and decades (top panels), and its corresponding cumulative distribution (bottom panels).

I found that, in the case of F & G stars, their variability increases from $\sigma = 0.14$ for timescales shorter that a month to $\sigma = 0.19$ at timescale greater than five years. K-dwarfs, on the other hand, reach their maximum variability level of $\sigma = 0.22$ in less than a month, showing only a marginal increase in variability across years and decades. Finally, M-dwarfs reach a variability of $\sigma = 0.35$ in less than a month which increases to $\sigma = 0.41$ for timescales longer than 5 years. These results imply that the bulk of the variability is reached in timescales shorter than a month, particularly for K-dwarfs; whilst the greatest increase in monthly to decade timescales is seen on F & G dwarfs.

Finally, in Figure 7.12, I additionally plotted the standard deviations of these distributions as a function of variability timescale, which highlights (1) the stark difference between the variability levels of M-dwarfs and FGK stars, and (2) a tentative increase of the variability level with timescale, as noted in Figure 7.11.

7.3.4 Dependence on X-ray activity

Figure 7.2 highlights two populations in the dataset: M-dwarfs which tend to be more active (with $\log L_{\mathrm{X}}/L_{\mathrm{bol}} = -3.0$) and FGK stars which tend to be less active (with $\log L_{\mathrm{X}}/L_{\mathrm{bol}} = -5$). This could be a result of M-dwarfs remaining X-ray saturated for much longer than FGK stars, which rapidly spin down and become unsaturated whilst still young [e.g. Tu et al., 2015; Johnstone et al., 2021]. I therefore, studied a possible link between X-ray variability and overall activity level that is independent of spectral type. To do so, I sought to find differences in X-ray variability on active and inactive FGK stars separately from M-dwarfs.

I considered stars in the dataset with at least 5 X-ray detections, and computed their population-level X-ray variability of active and inactive stars separately. I determined thresholds for low and high activities by computing the 32nd and 68th (1-sigma) percentiles of the distribution of $\log L_{\mathrm{X}}/L_{\mathrm{bol}}$, respectively, such that *low-activity* stars are those with X-ray activities below the 32nd percentile, and *high-activity* stars are those with activities greater than the 68th percentile.

For FGK stars, these thresholds corresponded to $\log L_{\mathrm{X}}/L_{\mathrm{bol}} = -5.1$ and -4.7, for the low and high activity thresholds, respectively, and for M-dwarfs, $\log L_{\mathrm{X}}/L_{\mathrm{bol}} = -3.3$ and -3.0, respectively. I found that FGK stars have X-ray variability levels of $\sigma = 0.21 \pm 0.12$ and $\sigma = 0.16 \pm 0.09$ for the *low-activity* and *high-activity* populations, respectively, suggesting a tentative preference for increased variability on low-activity FGK dwarfs.

On the other hand, M-dwarfs presented X-ray variability levels of $\sigma = 0.24 \pm 0.14$ and $\sigma = 0.36 \pm 0.12$ for the *low-activity* and *high-activity* cases, respectively. For M-dwarfs, the trend is opposite to that of FGK stars, where high activity M-dwarfs have a preference for higher X-ray variability. This suggests X-ray variability could be linked to the overall X-ray activity of M-dwarfs, where high activity stars are more variable as a result of, for instance, increased flare rate and flare energies.

In both populations of FGK and M-dwarfs, however, the X-ray variability levels of both the low and high activity stars agree within 1σ, and thus I was unable to find statistically significant evidence for differences in X-ray variability as a function of X-ray activity within stars of the same spectral type. In the case of M-dwarfs, it's possible that less active ones appear less variable because they are close to the detection limit of *XMM-Newton* such that they are no longer detected during inactive periods, cutting off the lower end of their variability distribution.

7.4 Discussion

7.4.1 X-ray variability

Relations between the X-ray activity of stars and their spin periods present a large scatter in the X-ray flux of about one order of magnitude each way. This scatter has been suggested to originate in short-term stellar X-ray variability [Tu et al., 2015; Johnstone et al., 2021]. In this chapter, I characterised the X-ray variability of individual FGKM stars in order to determine their contribution to the observed scatter.

In Section 7.2.3 I compiled a dataset of 1,000 FGKM stars in Gaia DR3 with multiple X-ray detections from *XMM-Newton* across 25 years of observations, and in Section 7.3 I determined their level of variability in the X-rays by measuring how much their coronal emission changes between observations.

Moreover, the sample I compiled contained many stars with few X-ray detections, which allowed for a population-level analysis, as well as few stars with many X-ray observations, which allowed for an individualised characterisation of their X-ray variability.

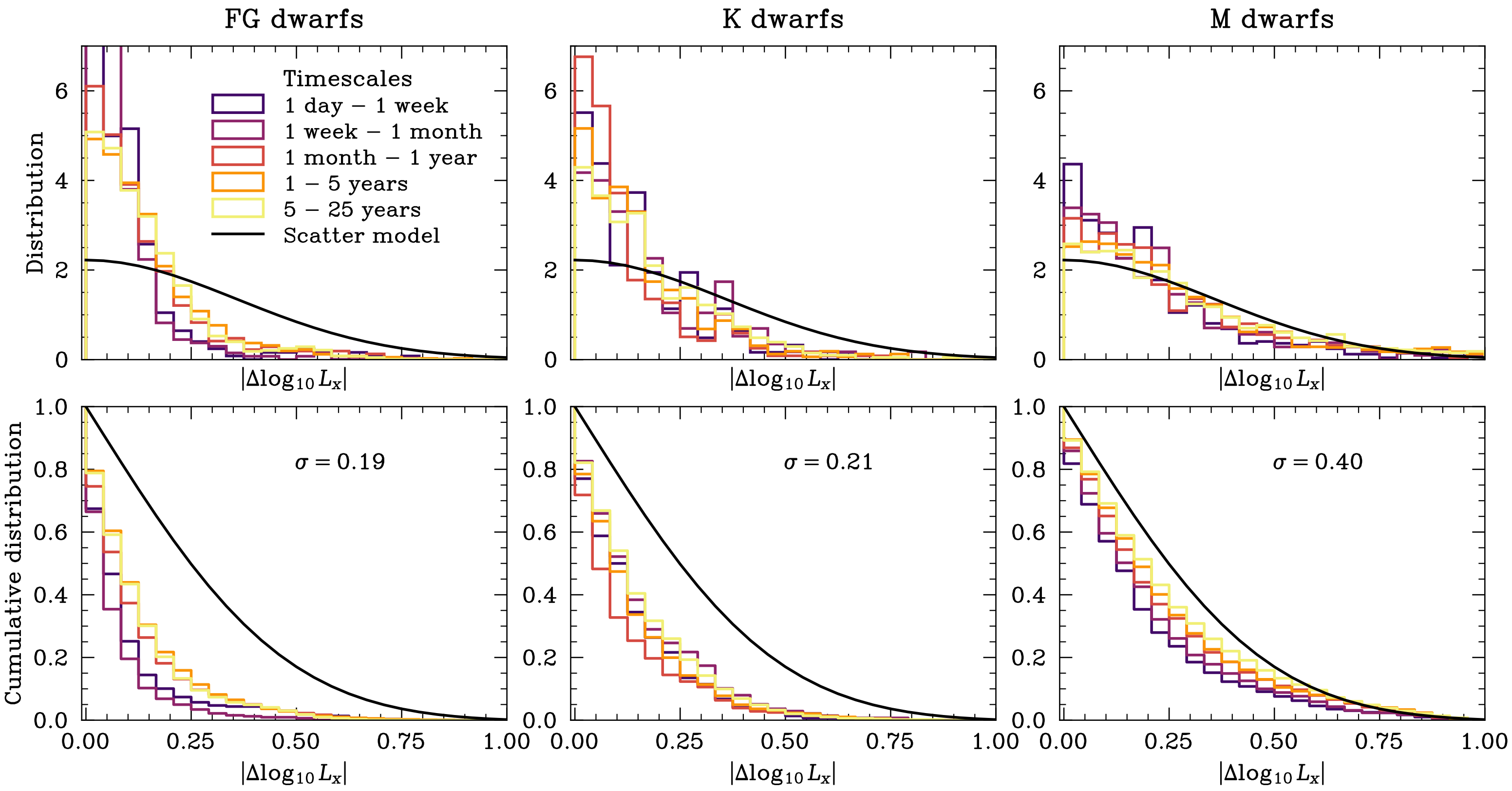

Figure 7.11: Histograms of the X-ray variability levels of F & G, K, and M dwarfs in the dataset, following Figure 7.9, highlighting the measured variability on a range of timescales from days to decades.

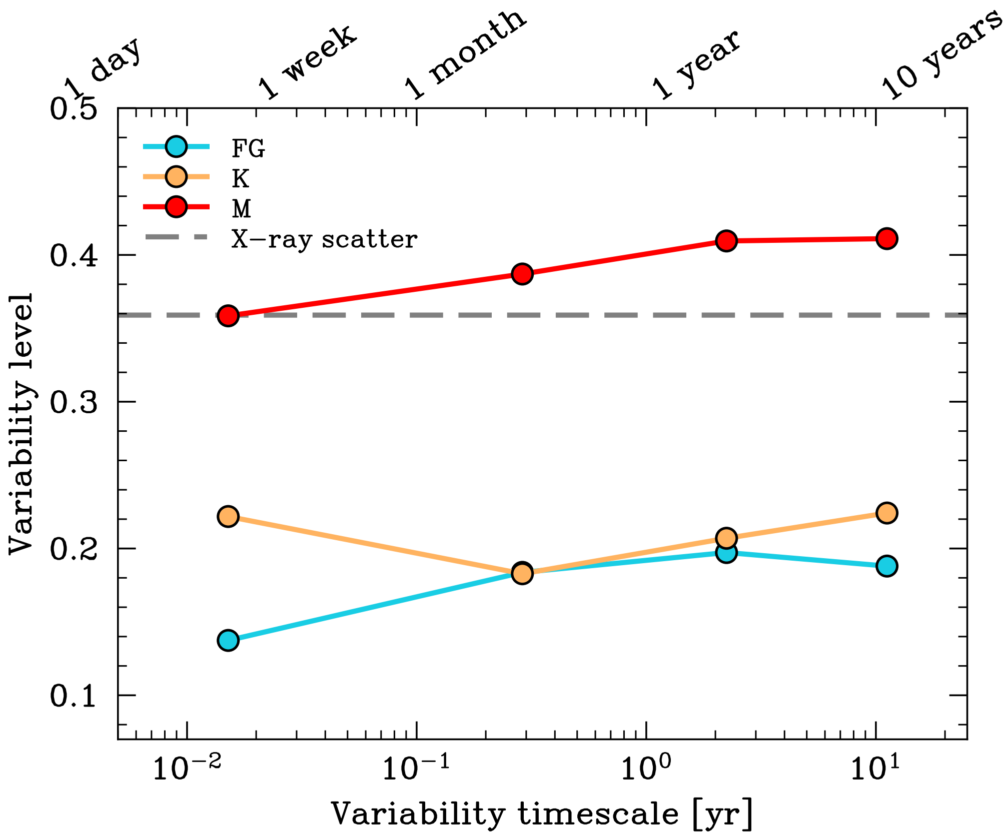

Figure 7.12: X-ray variability levels of F & G dwarfs (cyan), K-dwarfs (orange), and M-dwarfs (red) for a range of variability timescales spanning weeks to decades. The level of scatter observed in rotation-activity relations is shown as a grey dashed line.

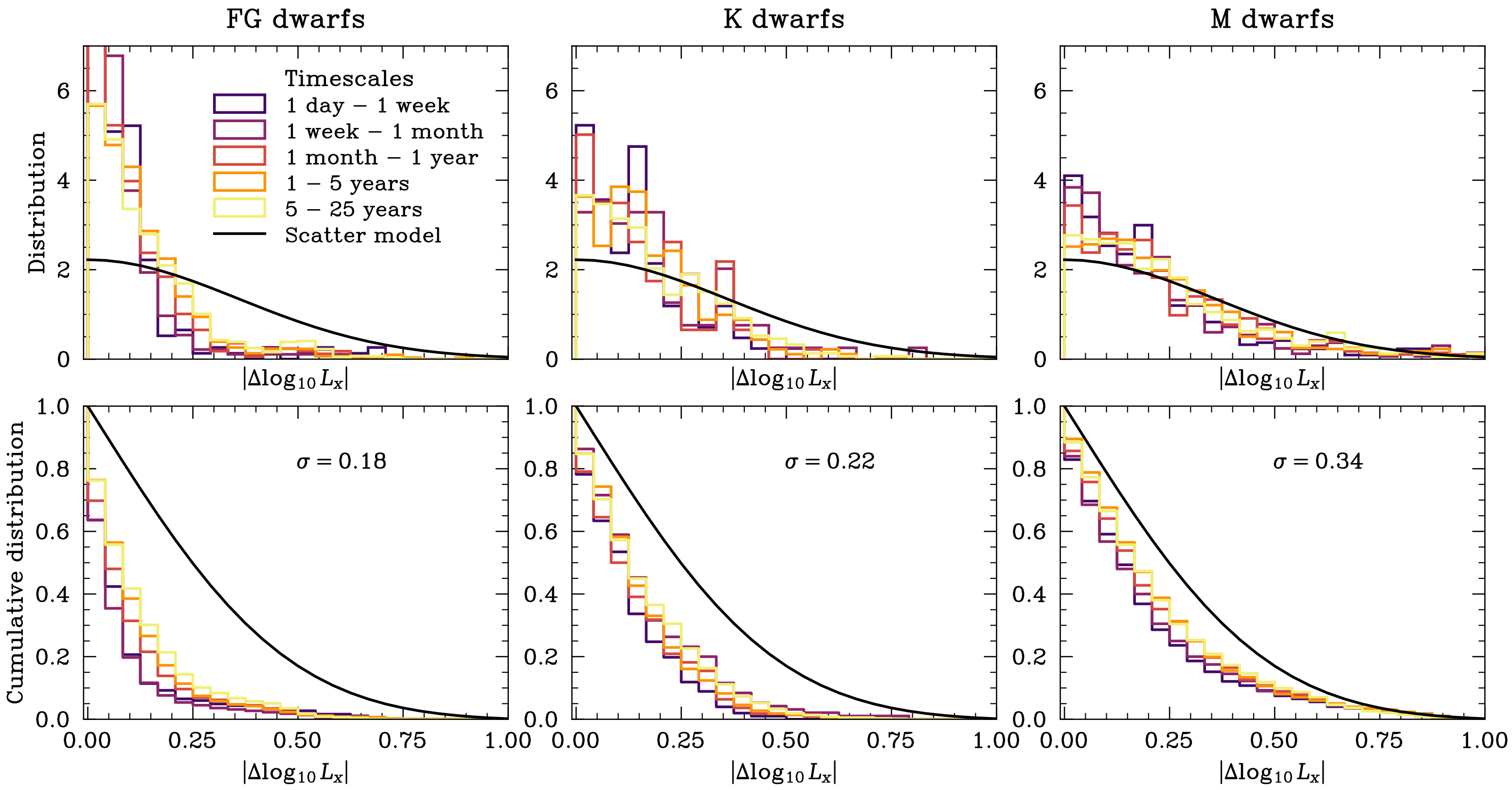

Figure 7.13: Following Figure 7.11, where only stars whose *XMM-Newton* observations have the `PN_FLAG` flag set to zero in the *4XMM* catalogue are included.

Overall, I found that FGK stars vary half as much as the scatter in rotation-activity relations [with $\sigma = 0.36$, Johnstone et al., 2021], whereas M dwarfs vary as much as the scatter. This trend persists across stars with both few and many X-ray detections and after further distance and quality cuts on the sample. Since the X-ray variability of FGK stars is lower in magnitude than this observed scatter by 40-50%, it cannot be solely responsible for it.

We already know that stellar X-ray emission varies following the birth, evolution, and decay of features in the corona, such as flares, activity cycles, and active regions, which evolve on different timescales, ranging from hours for flares to years for activity cycles [see review by Güdel et al., 2007]. Each feature contributes to the overall variability on their own characteristic timescales, and thus one would expect X-ray variability to increase with timescale; e.g. two measurements of the X-ray flux of a star separated by a day are likely to be more similar than two measurements separated by a month.

Marino et al. [2000] studied the X-ray variability of 55 M-dwarfs within 15 pc with *ROSAT* and *Einstein*, sampling timescales of months to decades. For each star, they calculated the ratios of each measured X-ray luminosity to the minimum X-ray luminosity in logarithmic scale, i.e. $\log L_{\mathrm{x}} - \log L_{\mathrm{x,min}}$; the width of the cumulative distribution of such values was thus used to determine the variability amplitude. This is similar to my analysis in Section 7.3, although my approach was more complete as I compared every available measurement with one another. Marino et al. [2000] arrived at three main conclusions: (1) the amplitude of variability is independent of X-ray activity and visual magnitude, (2) X-ray variability on M-dwarfs is likely caused for the most part by flare-like events, (3) and it likely originates in short-term timescales of months with little additional variation in long-term (~ 10 years) timescales. Marino et al. [2002] then applied this analysis to 40 field FGK stars in the solar neighbourhood with *ROSAT*; they found that the X-ray variability of FGK stars occurs on longer timescales of years, likely as a result of activity cycles, akin to the Sun. Moreover, the variability of FGK stars is smaller in amplitude compared to M-dwarfs by 20%.

Their results are in agreement with my findings in this chapter, where I found M-dwarfs are more variable in the X-rays than FGK stars by 40% (Section 7.3); and that most of the variability of M-dwarfs originates on timescales shorter than a month whilst F & G dwarfs increase their variability the most across timescales of years (Section 7.3.3).

Following Marino et al. [2003], this discrepancy may arise from X-ray variability being driven by different mechanisms on M-dwarfs and F & G stars; variability of M-dwarfs could arises from flares [Marino et al., 2000] whilst F & G stars present variability in both the short-term as well as in the long-term, likely due to activity cycles lasting years [Telleschi et al., 2005b]. In theory, activity cycles on M-dwarfs that are X-ray saturated could be muted as a result of the saturation itself, preventing them from becoming X-ray brighter than the saturation limit , whilst unsaturated FGK stars would have no such restriction.

Indeed, several FGK stars have been found to have X-ray activity cycles that closely follow simultaneous chromospheric activity cycles. Sanz-Forcada et al. [2019] characterised the X-ray activity cycle of the G0V star ι Hor and uncovered an activity cycle with period 1.6 years and amplitude of a factor of 2.3 between the minimum and the maximum X-ray flux. Similarly, ϵ Eri (K2V) has an activity cycle of 2.9 yr with an amplitude of a factor of 2 [Coffaro et al., 2020]; and HD 81809 (G1V) has an activity cycle lasting 7.3 yr with amplitude of a factor of 5 [Orlando et al., 2017].

ι Hor and ϵ Eri have variability amplitudes that are consistent with my findings for the populations of FGK stars, for which I estimated a 1σ variability level of a factor of 1.5 and a 2σ level of 2.3. The activity cycle on HD 81809, on the other hand, has a period that is longer that the other two stars as well as greater in amplitude by a factor of two; more akin to the activity cycle of the Sun, with an 11 yr cycle and an amplitude of one order of magnitude in the X-rays [Chamberlin et al., 2008; Johnstone et al., 2021]. Both HD 81809 and the Sun also have similar ages of $\sim$ 4 Gyr, unlike ι Hor and ϵ Eri, which are still young (600 Myr and 440 Myr, respectively). Coffaro et al. [2022] studied X-ray activity cycles on 8 G-type stars and noted an increase of the amplitude of their activity cycles with age together with a decrease in surface X-ray flux. If older FGK stars are more likely to display activity cycles that are longer in period and greater in amplitude, they are also generally fainter and thus more challenging to detect in the X-rays, potentially introducing a bias for younger stars with narrower variability amplitudes.

Johnstone et al. [2021] studied the X-ray variability of FGKM stars on timescales of months to years using archival X-ray observations from *ROSAT* and *XMM-Newton* from literature [Güdel et al., 1997; Telleschi et al., 2005b; Wright et al., 2011]. Overall, they found that M-dwarfs are more variable than FGK stars, and that the variability of M-dwarfs only reaches the level consistent with the X-ray scatter on yearly timescales. They thus attributed the scatter in the X-rays entirely to X-ray variability, motivated by the variability of both M-dwarfs and the Sun, although they did not consider the variability of FGK stars on yearly timescales [see Fig. 7 in Johnstone et al., 2021].

Johnstone et al. [2021] also characterised the scatter in the rotation-activity relation by fitting a broken power law to the stellar sample by Wright et al. [2011], plotting a histogram of the residuals of the data with the model, and fitting a gaussian distribution to it; the standard deviation of the fitted distribution corresponds to the scatter in the relation, which they determined to a factor of $|\Delta \log_{10} L_X| = 0.36$. The stellar sample that Wright et al. [2011] compiled consists of 824 stars with spin periods and X-ray luminosities acquired from literature. They combined X-ray surveys from several telescopes (*XMM-Newton*, *ROSAT*, and *Einstein*) of several open clusters (Hyades, Pleiades, Praesepe) as well as nearby field stars. Spectral types from G2 to M4 are almost equally sampled, dropping to fewer stars at later types down to M5.

If the scatter in the rotation-activity relation of FGK stars from Johnstone et al. [2021] cannot be explained with X-ray variability alone, there must be additional mechanisms that contribute to this scatter. Núñez et al. [2022] recently studied X-ray emission and rotation in the Hyades ($\sim$ 800 Myr) and Praesepe ($\sim$ 700 Myr) open clusters. They updated membership lists for the two clusters with *Gaia* DR2, and obtained rotation periods for many of their members from recent literature. They additionally re-analysed archival X-ray observations of the two clusters using data from the *ROSAT*, *Chandra*, *Swift*, and *XMM-Newton* observatories, which they used to fit rotation-activity relations to the cluster stars. Núñez et al. [2022] thus determined that in their rotation-activity relations, M-dwarfs span two orders of magnitude in the X-rays, whilst FGK stars span one order of magnitude, half as much as M-dwarfs. Assuming this span corresponds to a 3σ spread, and describing it with a normal distribution in $\log_{10} L_{\rm X}$, the spread of two orders of magnitude for M-dwarfs would correspond to a 3σ spread of $\times 1$ and thus a 1σ spread of $\times 1/3$. We thus obtain a standard deviation of $\sigma = 0.33$ for M-dwarfs and thus $\sigma = 0.17$ for FGK stars, which is half as much.

This is in very good agreement with my results in Section 7.3, where I determined M-dwarfs and FGK stars vary in the X-rays in very similar amounts. Therefore, in their sample of Hyades and Praesepe X-ray emitting stars, the scatter in the rotation-activity relation could indeed be entirely explained by X-ray variability. Núñez et al. [2022] also found no correlation between X-ray activity and the choice of X-ray observatory or the number of source counts for stars in the saturated regime, which suggests that the observed scatter is intrinsic to stars in the saturated regime. In their sample, the saturated regime is entirely populated by M-dwarfs, largely later than M3.5. In contrast, Johnstone et al. [2021] found no dependence of the spread in the rotation-activity relation in Rossby number on the sample of X-ray emitting stars by Wright et al. [2011], which included both field and cluster stars.

The scatter in the rotation-activity relation can also be explained by stars having intrinsic X-ray luminosities independent of their spin periods, where a star's coronal emission consistently lies below or above the rotation-activity relation. This additional contribution could come from stellar metallicity. Indeed, magnetic activity in stars has been found to be linked to their metallicities [e.g. Amard et al., 2020; See et al., 2023, 2024]. [Amard et al., 2020] argued that the presence of heavier elements increases the opacity of the star, which increases its temperature gradient in its interior, leading to a deeper convective layer and longer convective turnover times. This results in smaller Rossby numbers and stronger magnetic activity. Therefore, in principle, high-metallicity stars will be more X-ray active than low-metallicity stars at a given rotation period. See et al. [2024] further argued that, at later ages, this will mean that high-metallicity stars will be less active than their low-metallicity counterparts, as their stronger magnetic activity earlier in their life would have strengthened the emission of stellar wind and thus the rate at which they spin down.

Therefore, assembling a rotation-activity relation by combining stars with different metallicities could potentially contribute to the scatter in the X-rays. This could partly explain why Núñez et al. [2022] found the scatter for FGK stars was narrower than Johnstone et al. [2021] predicted, since Núñez et al. [2022] studied stars belonging to the same clusters (and thus with the same metallicities) whereas the sample Johnstone et al. [2021] used (by Wright et al. [2011]) combined stars from multiple clusters together with field stars.

7.4.2 Distance bias

I also assessed the impact of including distant stars in the dataset I compiled. Stars that are further away are fainter, and thus if their X-ray flux at Earth falls below a detection limit, they are no longer detected by *XMM-Newton*. Since stellar X-ray emission is not homogeneous across spectral types, spin periods, and ages, distance induces a bias against X-ray faint populations.

In Figure 7.14, I plotted the X-ray luminosities of all stars in the dataset

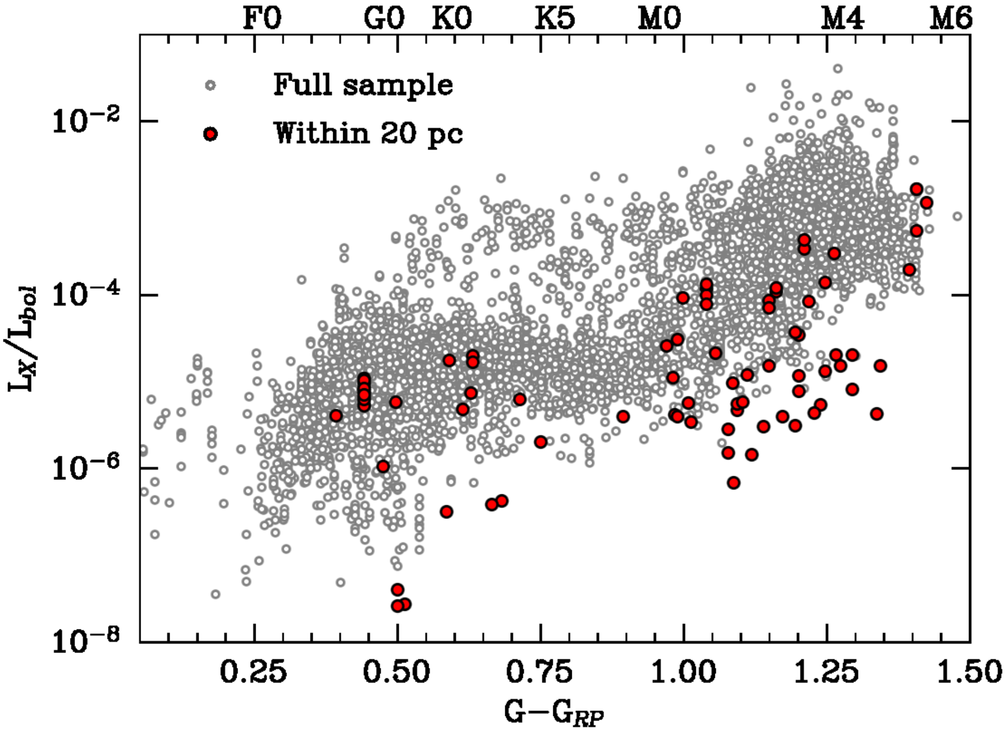

Figure 7.14: Plot of Gaia colour index $\mathrm{G}-\mathrm{G}_{\mathrm{RP}}$ against X-ray activity $\mathrm{L_X}/\mathrm{L_{bol}}$ for all stars in our sample (grey points), with those stars within 20 pc highlighted (red points).

as a function of spectral type, and further highlighted all stars within 20 pc of Earth in red. Figure 7.14 additionally demonstrates that nearby late M-dwarfs tend to have fainter X-ray activities ($10^{-6} - 10^{-4}$) compared to the total population ($10^{-4} - 10^{-2}$), suggesting we are missing a numerous population of M-dwarfs that are too X-ray faint to detect with *XMM-Newton* past a few tens of parsecs.

If we assume the detection limit of *XMM-Newton*, under which a source would not be detected, lies at an X-ray flux of about 10^{-15} erg cm^{-2} s^{-1} , and ignoring ISM absorption, one can estimate the maximum distance at which a star would still be detectable given its X-ray activity. The X-ray flux from a Sun-like star (G2V) with a low X-ray activity ($\log_{10}(L_X/L_{\rm bol}) \sim -6$) would fall below this limiting X-ray flux at a distance greater than 177 pc. Similarly, a K5V dwarf with the same X-ray activity would not be detectable past 80 pc. This limit lies even closer for low activity M4 stars (with $\log_{10}(L_X/L_{\rm bol}) \sim -5$), at only 48 pc.

These results imply the completeness for F & G stars in the dataset is good, as even less active ones would be detected within ∼200 pc, which is the maximum distance I adopted for my sample of Gaia stars. On the other hand, X-ray surveys of M-dwarfs (and potentially late K-dwarfs) are much more strongly biased towards the most X-ray active constituents of these populations on volume-limited samples past 50 pc.

Given these biases, in this section I assessed the impact of the choice of distance cut-off on my calculations of the population level X-ray variability of FGK & M stars. I repeated the analysis I performed in Section 7.3 but with different choices for the distance cut-off of 100 pc, 80 pc, and 50 pc. I found broadly consistent results across these subsets, with F & G dwarfs maintaining an overall variability level of $\sigma = 0.15$, K-dwarfs showing a slight decrease down from $\sigma = 0.22$ to $\sigma = 0.15 - 0.11$, and M-dwarfs maintaining $\sigma = 0.36 - 0.40$. I therefore find the variability levels on these volume-limited subsets are in agreement with my results on the full sample within 200 pc, where M-dwarfs are roughly 40% more variable than FGK stars.

7.4.3 Effects on atmospheric escape

In this section, I explore the impact of a X-ray irradiation that varies in the short-term on the evaporation histories of small close-in exoplanets. I simulated the evaporation histories of a model planet orbiting a G-dwarf (1 M$_\odot$), a K-dwarf (0.7 M$_\odot$), and an M-dwarf (0.25 M$_\odot$). To run these simulations, I adopted the

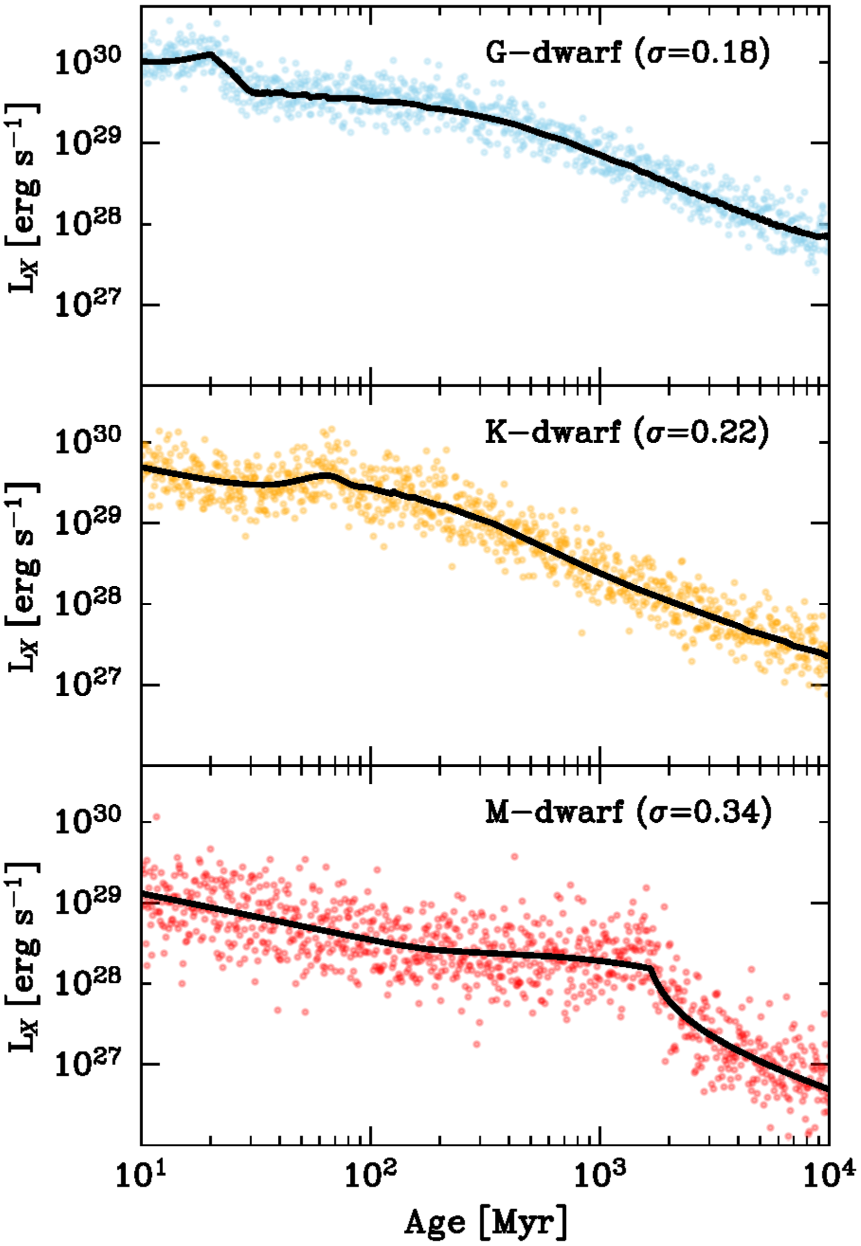

Figure 7.15: Evolution of the X-ray luminosity with age for a G-dwarf ($1\,\mathrm{M}_\odot$, top panel), a K-dwarf ($0.7\,\mathrm{M}_\odot$, middle panel), and an M-dwarf ($0.25\,\mathrm{M}_\odot$, bottom panel). The black lines represent X-ray emission histories from the models by Johnstone et al. [2021], which do not have short-term variability. The data points represent the same models with added X-ray variability with a level of scatter I determined in Section 7.3.

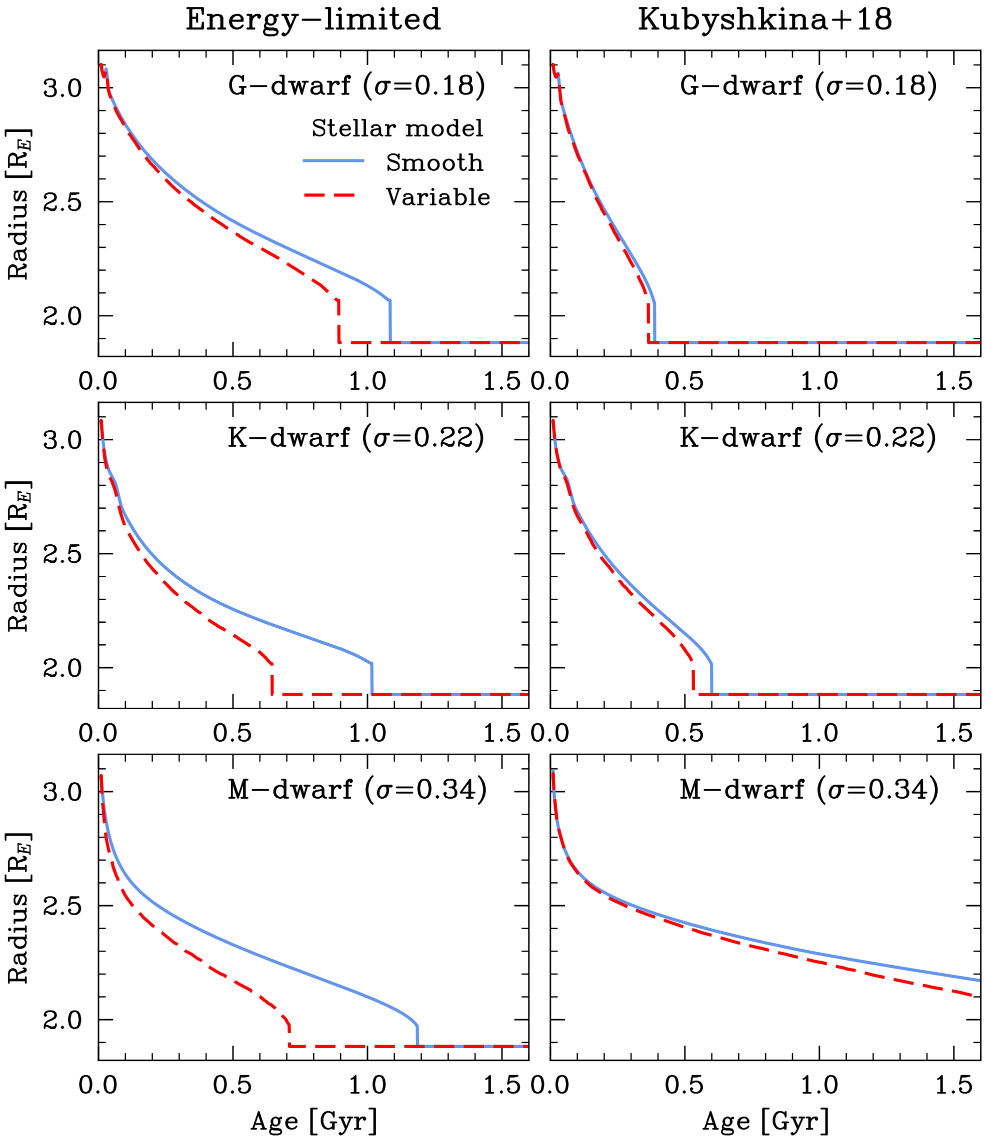

Figure 7.16: Evolution of planet radius with age for planets orbiting a G-dwarf (top panels), a K-dwarf (middle planels), and an M-dwarf (bottom panels), from simulations of atmospheric escape using stellar emission histories shown in Figure 7.15. The solid lines show evolution of planet radius under a "smooth" X-ray irradiation history with no short-term variability, whereas the dashed lines show evolution under a variable X-ray irradiation. Atmospheric evolution is also shown making use of two mass loss models: the energy-limited formulation [e.g. Watson et al., 1981; Erkaev et al., 2007], and the hydrodynamic model by Kubyshkina et al. [2018].

`photoevolver` code, which I presented in Section 2.5. I performed these simulation starting at an age of 10 Myr until 2 Gyr with fixed time steps of 1 Myr.

The model planet starts out as a typical sub-Neptune above the radius valley, with a mass of $8\,\mathrm{M_E}$ and an starting atmospheric mass fraction of 2%. In order to better compare the planet's atmospheric evolution around each star, in each case I chose the planet's orbital period such that it received an X-ray flux of $10^5\,\mathrm{erg\,cm^{-2}\,s^{-1}}$ at the beginning of the simulation; this corresponds to 5.4 d around the G-dwarf, 3.7 d around the K-dwarf, and 2.3 d around the M-dwarf.

To model the X-ray emission histories of the three stars, I adopted the stellar X-ray evolution models by Johnstone et al. [2021], shown in Figure 7.15 (black lines), which do not account for variability. I additionally simulated the evaporation histories of these planets under an X-ray irradiation that is variable. To do so, on each time step of the simulation, I scaled the X-ray luminosity predicted by Johnstone et al. [2021] by a random factor drawn from a normal distribution that matches the expected variability level of each star. I adopted the variability levels I determined in Section 7.4.1, where I filtered the *4XMM* catalogue for the detections that are the least likely to be spurious. In my analysis, I assumed that stellar X-ray variability follows a normal distribution in $\log L_\mathrm{X}$ in which the standard deviation σ corresponds to the variability level, which I found to be $\sigma = 0.18$ for G-dwarfs, $\sigma = 0.22$ for K-dwarfs, and $\sigma = 0.34$ for M-dwarfs. These stellar emission models with variability are shown in in Figure 7.15 as a scatter about the stellar models without variability (black lines).

The results of the simulations are shown on Figure 7.16. Overall, I found that X-ray variability results in enhanced evaporation rates and thus shorter lifetimes for the gaseous envelopes, compared to the stellar emission models without variability. For these particular planets, the gaseous envelopes are fully evaporated 200, 350, and 500 Myr earlier around the G, K, and M stars, respectively.

Moreover, I noted the impact on the mass loss rates is greater when assuming the planets' escape lie in the energy-limited regime, compared to the mass loss model by Kubyshkina et al. [2018], which additionally account for recombination-limited escape. Indeed, the lifetimes of the gaseous envelopes are only shortened by 20 Myr around the G-dwarf and 100 Myr around the K-dwarf. In the case of the M-dwarf, even though the planet is not stripped of its envelope, the evolution under a variable X-ray irradiation follows very closely the evolution with no variability, with only a difference of a fraction of a percent in the envelope mass fraction at 1.5 Gyr.

This is a consequence of how X-ray flux scales with mass loss rate on different escape regimes. In the energy-limited regime, the mass loss rates scale roughly linearly with X-ray flux ($\dot{m} \propto \mathrm{F}_\mathrm{X}^{0.9}$) whereas in the recombination-limited regime mass loss rates scale less strongly with flux, following a power law with an exponent below one ($\dot{m} \propto \mathrm{F}_\mathrm{X}^{0.6}$) [Murray-Clay et al., 2009a]. As a result, an increase of the X-ray flux by a factor of two (due to variability) results in mass loss rates also greater by a factor of two under the energy-limited regime, but only greater by a factor of about 1.5 under the recombination-limited regime. Ultimately, X-ray variability has a diminished effect for atmospheric escape in the recombination-limited regime.

7.5 Conclusions

In this chapter, I characterised the X-ray variability of FGKM stars in order to assess its contribution to the order-of-magnitude scatter observed in rotation-activity relations.

To do so, I assembled a sample of 1,000 FGKM stars in the *Gaia DR3* archive benefiting from multiple X-ray detections from *XMM-Newton*. I then characterised the variability level of stars in this sample from the degree by which their X-ray flux changes between observations. I identified two groups in the sample: (1) a large number of stars with few (2–10) X-ray detections each, which I was able to study individually, and (2) a small number of stars with many (> 10) X-ray detections, which allowed for a population-level characterisation of variability.

Overall, I found that F, G, & K dwarfs vary in the X-rays following a normal distribution in $\log L_\mathrm{X}$ with standard deviations of $\Delta \log L_\mathrm{X} = 0.18$ for F & G dwarfs $\Delta \log L_\mathrm{X} = 0.22$ for K-dwarfs, much less than the scatter of $\Delta \log L_\mathrm{X} = 0.36$ observed in rotation-activity relations. M-dwarfs, on the other hand, match this scatter much better, with an X-ray variability of $\Delta \log L_\mathrm{X} = 0.34$.

These results demonstrate that the spread observed in the rotation-activity relation *cannot* be explained with X-ray variability alone for FGK stars, at least in variability timescales of up to ~ 25 years. In the case of M-dwarfs, on the other hand, their variability is able to fully explain the observed scatter. Instead, additional contributions must be considered, such as intrinsic X-ray emission levels that are independent of spin period, possibly originating in stellar metallicity.

Finally, I carried out simulations of the evaporation histories of planets around G, K, & M dwarfs, and found that a variable X-ray irradiation history results in enhanced evaporation rates, shortening the survival of their gaseous envelopes by several hundred Myr.

In short, in this chapter I have demonstrated that (1) main sequence FGK stars showcase X-ray variability that is lower than expected, suggesting that the scatter seen in rotation-activity relations must have an alternative origin; and (2) X-ray variability can shorten the lifetimes of gaseous envelopes around close-in planets, reducing the timescales in which photoevaporation acts by up to several hundred Myr.

More generally, I have highlighted the importance of characterising the X-ray emission history of stars accurately in studies of the evolution of close-in planets, and its role in shaping exoplanet populations and the period-radius valley.

Chapter 8

Conclusions and future work

In this thesis, I have presented multiple X-ray observations of planet-hosting stars, characterising their coronal activity and the effects on the atmospheric evolution of their transiting planets. In this Chapter, I summarise the research and findings presented in this thesis as well as future avenues of research.

8.1 Summary of the thesis

8.1.1 Atmospheric escape on young planetary systems

In Chapters 3, 4, and 6 I studied the impact of the stellar XUV emission history on the long-term evolution of exoplanet atmospheres. In these chapters, I measured the current X-ray emission of planet-hosting stars with the *XMM-Newton* observatory, and used them to constrain models of stellar XUV emission history which in turn informed simulations of atmospheric escape of their transiting planets. Additionally, some of these stars host multi-planetary systems, where the unknown X-ray emission past of the host star can be negated by exploiting the fact that all planets in the system must have shared the same irradiation history.

In Chapter 3, I studied the K-dwarf K2-136, a member of the Hyades open cluster (800 Myr), and host to a three-planet system consisting of an Earth-sized planet, a mini-Neptune above the radius gap, and a super-Earth below the valley, in order of orbital separation. This unusual architecture, where a large gaseous planet (K2-136 c) lies interior to a smaller and denser planet (K2-136 d), raises the question of the survival of the envelope of the interior planet, despite the greater X-ray irradiation it has received. Using simulations of atmospheric escape, I determined that the middle planet, K2-136 c, kept its gaseous atmosphere thanks to its unusually large mass, which produced a deep gravitational potential that shielded it against atmospheric escape. On the other hand, the super-Earth, K2-136 d, was largely stripped of its atmosphere due to its low mass despite its greater orbital separation. Finally, the Earth-sized K2-136 b (with the shortest period) was likely stripped of any primordial H/He atmosphere shortly after the dispersal of the proto-planetary disk. Moreover, my analysis of *XMM-Newton* observations of K2-136 revealed the star, along with its cluster siblings in the Hyades, have X-ray luminosities lower by a factor of two than predicted by the X-ray evolution models by Johnstone et al. [2021].

In Chapter 6, I studied two additional planetary systems, TOI-1098 and TOI-451. TOI-1098 is a young F-dwarf hosting a sub-Neptune above the valley, and TOI-451 is a young Sun-like star in the Pleiades open cluster that hosts a three-planet system with a super-Earth followed by two mini-Neptunes. Both TOI-451 and TOI-1098 are younger than K2-136, aged 125 Myr and 250 Myr, respectively, and thus they are still active in the X-rays and their planets are still actively evolving under atmospheric escape. I determined that the super-Earth TOI-451 b lost its H/He atmosphere at the beginning of its evolution, whilst both TOI-451 cd as well as TOI-1098 b will experience significant evaporation in the future, with their survival of their envelopes resting on a more precise determination of their masses. I additionally compared my *XMM-Newton* observations of TOI-451 with archival *4XMM* observations of it parent cluster, the Pleiades, and found that X-ray evolution models were overestimating the X-ray emission of K-dwarfs by a factor of 2–3, akin to my results for the K2-136 and the Hyades in Chapter 3.

In Chapter 4, I characterised the X-ray emission from the sun-like star LTT 9779, hosting the only hot Neptune deep in the Neptunian desert, LTT 9779 b. The presence of a sizeable gaseous atmosphere on this planet at a short period of only 19 hours is puzzling, given that the X-ray irradiation from its host star is expected to have removed it via atmospheric escape. Using observations from *XMM-Newton* of the star, I determined LTT 9779 has an unusually faint X-ray emission, at least 15 times fainter than expected for its age; I thus simulated the past evaporation history of the planet and found that as a result, LTT 9779 b was able to hold onto its envelope to the present day. This discovery provided further evidence that the Neptunian desert is indeed sculpted by photoevaporation, as evidenced by the only known planet deep in the Neptunian desert with a gaseous envelope is also unusual in orbiting an X-ray faint star.

8.1.2 X-ray emission in stellar populations

In Chapters 5 and 7, I characterised the X-ray emission of main sequence stars at the population level with archival data from the *4XMM* catalogue of *XMM-Newton* observations, and compared them to models of stellar X-ray evolution.

In Chapter 5, I characterised the X-ray emission of stars in the Pleiades open cluster, aged 125 Myr. I cross-matched recent membership lists from Godoy-Rivera et al. [2021] curated with Gaia DR2 with the *4XMM* catalogue of X-ray emitting sources. By filtering for tidally interacting binaries, I determined that the X-ray emission of single F, G, and & K dwarfs in the Pleiades is fainter by a factor of 2–3 than the X-ray evolution models by Johnstone et al. [2021], which relies on older pre-*Gaia* membership lists for open clusters that may contain more contaminants and have not been filtered for binaries.

Finally, in Chapter 7, I characterised the X-ray variability of main sequence FGKM stars in timescales of days to decades, and compared it with the scatter in the X-rays observed in relations between X-ray activity and spin period, which has been suggested to originate in short-term variability. To do so, I assembled a volume-limited sample of main sequence single FGKM stars in Gaia DR3 within 200 pc, and sought detections of their X-ray emission in the *4XMM* catalogue of *XMM-Newton* observations. I identified 1000 Gaia stars detected in the X-rays multiple times in the past 25 years, sampling stars from F to M spectral types evenly. I thus determined that FGK stars vary in the X-rays half as much as expected compared to the scatter in rotation-activity relations, whereas M-dwarfs, on the other hand, have an X-ray variability that does match this scatter. Overall, I found that the X-ray scatter in rotation-activity relations for FGK stars cannot originate in X-ray variability alone, and alternative contributions must be considered. Finally, I found that taking variability in the X-ray irradiation of close-in exoplanets into account in simulations of their evaporation history, can significantly shorten the lifespan of their gaseous envelopes by several hundred Myr, particularly if they lie in the energy-limited regime of atmospheric escape.

8.2 Future work

In this section I lay out future avenues of research for the work presented in this thesis.

Characterising the high energy environment of multi-planet systems. Multi-planet systems are an ideal laboratory on which to test models of atmospheric escape and place constraints on the efficiency of evaporation. Since these planets must have shared the same high energy environment, their evaporation histories can be constrained against one another. Together with constraints on their present-day irradiation from *XMM-Newton*, we can also simultaneously test models of the X-ray evolution of their host star, as I have demonstrated in Chapters 3 with K2-136 as well as Chapter 2 with TOI-451.

This is particularly true on systems that have anti-size ordered or mixed architectures, where a mini-Neptune above the valley lies interior to a rocky world below it. In such systems, simulations of their evolution under atmospheric escape can provide even tighter constraints on their past and future evaporation histories as well as their internal structures.

Observatories such as *TESS* are revealing a plethora of new young planetary systems in which to test these models, and upcoming missions such as *PLATO* will greatly expand the exoplanet census as well improve the precision in stellar age and planetary radius, which in turn will prove vital in uncovering the underlying mechanisms that give rise to the radius gap.

Uncovering the origins of Neptune desert worlds. The Neptunian desert has recently been found to host a very small number of exoplanets with highly unusual characteristics. These include massive Neptune-sized planets that likely lack gaseous atmospheres despite their size, such as TOI-849 b [Armstrong et al., 2020], TOI-332 b [Osborn et al., 2023], and TOI-1853 b [Naponiello et al., 2023b], as well as hot Neptunes with gaseous atmospheres, such as LTT 9779 b [Jenkins et al., 2020], and more recently TOI-3071 b [Hacker et al., 2024] and TOI-3261 b [Nabbie et al., 2024].

Moreover, in Chapter 4 I discovered that LTT 9779 b, the first hot Neptune deep in the Neptunian desert, avoided being stripped of its atmosphere due to the inactive nature of its host star. As this region of parameter space is further probed with observatories such as *TESS*, new hot H/He-rich worlds are discovered inhabiting it. One of the next steps towards uncovering the origins of such worlds consists of characterising their high energy environment with X-ray observatories, which will tell us whether their host stars are similarly faint in their X-ray emission, failing to strip these planets of their envelopes, or whether alternative explanations are required for their presence so close to their stars.

Searching for water worlds. Whilst the radius gap as sculpted by atmospheric escape can be explained with the evaporation of rocky cores surrounded by H/He envelopes [e.g. Owen, 2019], planet formation models also predict ice-rich worlds should be present in large numbers [e.g. Jin and Mordasini, 2018]. Measurements of the radii and masses of exoplanets only allow us to place constraints on their bulk densities, however, and cannot on their own probe into their internal structures. Since both H/He and water can explain the existence low density worlds, the choice of internal structure induces a degeneracy that cannot be broken with knowledge of mass and radius alone.

In Chapters 3 and 6, I have shown that simulations of the evaporation history of close-in planets can be used to constrain their internal structures. The ideal targets for such analysis are small planets close to their stars that also have moderately low densities, below what is required for a purely rocky composition, and for which photoevaporation predicts that no H/He-rich envelope should remain in the present day. Their low densities could instead be explained with the presence of water, which is much more resistant to escape, offering an avenue to probe into the internal structures of such worlds.

I have already studied a small number of such planets, both in this thesis with TOI-451 b in Chapter 6, as well as part of my contributions as co-author, with TOI-3261 b [Nabbie et al., 2024], TOI-908 b [Hawthorn et al., 2023], and K2-370 b (Sozzetti et al. in press), where I showed that these low-density planets are unlikely to have retained a H/He-rich envelope until the present day.

Characterising the X-ray emission of planet-hosting stars.

In Chapter 7 I assembled a dataset of 4,421 main sequence *Gaia* stars with X-ray detections from *XMM-Newton*. This dataset could be used to find a link between X-ray emission and variability, and stellar metallicity by cross-matching it with a library of stellar metallicities, as metal-rich stars are thought to be more magnetically active (see Section 1.4.3). One step further would involve selecting stars that have additional measurements of their spin periods and/or ages, it would thus be possible to construct a rotation-metallicity-activity relation which may reduce the order-of-magnitude scatter in the X-rays seen in rotation-activity relations.

Finally, this dataset could also facilitate the search for X-ray transits of exoplanets. To date there is only one published X-ray transit, caused by the hot Jupiter HD 189733 b [Poppenhaeger et al., 2013]. This search would involve using the NASA Exoplanet Archive to select the stars in my dataset of X-ray emitting stars that host planets, then searching for X-ray observations that took place during a planetary transit, and finally searching for matching transits in the X-ray lightcurves themselves. The detection of further X-ray transits would place strong constraints on the structure of upper atmospheres of hot Jupiters, including a direct determination of the X-ray absorption depth (see Section 1.3.2).

Bibliography

L. Affer, G. Micela, M. Damasso, M. Perger, I. Ribas, A. Suárez Mascareño, J. I. González Hernández, R. Rebolo, E. Poretti, J. Maldonado, G. Leto, I. Pagano, G. Scandariato, R. Zanmar Sanchez, A. Sozzetti, A. S. Bonomo, L. Malavolta, J. C. Morales, A. Rosich, A. Bignamini, R. Gratton, S. Velasco, D. Cenadelli, R. Claudi, R. Cosentino, S. Desidera, P. Giacobbe, E. Herrero, M. Lafarga, A. F. Lanza, E. Molinari, and G. Piotto. HADES RV program with HARPS-N at the TNG GJ 3998: An early M-dwarf hosting a system of super-Earths. *A&A*, 593: A117, October 2016. doi: 10.1051/0004-6361/201628690.

Marcel A. Agüeros, Scott F. Anderson, Kevin R. Covey, Suzanne L. Hawley, Bruce Margon, Emily R. Newsom, Bettina Posselt, Nicole M. Silvestri, Paula Szkody, and Wolfgang Voges. X-Ray-Emitting Stars Identified from the ROSAT All-Sky Survey and the Sloan Digital Sky Survey. *ApJS*, 181(2):444–465, April 2009. doi: 10.1088/0067-0049/181/2/444.

Marcel A. Agüeros, Kevin R. Covey, Jenna J. Lemonias, Nicholas M. Law, Adam Kraus, Natasha Batalha, Joshua S. Bloom, S. Bradley Cenko, Mansi M. Kasliwal, Shrinivas R. Kulkarni, Peter E. Nugent, Eran O. Ofek, Dovi Poznanski, and Robert M. Quimby. The Factory and the Beehive. I. Rotation Periods for Low-mass Stars in Praesepe. *ApJ*, 740(2):110, October 2011. doi: 10.1088/0004-637X/740/2/110.

R. Allart, V. Bourrier, C. Lovis, D. Ehrenreich, J. J. Spake, A. Wyttenbach, L. Pino, F. Pepe, D. K. Sing, and A. Lecavelier des Etangs. Spectrally resolved helium absorption from the extended atmosphere of a warm Neptune-mass exoplanet. *Science*, 362(6421):1384–1387, December 2018. doi: 10.1126/science.aat5879.

R. Allart, V. Bourrier, C. Lovis, D. Ehrenreich, J. Aceituno, A. Guijarro, F. Pepe,

D. K. Sing, J. J. Spake, and A. Wyttenbach. High-resolution confirmation of an extended helium atmosphere around WASP-107b. *A&A*, 623:A58, March 2019. doi: 10.1051/0004-6361/201834917.

Roi Alonso, Timothy M. Brown, Guillermo Torres, David W. Latham, Alessandro Sozzetti, Georgi Mandushev, Juan A. Belmonte, David Charbonneau, Hans J. Deeg, Edward W. Dunham, Francis T. O'Donovan, and Robert P. Stefanik. TrES-1: The Transiting Planet of a Bright K0 V Star. *ApJ*, 613(2):L153–L156, October 2004. doi: 10.1086/425256.

Louis Amard and Sean P. Matt. The Impact of Metallicity on the Evolution of the Rotation and Magnetic Activity of Sun-like Stars. *ApJ*, 889(2):108, February 2020. doi: 10.3847/1538-4357/ab6173.

Louis Amard, Julia Roquette, and Sean P. Matt. Evidence for metallicity-dependent spin evolution in the Kepler field. *MNRAS*, 499(3):3481–3493, December 2020. doi: 10.1093/mnras/staa3038.

David J. Armstrong, Théo A. Lopez, Vardan Adibekyan, Richard A. Booth, Edward M. Bryant, Karen A. Collins, Magali Deleuil, Alexandre Emsenhuber, Chelsea X. Huang, George W. King, Jorge Lillo-Box, Jack J. Lissauer, Elisabeth Matthews, Olivier Mousis, Louise D. Nielsen, Hugh Osborn, Jon Otegi, Nuno C. Santos, Sérgio G. Sousa, Keivan G. Stassun, Dimitri Veras, Carl Ziegler, Jack S. Acton, Jose M. Almenara, David R. Anderson, David Barrado, Susana C. C. Barros, Daniel Bayliss, Claudia Belardi, Francois Bouchy, César Briceño, Matteo Brogi, David J. A. Brown, Matthew R. Burleigh, Sarah L. Casewell, Alexander Chaushev, David R. Ciardi, Kevin I. Collins, Knicole D. Colón, Benjamin F. Cooke, Ian J. M. Crossfield, Rodrigo F. Díaz, Elisa Delgado Mena, Olivier D. S. Demangeon, Caroline Dorn, Xavier Dumusque, Philipp Eigmüller, Michael Fausnaugh, Pedro Figueira, Tianjun Gan, Siddharth Gandhi, Samuel Gill, Erica J. Gonzales, Michael R. Goad, Maximilian N. Günther, Ravit Helled, Saeed Hojjatpanah, Steve B. Howell, James Jackman, James S. Jenkins, Jon M. Jenkins, Eric L. N. Jensen, Grant M. Kennedy, David W. Latham, Nicholas Law, Monika Lendl, Michael Lozovsky, Andrew W. Mann, Maximiliano Moyano, James McCormac, Farzana Meru, Christoph Mordasini, Ares Osborn, Don Pollacco, Didier Queloz, Liam Raynard, George R. Ricker, Pamela Rowden, Alexandre Santerne, Joshua E. Schlieder, Sara Seager, Lizhou Sha, Thiam-Guan Tan, Rosanna H. Tilbrook, Eric Ting, Stéphane Udry, Roland Vanderspek, Christopher A. Watson, Richard G. West, Paul A. Wilson, Joshua N. Winn, Peter Wheatley, Jesus Noel Villasenor, Jose I. Vines, and Zhuchang Zhan. A remnant planetary core in the hot-Neptune desert. *Nature*, 583(7814):39–42, July 2020. doi: 10.1038/s41586-020-2421-710.48550/arXiv.2003.10314.

K. A. Arnaud. XSPEC: The First Ten Years. In George H. Jacoby and Jeannette Barnes, editors, *Astronomical Data Analysis Software and Systems V*, volume 101 of *Astronomical Society of the Pacific Conference Series*, page 17, January 1996.

Martin Asplund, Nicolas Grevesse, A. Jacques Sauval, and Pat Scott. The Chemical Composition of the Sun. *ARA&A*, 47(1):481–522, September 2009. doi: 10.1146/annurev.astro.46.060407.145222.

M. Audard, M. Güdel, A. Sres, A. J. J. Raassen, and R. Mewe. A study of coronal abundances in RS CVn binaries%. *A&A*, 398:1137–1149, February 2003. doi: 10.1051/0004-6361:20021737.

M. Auvergne, P. Bodin, L. Boisnard, J. T. Buey, S. Chaintreuil, G. Epstein, M. Jouret, T. Lam-Trong, P. Levacher, A. Magnan, R. Perez, P. Plasson, J. Plesseria, G. Peter, M. Steller, D. Tiphène, A. Baglin, P. Agogué, T. Appourchaux, D. Barbet, T. Beaufort, R. Bellenger, R. Berlin, P. Bernardi, D. Blouin, P. Boumier, F. Bonneau, R. Briet, B. Butler, R. Cautain, F. Chiavassa, V. Costes, J. Cuvilho, V. Cunha-Parro, F. de Oliveira Fialho, M. Decaudin, J. M. Defise, S. Djalal, A. Docclo, R. Drummond, O. Dupuis, G. Exil, C. Fauré, A. Gaboriaud, P. Gamet, P. Gavalda, E. Grolleau, L. Gueguen, V. Guivarc'h, P. Guterman, J. Hasiba, G. Huntzinger, H. Hustaix, C. Imbert, G. Jeanville, B. Johlander, L. Jorda, P. Journoud, F. Karioty, L. Kerjean, L. Lafond, V. Lapeyrere, P. Landiech, T. Larqué, P. Laudet, J. Le Merrer, L. Leporati, B. Leruyet, B. Levieuge, A. Llebaria, L. Martin, E. Mazy, J. M. Mesnager, J. P. Michel, J. P. Moalic, W. Monjoin, D. Naudet, S. Neukirchner, K. Nguyen-Kim, M. Ollivier, J. L. Orcesi, H. Ottacher, A. Oulali, J. Parisot, S. Perruchot, A. Piacentino, L. Pinheiro da Silva, J. Platzer, B. Pontet, A. Pradines, C. Quentin, U. Rohbeck, G. Rolland, F. Rollenhagen, R. Romagnan, N. Russ, R. Samadi, R. Schmidt, N. Schwartz, I. Sebbag, H. Smit, W. Sunter, M. Tello, P. Toulouse, B. Ulmer, O. Vandermarcq, E. Vergnault, R. Wallner, G. Waultier, and P. Zanatta. The CoRoT satellite in flight: description and performance. *A&A*, 506(1):411–424, October 2009. doi: 10.1051/0004-6361/200810860.

Ellis A. Avallone, Jamie N. Tayar, Jennifer L. van Saders, Travis A. Berger, Zachary R. Claytor, Rachael L. Beaton, Johanna Teske, Diego Godoy-Rivera, and Kaike Pan. Rotation Distributions around the Kraft Break with TESS and Kepler: The Influences of Age, Metallicity, and Binarity. *arXiv e-prints*, art. arXiv:2203.15116, March 2022.

G. Bakos, R. W. Noyes, G. Kovács, K. Z. Stanek, D. D. Sasselov, and I. Domsa. Wide-Field Millimagnitude Photometry with the HAT: A Tool for Extrasolar Planet Detection. *PASP*, 116(817):266–277, March 2004. doi: 10.1086/382735.

G. Á. Bakos, G. Torres, A. Pál, J. Hartman, Géza Kovács, R. W. Noyes, D. W. Latham, D. D. Sasselov, B. Sipőcz, G. A. Esquerdo, D. A. Fischer, J. A. Johnson, G. W. Marcy, R. P. Butler, H. Isaacson, A. Howard, S. Vogt, Gábor Kovács, J. Fernandez, A. Moór, R. P. Stefanik, J. Lázár, I. Papp, and P. Sári. HAT-P-11b: A Super-Neptune Planet Transiting a Bright K Star in the Kepler Field. *ApJ*, 710(2):1724–1745, February 2010. doi: 10.1088/0004-637X/710/2/1724.

Sarah Ballard, Daniel Fabrycky, Francois Fressin, David Charbonneau, Jean-Michel Desert, Guillermo Torres, Geoffrey Marcy, Christopher J. Burke, Howard Isaacson, Christopher Henze, Jason H. Steffen, David R. Ciardi, Steven B. Howell, William D. Cochran, Michael Endl, Stephen T. Bryson, Jason F. Rowe, Matthew J. Holman, Jack J. Lissauer, Jon M. Jenkins, Martin Still, Eric B. Ford, Jessie L. Christiansen, Christopher K. Middour, Michael R. Haas, Jie Li, Jennifer R. Hall, Sean McCauliff, Natalie M. Batalha, David G. Koch, and William J. Borucki. The Kepler-19 System: A Transiting 2.2 R $_{\oplus}$ Planet and a Second Planet Detected via Transit Timing Variations. *ApJ*, 743(2):200, December 2011. doi: 10.1088/0004-637X/743/2/200.

I. Baraffe, F. Selsis, G. Chabrier, T. S. Barman, F. Allard, P. H. Hauschildt, and H. Lammer. The effect of evaporation on the evolution of close-in giant planets. *A&A*, 419:L13–L16, May 2004. doi: 10.1051/0004-6361:20040129.

A. Baranne, D. Queloz, M. Mayor, G. Adrianzyk, G. Knispel, D. Kohler, D. Lacroix, J. P. Meunier, G. Rimbaud, and A. Vin. ELODIE: A spectrograph for accurate radial velocity measurements. *A&AS*, 119:373–390, October 1996.

Khalid Barkaoui, Francisco J. Pozuelos, Coel Hellier, Barry Smalley, Louise D. Nielsen, Prajwal Niraula, Michaël Gillon, Julien de Wit, Simon Müller, Caroline

Dorn, Ravit Helled, Emmanuel Jehin, Brice-Olivier Demory, Valerie Van Grootel, Abderahmane Soubkiou, Mourad Ghachoui, David. R. Anderson, Zouhair Benkhaldoun, Francois Bouchy, Artem Burdanov, Laetitia Delrez, Elsa Ducrot, Lionel Garcia, Abdelhadi Jabiri, Monika Lendl, Pierre F. L. Maxted, Catriona A. Murray, Peter Pihlmann Pedersen, Didier Queloz, Daniel Sebastian, Oliver Turner, Stephane Udry, Mathilde Timmermans, Amaury H. M. J. Triaud, and Richard G. West. An extended low-density atmosphere around the Jupiter-sized planet WASP-193 b. *Nature Astronomy*, 8:909–919, July 2024. doi: 10.1038/s41550-024-02259-y.

Oscar Barragán, Suzanne Aigrain, Edward Gillen, and Fernando Gutiérrez-Canales. TESS Re-observes the Young Multi-planet System TOI-451: Refined Ephemeris and Activity Evolution. *Research Notes of the American Astronomical Society*, 5(3):51, March 2021. doi: 10.3847/2515-5172/abef70.

S. C. C. Barros, O. Demangeon, R. F. Díaz, J. Cabrera, N. C. Santos, J. P. Faria, and F. Pereira. Improving transit characterisation with Gaussian process modelling of stellar variability. *A&A*, 634:A75, February 2020. doi: 10.1051/0004-6361/201936086.

M. A. Barstow, S. L. Casewell, J. B. Holberg, and M. P. Kowalski. The status and future of EUV astronomy. *Advances in Space Research*, 53(6):1003–1013, March 2014. doi: 10.1016/j.asr.2013.08.007.

Matthew P. Battley, Don Pollacco, and David J. Armstrong. A search for young exoplanets in Sectors 1-5 of the TESS full-frame images. *MNRAS*, 496(2):1197–1216, August 2020. doi: 10.1093/mnras/staa1626.

Konstantin Batygin, Peter H. Bodenheimer, and Gregory P. Laughlin. In situ formation and dynamical evolution of hot jupiter systems. *The Astrophysical Journal*, 829(2):114, sep 2016. doi: 10.3847/0004-637X/829/2/114. URL `https://dx.doi.org/10.3847/0004-637X/829/2/114`.

C. Beaugé and D. Nesvorný. Emerging Trends in a Period-Radius Distribution of Close-in Planets. *ApJ*, 763(1):12, January 2013. doi: 10.1088/0004-637X/763/1/12.

J. P. Beaulieu, D. P. Bennett, P. Fouqué, A. Williams, M. Dominik, U. G. Jørgensen, D. Kubas, A. Cassan, C. Coutures, J. Greenhill, K. Hill, J. Menzies, P. D. Sackett, M. Albrow, S. Brillant, J. A. R. Caldwell, J. J. Calitz, K. H.

Cook, E. Corrales, M. Desort, S. Dieters, D. Dominis, J. Donatowicz, M. Hoffman, S. Kane, J. B. Marquette, R. Martin, P. Meintjes, K. Pollard, K. Sahu, C. Vinter, J. Wambsganss, K. Woller, K. Horne, I. Steele, D. M. Bramich, M. Burgdorf, C. Snodgrass, M. Bode, A. Udalski, M. K. Szymański, M. Kubiak, T. Więckowski, G. Pietrzyński, I. Soszyński, O. Szewczyk, Ł. Wyrzykowski, B. Paczyński, F. Abe, I. A. Bond, T. R. Britton, A. C. Gilmore, J. B. Hearnshaw, Y. Itow, K. Kamiya, P. M. Kilmartin, A. V. Korpela, K. Masuda, Y. Matsubara, M. Motomura, Y. Muraki, S. Nakamura, C. Okada, K. Ohnishi, N. J. Rattenbury, T. Sako, S. Sato, M. Sasaki, T. Sekiguchi, D. J. Sullivan, P. J. Tristram, P. C. M. Yock, and T. Yoshioka. Discovery of a cool planet of 5.5 Earth masses through gravitational microlensing. *Nature*, 439(7075):437–440, January 2006. doi: 10.1038/nature04441.

Lotfi Ben-Jaffel, Gilda E. Ballester, Antonio García Muñoz, Panayotis Lavvas, David K. Sing, Jorge Sanz-Forcada, Ofer Cohen, Tiffany Kataria, Gregory W. Henry, Lars Buchhave, Thomas Mikal-Evans, Hannah R. Wakeford, and Mercedes López-Morales. Signatures of strong magnetization and a metal-poor atmosphere for a Neptune-sized exoplanet. *Nature Astronomy*, 6:141–153, January 2022. doi: 10.1038/s41550-021-01505-x.

P. Benítez-Llambay, F. Masset, and C. Beaugé. The mass-period distribution of close-in exoplanets. *A&A*, 528:A2, April 2011. doi: 10.1051/0004-6361/201015774.

Katherine A. Bennett, Seth Redfield, Antonija Oklopčić, Ilaria Carleo, Joe P. Ninan, and Michael Endl. Nondetection of Helium in the Hot Jupiter WASP-48b. *AJ*, 165(6):264, June 2023. doi: 10.3847/1538-3881/acd34b.

Federico Biassoni, Andrea Caldiroli, Elena Gallo, Francesco Haardt, Riccardo Spinelli, and Francesco Borsa. Self-consistent modeling of metastable helium exoplanet transits. *A&A*, 682:A115, February 2024. doi: 10.1051/0004-6361/202347517.

Matthew R. Bolcar, Steve Aloezos, Vincent T. Bly, Christine Collins, Julie Crooke, Courtney D. Dressing, Lou Fantano, Lee D. Feinberg, Kevin France, Gene Gochar, Qian Gong, Jason E. Hylan, Andrew Jones, Irving Linares, Marc Postman, Laurent Pueyo, Aki Roberge, Lia Sacks, Steven Tompkins, and Garrett West. The Large UV/Optical/Infrared Surveyor (LUVOIR): Decadal Mission concept design update. In Howard A. MacEwen and James B. Breckinridge, editors, *Society of Photo-Optical Instrumentation Engineers (SPIE) Conference Series*, volume 10398 of *Society of Photo-Optical Instrumentation Engineers (SPIE) Conference Series*, page 1039809, September 2017. doi: 10.1117/12.2273848.

A. C. Boley, A. P. Granados Contreras, and B. Gladman. The In Situ Formation of Giant Planets at Short Orbital Periods. *ApJ*, 817(2):L17, February 2016. doi: 10.3847/2041-8205/817/2/L17.

William J. Borucki, David G. Koch, Gibor Basri, Natalie Batalha, Timothy M. Brown, Stephen T. Bryson, Douglas Caldwell, Jørgen Christensen-Dalsgaard, William D. Cochran, Edna DeVore, Edward W. Dunham, III Gautier, Thomas N., John C. Geary, Ronald Gilliland, Alan Gould, Steve B. Howell, Jon M. Jenkins, David W. Latham, Jack J. Lissauer, Geoffrey W. Marcy, Jason Rowe, Dimitar Sasselov, Alan Boss, David Charbonneau, David Ciardi, Laurance Doyle, Andrea K. Dupree, Eric B. Ford, Jonathan Fortney, Matthew J. Holman, Sara Seager, Jason H. Steffen, Jill Tarter, William F. Welsh, Christopher Allen, Lars A. Buchhave, Jessie L. Christiansen, Bruce D. Clarke, Santanu Das, Jean-Michel Désert, Michael Endl, Daniel Fabrycky, Francois Fressin, Michael Haas, Elliott Horch, Andrew Howard, Howard Isaacson, Hans Kjeldsen, Jeffery Kolodziejczak, Craig Kulesa, Jie Li, Philip W. Lucas, Pavel Machalek, Donald McCarthy, Phillip MacQueen, Søren Meibom, Thibaut Miquel, Andrej Prsa, Samuel N. Quinn, Elisa V. Quintana, Darin Ragozzine, William Sherry, Avi Shporer, Peter Tenenbaum, Guillermo Torres, Joseph D. Twicken, Jeffrey Van Cleve, Lucianne Walkowicz, Fred C. Witteborn, and Martin Still. Characteristics of Planetary Candidates Observed by Kepler. II. Analysis of the First Four Months of Data. *ApJ*, 736(1):19, July 2011. doi: 10.1088/0004-637X/736/1/19.

F. Bouchy, S. Udry, M. Mayor, C. Moutou, F. Pont, N. Iribarne, R. da Silva, S. Ilovaisky, D. Queloz, N. C. Santos, D. Ségransan, and S. Zucker. ELODIE metallicity-biased search for transiting Hot Jupiters. II. A very hot Jupiter transiting the bright K star HD 189733. *A&A*, 444(1):L15–L19, December 2005. doi: 10.1051/0004-6361:200500201.

V. Bourrier, A. Lecavelier des Etangs, D. Ehrenreich, Y. A. Tanaka, and A. A. Vidotto. An evaporating planet in the wind: stellar wind interactions with the radiatively braked exosphere of GJ 436 b. *A&A*, 591:A121, June 2016. doi: 10.1051/0004-6361/201628362.

V. Bourrier, A. Lecavelier des Etangs, D. Ehrenreich, J. Sanz-Forcada, R. Allart, G. E. Ballester, L. A. Buchhave, O. Cohen, D. Deming, T. M. Evans, A. García Muñoz, G. W. Henry, T. Kataria, P. Lavvas, N. Lewis, M. López-Morales, M. Marley, D. K. Sing, and H. R. Wakeford. Hubble PanCET: an extended upper atmosphere of neutral hydrogen around the warm Neptune GJ 3470b. *A&A*, 620:A147, December 2018. doi: 10.1051/0004-6361/201833675.

V. Bourrier, P. J. Wheatley, A. Lecavelier des Etangs, G. King, T. Louden, D. Ehrenreich, R. Fares, Ch Helling, J. Llama, M. M. Jardine, and A. A. Vidotto. MOVES III. Simultaneous X-ray and ultraviolet observations unveiling the variable environment of the hot Jupiter HD 189733b. *MNRAS*, 493(1):559–579, March 2020. doi: 10.1093/mnras/staa256.

Brendan P. Bowler. Imaging Extrasolar Giant Planets. *PASP*, 128(968):102001, October 2016. doi: 10.1088/1538-3873/128/968/102001.

Axel Brandenburg and Kandaswamy Subramanian. Astrophysical magnetic fields and nonlinear dynamo theory. *Phys. Rep.*, 417(1-4):1–209, October 2005. doi: 10.1016/j.physrep.2005.06.005.

Timothy D. Brandt and Chelsea X. Huang. Bayesian Ages for Early-type Stars from Isochrones Including Rotation, and a Possible Old Age for the Hyades. *ApJ*, 807(1):58, July 2015. doi: 10.1088/0004-637X/807/1/58.

K. R. Briggs and J. P. Pye. XMM-Newton and the Pleiades - I. Bright coronal sources and the X-ray emission from intermediate-type stars. *MNRAS*, 345(3): 714–726, November 2003. doi: 10.1046/j.1365-8711.2003.06991.x.

A. C. Brinkman, E. Behar, M. Güdel, M. Audard, A. J. F. den Boggende, G. Branduardi-Raymont, J. Cottam, C. Erd, J. W. den Herder, F. Jansen, J. S. Kaastra, S. M. Kahn, R. Mewe, F. B. S. Paerels, J. R. Peterson, A. P. Rasmussen, I. Sakelliou, and C. de Vries. First light measurements with the XMM-Newton reflection grating spectrometers: Evidence for an inverse first ionisation potential effect and anomalous Ne abundance in the Coronae of HR 1099. *A&A*, 365:L324–L328, January 2001. doi: 10.1051/0004-6361:20000047.

Matthew K. Browning, Mark S. Miesch, Allan Sacha Brun, and Juri Toomre. Dynamo Action in the Solar Convection Zone and Tachocline: Pumping and Organization of Toroidal Fields. *ApJ*, 648(2):L157–L160, September 2006. doi: 10.1086/507869.

Allan Sacha Brun, Mark S. Miesch, and Juri Toomre. Global-Scale Turbulent Convection and Magnetic Dynamo Action in the Solar Envelope. *ApJ*, 614(2): 1073–1098, October 2004. doi: 10.1086/423835.

T. R. Burnight. Soft x-radiation in the upper atmosphere. *Phys. Rev*, 76(165): 19–9, 1949.

E. T. Byram, T. A. Chubb, and H. Friedman. The Solar X-Ray Spectrum and the Density of the Upper Atmosphere. *J. Geophys. Res.*, 61(2):251–263, June 1956. doi: 10.1029/JZ061i002p00251.

Daniela Cardini and Angelo Cassatella. Color, Rotation, Age, and Chromospheric Activity Correlations in Late-Type Main-Sequence Stars. *ApJ*, 666(1):393–402, September 2007. doi: 10.1086/519991.

F. J. Carrera, J. Ebrero, S. Mateos, M. T. Ceballos, A. Corral, X. Barcons, M. J. Page, S. R. Rosen, M. G. Watson, J. A. Tedds, R. Della Ceca, T. Maccacaro, H. Brunner, M. Freyberg, G. Lamer, F. E. Bauer, and Y. Ueda. The XMM-Newton serendipitous survey. III. The AXIS X-ray source counts and angular clustering. *A&A*, 469(1):27–46, July 2007. doi: 10.1051/0004-6361:20066271.

R. C. Carrington. Description of a Singular Appearance seen in the Sun on September 1, 1859. *MNRAS*, 20:13–15, November 1859. doi: 10.1093/mnras/20.1.13.

W. Cash. Parameter estimation in astronomy through application of the likelihood ratio. *ApJ*, 228:939–947, March 1979. doi: 10.1086/156922.

A. Castro-González, V. Bourrier, J. Lillo-Box, J. B. Delisle, D. J. Armstrong, D. Barrado, and A. C. M. Correia. Mapping the exo-Neptunian landscape: A ridge between the desert and savanna. *A&A*, 689:A250, September 2024. doi: 10.1051/0004-6361/202450957.

R. C. Catura, L. W. Acton, and H. M. Johnson. Evidence for X-ray emission from Capella. *ApJ*, 196:L47–L49, March 1975. doi: 10.1086/181741.

C. Cecchi-Pestellini, A. Ciaravella, G. Micela, and T. Penz. The relative role of EUV radiation and X-rays in the heating of hydrogen-rich exoplanet atmospheres. *A&A*, 496(3):863–868, March 2009. doi: 10.1051/0004-6361/200809955.

H. M. Cegla, C. A. Watson, S. Shelyag, M. Mathioudakis, and S. Moutari. Stellar Surface Magnetoconvection as a Source of Astrophysical Noise. III. Sun-as-a-Star Simulations and Optimal Noise Diagnostics. *ApJ*, 879(1):55, July 2019. doi: 10.3847/1538-4357/ab16d3.

J. M. Chadney, M. Galand, Y. C. Unruh, T. T. Koskinen, and J. Sanz-Forcada. XUV-driven mass loss from extrasolar giant planets orbiting active stars. *Icarus*, 250:357–367, April 2015. doi: 10.1016/j.icarus.2014.12.012.

Joseph W. Chamberlain. Planetary coronae and atmospheric evaporation. *Planet. Space Sci.*, 11(8):901–960, August 1963. doi: 10.1016/0032-0633(63)90122-3.

Phillip C. Chamberlin, Thomas N. Woods, and Francis G. Eparvier. Flare Irradiance Spectral Model (FISM): Flare component algorithms and results. *Space Weather*, 6(5):S05001, May 2008. doi: 10.1029/2007SW000372.

Howard Chen and Leslie A. Rogers. Evolutionary Analysis of Gaseous Sub-Neptune-mass Planets with MESA. *ApJ*, 831(2):180, November 2016. doi: 10.3847/0004-637X/831/2/180.

Anna C. Childs, Alexa P. S. Hua, Rebecca G. Martin, Chao-Chin Yang, and Aaron M. Geller. Observational Signatures of a Previous Dynamical Instability in Multi-planet M-dwarf Systems. *ApJ*, 982(2):111, April 2025. doi: 10.3847/1538-4357/adbb53.

Jieun Choi, Aaron Dotter, Charlie Conroy, Matteo Cantiello, Bill Paxton, and Benjamin D. Johnson. Mesa Isochrones and Stellar Tracks (MIST). I. Solar-scaled Models. *ApJ*, 823(2):102, June 2016. doi: 10.3847/0004-637X/823/2/102.

Jessie L. Christiansen, Sakhee Bhure, Jon K. Zink, Kevin K. Hardegree-Ullman, Britt Duffy Adkins, Christina Hedges, Timothy D. Morton, Allyson Bieryla, David R. Ciardi, William D. Cochran, Courtney D. Dressing, Mark E. Everett, Howard Isaacson, John H. Livingston, Carl Ziegler, Perry Berlind, Michael L. Calkins, Gilbert A. Esquerdo, David W. Latham, Michael Endl, Phillip J. MacQueen, Benjamin J. Fulton, Lea A. Hirsch, Andrew W. Howard, Lauren M. Weiss, Bridgette E. Allen, Arthur Berberyann, Krys N. Ciardi, Ava

Dunlavy, Sofia H. Glassford, Fei Dai, Teruyuki Hirano, Motohide Tamura, Charles Beichman, Erica J. Gonzales, Joshua E. Schlieder, Thomas Barclay, Ian J. M. Crossfield, Emily A. Gilbert, Elisabeth C. Matthews, Steven Giacalone, and Erik A. Petigura. Scaling K2. V. Statistical Validation of 60 New Exoplanets From K2 Campaigns 2-18. *AJ*, 163(6):244, June 2022. doi: 10.3847/1538-3881/ac5c4c10.48550/arXiv.2203.02087.

David R. Ciardi, Daniel C. Fabrycky, Eric B. Ford, III Gautier, T. N., Steve B. Howell, Jack J. Lissauer, Darin Ragozzine, and Jason F. Rowe. On the Relative Sizes of Planets within Kepler Multiple-candidate Systems. *ApJ*, 763(1):41, January 2013. doi: 10.1088/0004-637X/763/1/41.

David R. Ciardi, Ian J. M. Crossfield, Adina D. Feinstein, Joshua E. Schlieder, Erik A. Petigura, Trevor J. David, Makennah Bristow, Rahul I. Patel, Lauren Arnold, Björn Benneke, Jessie L. Christiansen, Courtney D. Dressing, Benjamin J. Fulton, Andrew W. Howard, Howard Isaacson, Evan Sinukoff, and Beverly Thackeray. K2-136: A Binary System in the Hyades Cluster Hosting a Neptune-sized Planet. *AJ*, 155(1):10, January 2018. doi: 10.3847/1538-3881/aa9921.

Ryan Cloutier and Kristen Menou. Evolution of the Radius Valley around Low-mass Stars from Kepler and K2. *AJ*, 159(5):211, May 2020. doi: 10.3847/1538-3881/ab8237.

Ryan Cloutier, David Charbonneau, Drake Deming, Xavier Bonfils, and Nicola Astudillo-Defru. A More Precise Mass for GJ 1214 b and the Frequency of Multiplanet Systems Around Mid-M Dwarfs. *AJ*, 162(5):174, November 2021. doi: 10.3847/1538-3881/ac1584.

M. Coffaro, B. Stelzer, S. Orlando, J. Hall, T. S. Metcalfe, U. Wolter, M. Mittag, J. Sanz-Forcada, P. C. Schneider, and L. Ducci. An X-ray activity cycle on the young solar-like star epsilon Eridani. *A&A*, 636:A49, April 2020. doi: 10.1051/0004-6361/201936479.

Martina Coffaro, Beate Stelzer, and Salvatore Orlando. Characterizing X-ray activity cycles of young solar-like stars with solar observations. *Astronomische Nachrichten*, 343(4):e10066, May 2022. doi: 10.1002/asna.20210066.

N. Craig, M. Abbott, D. Finley, H. Jessop, S. B. Howell, M. Mathioudakis, J. Sommers, J. V. Vallerga, and R. F. Malina. The Extreme Ultraviolet Explorer Stellar Spectral Atlas. *ApJS*, 113(1):131–193, November 1997. doi: 10.1086/313052.

Steven R. Cranmer and Steven H. Saar. Testing a Predictive Theoretical Model for the Mass Loss Rates of Cool Stars. *ApJ*, 741(1):54, November 2011. doi: 10.1088/0004-637X/741/1/54.

Ian J. M. Crossfield, Diana Dragomir, Nicolas B. Cowan, Tansu Daylan, Ian Wong, Tiffany Kataria, Drake Deming, Laura Kreidberg, Thomas Mikal-Evans, Varoujan Gorjian, James S. Jenkins, Björn Benneke, Karen A. Collins, Christopher J. Burke, Christopher E. Henze, Scott McDermott, Ismael Mireles, David Watanabe, Bill Wohler, George Ricker, Roland Vanderspek, Sara Seager, and Jon M. Jenkins. Phase Curves of Hot Neptune LTT 9779b Suggest a High-metallicity Atmosphere. *ApJ*, 903(1):L7, November 2020. doi: 10.3847/2041-8213/abbc71.

P. E. Cubillos, L. Fossati, T. Koskinen, C. Huang, A. G. Sreejith, K. France, P. Wilson Cauley, and C. A. Haswell. The Hubble/STIS near-ultraviolet transmission spectrum of HD 189733 b. *A&A*, 671:A170, March 2023. doi: 10.1051/0004-6361/202245064.

Patricio E. Cubillos, Luca Fossati, Tommi Koskinen, Mitchell E. Young, Michael Salz, Kevin France, A. G. Sreejith, and Carole A. Haswell. Near-ultraviolet Transmission Spectroscopy of HD 209458b: Evidence of Ionized Iron Beyond the Planetary Roche Lobe. *AJ*, 159(3):111, March 2020. doi: 10.3847/1538-3881/ab6a0b.

Jason L. Curtis, Marcel A. Agüeros, Eric E. Mamajek, Jason T. Wright, and Jeffrey D. Cummings. TESS Reveals that the Nearby Pisces-Eridanus Stellar Stream is only 120 Myr Old. *AJ*, 158(2):77, August 2019. doi: 10.3847/1538-3881/ab2899.

R. M. Cutri, M. F. Skrutskie, S. van Dyk, C. A. Beichman, J. M. Carpenter, T. Chester, L. Cambresy, T. Evans, J. Fowler, J. Gizis, E. Howard, J. Huchra, T. Jarrett, E. L. Kopan, J. D. Kirkpatrick, R. M. Light, K. A. Marsh, H. McCallon, S. Schneider, R. Stiening, M. Sykes, M. Weinberg, W. A. Wheaton, S. Wheelock, and N. Zacarias. VizieR Online Data Catalog: 2MASS All-Sky Catalog of Point Sources (Cutri+ 2003). *VizieR Online Data Catalog*, art. II/246, June 2003.

S. Czesla, M. Lampón, J. Sanz-Forcada, A. García Muñoz, M. López-Puertas, L. Nortmann, D. Yan, E. Nagel, F. Yan, J. H. M. M. Schmitt, J. Aceituno, P. J. Amado, J. A. Caballero, N. Casasayas-Barris, Th. Henning, S. Khalafinejad, K. Molaverdikhani, D. Montes, E. Pallé, A. Reiners, P. C. Schneider, I. Ribas, A. Quirrenbach, M. R. Zapatero Osorio, and M. Zechmeister. Hα and He I absorption in HAT-P-32 b observed with CARMENES. Detection of Roche lobe overflow and mass loss. *A&A*, 657:A6, January 2022. doi: 10.1051/0004-6361/202039919.

Gennaro D'Angelo and Jack J. Lissauer. Formation of Giant Planets. In Hans J. Deeg and Juan Antonio Belmonte, editors, *Handbook of Exoplanets*, page 140. 2018. doi: 10.1007/978-3-319-55333-7_140.

James R. A. Davenport and Kevin R. Covey. Rotating Stars from Kepler Observed with Gaia DR2. *ApJ*, 868(2):151, December 2018. doi: 10.3847/1538-4357/aae842.

Timothy A. Davis and Peter J. Wheatley. Evidence for a lost population of close-in exoplanets. *MNRAS*, 396(2):1012–1017, June 2009. doi: 10.1111/j.1365-2966.2009.14763.x.

Rebekah I. Dawson and John Asher Johnson. Origins of Hot Jupiters. *ARA&A*, 56:175–221, September 2018. doi: 10.1146/annurev-astro-081817-051853.

Giulio Del Zanna and Helen E. Mason. Solar UV and X-ray spectral diagnostics. *Living Reviews in Solar Physics*, 15(1):5, December 2018. doi: 10.1007/s41116-018-0015-3.

O. D. S. Demangeon, F. Faedi, G. Hébrard, D. J. A. Brown, S. C. C. Barros, A. P. Doyle, P. F. L. Maxted, A. Collier Cameron, K. L. Hay, J. Alikakos, D. R. Anderson, D. J. Armstrong, P. Boumis, A. S. Bonomo, F. Bouchy, L. Delrez, M. Gillon, C. A. Haswell, C. Hellier, E. Jehin, F. Kiefer, K. W. F. Lam, M. Lendl, L. Mancini, J. McCormac, A. J. Norton, H. P. Osborn, E. Palle, F. Pepe, D. L. Pollacco, J. Prieto-Arranz, D. Queloz, D. Ségransan, B. Smalley, A. H. M. J. Triaud, S. Udry, R. West, and P. J. Wheatley. The discovery of WASP-151b, WASP-153b, WASP-156b: Insights on giant planet migration and the upper boundary of the Neptunian desert. *A&A*, 610:A63, March 2018. doi: 10.1051/0004-6361/201731735.

Robert C. Dempsey, Jeffrey L. Linsky, Thomas A. Fleming, and J. H. M. M. Schmitt. The ROSAT All-Sky Survey of Active Binary Coronae. I. Quiescent Fluxes for the RS Canum Venaticorum Systems. *ApJS*, 86:599, June 1993. doi: 10.1086/191791.

Robert C. Dempsey, Jeffrey L. Linsky, Thomas A. Fleming, and J. H. M. M. Schmitt. The ROSAT All-Sky Survey of Active Binary Coronae. III. Quiescent Coronal Properties for the BY Draconis-Type Binaries. *ApJ*, 478(1):358–366, March 1997. doi: 10.1086/303786.

V. Domingo, I. Ermolli, P. Fox, C. Fröhlich, M. Haberreiter, N. Krivova, G. Kopp, W. Schmutz, S. K. Solanki, H. C. Spruit, Y. Unruh, and A. Vögler. Solar Surface Magnetism and Irradiance on Time Scales from Days to the 11-Year Cycle. *Space Sci. Rev.*, 145(3-4):337–380, July 2009. doi: 10.1007/s11214-009-9562-1.

L. A. dos Santos, V. Bourrier, D. Ehrenreich, J. Sanz-Forcada, M. López-Morales, D. K. Sing, A. García Muñoz, G. W. Henry, P. Lavvas, A. Lecavelier des Etangs, T. Mikal-Evans, A. Vidal-Madjar, and H. R. Wakeford. HST PanCET program: non-detection of atmospheric escape in the warm Saturn-sized planet WASP-29 b. *A&A*, 649:A40, May 2021. doi: 10.1051/0004-6361/202140491.

Leonardo A. Dos Santos. Observations of planetary winds and outflows. In Aline A. Vidotto, Luca Fossati, and Jorick S. Vink, editors, *Winds of Stars and Exoplanets*, volume 370, pages 56–71, January 2023. doi: 10.1017/S1743921322004239.

Aaron Dotter, Brian Chaboyer, Darko Jevremović, Veselin Kostov, E. Baron, and Jason W. Ferguson. The Dartmouth Stellar Evolution Database. *ApJS*, 178(1): 89–101, September 2008. doi: 10.1086/589654.

Diana Dragomir, Ian J. M. Crossfield, Björn Benneke, Ian Wong, Tansu Daylan, Matias Diaz, Drake Deming, Paul Molliere, Laura Kreidberg, James S. Jenkins, David Berardo, Jessie L. Christiansen, Courtney D. Dressing, Varoujan Gorjian, Stephen R. Kane, Thomas Mikal-Evans, Farisa Y. Morales, Michael Werner, George R. Ricker, Roland Vanderspek, S. Seager, Joshua N. Winn, Jon M. Jenkins, Knicole D. Colón, Willie Fong, Natalia Guerrero, Katharine Hesse, Hugh P. Osborn, Mark E. Rose, Jeffrey C. Smith, and Eric B. Ting. Spitzer Reveals Evidence of Molecular Absorption in the Atmosphere of the Hot Neptune LTT 9779b. *ApJ*, 903(1):L6, November 2020. doi: 10.3847/2041-8213/abbc70.

X. Dumusque, S. Udry, C. Lovis, N. C. Santos, and M. J. P. F. G. Monteiro. Planetary detection limits taking into account stellar noise. I. Observational strategies to reduce stellar oscillation and granulation effects. *A&A*, 525:A140, January 2011. doi: 10.1051/0004-6361/201014097.

Gordian Edenhofer, Catherine Zucker, Philipp Frank, Andrew K. Saydjari, Joshua S. Speagle, Douglas Finkbeiner, and Torsten A. Enßlin. A parsec-scale Galactic 3D dust map out to 1.25 kpc from the Sun. *A&A*, 685:A82, May 2024. doi: 10.1051/0004-6361/202347628.

Bengt Edlén. Die Deutung der Emissionslinien im Spektrum der Sonnenkorona. Mit 6 Abbildungen. *Z. Astrophys.*, 22:30, January 1943.

Billy Edwards, Quentin Changeat, Angelos Tsiaras, Andrew Allan, Patrick Behr, Simone R. Hagey, Michael D. Himes, Sushuang Ma, Keivan G. Stassun, Luis Thomas, Alexandra Thompson, Aaron Boley, Luke Booth, Jeroen Bouwman, Kevin France, Nataliea Lowson, Annabella Meech, Caprice L. Phillips, Aline A. Vidotto, Kai Hou Yip, Michelle Bieger, Amelie Gressier, Estelle Janin, Ing-Guey Jiang, Pietro Leonardi, Subhajit Sarkar, Nour Skaf, Jake Taylor, Ming Yang, and Derek Ward-Thompson. Characterising a World Within the Hot Neptune Desert: Transit Observations of LTT 9779 b with HST WFC3. *arXiv e-prints*, art. arXiv:2306.13645, June 2023. doi: 10.48550/arXiv.2306.13645.

D. Ehrenreich, V. Bourrier, X. Bonfils, A. Lecavelier des Etangs, G. Hébrard, D. K. Sing, P. J. Wheatley, A. Vidal-Madjar, X. Delfosse, S. Udry, T. Forveille, and C. Moutou. Hint of a transiting extended atmosphere on 55 Cancri b. *A&A*, 547:A18, November 2012. doi: 10.1051/0004-6361/201219981.

David Ehrenreich, Vincent Bourrier, Peter J. Wheatley, Alain Lecavelier des Etangs, Guillaume Hébrard, Stéphane Udry, Xavier Bonfils, Xavier Delfosse, Jean-Michel Désert, David K. Sing, and Alfred Vidal-Madjar. A giant comet-like cloud of hydrogen escaping the warm Neptune-mass exoplanet GJ 436b. *Nature*, 522(7557):459–461, June 2015. doi: 10.1038/nature14501.

Scott G. Engle. Living with a Red Dwarf: X-Ray, UV, and Ca II Activity-Age Relationships of M Dwarfs. *ApJ*, 960(1):62, January 2024. doi: 10.3847/1538-4357/ad0840.

R. Erdélyi and I. Ballai. Heating of the solar and stellar coronae: a review. *Astronomische Nachrichten*, 328(8):726–733, October 2007. doi: 10.1002/asna.200710803.

N. V. Erkaev, Yu. N. Kulikov, H. Lammer, F. Selsis, D. Langmayr, G. F. Jaritz, and H. K. Biernat. Roche lobe effects on the atmospheric loss from "Hot Jupiters". *A&A*, 472(1):329–334, September 2007. doi: 10.1051/0004-6361:20066929.

C. Fabricius, X. Luri, F. Arenou, C. Babusiaux, A. Helmi, T. Muraveva, C. Reylé, F. Spoto, A. Vallenari, T. Antoja, E. Balbinot, C. Barache, N. Bauchet, A. Bragaglia, D. Busonero, T. Cantat-Gaudin, J. M. Carrasco, S. Diakité, M. Fabrizio, F. Figueras, A. Garcia-Gutierrez, A. Garofalo, C. Jordi, P. Kervella, S. Khanna, N. Leclerc, E. Licata, S. Lambert, P. M. Marrese, A. Masip, P. Ramos, N. Robichon, A. C. Robin, M. Romero-Gómez, S. Rubele, and M. Weiler. Gaia Early Data Release 3. Catalogue validation. *A&A*, 649:A5, May 2021a. doi: 10.1051/0004-6361/202039834.

C. Fabricius, X. Luri, F. Arenou, C. Babusiaux, A. Helmi, T. Muraveva, C. Reylé, F. Spoto, A. Vallenari, T. Antoja, E. Balbinot, C. Barache, N. Bauchet, A. Bragaglia, D. Busonero, T. Cantat-Gaudin, J. M. Carrasco, S. Diakité, M. Fabrizio, F. Figueras, A. Garcia-Gutierrez, A. Garofalo, C. Jordi, P. Kervella, S. Khanna, N. Leclerc, E. Licata, S. Lambert, P. M. Marrese, A. Masip, P. Ramos, N. Robichon, A. C. Robin, M. Romero-Gómez, S. Rubele, and M. Weiler. Gaia Early Data Release 3. Catalogue validation. *A&A*, 649:A5, May 2021b. doi: 10.1051/0004-6361/202039834.

J. P. Faria, R. D. Haywood, B. J. Brewer, P. Figueira, M. Oshagh, A. Santerne, and N. C. Santos. Uncovering the planets and stellar activity of CoRoT-7 using only radial velocities. *A&A*, 588:A31, April 2016. doi: 10.1051/0004-6361/201527899.

J. Farihi, L. Fossati, P. J. Wheatley, B. D. Metzger, J. Mauerhan, S. Bachman, B. T. Gänsicke, S. Redfield, P. W. Cauley, O. Kochukhov, N. Achilleos, and N. Stone. Magnetism, X-rays and accretion rates in WD 1145+017 and other polluted white dwarf systems. *MNRAS*, 474(1):947–960, February 2018. doi: 10.1093/mnras/stx2664.

D. Fedele, M. E. van den Ancker, Th. Henning, R. Jayawardhana, and J. M. Oliveira. Timescale of mass accretion in pre-main-sequence stars. *A&A*, 510: A72, February 2010. doi: 10.1051/0004-6361/200912810.

U. Feldman. Elemental abundances in the upper solar atmosphere. *Phys. Scr.*, 46 (3):202–220, September 1992. doi: 10.1088/0031-8949/46/3/002.

Jorge Fernández Fernández, Peter J. Wheatley, and George W. King. The shared evaporation history of three sub-Neptunes spanning the radius-period valley of a hyades star. *MNRAS*, 522(3):4251–4264, July 2023a. doi: 10.1093/mnras/stad1257.

Jorge Fernández Fernández, Peter J. Wheatley, and George W. King. The shared evaporation history of three sub-Neptunes spanning the radius-period valley of a hyades star. *MNRAS*, 522(3):4251–4264, July 2023b. doi: 10.1093/mnras/stad1257.

J. J. Fortney, M. S. Marley, and J. W. Barnes. Planetary Radii across Five Orders of Magnitude in Mass and Stellar Insolation: Application to Transits. *ApJ*, 659 (2):1661–1672, April 2007. doi: 10.1086/512120.

L. Fossati, C. A. Haswell, C. S. Froning, L. Hebb, S. Holmes, U. Kolb, Ch. Helling, A. Carter, P. Wheatley, A. Collier Cameron, B. Loeillet, D. Pollacco, R. Street, H. C. Stempels, E. Simpson, S. Udry, Y. C. Joshi, R. G. West, I. Skillen, and D. Wilson. Metals in the Exosphere of the Highly Irradiated Planet WASP-12b. *ApJ*, 714(2):L222–L227, May 2010. doi: 10.1088/2041-8205/714/2/L222.

L. Fossati, N. V. Erkaev, H. Lammer, P. E. Cubillos, P. Odert, I. Juvan, K. G. Kislyakova, M. Lendl, D. Kubyshkina, and S. J. Bauer. Aeronomical constraints to the minimum mass and maximum radius of hot low-mass planets. *A&A*, 598: A90, February 2017. doi: 10.1051/0004-6361/201629716.

Kevin France, R. O. Parke Loyd, Allison Youngblood, Alexander Brown, P. Christian Schneider, Suzanne L. Hawley, Cynthia S. Froning, Jeffrey L. Linsky, Aki Roberge, Andrea P. Buccino, James R. A. Davenport, Juan M. Fontenla, Lisa Kaltenegger, Adam F. Kowalski, Pablo J. D. Mauas, Yamila Miguel, Seth Redfield, Sarah Rugheimer, Feng Tian, Mariela C. Vieytes, Lucianne M. Walkowicz, and Kolby L. Weisenburger. The MUSCLES Treasury Survey. I. Motivation and Overview. *ApJ*, 820(2):89, April 2016. doi: 10.3847/0004-637X/820/2/89.

S. Freund, J. Robrade, P. C. Schneider, and J. H. M. M. Schmitt. Updated X-ray view of the Hyades cluster. *A&A*, 640:A66, August 2020. doi: 10.1051/0004-6361/201937304.

Benjamin J. Fulton, Erik A. Petigura, Andrew W. Howard, Howard Isaacson, Geoffrey W. Marcy, Phillip A. Cargile, Leslie Hebb, Lauren M. Weiss, John Asher Johnson, Timothy D. Morton, Evan Sinukoff, Ian J. M. Crossfield, and Lea A. Hirsch. The California-Kepler Survey. III. A Gap in the Radius Distribution of Small Planets. *AJ*, 154(3):109, September 2017. doi: 10.3847/1538-3881/aa80eb.

Gaia Collaboration, T. Prusti, J. H. J. de Bruijne, A. G. A. Brown, A. Vallenari, C. Babusiaux, C. A. L. Bailer-Jones, U. Bastian, M. Biermann, D. W. Evans, L. Eyer, F. Jansen, C. Jordi, S. A. Klioner, U. Lammers, L. Lindegren, X. Luri, and F. Mignard. The Gaia mission. *A&A*, 595:A1, November 2016. doi: 10.1051/0004-6361/201629272.

Gaia Collaboration, C. Babusiaux, F. van Leeuwen, M. A. Barstow, C. Jordi, A. Vallenari, D. Bossini, A. Bressan, T. Cantat-Gaudin, M. van Leeuwen, A. G. A. Brown, T. Prusti, J. H. J. de Bruijne, C. A. L. Bailer-Jones, M. Biermann, D. W. Evans, L. Eyer, F. Jansen, S. A. Klioner, U. Lammers, L. Lindegren, X. Luri, F. Mignard, C. Panem, D. Pourbaix, S. Randich, P. Sartoretti, H. I. Siddiqui, C. Soubiran, N. A. Walton, F. Arenou, U. Bastian, M. Cropper, R. Drimmel, D. Katz, M. G. Lattanzi, J. Bakker, C. Cacciari, J. Castañeda, L. Chaoul, N. Cheek, F. De Angeli, C. Fabricius, R. Guerra, B. Holl, E. Masana, R. Messineo, N. Mowlavi, K. Nienartowicz, P. Panuzzo, J. Portell, M. Riello, G. M. Seabroke, P. Tanga, F. Thévenin, G. Gracia-Abril, G. Comoretto, M. Garcia-Reinaldos, D. Teyssier, M. Altmann, R. Andrae, M. Audard, I. Bellas-Velidis, K. Benson, J. Berthier, R. Blomme, P. Burgess, G. Busso, B. Carry, A. Cellino, G. Clementini, M. Clotet, O. Creevey, M. Davidson, J. De Ridder, L. Delchambre, A. Dell'Oro, C. Ducourant, J. Fernández-Hernández, M. Fouesneau, Y. Frémat, L. Galluccio, M. García-Torres, J. González-Núñez, J. J. González-Vidal, E. Gosset, L. P. Guy, J. L. Halbwachs, N. C. Hambly, D. L. Harrison, J. Hernández, D. Hestroffer, S. T. Hodgkin, A. Hutton, G. Jasniewicz, A. Jean-Antoine-Piccolo, S. Jordan, A. J. Korn, A. Krone-Martins, A. C. Lanzafame, T. Lebzelter, W. Löffler, M. Manteiga, P. M. Marrese, J. M. Martín-Fleitas, A. Moitinho, A. Mora, K. Muinonen, J. Osinde, E. Pancino, T. Pauwels, J. M. Petit, A. Recio-Blanco, P. J. Richards, L. Rimoldini, A. C. Robin, L. M. Sarro, C. Siopis, M. Smith, A. Sozzetti, M. Süveges, J. Torra, W. van Reeven, U. Abbas, A. Abreu Aramburu, S. Accart, C. Aerts, G. Altavilla, M. A. Álvarez, R. Alvarez, J. Alves, R. I. Anderson, A. H. Andrei, E. Anglada Varela, E. Antiche, T. Antoja, B. Arcay, T. L. Astraatmadja,

N. Bach, S. G. Baker, L. Balaguer-Núñez, P. Balm, C. Barache, C. Barata, D. Barbato, F. Barblan, P. S. Barklem, D. Barrado, M. Barros, L. Bartholomé Muñoz, J. L. Bassilana, U. Becciani, M. Bellazzini, A. Berihuete, S. Bertone, L. Bianchi, O. Bienaymé, S. Blanco-Cuaresma, T. Boch, C. Boeche, A. Bombrun, R. Borrachero, S. Bouquillon, G. Bourda, A. Bragaglia, L. Bramante, M. A. Breddels, N. Brouillet, T. Brüsemeister, E. Brugaletta, B. Bucciarelli, A. Burlacu, D. Busonero, A. G. Butkevich, R. Buzzi, E. Caffau, R. Cancelliere, G. Cannizzaro, R. Carballo, T. Carlucci, J. M. Carrasco, L. Casamiquela, M. Castellani, A. Castro-Ginard, P. Charlot, L. Chemin, A. Chiavassa, G. Cocozza, G. Costigan, S. Cowell, F. Crifo, M. Crosta, C. Crowley, J. Cuypers, C. Dafonte, Y. Damerdji, A. Dapergolas, P. David, M. David, P. de Laverny, F. De Luise, R. De March, D. de Martino, R. de Souza, A. de Torres, J. Debosscher, E. del Pozo, M. Delbo, A. Delgado, H. E. Delgado, S. Diakite, C. Diener, E. Distefano, C. Dolding, P. Drazinos, J. Durán, B. Edvardsson, H. Enke, K. Eriksson, P. Esquej, G. Eynard Bontemps, C. Fabre, M. Fabrizio, S. Faigler, A. J. Falcão, M. Farràs Casas, L. Federici, G. Fedorets, P. Fernique, F. Figueras, F. Filippi, K. Findeisen, A. Fonti, E. Fraile, M. Fraser, B. Frézouls, M. Gai, S. Galleti, D. Garabato, F. García-Sedano, A. Garofalo, N. Garralda, A. Gavel, P. Gavras, J. Gerssen, R. Geyer, P. Giacobbe, G. Gilmore, S. Girona, G. Giuffrida, F. Glass, M. Gomes, M. Granvik, A. Gueguen, A. Guerrier, J. Guiraud, R. Gutié, R. Haigron, D. Hatzidimitriou, M. Hauser, M. Haywood, U. Heiter, A. Helmi, J. Heu, T. Hilger, D. Hobbs, W. Hofmann, G. Holland, H. E. Huckle, A. Hypki, V. Icardi, K. Janßen, G. Jevardat de Fombelle, P. G. Jonker, Á. L. Juhász, F. Julbe, A. Karampelas, A. Kewley, J. Klar, A. Kochoska, R. Kohley, K. Kolenberg, M. Kontizas, E. Kontizas, S. E. Koposov, G. Kordopatis, Z. Kostrzewa-Rutkowska, P. Koubsky, S. Lambert, A. F. Lanza, Y. Lasne, J. B. Lavigne, Y. Le Fustec, C. Le Poncin-Lafitte, Y. Lebreton, S. Leccia, N. Leclerc, I. Lecoeur-Taibi, H. Lenhardt, F. Leroux, S. Liao, E. Licata, H. E. P. Lindstrøm, T. A. Lister, E. Livanou, A. Lobel, M. López, S. Managau, R. G. Mann, G. Mantelet, O. Marchal, J. M. Marchant, M. Marconi, S. Marinoni, G. Marschalkó, D. J. Marshall, M. Martino, G. Marton, N. Mary, D. Massari, G. Matijevič, T. Mazeh, P. J. McMillan, S. Messina, D. Michalik, N. R. Millar, D. Molina, R. Molinaro, L. Molnár, P. Montegriffo, R. Mor, R. Morbidelli, T. Morel, D. Morris, A. F. Mulone, T. Muraveva, I. Musella, G. Nelemans, L. Nicastro, L. Noval, W. O'Mullane, C. Ordénovic, D. Ordóñez-Blanco, P. Osborne, C. Pagani, I. Pagano, F. Pailler, H. Palacin, L. Palaversa, A. Panahi, M. Pawlak, A. M.

Piersimoni, F. X. Pineau, E. Plachy, G. Plum, E. Poggio, E. Poujoulet, A. Prša, L. Pulone, E. Racero, S. Ragaini, N. Rambaux, M. Ramos-Lerate, S. Regibo, C. Reylé, F. Riclet, V. Ripepi, A. Riva, A. Rivard, G. Rixon, T. Roegiers, M. Roelens, M. Romero-Gómez, N. Rowell, F. Royer, L. Ruiz-Dern, G. Sadowski, T. Sagristà Sellés, J. Sahlmann, J. Salgado, E. Salguero, N. Sanna, T. Santana-Ros, M. Sarasso, H. Savietto, M. Schultheis, E. Sciacca, M. Segol, J. C. Segovia, D. Ségransan, I. C. Shih, L. Siltala, A. F. Silva, R. L. Smart, K. W. Smith, E. Solano, F. Solitro, R. Sordo, S. Soria Nieto, J. Souchay, A. Spagna, F. Spoto, U. Stampa, I. A. Steele, H. Steidelmüller, C. A. Stephenson, H. Stoev, F. F. Suess, J. Surdej, L. Szabados, E. Szegedi-Elek, D. Tapiador, F. Taris, G. Tauran, M. B. Taylor, R. Teixeira, D. Terrett, P. Teyssandier, W. Thuillot, A. Titarenko, F. Torra Clotet, C. Turon, A. Ulla, E. Utrilla, S. Uzzi, M. Vaillant, G. Valentini, V. Valette, A. van Elteren, E. Van Hemelryck, M. Vaschetto, A. Vecchiato, J. Veljanoski, Y. Viala, D. Vicente, S. Vogt, C. von Essen, H. Voss, V. Votruba, S. Voutsinas, G. Walmsley, M. Weiler, O. Wertz, T. Wevers, Ł. Wyrzykowski, A. Yoldas, M. Žerjal, H. Ziaeepour, J. Zorec, S. Zschocke, S. Zucker, C. Zurbach, and T. Zwitter. Gaia Data Release 2. Observational Hertzsprung-Russell diagrams. *A&A*, 616:A10, August 2018a. doi: 10.1051/0004-6361/201832843.

Gaia Collaboration, A. G. A. Brown, A. Vallenari, T. Prusti, J. H. J. de Bruijne, C. Babusiaux, C. A. L. Bailer-Jones, M. Biermann, D. W. Evans, L. Eyer, F. Jansen, C. Jordi, S. A. Klioner, U. Lammers, L. Lindegren, X. Luri, F. Mignard, C. Panem, D. Pourbaix, S. Randich, P. Sartoretti, H. I. Siddiqui, C. Soubiran, F. van Leeuwen, N. A. Walton, F. Arenou, U. Bastian, M. Cropper, R. Drimmel, D. Katz, M. G. Lattanzi, J. Bakker, C. Cacciari, J. Castañeda, L. Chaoul, N. Cheek, F. De Angeli, C. Fabricius, R. Guerra, B. Holl, E. Masana, R. Messineo, N. Mowlavi, K. Nienartowicz, P. Panuzzo, J. Portell, M. Riello, G. M. Seabroke, P. Tanga, F. Thévenin, G. Gracia-Abril, G. Comoretto, M. Garcia-Reinaldos, D. Teyssier, M. Altmann, R. Andrae, M. Audard, I. Bellas-Velidis, K. Benson, J. Berthier, R. Blomme, P. Burgess, G. Busso, B. Carry, A. Cellino, G. Clementini, M. Clotet, O. Creevey, M. Davidson, J. De Ridder, L. Delchambre, A. Dell'Oro, C. Ducourant, J. Fernández-Hernández, M. Fouesneau, Y. Frémat, L. Galluccio, M. García-Torres, J. González-Núñez, J. J. González-Vidal, E. Gosset, L. P. Guy, J. L. Halbwachs, N. C. Hambly, D. L. Harrison, J. Hernández, D. Hestroffer, S. T. Hodgkin, A. Hutton, G. Jasniewicz, A. Jean-Antoine-Piccolo, S. Jordan, A. J. Korn, A. Krone-Martins,

A. C. Lanzafame, T. Lebzelter, W. Löffler, M. Manteiga, P. M. Marrese, J. M. Martín-Fleitas, A. Moitinho, A. Mora, K. Muinonen, J. Osinde, E. Pancino, T. Pauwels, J. M. Petit, A. Recio-Blanco, P. J. Richards, L. Rimoldini, A. C. Robin, L. M. Sarro, C. Siopis, M. Smith, A. Sozzetti, M. Süveges, J. Torra, W. van Reeven, U. Abbas, A. Abreu Aramburu, S. Accart, C. Aerts, G. Altavilla, M. A. Álvarez, R. Alvarez, J. Alves, R. I. Anderson, A. H. Andrei, E. Anglada Varela, E. Antiche, T. Antoja, B. Arcay, T. L. Astraatmadja, N. Bach, S. G. Baker, L. Balaguer-Núñez, P. Balm, C. Barache, C. Barata, D. Barbato, F. Barblan, P. S. Barklem, D. Barrado, M. Barros, M. A. Barstow, S. Bartholomé Muñoz, J. L. Bassilana, U. Becciani, M. Bellazzini, A. Berihuete, S. Bertone, L. Bianchi, O. Bienaymé, S. Blanco-Cuaresma, T. Boch, C. Boeche, A. Bombrun, R. Borrachero, D. Bossini, S. Bouquillon, G. Bourda, A. Bragaglia, L. Bramante, M. A. Breddels, A. Bressan, N. Brouillet, T. Brüsemeister, E. Brugaletta, B. Bucciarelli, A. Burlacu, D. Busonero, A. G. Butkevich, R. Buzzi, E. Caffau, R. Cancelliere, G. Cannizzaro, T. Cantat-Gaudin, R. Carballo, T. Carlucci, J. M. Carrasco, L. Casamiquela, M. Castellani, A. Castro-Ginard, P. Charlot, L. Chemin, A. Chiavassa, G. Cocozza, G. Costigan, S. Cowell, F. Crifo, M. Crosta, C. Crowley, J. Cuypers, C. Dafonte, Y. Damerdji, A. Dapergolas, P. David, M. David, P. de Laverny, F. De Luise, R. De March, D. de Martino, R. de Souza, A. de Torres, J. Debosscher, E. del Pozo, M. Delbo, A. Delgado, H. E. Delgado, P. Di Matteo, S. Diakite, C. Diener, E. Distefano, C. Dolding, P. Drazinos, J. Durán, B. Edvardsson, H. Enke, K. Eriksson, P. Esquej, G. Eynard Bontemps, C. Fabre, M. Fabrizio, S. Faigler, A. J. Falcão, M. Farràs Casas, L. Federici, G. Fedorets, P. Fernique, F. Figueras, F. Filippi, K. Findeisen, A. Fonti, E. Fraile, M. Fraser, B. Frézouls, M. Gai, S. Galleti, D. Garabato, F. García-Sedano, A. Garofalo, N. Garralda, A. Gavel, P. Gavras, J. Gerssen, R. Geyer, P. Giacobbe, G. Gilmore, S. Girona, G. Giuffrida, F. Glass, M. Gomes, M. Granvik, A. Gueguen, A. Guerrier, J. Guiraud, R. Gutiérrez-Sánchez, R. Haigron, D. Hatzidimitriou, M. Hauser, M. Haywood, U. Heiter, A. Helmi, J. Heu, T. Hilger, D. Hobbs, W. Hofmann, G. Holland, H. E. Huckle, A. Hypki, V. Icardi, K. Janßen, G. Jevardat de Fombelle, P. G. Jonker, Á. L. Juhász, F. Julbe, A. Karampelas, A. Kewley, J. Klar, A. Kochoska, R. Kohley, K. Kolenberg, M. Kontizas, E. Kontizas, S. E. Koposov, G. Kordopatis, Z. Kostrzewa-Rutkowska, P. Koubsky, S. Lambert, A. F. Lanza, Y. Lasne, J. B. Lavigne, Y. Le Fustec, C. Le Poncin-Lafitte, Y. Lebreton, S. Leccia, N. Leclerc, I. Lecoeur-Taibi, H. Lenhardt, F. Leroux, S. Liao, E. Licata,

H. E. P. Lindstrøm, T. A. Lister, E. Livanou, A. Lobel, M. López, S. Managau, R. G. Mann, G. Mantelet, O. Marchal, J. M. Marchant, M. Marconi, S. Marinoni, G. Marschalkó, D. J. Marshall, M. Martino, G. Marton, N. Mary, D. Massari, G. Matijevič, T. Mazeh, P. J. McMillan, S. Messina, D. Michalik, N. R. Millar, D. Molina, R. Molinaro, L. Molnár, P. Montegriffo, R. Mor, R. Morbidelli, T. Morel, D. Morris, A. F. Mulone, T. Muraveva, I. Musella, G. Nelemans, L. Nicastro, L. Noval, W. O'Mullane, C. Ordénovic, D. Ordóñez-Blanco, P. Osborne, C. Pagani, I. Pagano, F. Pailler, H. Palacin, L. Palaversa, A. Panahi, M. Pawlak, A. M. Piersimoni, F. X. Pineau, E. Plachy, G. Plum, E. Poggio, E. Poujoulet, A. Prša, L. Pulone, E. Racero, S. Ragaini, N. Rambaux, M. Ramos-Lerate, S. Regibo, C. Reylé, F. Riclet, V. Ripepi, A. Riva, A. Rivard, G. Rixon, T. Roegiers, M. Roelens, M. Romero-Gómez, N. Rowell, F. Royer, L. Ruiz-Dern, G. Sadowski, T. Sagristà Sellés, J. Sahlmann, J. Salgado, E. Salguero, N. Sanna, T. Santana-Ros, M. Sarasso, H. Savietto, M. Schultheis, E. Sciacca, M. Segol, J. C. Segovia, D. Ségransan, I. C. Shih, L. Siltala, A. F. Silva, R. L. Smart, K. W. Smith, E. Solano, F. Solitro, R. Sordo, S. Soria Nieto, J. Souchay, A. Spagna, F. Spoto, U. Stampa, I. A. Steele, H. Steidelmüller, C. A. Stephenson, H. Stoev, F. F. Suess, J. Surdej, L. Szabados, E. Szegedi-Elek, D. Tapiador, F. Taris, G. Tauran, M. B. Taylor, R. Teixeira, D. Terrett, P. Teyssandier, W. Thuillot, A. Titarenko, F. Torra Clotet, C. Turon, A. Ulla, E. Utrilla, S. Uzzi, M. Vaillant, G. Valentini, V. Valette, A. van Elteren, E. Van Hemelryck, M. van Leeuwen, M. Vaschetto, A. Vecchiato, J. Veljanoski, Y. Viala, D. Vicente, S. Vogt, C. von Essen, H. Voss, V. Votruba, S. Voutsinas, G. Walmsley, M. Weiler, O. Wertz, T. Wevers, Ł. Wyrzykowski, A. Yoldas, M. Žerjal, H. Ziaeepour, J. Zorec, S. Zschocke, S. Zucker, C. Zurbach, and T. Zwitter. Gaia Data Release 2. Summary of the contents and survey properties. *A&A*, 616:A1, August 2018b. doi: 10.1051/0004-6361/201833051.

Gaia Collaboration, A. G. A. Brown, A. Vallenari, T. Prusti, J. H. J. de Bruijne, C. Babusiaux, and M. Biermann. Gaia Early Data Release 3: Summary of the contents and survey properties. *arXiv e-prints*, art. arXiv:2012.01533, December 2020.

Gaia Collaboration, A. Vallenari, A. G. A. Brown, T. Prusti, J. H. J. de Bruijne, F. Arenou, C. Babusiaux, M. Biermann, O. L. Creevey, C. Ducourant, D. W. Evans, L. Eyer, R. Guerra, A. Hutton, C. Jordi, S. A. Klioner, U. L. Lammers, and L. Lindegren. Gaia Data Release 3: Summary of the content and survey properties. *arXiv e-prints*, art. arXiv:2208.00211, July 2022.

A. García Muñoz. Physical and chemical aeronomy of HD 209458b. *Planet. Space Sci.*, 55(10):1426–1455, July 2007. doi: 10.1016/j.pss.2007.03.007.

B. Scott Gaudi, Keivan G. Stassun, Karen A. Collins, Thomas G. Beatty, George Zhou, David W. Latham, Allyson Bieryla, Jason D. Eastman, Robert J. Siverd, Justin R. Crepp, Erica J. Gonzales, Daniel J. Stevens, Lars A. Buchhave, Joshua Pepper, Marshall C. Johnson, Knicole D. Colon, Eric L. N. Jensen, Joseph E. Rodriguez, Valerio Bozza, Sebastiano Calchi Novati, Giuseppe D'Ago, Mary T. Dumont, Tyler Ellis, Clement Gaillard, Hannah Jang-Condell, David H. Kasper, Akihiko Fukui, Joao Gregorio, Ayaka Ito, John F. Kielkopf, Mark Manner, Kyle Matt, Norio Narita, Thomas E. Oberst, Phillip A. Reed, Gaetano Scarpetta, Denice C. Stephens, Rex R. Yeigh, Roberto Zambelli, B. J. Fulton, Andrew W. Howard, David J. James, Matthew Penny, Daniel Bayliss, Ivan A. Curtis, D. L. Depoy, Gilbert A. Esquerdo, Andrew Gould, Michael D. Joner, Rudolf B. Kuhn, Jonathan Labadie-Bartz, Michael B. Lund, Jennifer L. Marshall, Kim K. McLeod, Richard W. Pogge, Howard Relles, Christopher Stockdale, T. G. Tan, Mark Trueblood, and Patricia Trueblood. A giant planet undergoing extreme-ultraviolet irradiation by its hot massive-star host. *Nature*, 546(7659):514–518, June 2017. doi: 10.1038/nature22392.

N. Gehrels, G. Chincarini, P. Giommi, K. O. Mason, J. A. Nousek, A. A. Wells, N. E. White, S. D. Barthelmy, D. N. Burrows, L. R. Cominsky, K. C. Hurley, F. E. Marshall, P. Mészáros, P. W. A. Roming, L. Angelini, L. M. Barbier, T. Belloni, S. Campana, P. A. Caraveo, M. M. Chester, O. Citterio, T. L. Cline, M. S. Cropper, J. R. Cummings, A. J. Dean, E. D. Feigelson, E. E. Fenimore, D. A. Frail, A. S. Fruchter, G. P. Garmire, K. Gendreau, G. Ghisellini, J. Greiner, J. E. Hill, S. D. Hunsberger, H. A. Krimm, S. R. Kulkarni, P. Kumar, F. Lebrun, N. M. Lloyd-Ronning, C. B. Markwardt, B. J. Mattson, R. F. Mushotzky, J. P. Norris, J. Osborne, B. Paczynski, D. M. Palmer, H. S. Park, A. M. Parsons, J. Paul, M. J. Rees, C. S. Reynolds, J. E. Rhoads, T. P. Sasseen, B. E. Schaefer, A. T. Short, A. P. Smale, I. A. Smith, L. Stella, G. Tagliaferri, T. Takahashi, M. Tashiro, L. K. Townsley, J. Tueller, M. J. L. Turner, M. Vietri, W. Voges, M. J. Ward, R. Willingale, F. M. Zerbi, and W. W. Zhang. The Swift Gamma-Ray Burst Mission. *ApJ*, 611(2):1005–1020, August 2004. doi: 10.1086/422091.

N. P. Gentile Fusillo, P. E. Tremblay, E. Cukanovaite, A. Vorontseva, R. Lallement, M. Hollands, B. T. Gänsicke, K. B. Burdge, J. McCleery, and S. Jordan. A catalogue of white dwarfs in Gaia EDR3. *MNRAS*, 508(3):3877–3896, December 2021. doi: 10.1093/mnras/stab2672.

R. Giacconi, G. Branduardi, U. Briel, A. Epstein, D. Fabricant, E. Feigelson, W. Forman, P. Gorenstein, J. Grindlay, H. Gursky, F. R. Harnden, J. P. Henry, C. Jones, E. Kellogg, D. Koch, S. Murray, E. Schreier, F. Seward, H. Tananbaum, K. Topka, L. Van Speybroeck, S. S. Holt, R. H. Becker, E. A. Boldt, P. J. Serlemitsos, G. Clark, C. Canizares, T. Markert, R. Novick, D. Helfand, and K. Long. The Einstein (HEAO 2) X-ray Observatory. *ApJ*, 230:540–550, June 1979. doi: 10.1086/157110.

Edward Gillen, Joshua T. Briegal, Simon T. Hodgkin, Daniel Foreman-Mackey, Floor Van Leeuwen, James A. G. Jackman, James McCormac, Richard G. West, Didier Queloz, Daniel Bayliss, Michael R. Goad, Christopher A. Watson, Peter J. Wheatley, Claudia Belardi, Matthew R. Burleigh, Sarah L. Casewell, James S. Jenkins, Liam Raynard, Alexis M. S. Smith, Rosanna H. Tilbrook, and Jose I. Vines. NGTS clusters survey - I. Rotation in the young benchmark open cluster Blanco 1. *MNRAS*, 492(1):1008–1024, February 2020. doi: 10.1093/mnras/stz3251.

Michaël Gillon, Amaury H. M. J. Triaud, Brice-Olivier Demory, Emmanuël Jehin, Eric Agol, Katherine M. Deck, Susan M. Lederer, Julien de Wit, Artem Burdanov, James G. Ingalls, Emeline Bolmont, Jeremy Leconte, Sean N. Raymond, Franck Selsis, Martin Turbet, Khalid Barkaoui, Adam Burgasser, Matthew R. Burleigh, Sean J. Carey, Aleksander Chaushev, Chris M. Copperwheat, Laetitia Delrez, Catarina S. Fernandes, Daniel L. Holdsworth, Enrico J. Kotze, Valérie Van Grootel, Yaseen Almleaky, Zouhair Benkhaldoun, Pierre Magain, and Didier Queloz. Seven temperate terrestrial planets around the nearby ultracool dwarf star TRAPPIST-1. *Nature*, 542(7642):456–460, February 2017. doi: 10.1038/nature21360.

P. A. Gilman. Dynamically consistent nonlinear dynamos driven by convection in a rotating spherical shell. II - Dynamos with cycles and strong feedbacks. *ApJS*, 53:243–268, October 1983. doi: 10.1086/190891.

Sivan Ginzburg, Hilke E. Schlichting, and Re'em Sari. Super-Earth Atmospheres:

Self-consistent Gas Accretion and Retention. *ApJ*, 825(1):29, July 2016. doi: 10.3847/0004-637X/825/1/29.

Sivan Ginzburg, Hilke E. Schlichting, and Re'em Sari. Core-powered mass-loss and the radius distribution of small exoplanets. *MNRAS*, 476(1):759–765, May 2018. doi: 10.1093/mnras/sty290.

Diego Godoy-Rivera, Marc H. Pinsonneault, and Luisa M. Rebull. Stellar Rotation in the Gaia Era: Revised Open Clusters' Sequences. *ApJS*, 257(2):46, December 2021. doi: 10.3847/1538-4365/ac2058.

Jonathan Goodman and Jonathan Weare. Ensemble samplers with affine invariance. *Communications in Applied Mathematics and Computational Science*, 5 (1):65–80, January 2010. doi: 10.2140/camcos.2010.5.65.

A. Gould, A. Udalski, D. An, D. P. Bennett, A. Y. Zhou, S. Dong, N. J. Rattenbury, B. S. Gaudi, P. C. M. Yock, I. A. Bond, G. W. Christie, K. Horne, J. Anderson, K. Z. Stanek, D. L. DePoy, C. Han, J. McCormick, B. G. Park, R. W. Pogge, S. D. Poindexter, I. Soszyński, M. K. Szymański, M. Kubiak, G. Pietrzyński, O. Szewczyk, Ł. Wyrzykowski, K. Ulaczyk, B. Paczyński, D. M. Bramich, C. Snodgrass, I. A. Steele, M. J. Burgdorf, M. F. Bode, C. S. Botzler, S. Mao, and S. C. Swaving. Microlens OGLE-2005-BLG-169 Implies That Cool Neptune-like Planets Are Common. *ApJ*, 644(1):L37–L40, June 2006. doi: 10.1086/505421.

W. Grotrian. Zur Frage der Deutung der Linien im Spektrum der Sonnenkorona. *Naturwissenschaften*, 27(13):214–214, March 1939. doi: 10.1007/BF01488890.

M. G. Guarcello, G. Micela, S. Sciortino, J. López-Santiago, C. Argiroffi, F. Reale, E. Flaccomio, J. D. Alvarado-Gómez, V. Antoniou, J. J. Drake, I. Pillitteri, L. M. Rebull, and J. Stauffer. Simultaneous Kepler/K2 and XMM-Newton observations of superflares in the Pleiades. *A&A*, 622:A210, February 2019. doi: 10.1051/0004-6361/201834370.

M. Güdel, S. L. Skinner, S. Yu. Mel'Nikov, M. Audard, A. Telleschi, and K. R. Briggs. X-rays from T Tauri: a test case for accreting T Tauri stars. *A&A*, 468 (2):529–540, June 2007. doi: 10.1051/0004-6361:20066318.

Manuel Güdel. X-ray astronomy of stellar coronae. *A&ARv*, 12(2-3):71–237, September 2004. doi: 10.1007/s00159-004-0023-2.

Manuel Güdel, Edward F. Guinan, and Stephen L. Skinner. The X-Ray Sun in Time: A Study of the Long-Term Evolution of Coronae of Solar-Type Stars. *ApJ*, 483(2):947–960, July 1997. doi: 10.1086/304264.

G. Guerrero, P. K. Smolarkiewicz, E. M. de Gouveia Dal Pino, A. G. Kosovichev, and N. N. Mansour. On the Role of Tachoclines in Solar and Stellar Dynamos. *ApJ*, 819(2):104, March 2016. doi: 10.3847/0004-637X/819/2/104.

J. H. Guo. Escaping Particle Fluxes in the Atmospheres of Close-in Exoplanets. I. Model of Hydrogen. *ApJ*, 733(2):98, June 2011. doi: 10.1088/0004-637X/733/2/98.

J. H. Guo. Escaping Particle Fluxes in the Atmospheres of Close-in Exoplanets. II. Reduced Mass-loss Rates and Anisotropic Winds. *ApJ*, 766(2):102, April 2013. doi: 10.1088/0004-637X/766/2/102.

Akash Gupta and Hilke E. Schlichting. Sculpting the valley in the radius distribution of small exoplanets as a by-product of planet formation: the core-powered mass-loss mechanism. *MNRAS*, 487(1):24–33, July 2019. doi: 10.1093/mnras/stz1230.

Akash Gupta and Hilke E. Schlichting. Signatures of the core-powered mass-loss mechanism in the exoplanet population: dependence on stellar properties and observational predictions. *MNRAS*, 493(1):792–806, March 2020. doi: 10.1093/mnras/staa315.

H. Gursky, H. Schnopper, and D. Parsignault. The hard X-ray experiment on the Astronomical Netherlands Satellite. *ApJ*, 201:L127–L131, November 1975. doi: 10.1086/181958.

Alejandro Hacker, Rodrigo F. Díaz, David J. Armstrong, Jorge Fernández Fernández, Simon Müller, Elisa Delgado-Mena, Sérgio G. Sousa, Vardan Adibekyan, Keivan G. Stassun, Karen A. Collins, Samuel W. Yee, Daniel Bayliss, Allyson Bieryla, François Bouchy, R. Paul Butler, Jeffrey D. Crane, Xavier Dumusque, Joel D. Hartman, Ravit Helled, Jon Jenkins, Marcelo Aron F. Keniger, Hannah Lewis, Jorge Lillo-Box, Michael B. Lund, Louise D. Nielsen, Ares Osborn, David Osip, Martin Paegert, Don J. Radford, Nuno C. Santos, Sara Seager, Stephen A. Shectman, Gregor Srdoc, Paul A. Strøm, Thiam-Guan Tan, Johanna K. Teske, Michael Vezie, David Watanabe, Cristilyn N. Watkins, Peter J. Wheatley, Joshua N. Winn, Bill Wohler, and Carl Ziegler. TOI-2374 b and TOI-3071 b: two metal-rich sub-Saturns well within the Neptunian desert. *MNRAS*, 532(2):1612–1634, August 2024. doi: 10.1093/mnras/stae1420.

Nathan C. Hara and Eric B. Ford. Statistical Methods for Exoplanet Detection with Radial Velocities. *Annual Review of Statistics and Its Application*, 10(1): 623–649, March 2023. doi: 10.1146/annurev-statistics-033021-012225.

J. D. Hartman, B. S. Gaudi, M. H. Pinsonneault, K. Z. Stanek, M. J. Holman, B. A. McLeod, S. Meibom, J. A. Barranco, and J. S. Kalirai. Deep MMT Transit Survey of the Open Cluster M37. III. Stellar Rotation at 550 Myr. *ApJ*, 691(1): 342–364, January 2009. doi: 10.1088/0004-637X/691/1/342.

J. D. Hartman, G. Á. Bakos, G. Kovács, and R. W. Noyes. A large sample of photometric rotation periods for FGK Pleiades stars. *MNRAS*, 408(1):475–489, October 2010. doi: 10.1111/j.1365-2966.2010.17147.x.

David H. Hathaway. The Solar Cycle. *Living Reviews in Solar Physics*, 7(1):1, December 2010. doi: 10.12942/lrsp-2010-1.

Faith Hawthorn, Daniel Bayliss, David J. Armstrong, Jorge Fernández Fernández, Ares Osborn, Sérgio G. Sousa, Vardan Adibekyan, Jeanne Davoult, Karen A. Collins, Yann Alibert, Susana C. C. Barros, François Bouchy, Matteo Brogi, David R. Ciardi, Tansu Daylan, Elisa Delgado Mena, Olivier D. S. Demangeon, Rodrigo F. Díaz, Tianjun Gan, Keith Horne, Sergio Hoyer, Jon M. Jenkins, Eric L. N. Jensen, John F. Kielkopf, Veselin Kostov, David W. Latham, Alan M. Levine, Jorge Lillo-Box, Louise D. Nielsen, Hugh P. Osborn, George R. Ricker, José Rodrigues, Nuno C. Santos, Richard P. Schwarz, Sara Seager, Juan Serrano Bell, Avi Shporer, Chris Stockdale, Paul A. Strøm, Peter Tenenbaum, Stéphane Udry, Peter J. Wheatley, Joshua N. Winn, and Carl Ziegler. TOI-908: a planet at the edge of the Neptune desert transiting a G-type star. *MNRAS*, 524(3): 3877–3893, September 2023. doi: 10.1093/mnras/stad1840.

Hisashi Hayakawa, Sabrina Bechet, Frédéric Clette, Hugh S. Hudson, Hiroyuki Maehara, Kosuke Namekata, and Yuta Notsu. Magnitude Estimates for the Carrington Flare in 1859 September: As Seen from the Original Records. *ApJ*, 954(1):L3, September 2023. doi: 10.3847/2041-8213/acd853.

R. D. Haywood, A. Collier Cameron, D. Queloz, S. C. C. Barros, M. Deleuil, R. Fares, M. Gillon, A. F. Lanza, C. Lovis, C. Moutou, F. Pepe, D. Pollacco,

A. Santerne, D. Ségransan, and Y. C. Unruh. Planets and stellar activity: hide and seek in the CoRoT-7 system. *MNRAS*, 443(3):2517–2531, September 2014. doi: 10.1093/mnras/stu1320.

M. Hesse and P. A. Cassak. Magnetic Reconnection in the Space Sciences: Past, Present, and Future. *Journal of Geophysical Research (Space Physics)*, 125(2): e25935, February 2020. doi: 10.1029/2018JA025935.

Cynthia S. K. Ho and Vincent Van Eylen. A deep radius valley revealed by Kepler short cadence observations. *MNRAS*, 519(3):4056–4073, March 2023. doi: 10.1093/mnras/stac3802.

Cynthia S. K. Ho, James G. Rogers, Vincent Van Eylen, James E. Owen, and Hilke E. Schlichting. Shallower radius valley around low-mass hosts: evidence for icy planets, collisions, or high-energy radiation scatter. *MNRAS*, 531(3): 3698–3714, July 2024. doi: 10.1093/mnras/stae1376.

R. Hodgson. On a curious Appearance seen in the Sun. *MNRAS*, 20:15–16, November 1859. doi: 10.1093/mnras/20.1.15.

M. Holmström, A. Ekenbäck, F. Selsis, T. Penz, H. Lammer, and P. Wurz. Energetic neutral atoms as the explanation for the high-velocity hydrogen around HD 209458b. *Nature*, 451(7181):970–972, February 2008. doi: 10.1038/nature06600.

Steve B. Howell, Charlie Sobeck, Michael Haas, Martin Still, Thomas Barclay, Fergal Mullally, John Troeltzsch, Suzanne Aigrain, Stephen T. Bryson, Doug Caldwell, William J. Chaplin, William D. Cochran, Daniel Huber, Geoffrey W. Marcy, Andrea Miglio, Joan R. Najita, Marcie Smith, J. D. Twicken, and Jonathan J. Fortney. The K2 Mission: Characterization and Early Results. *PASP*, 126(938):398, April 2014. doi: 10.1086/676406.

S. Hoyer, J. S. Jenkins, V. Parmentier, M. Deleuil, G. Scandariato, T. G. Wilson, M. R. Díaz, I. J. M. Crossfield, D. Dragomir, T. Kataria, M. Lendl, R. Ramirez, P. A. Peña Rojas, and J. I. Vinés. The extremely high albedo of LTT 9779 b revealed by CHEOPS. An ultrahot Neptune with a highly metallic atmosphere. *A&A*, 675:A81, July 2023. doi: 10.1051/0004-6361/202346117.

Daniel Huber, William J. Chaplin, Jørgen Christensen-Dalsgaard, Ronald L. Gilliland, Hans Kjeldsen, Lars A. Buchhave, Debra A. Fischer, Jack J. Lissauer, Jason F. Rowe, Roberto Sanchis-Ojeda, Sarbani Basu, Rasmus Handberg, Saskia Hekker, Andrew W. Howard, Howard Isaacson, Christoffer Karoff, David W. Latham, Mikkel N. Lund, Mia Lundkvist, Geoffrey W. Marcy, Andrea Miglio, Victor Silva Aguirre, Dennis Stello, Torben Arentoft, Thomas Barclay, Timothy R. Bedding, Christopher J. Burke, Jessie L. Christiansen, Yvonne P. Elsworth, Michael R. Haas, Steven D. Kawaler, Travis S. Metcalfe, Fergal Mullally, and Susan E. Thompson. Fundamental Properties of Kepler Planet-candidate Host Stars using Asteroseismology. *ApJ*, 767(2):127, April 2013. doi: 10.1088/0004-637X/767/2/127.

D. M. Hunten. Thermal and nonthermal escape mechanisms for terrestrial bodies. *Planet. Space Sci.*, 30(8):773–783, August 1982. doi: 10.1016/0032-0633(82)90110-6.

S. Ida and D. N. C. Lin. Toward a Deterministic Model of Planetary Formation. V. Accumulation Near the Ice Line and Super-Earths. *ApJ*, 685(1):584–595, September 2008. doi: 10.1086/590401.

Dmitry E. Ionov, Yaroslav N. Pavlyuchenkov, and Valery I. Shematovich. Survival of a planet in short-period Neptunian desert under effect of photoevaporation. *MNRAS*, 476(4):5639–5644, June 2018. doi: 10.1093/mnras/sty626.

Jonathan Irwin, Simon Hodgkin, Suzanne Aigrain, Leslie Hebb, Jerome Bouvier, Cathie Clarke, Estelle Moraux, and D. M. Bramich. The Monitor project: rotation of low-mass stars in the open cluster NGC2516. *MNRAS*, 377(2):741–758, May 2007. doi: 10.1111/j.1365-2966.2007.11640.x.

Jonathan Irwin, Suzanne Aigrain, Jerome Bouvier, Leslie Hebb, Simon Hodgkin, Mike Irwin, and Estelle Moraux. The Monitor project: rotation periods of low-mass stars in M50. *MNRAS*, 392(4):1456–1466, February 2009a. doi: 10.1111/j.1365-2966.2008.14158.x.

Jonathan Irwin, David Charbonneau, Philip Nutzman, and Emilio Falco. The MEarth project: searching for transiting habitable super-Earths around nearby M dwarfs. In Frédéric Pont, Dimitar Sasselov, and Matthew J. Holman, editors, *Transiting Planets*, volume 253, pages 37–43, February 2009b. doi: 10.1017/S1743921308026215.

Alan P. Jackson, Timothy A. Davis, and Peter J. Wheatley. The coronal X-ray-age relation and its implications for the evaporation of exoplanets. *MNRAS*, 422(3):2024–2043, May 2012. doi: 10.1111/j.1365-2966.2012.20657.x.

Brian Jackson, Phil Arras, Kaloyan Penev, Sarah Peacock, and Pablo Marchant. A New Model of Roche Lobe Overflow for Short-period Gaseous Planets and Binary Stars. *ApJ*, 835(2):145, February 2017. doi: 10.3847/1538-4357/835/2/145.

N. Jagoda, G. Austin, S. Mickiewicz, and R. Goddard. The UHURU X-Ray Instrument. *IEEE Transactions on Nuclear Science*, 19(1):579, February 1972. doi: 10.1109/TNS.1972.4326562.

F. Jansen, D. Lumb, B. Altieri, J. Clavel, M. Ehle, C. Erd, C. Gabriel, M. Guainazzi, P. Gondoin, R. Much, R. Munoz, M. Santos, N. Schartel, D. Texier, and G. Vacanti. XMM-Newton observatory. I. The spacecraft and operations. *A&A*, 365:L1–L6, January 2001. doi: 10.1051/0004-6361:20000036.

M. Jardine and Y. C. Unruh. Coronal emission and dynamo saturation. *A&A*, 346:883–891, June 1999.

J.H. Jeans. The dynamical theory of gases. *Nature*, 117(2939):299–299, February 1926. doi: 10.1038/117299d0. URL `https://doi.org/10.1038/117299d0`.

James S. Jenkins, Matías R. Díaz, Nicolás T. Kurtovic, Néstor Espinoza, Jose I. Vines, Pablo A. Peña Rojas, Rafael Brahm, Pascal Torres, Pía Cortés-Zuleta, Maritza G. Soto, Eric D. Lopez, George W. King, Peter J. Wheatley, Joshua N. Winn, David R. Ciardi, George Ricker, Roland Vanderspek, David W. Latham, Sara Seager, Jon M. Jenkins, Charles A. Beichman, Allyson Bieryla, Christopher J. Burke, Jessie L. Christiansen, Christopher E. Henze, Todd C. Klaus, Sean McCauliff, Mayuko Mori, Norio Narita, Taku Nishiumi, Motohide Tamura, Jerome Pitogo de Leon, Samuel N. Quinn, Jesus Noel Villaseñor, Michael Vezie, Jack J. Lissauer, Karen A. Collins, Kevin I. Collins, Giovanni Isopi, Franco Mallia, Andrea Ercolino, Cristobal Petrovich, Andrés Jordán, Jack S. Acton, David J. Armstrong, Daniel Bayliss, François Bouchy, Claudia Belardi, Edward M. Bryant, Matthew R. Burleigh, Juan Cabrera, Sarah L. Casewell, Alexander Chaushev, Benjamin F. Cooke, Philipp Eigmüller, Anders Erikson, Emma Foxell, Boris T. Gänsicke, Samuel Gill, Edward Gillen, Maximilian N. Günther, Michael R. Goad, Matthew J. Hooton, James A. G. Jackman, Tom Louden, James McCormac, Maximiliano Moyano, Louise D. Nielsen, Don Pollacco, Didier Queloz, Heike Rauer, Liam Raynard, Alexis M. S. Smith, Rosanna H. Tilbrook, Ruth Titz-Weider, Oliver Turner, Stéphane

Udry, Simon. R. Walker, Christopher A. Watson, Richard G. West, Enric Palle, Carl Ziegler, Nicholas Law, and Andrew W. Mann. An ultrahot Neptune in the Neptune desert. *Nature Astronomy*, 4:1148–1157, January 2020. doi: 10.1038/s41550-020-1142-z.

Adam G. Jensen, P. Wilson Cauley, Seth Redfield, William D. Cochran, and Michael Endl. Hydrogen and Sodium Absorption in the Optical Transmission Spectrum of WASP-12b. *AJ*, 156(4):154, October 2018. doi: 10.3847/1538-3881/aadca7.

Sheng Jin and Christoph Mordasini. Compositional Imprints in Density-Distance-Time: A Rocky Composition for Close-in Low-mass Exoplanets from the Location of the Valley of Evaporation. *ApJ*, 853(2):163, February 2018. doi: 10.3847/1538-4357/aa9f1e.

Sheng Jin, Christoph Mordasini, Vivien Parmentier, Roy van Boekel, Thomas Henning, and Jianghui Ji. Planetary Population Synthesis Coupled with Atmospheric Escape: A Statistical View of Evaporation. *ApJ*, 795(1):65, November 2014. doi: 10.1088/0004-637X/795/1/65.

John Asher Johnson, Erik A. Petigura, Benjamin J. Fulton, Geoffrey W. Marcy, Andrew W. Howard, Howard Isaacson, Leslie Hebb, Phillip A. Cargile, Timothy D. Morton, Lauren M. Weiss, Joshua N. Winn, Leslie A. Rogers, Evan Sinukoff, and Lea A. Hirsch. The California-Kepler Survey. II. Precise Physical Properties of 2025 Kepler Planets and Their Host Stars. *AJ*, 154(3):108, September 2017. doi: 10.3847/1538-3881/aa80e7.

C. P. Johnstone, M. Güdel, I. Brott, and T. Lüftinger. Stellar winds on the main-sequence. II. The evolution of rotation and winds. *A&A*, 577:A28, May 2015a. doi: 10.1051/0004-6361/201425301.

C. P. Johnstone, M. Güdel, A. Stökl, H. Lammer, L. Tu, K. G. Kislyakova, T. Lüftinger, P. Odert, N. V. Erkaev, and E. A. Dorfi. The Evolution of Stellar Rotation and the Hydrogen Atmospheres of Habitable-zone Terrestrial Planets. *ApJ*, 815(1):L12, December 2015b. doi: 10.1088/2041-8205/815/1/L12.

C. P. Johnstone, M. Bartel, and M. Güdel. The active lives of stars: A complete description of the rotation and XUV evolution of F, G, K, and M dwarfs. *A&A*, 649:A96, May 2021. doi: 10.1051/0004-6361/202038407.

T. Kallinger, J. De Ridder, S. Hekker, S. Mathur, B. Mosser, M. Gruberbauer, R. A. García, C. Karoff, and J. Ballot. The connection between stellar granulation and oscillation as seen by the Kepler mission. *A&A*, 570:A41, October 2014. doi: 10.1051/0004-6361/201424313.

Christoffer Karoff, Travis S. Metcalfe, Ângela R. G. Santos, Benjamin T. Montet, Howard Isaacson, Veronika Witzke, Alexander I. Shapiro, Savita Mathur, Guy R. Davies, Mikkel N. Lund, Rafael A. Garcia, Allan S. Brun, David Salabert, Pedro P. Avelino, Jennifer van Saders, Ricky Egeland, Margarida S. Cunha, Tiago L. Campante, William J. Chaplin, Natalie Krivova, Sami K. Solanki, Maximilian Stritzinger, and Mads F. Knudsen. The Influence of Metallicity on Stellar Differential Rotation and Magnetic Activity. *ApJ*, 852(1):46, January 2018. doi: 10.3847/1538-4357/aaa026.

D. Katz, P. Sartoretti, A. Guerrier, P. Panuzzo, G. M. Seabroke, F. Thévenin, M. Cropper, K. Benson, R. Blomme, R. Haigron, O. Marchal, M. Smith, S. Baker, L. Chemin, Y. Damerdji, M. David, C. Dolding, Y. Frémat, E. Gosset, K. Janßen, G. Jasniewicz, A. Lobel, G. Plum, N. Samaras, O. Snaith, C. Soubiran, O. Vanel, T. Zwitter, T. Antoja, F. Arenou, C. Babusiaux, N. Brouillet, E. Caffau, P. Di Matteo, C. Fabre, C. Fabricius, F. Fragkoudi, M. Haywood, H. E. Huckle, C. Hottier, Y. Lasne, N. Leclerc, A. Mastrobuono-Battisti, F. Royer, D. Teyssier, J. Zorec, F. Crifo, A. Jean-Antoine Piccolo, C. Turon, and Y. Viala. Gaia Data Release 3. Properties and validation of the radial velocities. *A&A*, 674:A5, June 2023. doi: 10.1051/0004-6361/202244220.

M. L. Khodachenko, I. F. Shaikhislamov, H. Lammer, K. G. Kislyakova, L. Fossati, C. P. Johnstone, O. V. Arkhypov, A. G. Berezutsky, I. B. Miroshnichenko, and V. G. Posukh. Lyα Absorption at Transits of HD 209458b: A Comparative Study of Various Mechanisms Under Different Conditions. *ApJ*, 847(2):126, October 2017. doi: 10.3847/1538-4357/aa88ad.

George W. King and Peter J. Wheatley. EUV irradiation of exoplanet atmospheres occurs on Gyr time-scales. *MNRAS*, 501(1):L28–L32, January 2021. doi: 10.1093/mnrasl/slaa186.

George W. King, Peter J. Wheatley, Michael Salz, Vincent Bourrier, Stefan Czesla, David Ehrenreich, James Kirk, Alain Lecavelier des Etangs, Tom Louden, Jürgen Schmitt, and P. Christian Schneider. The XUV environments of exoplanets from Jupiter-size to super-Earth. *MNRAS*, 478(1):1193–1208, July 2018. doi: 10.1093/mnras/sty1110.

George W. King, Peter J. Wheatley, Vincent Bourrier, and David Ehrenreich. The XUV irradiation and likely atmospheric escape of the super-Earth π Men c. *MNRAS*, 484(1):L49–L53, March 2019. doi: 10.1093/mnrasl/slz003.

James Kirk, Munazza K. Alam, Mercedes López-Morales, and Li Zeng. Confirmation of WASP-107b's Extended Helium Atmosphere with Keck II/NIRSPEC. *AJ*, 159(3):115, March 2020. doi: 10.3847/1538-3881/ab6e66.

K. G. Kislyakova, C. P. Johnstone, P. Odert, N. V. Erkaev, H. Lammer, T. Lüftinger, M. Holmström, M. L. Khodachenko, and M. Güdel. Stellar wind interaction and pick-up ion escape of the Kepler-11 "super-Earths". *A&A*, 562: A116, February 2014. doi: 10.1051/0004-6361/201322933.

Kristina G. Kislyakova, Helmut Lammer, Mats Holmström, Mykhaylo Panchenko, Petra Odert, Nikolai V. Erkaev, Martin Leitzinger, Maxim L. Khodachenko, Yuri N. Kulikov, Manuel Güdel, and Arnold Hanslmeier. XUV-Exposed, Non-Hydrostatic Hydrogen-Rich Upper Atmospheres of Terrestrial Planets. Part II: Hydrogen Coronae and Ion Escape. *Astrobiology*, 13(11):1030–1048, November 2013. doi: 10.1089/ast.2012.0958.

H. Kjeldsen and T. R. Bedding. Amplitudes of stellar oscillations: the implications for asteroseismology. *A&A*, 293:87–106, January 1995. doi: 10.48550/arXiv.astro-ph/9403015.

James A. Klimchuk. On Solving the Coronal Heating Problem. *Sol. Phys.*, 234 (1):41–77, March 2006. doi: 10.1007/s11207-006-0055-z.

T. T. Koskinen, M. J. Harris, R. V. Yelle, and P. Lavvas. The escape of heavy atoms from the ionosphere of HD209458b. I. A photochemical-dynamical model of the thermosphere. *Icarus*, 226(2):1678–1694, November 2013. doi: 10.1016/j.icarus.2012.09.027.

Tommi T. Koskinen, Panayotis Lavvas, Chenliang Huang, Galen Bergsten, Rachel B. Fernandes, and Mitchell E. Young. Mass Loss by Atmospheric Escape from Extremely Close-in Planets. *ApJ*, 929(1):52, April 2022. doi: 10.3847/1538-4357/ac4f45.

Veselin B. Kostov, Jerome A. Orosz, Adina D. Feinstein, William F. Welsh, Wolf Cukier, Nader Haghighipour, Billy Quarles, David V. Martin, Benjamin T. Montet, Guillermo Torres, Amaury H. M. J. Triaud, Thomas Barclay, Patricia Boyd, Cesar Briceno, Andrew Collier Cameron, Alexandre C. M. Correia, Emily A. Gilbert, Samuel Gill, Michaël Gillon, Jacob Haqq-Misra, Coel Hellier, Courtney Dressing, Daniel C. Fabrycky, Gabor Furesz, Jon M. Jenkins, Stephen R. Kane, Ravi Kopparapu, Vedad Kunovac Hodžić, David W. Latham, Nicholas Law, Alan M. Levine, Gongjie Li, Chris Lintott, Jack J. Lissauer, Andrew W. Mann, Tsevi Mazeh, Rosemary Mardling, Pierre F. L. Maxted, Nora Eisner, Francesco Pepe, Joshua Pepper, Don Pollacco, Samuel N. Quinn, Elisa V. Quintana, Jason F. Rowe, George Ricker, Mark E. Rose, S. Seager, Alexandre Santerne, Damien Ségransan, Donald R. Short, Jeffrey C. Smith, Matthew R. Standing, Andrei Tokovinin, Trifon Trifonov, Oliver Turner, Joseph D. Twicken, Stéphane Udry, Roland Vanderspek, Joshua N. Winn, Eric T. Wolf, Carl Ziegler, Peter Ansorge, Frank Barnet, Joel Bergeron, Marc Huten, Giuseppe Pappa, and Timo van der Straeten. TOI-1338: TESS' First Transiting Circumbinary Planet. *AJ*, 159(6):253, June 2020. doi: 10.3847/1538-3881/ab8a48.

Ralph P. Kraft, David N. Burrows, and John A. Nousek. Determination of Confidence Limits for Experiments with Low Numbers of Counts. *ApJ*, 374:344, June 1991. doi: 10.1086/170124.

Robert P. Kraft. Studies of Stellar Rotation. V. The Dependence of Rotation on Age among Solar-Type Stars. *ApJ*, 150:551, November 1967. doi: 10.1086/149359.

Adam L. Kraus, Michael J. Ireland, Daniel Huber, Andrew W. Mann, and Trent J. Dupuy. The Impact of Stellar Multiplicity on Planetary Systems. I. The Ruinous Influence of Close Binary Companions. *AJ*, 152(1):8, July 2016. doi: 10.3847/0004-6256/152/1/8.

Laura Kreidberg and Antonija Oklopčić. Non-detection of a Helium Exosphere for the Hot Jupiter WASP-12b. *Research Notes of the American Astronomical Society*, 2(2):44, June 2018. doi: 10.3847/2515-5172/aac887.

D. Kubyshkina, L. Fossati, N. V. Erkaev, P. E. Cubillos, C. P. Johnstone, K. G. Kislyakova, H. Lammer, M. Lendl, and P. Odert. Overcoming the Limitations of the Energy-limited Approximation for Planet Atmospheric Escape. *ApJ*, 866(2):L18, October 2018. doi: 10.3847/2041-8213/aae586.

Daria Kubyshkina, Aline A. Vidotto, Carolina Villarreal D'Angelo, Stephen Carolan, Gopal Hazra, and Ilaria Carleo. Atmospheric mass-loss and stellar wind effects in young and old systems - I. Comparative 3D study of TOI-942 and TOI-421 systems. *MNRAS*, 510(2):2111–2126, February 2022. doi: 10.1093/mnras/stab3594.

Daria I. Kubyshkina and Luca Fossati. Extending a Grid of Hydrodynamic Planetary Upper Atmosphere Models. *Research Notes of the American Astronomical Society*, 5(4):74, April 2021. doi: 10.3847/2515-5172/abf498.

Michelle Kunimoto, Andrew Vanderburg, Chelsea X. Huang, M. Ryleigh Davis, Laura Affer, Andrew Collier Cameron, David Charbonneau, Rosario Cosentino, Mario Damasso, Xavier Dumusque, A. F. Martnez Fiorenzano, Adriano Ghedina, R. D. Haywood, Florian Lienhard, Mercedes López-Morales, Michel Mayor, Francesco Pepe, Matteo Pinamonti, Ennio Poretti, Jesús Maldonado, Ken Rice, Alessandro Sozzetti, Thomas G. Wilson, Stéphane Udry, Jay Baptista, Khalid Barkaoui, Juliette Becker, Paul Benni, Allyson Bieryla, Pau Bosch-Cabot, David R. Ciardi, Karen A. Collins, Kevin I. Collins, Elise Evans, Trent J. Dupuy, Maria V. Goliguzova, Pere Guerra, Adam Kraus, Jack J. Lissauer, Daniel Huber, Felipe Murgas, Enric Palle, Samuel N. Quinn, Boris S. Safonov, Richard P. Schwarz, Avi Shporer, Keivan G. Stassun, Jon M. Jenkins, David W. Latham, George R. Ricker, Sara Seager, Roland Vanderspek, Joshua Winn, Zahra Essack, Hannah M. Lewis, and Mark E. Rose. TOI-4010: A System of Three Large Short-period Planets with a Massive Long-period Companion. *AJ*, 166 (1):7, July 2023. doi: 10.3847/1538-3881/acd537.

H. Kurokawa and L. Kaltenegger. Atmospheric mass-loss and evolution of short-period exoplanets: the examples of CoRoT-7b and Kepler-10b. *MNRAS*, 433 (4):3239–3245, August 2013. doi: 10.1093/mnras/stt965.

H. Kurokawa and T. Nakamoto. Mass-loss Evolution of Close-in Exoplanets: Evaporation of Hot Jupiters and the Effect on Population. *ApJ*, 783(1):54, March 2014. doi: 10.1088/0004-637X/783/1/54.

G. Lacedelli, T. G. Wilson, L. Malavolta, M. J. Hooton, A. Collier Cameron, Y. Alibert, A. Mortier, A. Bonfanti, R. D. Haywood, S. Hoyer, G. Piotto, A. Bekkelien, A. M. Vanderburg, W. Benz, X. Dumusque, A. Deline, M. López-Morales, L. Borsato, K. Rice, L. Fossati, D. W. Latham, A. Brandeker, E. Poretti, S. G.

Sousa, A. Sozzetti, S. Salmon, C. J. Burke, V. Van Grootel, M. M. Fausnaugh, V. Adibekyan, C. X. Huang, H. P. Osborn, A. J. Mustill, E. Pallé, V. Bourrier, V. Nascimbeni, R. Alonso, G. Anglada, T. Bárczy, D. Barrado y Navascues, S. C. C. Barros, W. Baumjohann, M. Beck, T. Beck, N. Billot, X. Bonfils, C. Broeg, L. A. Buchhave, J. Cabrera, S. Charnoz, R. Cosentino, Sz Csizmadia, M. B. Davies, M. Deleuil, L. Delrez, O. Demangeon, B. O. Demory, D. Ehrenreich, A. Erikson, E. Esparza-Borges, H. G. Florén, A. Fortier, M. Fridlund, D. Futyan, D. Gandolfi, A. Ghedina, M. Gillon, M. Güdel, P. Guterman, A. Harutyunyan, K. Heng, K. G. Isaak, J. M. Jenkins, L. Kiss, J. Laskar, A. Lecavelier des Etangs, M. Lendl, C. Lovis, D. Magrin, L. Marafatto, A. F. Martinez Fiorenzano, P. F. L. Maxted, M. Mayor, G. Micela, E. Molinari, F. Murgas, N. Narita, G. Olofsson, R. Ottensamer, I. Pagano, A. Pasetti, M. Pedani, F. A. Pepe, G. Peter, D. F. Phillips, D. Pollacco, D. Queloz, R. Ragazzoni, N. Rando, F. Ratti, H. Rauer, I. Ribas, N. C. Santos, D. Sasselov, G. Scandariato, S. Seager, D. Ségransan, L. M. Serrano, A. E. Simon, A. M. S. Smith, M. Steinberger, M. Steller, Gy Szabó, N. Thomas, J. D. Twicken, S. Udry, N. Walton, and J. N. Winn. Investigating the architecture and internal structure of the TOI-561 system planets with CHEOPS, HARPS-N, and TESS. *MNRAS*, 511(3):4551–4571, April 2022. doi: 10.1093/mnras/stac199.

A. M. Lagrange, M. Bonnefoy, G. Chauvin, D. Apai, D. Ehrenreich, A. Boccaletti, D. Gratadour, D. Rouan, D. Mouillet, S. Lacour, and M. Kasper. A Giant Planet Imaged in the Disk of the Young Star β Pictoris. *Science*, 329(5987):57, July 2010a. doi: 10.1126/science.1187187.

A. M. Lagrange, M. Desort, and N. Meunier. Using the Sun to estimate Earth-like planets detection capabilities . I. Impact of cold spots. *A&A*, 512:A38, March 2010b. doi: 10.1051/0004-6361/200913071.

J. Martin Laming. The FIP and Inverse FIP Effects in Solar and Stellar Coronae. *Living Reviews in Solar Physics*, 12(1):2, September 2015. doi: 10.1007/lrsp-2015-2.

H. Lammer, F. Selsis, I. Ribas, E. F. Guinan, S. J. Bauer, and W. W. Weiss. Atmospheric Loss of Exoplanets Resulting from Stellar X-Ray and Extreme-Ultraviolet Heating. *ApJ*, 598(2):L121–L124, December 2003. doi: 10.1086/380815.

H. Lammer, P. Odert, M. Leitzinger, M. L. Khodachenko, M. Panchenko, Yu. N. Kulikov, T. L. Zhang, H. I. M. Lichtenegger, N. V. Erkaev, G. Wuchterl, G. Micela, T. Penz, H. K. Biernat, J. Weingrill, M. Steller, H. Ottacher, J. Hasiba, and A. Hanslmeier. Determining the mass loss limit for close-in exoplanets: what can we learn from transit observations? *A&A*, 506(1):399–410, October 2009. doi: 10.1051/0004-6361/200911922.

H. Lammer, N. V. Erkaev, L. Fossati, I. Juvan, P. Odert, P. E. Cubillos, E. Guenther, K. G. Kislyakova, C. P. Johnstone, T. Lüftinger, and M. Güdel. Identifying the 'true' radius of the hot sub-Neptune CoRoT-24b by mass-loss modelling. *MNRAS*, 461(1):L62–L66, September 2016. doi: 10.1093/mnrasl/slw095.

A. Lecavelier Des Etangs. A diagram to determine the evaporation status of extrasolar planets. *A&A*, 461(3):1185–1193, January 2007. doi: 10.1051/0004-6361:20065014.

A. Lecavelier Des Etangs, D. Ehrenreich, A. Vidal-Madjar, G. E. Ballester, J. M. Désert, R. Ferlet, G. Hébrard, D. K. Sing, K. O. Tchakoumegni, and S. Udry. Evaporation of the planet HD 189733b observed in H I Lyman-α. *A&A*, 514:A72, May 2010. doi: 10.1051/0004-6361/200913347.

A. Lecavelier des Etangs, V. Bourrier, P. J. Wheatley, H. Dupuy, D. Ehrenreich, A. Vidal-Madjar, G. Hébrard, G. E. Ballester, J. M. Désert, R. Ferlet, and D. K. Sing. Temporal variations in the evaporating atmosphere of the exoplanet HD 189733b. *A&A*, 543:L4, July 2012. doi: 10.1051/0004-6361/201219363.

Eve J. Lee and Eugene Chiang. Breeding Super-Earths and Birthing Super-puffs in Transitional Disks. *ApJ*, 817(2):90, February 2016. doi: 10.3847/0004-637X/817/2/90.

Eve J. Lee, Eugene Chiang, and Chris W. Ormel. Make Super-Earths, Not Jupiters: Accreting Nebular Gas onto Solid Cores at 0.1 AU and Beyond. *ApJ*, 797(2):95, December 2014. doi: 10.1088/0004-637X/797/2/95.

A. Léger, D. Rouan, J. Schneider, P. Barge, M. Fridlund, B. Samuel, M. Ollivier, E. Guenther, M. Deleuil, H. J. Deeg, M. Auvergne, R. Alonso, S. Aigrain, A. Alapini, J. M. Almenara, A. Baglin, M. Barbieri, H. Bruntt, P. Bordé, F. Bouchy, J. Cabrera, C. Catala, L. Carone, S. Carpano, Sz. Csizmadia, R. Dvorak, A. Erikson, S. Ferraz-Mello, B. Foing, F. Fressin, D. Gandolfi, M. Gillon, Ph.

Gondoin, O. Grasset, T. Guillot, A. Hatzes, G. Hébrard, L. Jorda, H. Lammer, A. Llebaria, B. Loeillet, M. Mayor, T. Mazeh, C. Moutou, M. Pätzold, F. Pont, D. Queloz, H. Rauer, S. Renner, R. Samadi, A. Shporer, Ch. Sotin, B. Tingley, G. Wuchterl, M. Adda, P. Agogu, T. Appourchaux, H. Ballans, P. Baron, T. Beaufort, R. Bellenger, R. Berlin, P. Bernardi, D. Blouin, F. Baudin, P. Bodin, L. Boisnard, L. Boit, F. Bonneau, S. Borzeix, R. Briet, J. T. Buey, B. Butler, D. Cailleau, R. Cautain, P. Y. Chabaud, S. Chaintreuil, F. Chiavassa, V. Costes, V. Cuna Parrho, F. de Oliveira Fialho, M. Decaudin, J. M. Defise, S. Djalal, G. Epstein, G. E. Exil, C. Fauré, T. Fenouillet, A. Gaboriaud, A. Gallic, P. Gamet, P. Gavalda, E. Grolleau, R. Gruneisen, L. Gueguen, V. Guis, V. Guivarc'h, P. Guterman, D. Hallouard, J. Hasiba, F. Heuripeau, G. Huntzinger, H. Hustaix, C. Imad, C. Imbert, B. Johlander, M. Jouret, P. Journoud, F. Karioty, L. Kerjean, V. Lafaille, L. Lafond, T. Lam-Trong, P. Landiech, V. Lapeyrere, T. Larqué, P. Laudet, N. Lautier, H. Lecann, L. Lefevre, B. Leruyet, P. Levacher, A. Magnan, E. Mazy, F. Mertens, J. M. Mesnager, J. C. Meunier, J. P. Michel, W. Monjoin, D. Naudet, K. Nguyen-Kim, J. L. Orcesi, H. Ottacher, R. Perez, G. Peter, P. Plasson, J. Y. Plesseria, B. Pontet, A. Pradines, C. Quentin, J. L. Reynaud, G. Rolland, F. Rollenhagen, R. Romagnan, N. Russ, R. Schmidt, N. Schwartz, I. Sebbag, G. Sedes, H. Smit, M. B. Steller, W. Sunter, C. Surace, M. Tello, D. Tiphène, P. Toulouse, B. Ulmer, O. Vandermarcq, E. Vergnault, A. Vuillemin, and P. Zanatta. Transiting exoplanets from the CoRoT space mission. VIII. CoRoT-7b: the first super-Earth with measured radius. *A&A*, 506(1):287–302, October 2009. doi: 10.1051/0004-6361/200911933.

L. Lindegren, S. A. Klioner, J. Hernández, A. Bombrun, M. Ramos-Lerate, H. Steidelmüller, U. Bastian, M. Biermann, A. de Torres, E. Gerlach, R. Geyer, T. Hilger, D. Hobbs, U. Lammers, P. J. McMillan, C. A. Stephenson, J. Castañeda, M. Davidson, C. Fabricius, G. Gracia-Abril, J. Portell, N. Rowell, D. Teyssier, F. Torra, S. Bartolomé, M. Clotet, N. Garralda, J. J. González-Vidal, J. Torra, U. Abbas, M. Altmann, E. Anglada Varela, L. Balaguer-Núñez, Z. Balog, C. Barache, U. Becciani, M. Bernet, S. Bertone, L. Bianchi, S. Bouquillon, A. G. A. Brown, B. Bucciarelli, D. Busonero, A. G. Butkevich, R. Buzzi, R. Cancelliere, T. Carlucci, P. Charlot, M. R. L. Cioni, M. Crosta, C. Crowley, E. F. del Peloso, E. del Pozo, R. Drimmel, P. Esquej, A. Fienga, E. Fraile, M. Gai, M. Garcia-Reinaldos, R. Guerra, N. C. Hambly, M. Hauser, K. Janßen,

S. Jordan, Z. Kostrzewa-Rutkowska, M. G. Lattanzi, S. Liao, E. Licata, T. A. Lister, W. Löffler, J. M. Marchant, A. Masip, F. Mignard, A. Mints, D. Molina, A. Mora, R. Morbidelli, C. P. Murphy, C. Pagani, P. Panuzzo, X. Peñalosa Esteller, E. Poggio, P. Re Fiorentin, A. Riva, A. Sagristà Sellés, V. Sanchez Gimenez, M. Sarasso, E. Sciacca, H. I. Siddiqui, R. L. Smart, D. Souami, A. Spagna, I. A. Steele, F. Taris, E. Utrilla, W. van Reeven, and A. Vecchiato. Gaia Early Data Release 3. The astrometric solution. *A&A*, 649:A2, May 2021. doi: 10.1051/0004-6361/202039709.

Jeffrey L. Linsky, Hao Yang, Kevin France, Cynthia S. Froning, James C. Green, John T. Stocke, and Steven N. Osterman. Observations of Mass Loss from the Transiting Exoplanet HD 209458b. *ApJ*, 717(2):1291–1299, July 2010a. doi: 10.1088/0004-637X/717/2/1291.

Jeffrey L. Linsky, Hao Yang, Kevin France, Cynthia S. Froning, James C. Green, John T. Stocke, and Steven N. Osterman. Observations of Mass Loss from the Transiting Exoplanet HD 209458b. *ApJ*, 717(2):1291–1299, July 2010b. doi: 10.1088/0004-637X/717/2/1291.

D. C. Linssen and A. Oklopčić. Expanding the inventory of spectral lines used to trace atmospheric escape in exoplanets. *A&A*, 675:A193, July 2023. doi: 10.1051/0004-6361/202346583.

John H. Livingston, Fei Dai, Teruyuki Hirano, Davide Gandolfi, Grzegorz Nowak, Michael Endl, Sergio Velasco, Akihiko Fukui, Norio Narita, Jorge Prieto-Arranz, Oscar Barragan, Felice Cusano, Simon Albrecht, Juan Cabrera, William D. Cochran, Szilard Csizmadia, Hans J. Deeg, Philipp Eigmüller, Anders Erikson, Malcolm Fridlund, Sascha Grziwa, Eike W. Guenther, Artie P. Hatzes, Kiyoe Kawauchi, Judith Korth, David Nespral, Enric Palle, Martin Pätzold, Carina M. Persson, Heike Rauer, Alexis M. S. Smith, Motohide Tamura, Yusuke Tanaka, Vincent Van Eylen, Noriharu Watanabe, and Joshua N. Winn. Three Small Planets Transiting a Hyades Star. *AJ*, 155(3):115, March 2018. doi: 10.3847/1538-3881/aaa841.

Eric D. Lopez and Jonathan J. Fortney. The Role of Core Mass in Controlling Evaporation: The Kepler Radius Distribution and the Kepler-36 Density Dichotomy. *ApJ*, 776(1):2, October 2013. doi: 10.1088/0004-637X/776/1/2.

Eric D. Lopez and Jonathan J. Fortney. Understanding the Mass-Radius Relation for Sub-neptunes: Radius as a Proxy for Composition. *ApJ*, 792(1):1, September 2014. doi: 10.1088/0004-637X/792/1/1.

Eric D. Lopez and Ken Rice. How formation time-scales affect the period dependence of the transition between rocky super-Earths and gaseous sub-Neptunesand implications for $\eta_\oplus$. *MNRAS*, 479(4):5303–5311, October 2018. doi: 10.1093/mnras/sty1707.

Eric D. Lopez, Jonathan J. Fortney, and Neil Miller. How Thermal Evolution and Mass-loss Sculpt Populations of Super-Earths and Sub-Neptunes: Application to the Kepler-11 System and Beyond. *ApJ*, 761(1):59, December 2012. doi: 10.1088/0004-637X/761/1/59.

Tom Louden, Peter J. Wheatley, and Kevin Briggs. Reconstructing the high-energy irradiation of the evaporating hot Jupiter HD 209458b. *MNRAS*, 464(2): 2396–2402, January 2017. doi: 10.1093/mnras/stw2421.

R. O. Parke Loyd, T. T. Koskinen, Kevin France, Christian Schneider, and Seth Redfield. Ultraviolet C II and Si III Transit Spectroscopy and Modeling of the Evaporating Atmosphere of GJ436b. *ApJ*, 834(2):L17, January 2017. doi: 10.3847/2041-8213/834/2/L17.

M. S. Lundkvist, H. Kjeldsen, S. Albrecht, G. R. Davies, S. Basu, D. Huber, A. B. Justesen, C. Karoff, V. Silva Aguirre, V. van Eylen, C. Vang, T. Arentoft, T. Barclay, T. R. Bedding, T. L. Campante, W. J. Chaplin, J. Christensen-Dalsgaard, Y. P. Elsworth, R. L. Gilliland, R. Handberg, S. Hekker, S. D. Kawaler, M. N. Lund, T. S. Metcalfe, A. Miglio, J. F. Rowe, D. Stello, B. Tingley, and T. R. White. Hot super-Earths stripped by their host stars. *Nature Communications*, 7:11201, April 2016. doi: 10.1038/ncomms11201.

Rafael Luque and Enric Pallé. Density, not radius, separates rocky and water-rich small planets orbiting M dwarf stars. *Science*, 377(6611):1211–1214, September 2022. doi: 10.1126/science.abl7164.

B. Macintosh, J. R. Graham, T. Barman, R. J. De Rosa, Q. Konopacky, M. S. Marley, C. Marois, E. L. Nielsen, L. Pueyo, A. Rajan, J. Rameau, D. Saumon, J. J. Wang, J. Patience, M. Ammons, P. Arriaga, E. Artigau, S. Beckwith, J. Brewster, S. Bruzzone, J. Bulger, B. Burningham, A. S. Burrows, C. Chen,

E. Chiang, J. K. Chilcote, R. I. Dawson, R. Dong, R. Doyon, Z. H. Draper, G. Duchêne, T. M. Esposito, D. Fabrycky, M. P. Fitzgerald, K. B. Follette, J. J. Fortney, B. Gerard, S. Goodsell, A. Z. Greenbaum, P. Hibon, S. Hinkley, T. H. Cotten, L. W. Hung, P. Ingraham, M. Johnson-Groh, P. Kalas, D. Lafreniere, J. E. Larkin, J. Lee, M. Line, D. Long, J. Maire, F. Marchis, B. C. Matthews, C. E. Max, S. Metchev, M. A. Millar-Blanchaer, T. Mittal, C. V. Morley, K. M. Morzinski, R. Murray-Clay, R. Oppenheimer, D. W. Palmer, R. Patel, M. D. Perrin, L. A. Poyneer, R. R. Rafikov, F. T. Rantakyrö, E. L. Rice, P. Rojo, A. R. Rudy, J. B. Ruffio, M. T. Ruiz, N. Sadakuni, L. Saddlemyer, M. Salama, D. Savransky, A. C. Schneider, A. Sivaramakrishnan, I. Song, R. Soummer, S. Thomas, G. Vasisht, J. K. Wallace, K. Ward-Duong, S. J. Wiktorowicz, S. G. Wolff, and B. Zuckerman. Discovery and spectroscopy of the young jovian planet 51 Eri b with the Gemini Planet Imager. *Science*, 350(6256):64–67, October 2015. doi: 10.1126/science.aac5891.

A. Maggio, I. Pillitteri, C. Argiroffi, S. Benatti, J. Sanz-Forcada, V. D'Orazi, K. Biazzo, F. Borsa, L. Cabona, R. Claudi, S. Desidera, D. Locci, D. Nardiello, L. Mancini, G. Micela, M. Rainer, R. Spinelli, A. Bignamini, and M. Damasso. X-Ray and Ultraviolet Emission of the Young Planet-hosting Star V1298 Tau from Coordinated Observations with XMM-Newton and Hubble Space Telescope. *ApJ*, 951(1):18, July 2023. doi: 10.3847/1538-4357/acd339.

Eric E. Mamajek and Lynne A. Hillenbrand. Improved Age Estimation for Solar-Type Dwarfs Using Activity-Rotation Diagnostics. *ApJ*, 687(2):1264–1293, November 2008. doi: 10.1086/591785.

Andrew W. Mann, Andrew Vanderburg, Aaron C. Rizzuto, Adam L. Kraus, Perry Berlind, Allyson Bieryla, Michael L. Calkins, Gilbert A. Esquerdo, David W. Latham, Gregory N. Mace, Nathan R. Morris, Samuel N. Quinn, Kimberly R. Sokal, and Robert P. Stefanik. Zodiacal Exoplanets in Time (ZEIT). VI. A Three-planet System in the Hyades Cluster Including an Earth-sized Planet. *AJ*, 155(1):4, January 2018. doi: 10.3847/1538-3881/aa9791.

Megan Mansfield, Jacob L. Bean, Antonija Oklopčić, Laura Kreidberg, Jean-Michel Désert, Eliza M. R. Kempton, Michael R. Line, Jonathan J. Fortney, Gregory W. Henry, Matthias Mallonn, Kevin B. Stevenson, Diana Dragomir, Romain Allart, and Vincent Bourrier. Detection of Helium in the Atmosphere of the Exo-Neptune HAT-P-11b. *ApJ*, 868(2):L34, December 2018. doi: 10.3847/2041-8213/aaf166.

A. Marino, G. Micela, and G. Peres. A systematic analysis of X-ray variability of dM stars. *A&A*, 353:177–185, January 2000.

A. Marino, G. Micela, G. Peres, and S. Sciortino. On X-ray variability in ROSAT-PSPC observations of F7-K2 stars. *A&A*, 383:210–217, January 2002. doi: 10.1051/0004-6361:20011693.

A. Marino, G. Micela, G. Peres, and S. Sciortino. X-ray variability of Pleiades late-type stars as observed with the ROSAT-PSPC. *A&A*, 406:629–638, August 2003. doi: 10.1051/0004-6361:20030689.

Christian Marois, Bruce Macintosh, Travis Barman, B. Zuckerman, Inseok Song, Jennifer Patience, David Lafrenière, and René Doyon. Direct Imaging of Multiple Planets Orbiting the Star HR 8799. *Science*, 322(5906):1348, November 2008. doi: 10.1126/science.1166585.

Eduardo L. Martín, Nicolas Lodieu, Yakiv Pavlenko, and Víctor J. S. Béjar. The Lithium Depletion Boundary and the Age of the Hyades Cluster. *ApJ*, 856(1): 40, March 2018. doi: 10.3847/1538-4357/aaaeb8.

Titos Matsakos and Arieh Königl. On the Origin of the Sub-Jovian Desert in the Orbital-period-Planetary-mass Plane. *ApJ*, 820(1):L8, March 2016. doi: 10.3847/2041-8205/820/1/L8.

J. L. Matteson, R. M. Pelling, and L. E. Peterson. The UCSD/MIT hard X-ray and low-energy gamma-ray experiment for HEAO-A. In B. G. Taylor, editor, *The Context and Status of Gamma-Ray Astronomy*, pages 177–184, November 1974.

A. Mayo, C. Dressing, L. Buchhave, and The Harps-N Collaboration. The First Mass Measurement for a Sub-Neptune in an Open Cluster. In *Bulletin of the AAS*, volume 53 of *Bulletin of the AAS*, page 117.04, January 2021.

Andrew W. Mayo, Courtney D. Dressing, Andrew Vanderburg, Charles D. Fortenbach, Florian Lienhard, Luca Malavolta, Annelies Mortier, Alejandro Núñez, Tyler Richey-Yowell, Emma V. Turtelboom, Aldo S. Bonomo, David W. Latham, Mercedes López-Morales, Evgenya Shkolnik, Alessandro Sozzetti, Marcel A. Agüeros, Luca Borsato, David Charbonneau, Rosario Cosentino, Stephanie T. Douglas, Xavier Dumusque, Adriano Ghedina, Rose Gibson, Valentina Granata, Avet Harutyunyan, R. D. Haywood, Gaia Lacedelli, Vania Lorenzi, Antonio Magazzù, A. F. Martinez Fiorenzano, Giuseppina Micela, Emilio Molinari, Marco Montalto, Domenico Nardiello, Valerio Nascimbeni, Isabella Pagano, Giampaolo Piotto, Lorenzo Pino, Ennio Poretti, Gaetano Scandariato, Stephane Udry, and Lars A. Buchhave. Hyades Member K2-136c: The Smallest Planet in an Open Cluster with a Precisely Measured Mass. *arXiv e-prints*, art. arXiv:2304.02779, April 2023. doi: 10.48550/arXiv.2304.02779.

M. Mayor, F. Pepe, D. Queloz, F. Bouchy, G. Rupprecht, G. Lo Curto, G. Avila, W. Benz, J. L. Bertaux, X. Bonfils, Th. Dall, H. Dekker, B. Delabre, W. Eckert, M. Fleury, A. Gilliotte, D. Gojak, J. C. Guzman, D. Kohler, J. L. Lizon, A. Longinotti, C. Lovis, D. Megevand, L. Pasquini, J. Reyes, J. P. Sivan, D. Sosnowska, R. Soto, S. Udry, A. van Kesteren, L. Weber, and U. Weilenmann. Setting New Standards with HARPS. *The Messenger*, 114:20–24, December 2003.

Michel Mayor and Didier Queloz. A Jupiter-mass companion to a solar-type star. *Nature*, 378(6555):355–359, November 1995. doi: 10.1038/378355a0.

T. Mazeh, T. Holczer, and S. Faigler. Dearth of short-period Neptunian exoplanets: A desert in period-mass and period-radius planes. *A&A*, 589:A75, May 2016. doi: 10.1051/0004-6361/201528065.

A. McQuillan, S. Aigrain, and T. Mazeh. Measuring the rotation period distribution of field M dwarfs with Kepler. *MNRAS*, 432(2):1203–1216, June 2013. doi: 10.1093/mnras/stt536.

Søren Meibom, Robert D. Mathieu, and Keivan G. Stassun. Stellar Rotation in M35: Mass-Period Relations, Spin-Down Rates, and Gyrochronology. *ApJ*, 695 (1):679–694, April 2009. doi: 10.1088/0004-637X/695/1/679.

N. Meunier, A. M. Lagrange, S. Borgniet, and M. Rieutord. Using the Sun to estimate Earth-like planet detection capabilities. VI. Simulation of granulation and supergranulation radial velocity and photometric time series. *A&A*, 583: A118, November 2015. doi: 10.1051/0004-6361/201525721.

Steve Miller, Tom Stallard, Jonathan Tennyson, and Henrik Melin. Cooling by

H3+ Emission. *Journal of Physical Chemistry A*, 117(39):9770–9777, October 2013. doi: 10.1021/jp312468b.

Sarah Millholland, Songhu Wang, and Gregory Laughlin. Kepler Multi-planet Systems Exhibit Unexpected Intra-system Uniformity in Mass and Radius. *ApJ*, 849(2):L33, November 2017. doi: 10.3847/2041-8213/aa9714.

Ryan Miranda and Dong Lai. Trapping of low-mass planets outside the truncated inner edges of protoplanetary discs. *MNRAS*, 473(4):5267–5274, February 2018. doi: 10.1093/mnras/stx2706.

William Misener and Hilke E. Schlichting. To cool is to keep: residual H/He atmospheres of super-Earths and sub-Neptunes. *MNRAS*, 503(4):5658–5674, June 2021. doi: 10.1093/mnras/stab895.

E. Moraux, S. Artemenko, J. Bouvier, J. Irwin, M. Ibrahimov, T. Magakian, K. Grankin, E. Nikogossian, C. Cardoso, S. Hodgkin, S. Aigrain, and T. A. Movsessian. The Monitor Project: stellar rotation at 13 Myr. I. A photometric monitoring survey of the young open cluster h Persei. *A&A*, 560:A13, December 2013. doi: 10.1051/0004-6361/201321508.

C. Mordasini, Y. Alibert, and W. Benz. Extrasolar planet population synthesis. I. Method, formation tracks, and mass-distance distribution. *A&A*, 501(3):1139–1160, July 2009. doi: 10.1051/0004-6361/200810301.

Olivier Mousis, Magali Deleuil, Artyom Aguichine, Emmanuel Marcq, Joseph Naar, Lorena Acuña Aguirre, Bastien Brugger, and Thomas Gonçalves. Irradiated Ocean Planets Bridge Super-Earth and Sub-Neptune Populations. *ApJ*, 896(2):L22, June 2020. doi: 10.3847/2041-8213/ab9530.

Ruth A. Murray-Clay, Eugene I. Chiang, and Norman Murray. Atmospheric Escape From Hot Jupiters. *ApJ*, 693(1):23–42, March 2009a. doi: 10.1088/0004-637X/693/1/23.

Ruth A. Murray-Clay, Eugene I. Chiang, and Norman Murray. Atmospheric Escape From Hot Jupiters. *ApJ*, 693(1):23–42, March 2009b. doi: 10.1088/0004-637X/693/1/23.

Emma Nabbie, Chelsea X. Huang, Jennifer A. Burt, David J. Armstrong, Eric E. Mamajek, Vardan Adibekyan, Sérgio G. Sousa, Eric D. Lopez, Daniel Thorngren, Jorge Fernández Fernández, Gongjie Li, James S. Jenkins, Jose I. Vines, João Gomes da Silva, Robert A. Wittenmyer, Daniel Bayliss, César Briceño, Karen A. Collins, Xavier Dumusque, Keith Horne, Marcelo Aron F. Keniger, Nicholas Law, Jorge Lillo-Box, Shang-Fei Liu, Andrew W. Mann, Louise D. Nielsen, Ares Osborn, Howard M. Relles, José J. Rodrigues, Juan Serrano Bell, Gregor Srdoc, Chris Stockdale, Paul A. Strøm, Cristilyn N. Watkins, Peter J. Wheatley, Duncan J. Wright, George Zhou, Carl Ziegler, George Ricker, Sara Seager, Roland Vanderspek, Joshua N. Winn, Jon M. Jenkins, Michael Fausnaugh, Michelle Kunimoto, Hugh P. Osborn, Samuel N. Quinn, and Bill Wohler. Surviving in the Hot-Neptune Desert: The Discovery of the Ultrahot Neptune TOI-3261b. *AJ*, 168(3):132, September 2024. doi: 10.3847/1538-3881/ad60be.

Valery M. Nakariakov and Erwin Verwichte. Coronal Waves and Oscillations. *Living Reviews in Solar Physics*, 2(1):3, May 2005. doi: 10.12942/lrsp-2005-3.

Luca Naponiello, Luigi Mancini, Alessandro Sozzetti, Aldo S. Bonomo, Alessandro Morbidelli, Jingyao Dou, Li Zeng, Zoe M. Leinhardt, Katia Biazzo, Patricio E. Cubillos, Matteo Pinamonti, Daniele Locci, Antonio Maggio, Mario Damasso, Antonino F. Lanza, Jack J. Lissauer, Karen A. Collins, Philip J. Carter, Eric L. N. Jensen, Andrea Bignamini, Walter Boschin, Luke G. Bouma, David R. Ciardi, Rosario Cosentino, Ian Crossfield, Silvano Desidera, Xavier Dumusque, Aldo F. M. Fiorenzano, Akihiko Fukui, Paolo Giacobbe, Crystal L. Gnilka, Adriano Ghedina, Gloria Guilluy, Avet Harutyunyan, Steve B. Howell, Jon M. Jenkins, Michael B. Lund, John F. Kielkopf, Katie V. Lester, Luca Malavolta, Andrew W. Mann, Rachel A. Matson, Elisabeth C. Matthews, Domenico Nardiello, Norio Narita, Emanuele Pace, Isabella Pagano, Enric Palle, Marco Pedani, Sara Seager, Joshua E. Schlieder, Richard P. Schwarz, Avi Shporer, Joseph D. Twicken, Joshua N. Winn, Carl Ziegler, and Tiziano Zingales. A super-massive Neptune-sized planet. *Nature*, 622(7982):255–260, October 2023a. doi: 10.1038/s41586-023-06499-2.

Luca Naponiello, Luigi Mancini, Alessandro Sozzetti, Aldo S. Bonomo, Alessandro Morbidelli, Jingyao Dou, Li Zeng, Zoe M. Leinhardt, Katia Biazzo, Patricio E. Cubillos, Matteo Pinamonti, Daniele Locci, Antonio Maggio, Mario Damasso, Antonino F. Lanza, Jack J. Lissauer, Karen A. Collins, Philip J. Carter, Eric L. N. Jensen, Andrea Bignamini, Walter Boschin, Luke G. Bouma, David R. Ciardi, Rosario Cosentino, Ian Crossfield, Silvano Desidera, Xavier Dumusque, Aldo F. M. Fiorenzano, Akihiko Fukui, Paolo Giacobbe, Crystal L. Gnilka, Adriano Ghedina, Gloria Guilluy, Avet Harutyunyan, Steve B. Howell, Jon M. Jenkins, Michael B. Lund, John F. Kielkopf, Katie V. Lester, Luca Malavolta, Andrew W. Mann, Rachel A. Matson, Elisabeth C. Matthews, Domenico Nardiello, Norio Narita, Emanuele Pace, Isabella Pagano, Enric Palle, Marco Pedani, Sara Seager, Joshua E. Schlieder, Richard P. Schwarz, Avi Shporer, Joseph D. Twicken, Joshua N. Winn, Carl Ziegler, and Tiziano Zingales. A super-massive Neptune-sized planet. *Nature*, 622(7982):255–260, October 2023b. doi: 10.1038/s41586-023-06499-2.

Elisabeth R. Newton, Andrew W. Mann, Adam L. Kraus, John H. Livingston, Andrew Vanderburg, Jason L. Curtis, Pa Chia Thao, Keith Hawkins, Mackenna L. Wood, Aaron C. Rizzuto, Abderahmane Soubkiou, Benjamin M. Tofflemire, George Zhou, Ian J. M. Crossfield, Logan A. Pearce, Karen A. Collins, Dennis M. Conti, Thiam-Guan Tan, Steven Villeneuva, Alton Spencer, Diana Dragomir, Samuel N. Quinn, Eric L. N. Jensen, Kevin I. Collins, Chris Stockdale, Ryan Cloutier, Coel Hellier, Zouhair Benkhaldoun, Carl Ziegler, César Briceño, Nicholas Law, Björn Benneke, Jessie L. Christiansen, Varoujan Gorjian, Stephen R. Kane, Laura Kreidberg, Farisa Y. Morales, Michael W. Werner, Joseph D. Twicken, Alan M. Levine, David R. Ciardi, Natalia M. Guerrero, Katharine Hesse, Elisa V. Quintana, Bernie Shiao, Jeffrey C. Smith, Guillermo Torres, George R. Ricker, Roland Vanderspek, Sara Seager, Joshua N. Winn, Jon M. Jenkins, and David W. Latham. TESS Hunt for Young and Maturing Exoplanets (THYME). IV. Three Small Planets Orbiting a 120 Myr Old Star in the Pisces-Eridanus Stream. *AJ*, 161(2):65, February 2021. doi: 10.3847/1538-3881/abccc6.

R. Nordon, E. Behar, and S. A. Drake. Variability of a stellar corona on a time scale of days. Evidence for abundance fractionation in an emerging coronal active region. *A&A*, 550:A22, February 2013. doi: 10.1051/0004-6361/201220491.

Lisa Nortmann, Enric Pallé, Michael Salz, Jorge Sanz-Forcada, Evangelos Nagel, F. Javier Alonso-Floriano, Stefan Czesla, Fei Yan, Guo Chen, Ignas A. G. Snellen, Mathias Zechmeister, Jürgen H. M. M. Schmitt, Manuel López-Puertas, Núria Casasayas-Barris, Florian F. Bauer, Pedro J. Amado, José A. Caballero, Stefan Dreizler, Thomas Henning, Manuel Lampón, David Montes, Karan Molaverdikhani, Andreas Quirrenbach, Ansgar Reiners, Ignasi Ribas, Alejandro Sánchez-López, P. Christian Schneider, and María R. Zapatero Osorio.

Ground-based detection of an extended helium atmosphere in the Saturn-mass exoplanet WASP-69b. *Science*, 362(6421):1388–1391, December 2018. doi: 10.1126/science.aat5348.

R. W. Noyes. The relation between rotation and magnetic activity on lower main sequence stars as derived from chromospheric indicators. In J. O. Stenflo, editor, *Solar and Stellar Magnetic Fields: Origins and Coronal Effects*, volume 102, pages 133–146, January 1983.

R. W. Noyes, L. W. Hartmann, S. L. Baliunas, D. K. Duncan, and A. H. Vaughan. Rotation, convection, and magnetic activity in lower main-sequence stars. *ApJ*, 279:763–777, April 1984. doi: 10.1086/161945.

Alejandro Núñez, Marcel A. Agüeros, Kevin R. Covey, Stephanie T. Douglas, Jeremy J. Drake, Rayna Rampalli, Emily C. Bowsher, Phillip A. Cargile, Adam L. Kraus, and Nicholas M. Law. The Factory and the Beehive. IV. A Comprehensive Study of the Rotation X-Ray Activity Relation in Praesepe and the Hyades. *ApJ*, 931(1):45, May 2022. doi: 10.3847/1538-4357/ac6517.

Antonija Oklopčić. Helium Absorption at 1083 nm from Extended Exoplanet Atmospheres: Dependence on Stellar Radiation. *ApJ*, 881(2):133, August 2019. doi: 10.3847/1538-4357/ab2f7f.

Antonija Oklopčić and Christopher M. Hirata. A New Window into Escaping Exoplanet Atmospheres: 10830 Å Line of Helium. *ApJ*, 855(1):L11, March 2018. doi: 10.3847/2041-8213/aaada9.

S. Orlando, F. Favata, G. Micela, S. Sciortino, A. Maggio, J. H. M. M. Schmitt, J. Robrade, and M. Mittag. Fifteen years in the high-energy life of the solar-type star HD 81809. XMM-Newton observations of a stellar activity cycle. *A&A*, 605: A19, September 2017. doi: 10.1051/0004-6361/201731301.

Ares Osborn, David J. Armstrong, Jorge Fernández Fernández, Henrik Knierim, Vardan Adibekyan, Karen A. Collins, Elisa Delgado-Mena, Malcolm Fridlund, João Gomes da Silva, Coel Hellier, David G. Jackson, George W. King, Jorge Lillo-Box, Rachel A. Matson, Elisabeth C. Matthews, Nuno C. Santos, Sérgio G. Sousa, Keivan G. Stassun, Thiam-Guan Tan, George R. Ricker, Roland Vanderspek, David W. Latham, Sara Seager, Joshua N. Winn, Jon M. Jenkins, Daniel Bayliss, Luke G. Bouma, David R. Ciardi, Kevin I. Collins, Knicole D.

Colón, Ian J. M. Crossfield, Olivier D. S. Demangeon, Rodrigo F. Díaz, Caroline Dorn, Xavier Dumusque, Marcelo Aron Fetzner Keniger, Pedro Figueira, Tianjun Gan, Robert F. Goeke, Andreas Hadjigeorghiou, Faith Hawthorn, Ravit Helled, Steve B. Howell, Louise D. Nielsen, Hugh P. Osborn, Samuel N. Quinn, Ramotholo Sefako, Avi Shporer, Paul A. Strøm, Joseph D. Twicken, Andrew Vanderburg, and Peter J. Wheatley. TOI-332 b: A super dense Neptune found deep within the Neptunian desert. *MNRAS*, August 2023. doi: 10.1093/mnras/stad2575.

J. F. Otegi, F. Bouchy, and R. Helled. Revisited mass-radius relations for exoplanets below 120 $M_\oplus$. *A&A*, 634:A43, February 2020. doi: 10.1051/0004-6361/201936482.

James E. Owen. Atmospheric Escape and the Evolution of Close-In Exoplanets. *Annual Review of Earth and Planetary Sciences*, 47:67–90, May 2019. doi: 10.1146/annurev-earth-053018-060246.

James E. Owen and Marcelo A. Alvarez. UV Driven Evaporation of Close-in Planets: Energy-limited, Recombination-limited, and Photon-limited Flows. *ApJ*, 816(1):34, January 2016. doi: 10.3847/0004-637X/816/1/34.

James E. Owen and Beatriz Campos Estrada. EvapMass: Minimum mass of planets predictor. Astrophysics Source Code Library, record ascl:2011.015, November 2020a.

James E. Owen and Beatriz Campos Estrada. Testing exoplanet evaporation with multitransiting systems. *MNRAS*, 491(4):5287–5297, February 2020b. doi: 10.1093/mnras/stz3435.

James E. Owen and Alan P. Jackson. Planetary evaporation by UV & X-ray radiation: basic hydrodynamics. *MNRAS*, 425(4):2931–2947, October 2012. doi: 10.1111/j.1365-2966.2012.21481.x.

James E. Owen and Dong Lai. Photoevaporation and high-eccentricity migration created the sub-Jovian desert. *MNRAS*, 479(4):5012–5021, October 2018. doi: 10.1093/mnras/sty1760.

James E. Owen and Hilke E. Schlichting. Mapping out the parameter space for photoevaporation and core-powered mass-loss. *MNRAS*, 528(2):1615–1629, February 2024. doi: 10.1093/mnras/stad3972.

James E. Owen and Yanqin Wu. Kepler Planets: A Tale of Evaporation. *ApJ*, 775 (2):105, October 2013. doi: 10.1088/0004-637X/775/2/105.

James E. Owen and Yanqin Wu. Atmospheres of Low-mass Planets: The "Boil-off". *ApJ*, 817(2):107, February 2016. doi: 10.3847/0004-637X/817/2/10710.48550/arXiv.1506.02049.

James E. Owen and Yanqin Wu. The Evaporation Valley in the Kepler Planets. *ApJ*, 847(1):29, September 2017. doi: 10.3847/1538-4357/aa890a.

A. Pál, G. Á. Bakos, G. Torres, R. W. Noyes, D. W. Latham, Géza Kovács, G. W. Marcy, D. A. Fischer, R. P. Butler, D. D. Sasselov, B. Sipőcz, G. A. Esquerdo, Gábor Kovács, R. Stefanik, J. Lázár, I. Papp, and P. Sári. HAT-P-7b: An Extremely Hot Massive Planet Transiting a Bright Star in the Kepler Field. *ApJ*, 680(2):1450–1456, June 2008. doi: 10.1086/588010.

R. Pallavicini, L. Golub, R. Rosner, G. S. Vaiana, T. Ayres, and J. L. Linsky. Relations among stellar X-ray emission observed from Einstein, stellar rotation and bolometric luminosity. *ApJ*, 248:279–290, August 1981. doi: 10.1086/159152.

E. Palle, L. Nortmann, N. Casasayas-Barris, M. Lampón, M. López-Puertas, J. A. Caballero, J. Sanz-Forcada, L. M. Lara, E. Nagel, F. Yan, F. J. Alonso-Floriano, P. J. Amado, G. Chen, C. Cifuentes, M. Cortés-Contreras, S. Czesla, K. Molaverdikhani, D. Montes, V. M. Passegger, A. Quirrenbach, A. Reiners, I. Ribas, A. Sánchez-López, A. Schweitzer, M. Stangret, M. R. Zapatero Osorio, and M. Zechmeister. A He I upper atmosphere around the warm Neptune GJ 3470 b. *A&A*, 638:A61, June 2020. doi: 10.1051/0004-6361/202037719.

E. N. Parker. The Hydrodynamic Theory of Solar Corpuscular Radiation and Stellar Winds. *ApJ*, 132:821, November 1960. doi: 10.1086/146985.

E. N. Parker. Dynamical Properties of Stellar Coronas and Stellar Winds. I. Integration of the Momentum Equation. *ApJ*, 139:72, January 1964. doi: 10.1086/147740.

E. N. Parker. Sunspots and the physics of magnetic flux tubes. IX. Umbral dots and longitudinal overstability. *ApJ*, 234:333–347, November 1979. doi: 10.1086/157501.

Bill Paxton, Pablo Marchant, Josiah Schwab, Evan B. Bauer, Lars Bildsten, Matteo Cantiello, Luc Dessart, R. Farmer, H. Hu, N. Langer, R. H. D. Townsend, Dean M. Townsley, and F. X. Timmes. Modules for Experiments in Stellar Astrophysics (MESA): Binaries, Pulsations, and Explosions. *ApJS*, 220(1):15, September 2015. doi: 10.1088/0067-0049/220/1/15.

Mark J. Pecaut and Eric E. Mamajek. Intrinsic Colors, Temperatures, and Bolometric Corrections of Pre-main-sequence Stars. *ApJS*, 208(1):9, September 2013. doi: 10.1088/0067-0049/208/1/9.

T. Penz, N. V. Erkaev, Yu. N. Kulikov, D. Langmayr, H. Lammer, G. Micela, C. Cecchi-Pestellini, H. K. Biernat, F. Selsis, P. Barge, M. Deleuil, and A. Léger. Mass loss from "Hot Jupiters"—Implications for CoRoT discoveries, Part II: Long time thermal atmospheric evaporation modeling. *Planet. Space Sci.*, 56 (9):1260–1272, July 2008. doi: 10.1016/j.pss.2008.04.005.

F. Pepe, S. Cristiani, R. Rebolo, N. C. Santos, H. Dekker, A. Cabral, P. Di Marcantonio, P. Figueira, G. Lo Curto, C. Lovis, M. Mayor, D. Mégevand, P. Molaro, M. Riva, M. R. Zapatero Osorio, M. Amate, A. Manescau, L. Pasquini, F. M. Zerbi, V. Adibekyan, M. Abreu, M. Affolter, Y. Alibert, M. Aliverti, R. Allart, C. Allende Prieto, D. Álvarez, D. Alves, G. Avila, V. Baldini, T. Bandy, S. C. C. Barros, W. Benz, A. Bianco, F. Borsa, V. Bourrier, F. Bouchy, C. Broeg, G. Calderone, R. Cirami, J. Coelho, P. Conconi, I. Coretti, C. Cumani, G. Cupani, V. D'Odorico, M. Damasso, S. Deiries, B. Delabre, O. D. S. Demangeon, X. Dumusque, D. Ehrenreich, J. P. Faria, A. Fragoso, L. Genolet, M. Genoni, R. Génova Santos, J. I. González Hernández, I. Hughes, O. Iwert, F. Kerber, J. Knudstrup, M. Landoni, B. Lavie, J. Lillo-Box, J. L. Lizon, C. Maire, C. J. A. P. Martins, A. Mehner, G. Micela, A. Modigliani, M. A. Monteiro, M. J. P. F. G. Monteiro, M. Moschetti, M. T. Murphy, N. Nunes, L. Oggioni, A. Oliveira, M. Oshagh, E. Pallé, G. Pariani, E. Poretti, J. L. Rasilla, J. Rebordão, E. M. Redaelli, S. Santana Tschudi, P. Santin, P. Santos, D. Ségransan, T. M. Schmidt, A. Segovia, D. Sosnowska, A. Sozzetti, S. G. Sousa, P. Spanò, A. Suárez Mascareño, H. Tabernero, F. Tenegi, S. Udry, and A. Zanutta. ESPRESSO at VLT. On-sky performance and first results. *A&A*, 645:A96, January 2021. doi: 10.1051/0004-6361/202038306.

Joshua Pepper, Andrew Gould, and D. L. Depoy. KELT: The Kilodegree Extremely Little Telescope. In Stephen S. Holt and Drake Deming, editors, *The Search for Other Worlds*, volume 713 of *American Institute of Physics Conference Series*, pages 185–188. AIP, June 2004. doi: 10.1063/1.1774522.

M. A. C. Perryman, A. G. A. Brown, Y. Lebreton, A. Gomez, C. Turon, G. Cayrel de Strobel, J. C. Mermilliod, N. Robichon, J. Kovalevsky, and F. Crifo. The Hyades: distance, structure, dynamics, and age. *A&A*, 331:81–120, March 1998.

Erik A. Petigura, Andrew W. Howard, Geoffrey W. Marcy, John Asher Johnson, Howard Isaacson, Phillip A. Cargile, Leslie Hebb, Benjamin J. Fulton, Lauren M. Weiss, Timothy D. Morton, Joshua N. Winn, Leslie A. Rogers, Evan Sinukoff, Lea A. Hirsch, and Ian J. M. Crossfield. The California-Kepler Survey. I. High-resolution Spectroscopy of 1305 Stars Hosting Kepler Transiting Planets. *AJ*, 154(3):107, September 2017. doi: 10.3847/1538-3881/aa80de.

N. Pizzolato, A. Maggio, G. Micela, S. Sciortino, and P. Ventura. The stellar activity-rotation relationship revisited: Dependence of saturated and non-saturated X-ray emission regimes on stellar mass for late-type dwarfs. *A&A*, 397:147–157, January 2003. doi: 10.1051/0004-6361:20021560.

D. L. Pollacco, I. Skillen, A. Collier Cameron, D. J. Christian, C. Hellier, J. Irwin, T. A. Lister, R. A. Street, R. G. West, D. R. Anderson, W. I. Clarkson, H. Deeg, B. Enoch, A. Evans, A. Fitzsimmons, C. A. Haswell, S. Hodgkin, K. Horne, S. R. Kane, F. P. Keenan, P. F. L. Maxted, A. J. Norton, J. Osborne, N. R. Parley, R. S. I. Ryans, B. Smalley, P. J. Wheatley, and D. M. Wilson. The WASP Project and the SuperWASP Cameras. *PASP*, 118(848):1407–1418, October 2006. doi: 10.1086/508556.

K. Poppenhaeger. Helium absorption in exoplanet atmospheres is connected to stellar coronal abundances. *MNRAS*, 512(2):1751–1764, May 2022. doi: 10.1093/mnras/stac507.

K. Poppenhaeger, J. H. M. M. Schmitt, and S. J. Wolk. Transit Observations of the Hot Jupiter HD 189733b at X-Ray Wavelengths. *ApJ*, 773(1):62, August 2013. doi: 10.1088/0004-637X/773/1/62.

K. Poppenhaeger, L. Ketzer, and M. Mallonn. X-ray irradiation and evaporation of the four young planets around V1298 Tau. *MNRAS*, 500(4):4560–4572, January 2021. doi: 10.1093/mnras/staa1462.

P. Predehl, R. Andritschke, V. Arefiev, V. Babyshkin, O. Batanov, W. Becker, H. Böhringer, A. Bogomolov, T. Boller, K. Borm, W. Bornemann, H. Bräuninger, M. Brüggen, H. Brunner, M. Brusa, E. Bulbul, M. Buntov,

V. Burwitz, W. Burkert, N. Clerc, E. Churazov, D. Coutinho, T. Dauser, K. Dennerl, V. Doroshenko, J. Eder, V. Emberger, T. Eraerds, A. Finoguenov, M. Freyberg, P. Friedrich, S. Friedrich, M. Fürmetz, A. Georgakakis, M. Gilfanov, S. Granato, C. Grossberger, A. Gueguen, P. Gureev, F. Haberl, O. Hälker, G. Hartner, G. Hasinger, H. Huber, L. Ji, A. v. Kienlin, W. Kink, F. Korotkov, I. Kreykenbohm, G. Lamer, I. Lomakin, I. Lapshov, T. Liu, C. Maitra, N. Meidinger, B. Menz, A. Merloni, T. Mernik, B. Mican, J. Mohr, S. Müller, K. Nandra, V. Nazarov, F. Pacaud, M. Pavlinsky, E. Perinati, E. Pfeffermann, D. Pietschner, M. E. Ramos-Ceja, A. Rau, J. Reiffers, T. H. Reiprich, J. Robrade, M. Salvato, J. Sanders, A. Santangelo, M. Sasaki, H. Scheuerle, C. Schmid, J. Schmitt, A. Schwope, A. Shirshakov, M. Steinmetz, I. Stewart, L. Strüder, R. Sunyaev, C. Tenzer, L. Tiedemann, J. Trümper, V. Voron, P. Weber, J. Wilms, and V. Yaroshenko. The eROSITA X-ray telescope on SRG. *A&A*, 647:A1, March 2021. doi: 10.1051/0004-6361/202039313.

Eric Priest and Terry Forbes. *Magnetic Reconnection: MHD Theory and Applications*. Cambridge University Press, 2000. doi: 10.1017/CBO9780511525087.

J. P. Pye, S. Rosen, D. Fyfe, and A. C. Schröder. A survey of stellar X-ray flares from the XMM-Newton serendipitous source catalogue: HIPPARCOS-Tycho cool stars. *A&A*, 581:A28, September 2015. doi: 10.1051/0004-6361/201526217.

D. Queloz, M. Mayor, L. Weber, A. Blécha, M. Burnet, B. Confino, D. Naef, F. Pepe, N. Santos, and S. Udry. The CORALIE survey for southern extra-solar planets. I. A planet orbiting the star Gliese 86. *A&A*, 354:99–102, February 2000.

A. Quirrenbach, P. J. Amado, J. A. Caballero, R. Mundt, A. Reiners, I. Ribas, W. Seifert, M. Abril, J. Aceituno, F. J. Alonso-Floriano, M. Ammler-von Eiff, R. Antona Jiménez, H. Anwand-Heerwart, M. Azzaro, F. Bauer, D. Barrado, S. Becerril, V. J. S. Béjar, D. Benítez, Z. M. Berdiñas, M. C. Cárdenas, E. Casal, A. Claret, J. Colomé, M. Cortés-Contreras, S. Czesla, M. Doellinger, S. Dreizler, C. Feiz, M. Fernández, D. Galadí, M. C. Gálvez-Ortiz, A. García-Piquer, M. L. García-Vargas, R. Garrido, L. Gesa, V. Gómez Galera, E. González Álvarez, J. I. González Hernández, U. Grözinger, J. Guàrdia, E. W. Guenther, E. de Guindos, J. Gutiérrez-Soto, H. J. Hagen, A. P. Hatzes, P. H. Hauschildt, J. Helmling, T. Henning, D. Hermann, L. Hernández Castaño, E. Herrero, D. Hidalgo, G. Holgado, A. Huber, K. F. Huber, S. Jeffers, V. Joergens, E. de Juan, M. Kehr,

R. Klein, M. Kürster, A. Lamert, S. Lalitha, W. Laun, U. Lemke, R. Lenzen, Mauro López del Fresno, B. López Martí, J. López-Santiago, U. Mall, H. Mandel, E. L. Martín, S. Martín-Ruiz, H. Martínez-Rodríguez, C. J. Marvin, R. J. Mathar, E. Mirabet, D. Montes, R. Morales Muñoz, A. Moya, V. Naranjo, A. Ofir, R. Oreiro, E. Pallé, J. Panduro, V. M. Passegger, A. Pérez-Calpena, D. Pérez Medialdea, M. Perger, M. Pluto, A. Ramón, R. Rebolo, P. Redondo, S. Reffert, S. Reinhardt, P. Rhode, H. W. Rix, F. Rodler, E. Rodríguez, C. Rodríguez-López, E. Rodríguez-Pérez, R. R. Rohloff, A. Rosich, E. Sánchez-Blanco, M. A. Sánchez Carrasco, J. Sanz-Forcada, L. F. Sarmiento, S. Schäfer, J. Schiller, C. Schmidt, J. H. M. M. Schmitt, E. Solano, O. Stahl, C. Storz, J. Stürmer, J. C. Suárez, R. G. Ulbrich, G. Veredas, K. Wagner, J. Winkler, M. R. Zapatero Osorio, M. Zechmeister, F. J. Abellán de Paco, G. Anglada-Escudé, C. del Burgo, A. Klutsch, J. L. Lizon, M. López-Morales, J. C. Morales, M. A. C. Perryman, S. M. Tulloch, and W. Xu. CARMENES instrument overview. In Suzanne K. Ramsay, Ian S. McLean, and Hideki Takami, editors, *Ground-based and Airborne Instrumentation for Astronomy V*, volume 9147 of *Society of Photo-Optical Instrumentation Engineers (SPIE) Conference Series*, page 91471F, July 2014. doi: 10.1117/12.2056453.

H. Rauer, C. Catala, C. Aerts, T. Appourchaux, W. Benz, A. Brandeker, J. Christensen-Dalsgaard, M. Deleuil, L. Gizon, M. J. Goupil, M. Güdel, E. Janot-Pacheco, M. Mas-Hesse, I. Pagano, G. Piotto, D. Pollacco, Ċ. Santos, A. Smith, J. C. Suárez, R. Szabó, S. Udry, V. Adibekyan, Y. Alibert, J. M. Almenara, P. Amaro-Seoane, M. Ammler-von Eiff, M. Asplund, E. Antonello, S. Barnes, F. Baudin, K. Belkacem, M. Bergemann, G. Bihain, A. C. Birch, X. Bonfils, I. Boisse, A. S. Bonomo, F. Borsa, I. M. Brandão, E. Brocato, S. Brun, M. Burleigh, R. Burston, J. Cabrera, S. Cassisi, W. Chaplin, S. Charpinet, C. Chiappini, R. P. Church, Sz. Csizmadia, M. Cunha, M. Damasso, M. B. Davies, H. J. Deeg, R. F. Díaz, S. Dreizler, C. Dreyer, P. Eggenberger, D. Ehrenreich, P. Eigmüller, A. Erikson, R. Farmer, S. Feltzing, F. de Oliveira Fialho, P. Figueira, T. Forveille, M. Fridlund, R. A. García, P. Giommi, G. Giuffrida, M. Godolt, J. Gomes da Silva, T. Granzer, J. L. Grenfell, A. Grotsch-Noels, E. Günther, C. A. Haswell, A. P. Hatzes, G. Hébrard, S. Hekker, R. Helled, K. Heng, J. M. Jenkins, A. Johansen, M. L. Khodachenko, K. G. Kislyakova, W. Kley, U. Kolb, N. Krivova, F. Kupka, H. Lammer, A. F. Lanza, Y. Lebreton, D. Magrin, P. Marcos-Arenal, P. M. Marrese, J. P. Marques, J. Martins, S. Mathis, S. Mathur, S. Messina, A. Miglio, J. Montalban, M. Montalto, M. J. P. F. G. Monteiro, H. Moradi, E. Moravveji, C. Mordasini, T. Morel, A. Mortier, V. Nascimbeni, R. P. Nelson, M. B. Nielsen, L. Noack, A. J. Norton, A. Ofir, M. Oshagh, R. M. Ouazzani, P. Pápics, V. C. Parro, P. Petit, B. Plez, E. Poretti, A. Quirrenbach, R. Ragazzoni, G. Raimondo, M. Rainer, D. R. Reese, R. Redmer, S. Reffert, B. Rojas-Ayala, I. W. Roxburgh, S. Salmon, A. Santerne, J. Schneider, J. Schou, S. Schuh, H. Schunker, A. Silva-Valio, R. Silvotti, I. Skillen, I. Snellen, F. Sohl, S. G. Sousa, A. Sozzetti, D. Stello, K. G. Strassmeier, M. Švanda, Gy. M. Szabó, A. Tkachenko, D. Valencia, V. Van Grootel, S. D. Vauclair, P. Ventura, F. W. Wagner, N. A. Walton, J. Weingrill, S. C. Werner, P. J. Wheatley, and K. Zwintz. The PLATO 2.0 mission. *Experimental Astronomy*, 38(1-2):249–330, November 2014. doi: 10.1007/s10686-014-9383-4.

L. M. Rebull, S. C. Wolff, and S. E. Strom. Stellar Rotation in Young Clusters: The First 4 Million Years. *AJ*, 127(2):1029–1051, February 2004. doi: 10.1086/380931.

Seth Redfield and Jeffrey L. Linsky. Microstructure of the Local Interstellar Cloud and the Identification of the Hyades Cloud. *ApJ*, 551(1):413–428, April 2001. doi: 10.1086/320096.

Álvaro Ribas, Hervé Bouy, and Bruno Merín. Protoplanetary disk lifetimes vs. stellar mass and possible implications for giant planet populations. *A&A*, 576: A52, April 2015. doi: 10.1051/0004-6361/201424846.

Ignasi Ribas, Edward F. Guinan, Manuel Güdel, and Marc Audard. Evolution of the Solar Activity over Time and Effects on Planetary Atmospheres. I. High-Energy Irradiances (1-1700 Å). *ApJ*, 622(1):680–694, March 2005. doi: 10.1086/427977.

A. J. W. Richert, K. V. Getman, E. D. Feigelson, M. A. Kuhn, P. S. Broos, M. S. Povich, M. R. Bate, and G. P. Garmire. Circumstellar disc lifetimes in numerous galactic young stellar clusters. *MNRAS*, 477(4):5191–5206, July 2018. doi: 10.1093/mnras/sty949.

George R. Ricker, Joshua N. Winn, Roland Vanderspek, David W. Latham, Gáspár Á. Bakos, Jacob L. Bean, Zachory K. Berta-Thompson, Timothy M. Brown, Lars Buchhave, Nathaniel R. Butler, R. Paul Butler, William J. Chaplin, David Charbonneau, Jørgen Christensen-Dalsgaard, Mark Clampin, Drake

Deming, John Doty, Nathan De Lee, Courtney Dressing, Edward W. Dunham, Michael Endl, Francois Fressin, Jian Ge, Thomas Henning, Matthew J. Holman, Andrew W. Howard, Shigeru Ida, Jon M. Jenkins, Garrett Jernigan, John Asher Johnson, Lisa Kaltenegger, Nobuyuki Kawai, Hans Kjeldsen, Gregory Laughlin, Alan M. Levine, Douglas Lin, Jack J. Lissauer, Phillip MacQueen, Geoffrey Marcy, Peter R. McCullough, Timothy D. Morton, Norio Narita, Martin Paegert, Enric Palle, Francesco Pepe, Joshua Pepper, Andreas Quirrenbach, Stephen A. Rinehart, Dimitar Sasselov, Bun'ei Sato, Sara Seager, Alessandro Sozzetti, Keivan G. Stassun, Peter Sullivan, Andrew Szentgyorgyi, Guillermo Torres, Stephane Udry, and Joel Villasenor. Transiting Exoplanet Survey Satellite (TESS). *Journal of Astronomical Telescopes, Instruments, and Systems*, 1: 014003, January 2015. doi: 10.1117/1.JATIS.1.1.014003.

M. Riello, F. De Angeli, D. W. Evans, P. Montegriffo, J. M. Carrasco, G. Busso, L. Palaversa, P. W. Burgess, C. Diener, M. Davidson, N. Rowell, C. Fabricius, C. Jordi, M. Bellazzini, E. Pancino, D. L. Harrison, C. Cacciari, F. van Leeuwen, N. C. Hambly, S. T. Hodgkin, P. J. Osborne, G. Altavilla, M. A. Barstow, A. G. A. Brown, M. Castellani, S. Cowell, F. De Luise, G. Gilmore, G. Giuffrida, S. Hidalgo, G. Holland, S. Marinoni, C. Pagani, A. M. Piersimoni, L. Pulone, S. Ragaini, M. Rainer, P. J. Richards, N. Sanna, N. A. Walton, M. Weiler, and A. Yoldas. Gaia Early Data Release 3. Photometric content and validation. *A&A*, 649:A3, May 2021. doi: 10.1051/0004-6361/202039587.

J. Robrade, J. H. M. M. Schmitt, and F. Favata. Coronal activity cycles in nearby G and K stars. XMM-Newton monitoring of 61 Cygni and α Centauri. *A&A*, 543:A84, July 2012. doi: 10.1051/0004-6361/201219046.

Keighley E. Rockcliffe, Elisabeth R. Newton, Allison Youngblood, Girish M. Duvvuri, Peter Plavchan, Peter Gao, Andrew W. Mann, and Patrick J. Lowrance. The Variable Detection of Atmospheric Escape around the Young, Hot Neptune AU Mic b. *AJ*, 166(2):77, August 2023. doi: 10.3847/1538-3881/ace536.

Joseph E. Rodriguez, Juliette C. Becker, Jason D. Eastman, Sam Hadden, Andrew Vanderburg, Tali Khain, Samuel N. Quinn, Andrew Mayo, Courtney D. Dressing, Joshua E. Schlieder, David R. Ciardi, David W. Latham, Saul Rappaport, Fred C. Adams, Perry Berlind, Allyson Bieryla, Michael L. Calkins, Gilbert A. Esquerdo, Martti H. Kristiansen, Mark Omohundro, Hans Martin Schwengeler, Keivan G. Stassun, and Ivan Terentev. A Compact Multi-planet System with a Significantly Misaligned Ultra Short Period Planet. *AJ*, 156(5):245, November 2018. doi: 10.3847/1538-3881/aae530.

James G. Rogers and James E. Owen. Unveiling the planet population at birth. *MNRAS*, 503(1):1526–1542, May 2021. doi: 10.1093/mnras/stab529.

James G. Rogers, Akash Gupta, James E. Owen, and Hilke E. Schlichting. Photoevaporation versus core-powered mass-loss: model comparison with the 3D radius gap. *MNRAS*, 508(4):5886–5902, December 2021. doi: 10.1093/mnras/stab2897.

James G. Rogers, Hilke E. Schlichting, and James E. Owen. Conclusive Evidence for a Population of Water Worlds around M Dwarfs Remains Elusive. *ApJ*, 947 (1):L19, April 2023. doi: 10.3847/2041-8213/acc86f.

James G. Rogers, James E. Owen, and Hilke E. Schlichting. Under the light of a new star: evolution of planetary atmospheres through protoplanetary disc dispersal and boil-off. *MNRAS*, 529(3):2716–2733, April 2024. doi: 10.1093/mnras/stae563.

R. Rosner, W. H. Tucker, and G. S. Vaiana. Dynamics of the quiescent solar corona. *ApJ*, 220:643–645, March 1978. doi: 10.1086/155949.

M. Salz, P. C. Schneider, S. Czesla, and J. H. M. M. Schmitt. Energy-limited escape revised. The transition from strong planetary winds to stable thermospheres. *A&A*, 585:L2, January 2016. doi: 10.1051/0004-6361/201527042.

Roberto Sanchis-Ojeda, Saul Rappaport, Joshua N. Winn, Michael C. Kotson, Alan Levine, and Ileyk El Mellah. A Study of the Shortest-period Planets Found with Kepler. *ApJ*, 787(1):47, May 2014. doi: 10.1088/0004-637X/787/1/47.

J. Sanz-Forcada, G. Micela, I. Ribas, A. M. T. Pollock, C. Eiroa, A. Velasco, E. Solano, and D. García-Álvarez. Estimation of the XUV radiation onto close planets and their evaporation. *A&A*, 532:A6, August 2011. doi: 10.1051/0004-6361/201116594.

J. Sanz-Forcada, B. Stelzer, M. Coffaro, S. Raetz, and J. D. Alvarado-Gómez. Multi-wavelength variability of the young solar analog ı Horologii. X-ray cycle, star spots, flares, and UV emission. *A&A*, 631:A45, November 2019. doi: 10.1051/0004-6361/201935703.

Jorge Sanz-Forcada. X-exoplanets coronal models and planet photoevaporation. *Astronomische Nachrichten*, 343(4):e20008, May 2022. doi: 10.1002/asna.20220008.

Jorge Sanz-Forcada, Manuel López-Puertas, Lisa Nortmann, and Manuel Lampón. The He I 10830 line in exoplanets, triggered by coronal emission. In *Cambridge Workshop on Cool Stars, Stellar Systems, and the Sun*, Cambridge Workshop on Cool Stars, Stellar Systems, and the Sun, page 138, December 2022. doi: 10.5281/zenodo.7561725.

Bradley E. Schaefer, Jeremy R. King, and Constantine P. Deliyannis. Superflares on Ordinary Solar-Type Stars. *ApJ*, 529(2):1026–1030, February 2000. doi: 10.1086/308325.

S. Seager and D. D. Sasselov. Theoretical Transmission Spectra during Extrasolar Giant Planet Transits. *ApJ*, 537(2):916–921, July 2000. doi: 10.1086/309088.

S. Seager, M. Kuchner, C. A. Hier-Majumder, and B. Militzer. Mass-Radius Relationships for Solid Exoplanets. *ApJ*, 669(2):1279–1297, November 2007. doi: 10.1086/521346.

Victor See, Julia Roquette, Louis Amard, and Sean Matt. Further evidence of the link between activity and metallicity using the flaring properties of stars in the Kepler field. *MNRAS*, 524(4):5781–5786, October 2023. doi: 10.1093/mnras/stad2020.

Victor See, Yuxi, Lu, Louis Amard, and Julia Roquette. The impact of stellar metallicity on rotation and activity evolution in the Kepler field using gyro-kinematic ages. *arXiv e-prints*, art. arXiv:2405.00779, May 2024. doi: 10.48550/arXiv.2405.00779.

V. I. Shematovich, D. E. Ionov, and H. Lammer. Heating efficiency in hydrogen-dominated upper atmospheres. *A&A*, 571:A94, November 2014. doi: 10.1051/0004-6361/201423573.

V. Silva Aguirre, G. R. Davies, S. Basu, J. Christensen-Dalsgaard, O. Creevey, T. S. Metcalfe, T. R. Bedding, L. Casagrande, R. Handberg, M. N. Lund, P. E. Nissen, W. J. Chaplin, D. Huber, A. M. Serenelli, D. Stello, V. Van Eylen, T. L. Campante, Y. Elsworth, R. L. Gilliland, S. Hekker, C. Karoff, S. D. Kawaler,

H. Kjeldsen, and M. S. Lundkvist. Ages and fundamental properties of Kepler exoplanet host stars from asteroseismology. *MNRAS*, 452(2):2127–2148, September 2015. doi: 10.1093/mnras/stv1388.

P. Simon. Le cycle solaire. *L'Astronomie*, 97:526–541, December 1983.

Gregory V. A. Simonian, Marc H. Pinsonneault, and Donald M. Terndrup. Rapid Rotation in the Kepler Field: Not a Single Star Phenomenon. *ApJ*, 871(2):174, February 2019. doi: 10.3847/1538-4357/aaf97c.

David K. Sing, Panayotis Lavvas, Gilda E. Ballester, Alain Lecavelier des Etangs, Mark S. Marley, Nikolay Nikolov, Lotfi Ben-Jaffel, Vincent Bourrier, Lars A. Buchhave, Drake L. Deming, David Ehrenreich, Thomas Mikal-Evans, Tiffany Kataria, Nikole K. Lewis, Mercedes López-Morales, Antonio García Muñoz, Gregory W. Henry, Jorge Sanz-Forcada, Jessica J. Spake, Hannah R. Wakeford, and PanCET Collaboration. The Hubble Space Telescope PanCET Program: Exospheric Mg II and Fe II in the Near-ultraviolet Transmission Spectrum of WASP-121b Using Jitter Decorrelation. *AJ*, 158(2):91, August 2019. doi: 10.3847/1538-3881/ab2986.

K. P. Singh, N. E. White, and S. A. Drake. Corona(e) of AR Lacertae. I. The Temperature and Abundance Distribution. *ApJ*, 456:766, January 1996. doi: 10.1086/176695.

A. Skumanich. Time Scales for Ca II Emission Decay, Rotational Braking, and Lithium Depletion. *ApJ*, 171:565, February 1972. doi: 10.1086/151310.

Randall K. Smith, Nancy S. Brickhouse, Duane A. Liedahl, and John C. Raymond. Collisional Plasma Models with APEC/APED: Emission-Line Diagnostics of Hydrogen-like and Helium-like Ions. *ApJ*, 556(2):L91–L95, August 2001. doi: 10.1086/322992.

F. Spada, P. Demarque, Y. C. Kim, and A. Sills. The Radius Discrepancy in Low-mass Stars: Single versus Binaries. *ApJ*, 776(2):87, October 2013. doi: 10.1088/0004-637X/776/2/87.

J. J. Spake, D. K. Sing, T. M. Evans, Oklopčić, A. , V. Bourrier, L. Kreidberg, B. V. Rackham, J. Irwin, D. Ehrenreich, A. Wyttenbach, H. R. Wakeford, Y. Zhou,

K. L. Chubb, N. Nikolov, J. M. Goyal, G. W. Henry, M. H. Williamson, S. Blumenthal, D. R. Anderson, C. Hellier, D. Charbonneau, S. Udry, and N. Madhusudhan. Helium in the eroding atmosphere of an exoplanet. *Nature*, 557 (7703):68–70, May 2018. doi: 10.1038/s41586-018-0067-5.

Jason H. Steffen, Daniel C. Fabrycky, Eric Agol, Eric B. Ford, Robert C. Morehead, William D. Cochran, Jack J. Lissauer, Elisabeth R. Adams, William J. Borucki, Steve Bryson, Douglas A. Caldwell, Andrea Dupree, Jon M. Jenkins, Paul Robertson, Jason F. Rowe, Shawn Seader, Susan Thompson, and Joseph D. Twicken. Transit timing observations from Kepler - VII. Confirmation of 27 planets in 13 multiplanet systems via transit timing variations and orbital stability. *MNRAS*, 428(2):1077–1087, January 2013a. doi: 10.1093/mnras/sts090.

Jason H. Steffen, Daniel C. Fabrycky, Eric Agol, Eric B. Ford, Robert C. Morehead, William D. Cochran, Jack J. Lissauer, Elisabeth R. Adams, William J. Borucki, Steve Bryson, Douglas A. Caldwell, Andrea Dupree, Jon M. Jenkins, Paul Robertson, Jason F. Rowe, Shawn Seader, Susan Thompson, and Joseph D. Twicken. Transit timing observations from Kepler - VII. Confirmation of 27 planets in 13 multiplanet systems via transit timing variations and orbital stability. *MNRAS*, 428(2):1077–1087, January 2013b. doi: 10.1093/mnras/sts090.

L. Strüder, U. Briel, K. Dennerl, R. Hartmann, E. Kendziorra, N. Meidinger, E. Pfeffermann, C. Reppin, B. Aschenbach, W. Bornemann, H. Bräuninger, W. Burkert, M. Elender, M. Freyberg, F. Haberl, G. Hartner, F. Heuschmann, H. Hippmann, E. Kastelic, S. Kemmer, G. Kettenring, W. Kink, N. Krause, S. Müller, A. Oppitz, W. Pietsch, M. Popp, P. Predehl, A. Read, K. H. Stephan, D. Stötter, J. Trümper, P. Holl, J. Kemmer, H. Soltau, R. Stötter, U. Weber, U. Weichert, C. von Zanthier, D. Carathanassis, G. Lutz, R. H. Richter, P. Solc, H. Böttcher, M. Kuster, R. Staubert, A. Abbey, A. Holland, M. Turner, M. Balasini, G. F. Bignami, N. La Palombara, G. Villa, W. Buttler, F. Gianini, R. Lainé, D. Lumb, and P. Dhez. The European Photon Imaging Camera on XMM-Newton: The pn-CCD camera. *A&A*, 365:L18–L26, January 2001. doi: 10.1051/0004-6361:20000066.

S. Sulis, M. Lendl, H. M. Cegla, L. F. Rodríguez Díaz, L. Bigot, V. Van Grootel, A. Bekkelien, A. Collier Cameron, P. F. L. Maxted, A. E. Simon, C. Lovis, G. Scandariato, G. Bruno, D. Nardiello, A. Bonfanti, M. Fridlund, C. M. Persson, S. Salmon, S. G. Sousa, T. G. Wilson, A. Krenn, S. Hoyer, A. Santerne,

D. Ehrenreich, Y. Alibert, R. Alonso, G. Anglada, T. Bárczy, D. Barrado y Navascues, S. C. C. Barros, W. Baumjohann, M. Beck, T. Beck, W. Benz, N. Billot, X. Bonfils, L. Borsato, A. Brandeker, C. Broeg, J. Cabrera, S. Charnoz, C. Corral van Damme, Sz. Csizmadia, M. B. Davies, M. Deleuil, A. Deline, L. Delrez, O. D. S. Demangeon, B. O. Demory, A. Erikson, A. Fortier, L. Fossati, D. Gandolfi, M. Gillon, M. Güdel, K. Heng, K. G. Isaak, L. L. Kiss, J. Laskar, A. Lecavelier des Etangs, D. Magrin, M. Munari, V. Nascimbeni, G. Olofsson, R. Ottensamer, I. Pagano, E. Pallé, G. Peter, G. Piotto, D. Pollacco, D. Queloz, R. Ragazzoni, N. Rando, H. Rauer, I. Ribas, M. Rieder, N. C. Santos, D. Ségransan, A. M. S. Smith, M. Steinberger, M. Steller, Gy. M. Szabó, N. Thomas, S. Udry, N. A. Walton, and D. Wolter. Connecting photometric and spectroscopic granulation signals with CHEOPS and ESPRESSO. *A&A*, 670:A24, February 2023. doi: 10.1051/0004-6361/202244223.

Gy. M. Szabó and L. L. Kiss. A Short-period Censor of Sub-Jupiter Mass Exoplanets with Low Density. *ApJ*, 727(2):L44, February 2011. doi: 10.1088/2041-8205/727/2/L44.

Jean-Louis Tassoul. *Theory of rotating stars.* 1978.

M. B. Taylor. TOPCAT & STIL: Starlink Table/VOTable Processing Software. In P. Shopbell, M. Britton, and R. Ebert, editors, *Astronomical Data Analysis Software and Systems XIV*, volume 347 of *Astronomical Society of the Pacific Conference Series*, page 29, December 2005.

Alessandra Telleschi, Manuel Güdel, Kevin Briggs, Marc Audard, Jan-Uwe Ness, and Stephen L. Skinner. Coronal Evolution of the Sun in Time: High-Resolution X-Ray Spectroscopy of Solar Analogs with Different Ages. *ApJ*, 622(1):653–679, March 2005a. doi: 10.1086/428109.

Alessandra Telleschi, Manuel Güdel, Kevin Briggs, Marc Audard, Jan-Uwe Ness, and Stephen L. Skinner. Coronal Evolution of the Sun in Time: High-Resolution X-Ray Spectroscopy of Solar Analogs with Different Ages. *ApJ*, 622(1):653–679, March 2005b. doi: 10.1086/428109.

F. Tian and O. B. Toon. Atmospheric Escape from Planetary Atmospheres. In *AGU Fall Meeting Abstracts*, volume 2005, pages SA53B–1170, December 2005.

Benjamin M. Tofflemire, Aaron C. Rizzuto, Elisabeth R. Newton, Adam L. Kraus, Andrew W. Mann, Andrew Vanderburg, Tyler Nelson, Keith Hawkins, Mackenna L. Wood, George Zhou, Samuel N. Quinn, Steve B. Howell, Karen A. Collins, Richard P. Schwarz, Keivan G. Stassun, Luke G. Bouma, Zahra Essack, Hugh Osborn, Patricia T. Boyd, Gábor Fűrész, Ana Glidden, Joseph D. Twicken, Bill Wohler, Brian McLean, George R. Ricker, Roland Vanderspek, David W. Latham, S. Seager, Joshua N. Winn, and Jon M. Jenkins. TESS Hunt for Young and Maturing Exoplanets (THYME). V. A Sub-Neptune Transiting a Young Star in a Newly Discovered 250 Myr Association. *AJ*, 161(4):171, April 2021. doi: 10.3847/1538-3881/abdf53.

Lin Tu, Colin P. Johnstone, Manuel Güdel, and Helmut Lammer. The extreme ultraviolet and X-ray Sun in Time: High-energy evolutionary tracks of a solar-like star. *A&A*, 577:L3, May 2015. doi: 10.1051/0004-6361/201526146.

M. J. L. Turner, A. Abbey, M. Arnaud, M. Balasini, M. Barbera, E. Belsole, P. J. Bennie, J. P. Bernard, G. F. Bignami, M. Boer, U. Briel, I. Butler, C. Cara, C. Chabaud, R. Cole, A. Collura, M. Conte, A. Cros, M. Denby, P. Dhez, G. Di Coco, J. Dowson, P. Ferrando, S. Ghizzardi, F. Gianotti, C. V. Goodall, L. Gretton, R. G. Griffiths, O. Hainaut, J. F. Hochedez, A. D. Holland, E. Jourdain, E. Kendziorra, A. Lagostina, R. Laine, N. La Palombara, M. Lortholary, D. Lumb, P. Marty, S. Molendi, C. Pigot, E. Poindron, K. A. Pounds, J. N. Reeves, C. Reppin, R. Rothenflug, P. Salvetat, J. L. Sauvageot, D. Schmitt, S. Sembay, A. D. T. Short, J. Spragg, J. Stephen, L. Strüder, A. Tiengo, M. Trifoglio, J. Trümper, S. Vercellone, L. Vigroux, G. Villa, M. J. Ward, S. Whitehead, and E. Zonca. The European Photon Imaging Camera on XMM-Newton: The MOS cameras. *A&A*, 365:L27–L35, January 2001. doi: 10.1051/0004-6361:20000087.

A. Udalski, M. Szymanski, J. Kaluzny, M. Kubiak, and Mario Mateo. The Optical Gravitational Lensing Experiment. *Acta Astron.*, 42:253–284, October 1992.

G. S. Vaiana, J. P. Cassinelli, G. Fabbiano, R. Giacconi, L. Golub, P. Gorenstein, B. M. Haisch, Jr. Harnden, F. R., H. M. Johnson, J. L. Linsky, C. W. Maxson, R. Mewe, R. Rosner, F. Seward, K. Topka, and C. Zwaan. Results from an extensive Einstein stellar survey. *ApJ*, 245:163–182, April 1981. doi: 10.1086/158797.

V. Van Eylen, Camilla Agentoft, M. S. Lundkvist, H. Kjeldsen, J. E. Owen, B. J. Fulton, E. Petigura, and I. Snellen. An asteroseismic view of the radius valley:

stripped cores, not born rocky. *MNRAS*, 479(4):4786–4795, October 2018. doi: 10.1093/mnras/sty1783.

Jennifer L. van Saders and Marc H. Pinsonneault. Fast Star, Slow Star; Old Star, Young Star: Subgiant Rotation as a Population and Stellar Physics Diagnostic. *ApJ*, 776(2):67, October 2013. doi: 10.1088/0004-637X/776/2/67.

Julia Venturini, Octavio M. Guilera, Jonas Haldemann, María P. Ronco, and Christoph Mordasini. The nature of the radius valley. Hints from formation and evolution models. *A&A*, 643:L1, November 2020. doi: 10.1051/0004-6361/202039141.

A. Vidal-Madjar, A. Lecavelier des Etangs, J. M. Désert, G. E. Ballester, R. Ferlet, G. Hébrard, and M. Mayor. An extended upper atmosphere around the extrasolar planet HD209458b. *Nature*, 422(6928):143–146, March 2003. doi: 10.1038/nature01448.

A. Vidal-Madjar, J. M. Désert, A. Lecavelier des Etangs, G. Hébrard, G. E. Ballester, D. Ehrenreich, R. Ferlet, J. C. McConnell, M. Mayor, and C. D. Parkinson. Detection of Oxygen and Carbon in the Hydrodynamically Escaping Atmosphere of the Extrasolar Planet HD 209458b. *ApJ*, 604(1):L69–L72, March 2004. doi: 10.1086/383347.

A. A. Vidotto and A. Cleary. Stellar wind effects on the atmospheres of close-in giants: a possible reduction in escape instead of increased erosion. *MNRAS*, 494 (2):2417–2428, May 2020. doi: 10.1093/mnras/staa852.

O. Vilhu. The nature of magnetic activity in lower main sequence stars. *A&A*, 133:117–126, April 1984.

Osmi Vilhu and Frederick M. Walter. Chromospheric-Coronal Activity at Saturated Levels. *ApJ*, 321:958, October 1987. doi: 10.1086/165689.

Pauli Virtanen, Ralf Gommers, Travis E. Oliphant, Matt Haberland, Tyler Reddy, David Cournapeau, Evgeni Burovski, Pearu Peterson, Warren Weckesser, Jonathan Bright, Stéfan J. van der Walt, Matthew Brett, Joshua Wilson, K. Jarrod Millman, Nikolay Mayorov, Andrew R. J. Nelson, Eric Jones, Robert Kern, Eric Larson, C J Carey, İlhan Polat, Yu Feng, Eric W. Moore, Jake VanderPlas, Denis Laxalde, Josef Perktold, Robert Cimrman, Ian Henriksen, E. A. Quintero, Charles R. Harris, Anne M. Archibald, Antônio H. Ribeiro, Fabian Pedregosa, Paul van Mulbregt, and SciPy 1.0 Contributors. SciPy 1.0: Fundamental Algorithms for Scientific Computing in Python. *Nature Methods*, 17:261–272, 2020. doi: 10.1038/s41592-019-0686-2.

Shreyas Vissapragada, Heather A. Knutson, Michael Greklek-McKeon, Antonija Oklopčić, Fei Dai, Leonardo A. dos Santos, Nemanja Jovanovic, Dimitri Mawet, Maxwell A. Millar-Blanchaer, Kimberly Paragas, Jessica J. Spake, Samaporn Tinyanont, and Gautam Vasisht. The Upper Edge of the Neptune Desert Is Stable Against Photoevaporation. *AJ*, 164(6):234, December 2022. doi: 10.3847/1538-3881/ac92f2.

Shreyas Vissapragada, Patrick McCreery, Leonardo A. Dos Santos, Néstor Espinoza, Andrew McWilliam, Noriyuki Matsunaga, Jéa Adams Redai, Patrick Behr, Kevin France, Satoshi Hamano, Charlie Hull, Yuji Ikeda, Haruki Katoh, Hideyo Kawakita, Mercedes López-Morales, Kevin N. Ortiz Ceballos, Shogo Otsubo, Yuki Sarugaku, and Tomomi Takeuchi. A High-resolution Non-detection of Escaping Helium in the Ultrahot Neptune LTT 9779b: Evidence for Weakened Evaporation. *ApJ*, 962(1):L19, February 2024. doi: 10.3847/2041-8213/ad23cf.

S. S. Vogt, S. L. Allen, B. C. Bigelow, L. Bresee, B. Brown, T. Cantrall, A. Conrad, M. Couture, C. Delaney, H. W. Epps, D. Hilyard, D. F. Hilyard, E. Horn, N. Jern, D. Kanto, M. J. Keane, R. I. Kibrick, J. W. Lewis, J. Osborne, G. H. Pardeilhan, T. Pfister, T. Ricketts, L. B. Robinson, R. J. Stover, D. Tucker, J. Ward, and M. Z. Wei. HIRES: the high-resolution echelle spectrometer on the Keck 10-m Telescope. In David L. Crawford and Eric R. Craine, editors, *Instrumentation in Astronomy VIII*, volume 2198 of *Society of Photo-Optical Instrumentation Engineers (SPIE) Conference Series*, page 362, June 1994. doi: 10.1117/12.176725.

B. M. Walsh, K. D. Kuntz, M. R. Collier, D. G. Sibeck, S. L. Snowden, and N. E. Thomas. Energetic particle impact on X-ray imaging with XMM-Newton. *Space Weather*, 12(6):387–394, June 2014. doi: 10.1002/2014SW001046.

F. Walter, P. Charles, and S. Bowyer. X-ray emission from UX Arietis: RS Canum Venaticorum systems as a class of coronal X-ray sources. *ApJ*, 225:L119–L122, November 1978. doi: 10.1086/182807.

F. M. Walter. On the Coronae of rapidly rotating stars. III. an improved coronal rotation-activity relation in late type dwarfs. *ApJ*, 253:745–751, February 1982. doi: 10.1086/159675.

B. J. Wargelin, S. H. Saar, G. Pojmański, J. J. Drake, and V. L. Kashyap. Optical, UV, and X-ray evidence for a 7-yr stellar cycle in Proxima Centauri. *MNRAS*, 464(3):3281–3296, January 2017. doi: 10.1093/mnras/stw2570.

A. J. Watson, T. M. Donahue, and J. C. G. Walker. The dynamics of a rapidly escaping atmosphere: Applications to the evolution of Earth and Venus. *Icarus*, 48(2):150–166, November 1981. doi: 10.1016/0019-1035(81)90101-9.

N. A. Webb, M. Coriat, I. Traulsen, J. Ballet, C. Motch, F. J. Carrera, F. Koliopanos, J. Authier, I. de la Calle, M. T. Ceballos, E. Colomo, D. Chuard, M. Freyberg, T. Garcia, M. Kolehmainen, G. Lamer, D. Lin, P. Maggi, L. Michel, C. G. Page, M. J. Page, J. V. Perea-Calderon, F. X. Pineau, P. Rodriguez, S. R. Rosen, M. Santos Lleo, R. D. Saxton, A. Schwope, L. Tomás, M. G. Watson, and A. Zakardjian. The XMM-Newton serendipitous survey. IX. The fourth XMM-Newton serendipitous source catalogue. *A&A*, 641:A136, September 2020. doi: 10.1051/0004-6361/201937353.

Lauren M. Weiss, Geoffrey W. Marcy, Erik A. Petigura, Benjamin J. Fulton, Andrew W. Howard, Joshua N. Winn, Howard T. Isaacson, Timothy D. Morton, Lea A. Hirsch, Evan J. Sinukoff, Andrew Cumming, Leslie Hebb, and Phillip A. Cargile. The California-Kepler Survey. V. Peas in a Pod: Planets in a Kepler Multi-planet System Are Similar in Size and Regularly Spaced. *AJ*, 155(1):48, January 2018. doi: 10.3847/1538-3881/aa9ff6.

Lauren M. Weiss, Sarah C. Millholland, Erik A. Petigura, Fred C. Adams, Konstantin Batygin, Anthony M. Bloch, and Christoph Mordasini. Architectures of Compact Multi-planet Systems: Diversity and Uniformity. *arXiv e-prints*, art. arXiv:2203.10076, March 2022.

Martin C. Weisskopf, Harvey D. Tananbaum, Leon P. Van Speybroeck, and Stephen L. O'Dell. Chandra X-ray Observatory (CXO): overview. In Joachim E. Truemper and Bernd Aschenbach, editors, *X-Ray Optics, Instruments, and Missions III*, volume 4012 of *Society of Photo-Optical Instrumentation Engineers (SPIE) Conference Series*, pages 2–16, July 2000. doi: 10.1117/12.391545.

Richard G. West, Edward Gillen, Daniel Bayliss, Matthew R. Burleigh, Laetitia Delrez, Maximilian N. Günther, Simon T. Hodgkin, James A. G. Jackman, James S. Jenkins, George King, James McCormac, Louise D. Nielsen, Liam Raynard, Alexis M. S. Smith, Maritza Soto, Oliver Turner, Peter J. Wheatley, Yaseen Almleaky, David J. Armstrong, Claudia Belardi, François Bouchy, Joshua T. Briegal, Artem Burdanov, Juan Cabrera, Sarah L. Casewell, Alexander Chaushev, Bruno Chazelas, Paul Chote, Benjamin F. Cooke, Szilard Csizmadia, Elsa Ducrot, Philipp Eigmüller, Anders Erikson, Emma Foxell, Boris T. Gänsicke, Michaël Gillon, Michael R. Goad, Emmanuël Jehin, Gregory Lambert, Emma S. Longstaff, Tom Louden, Maximiliano Moyano, Catriona Murray, Don Pollacco, Didier Queloz, Heike Rauer, Sandrine Sohy, Samantha J. Thompson, Stéphane Udry, Simon R. Walker, and Christopher A. Watson. NGTS-4b: A sub-Neptune transiting in the desert. *MNRAS*, 486(4):5094–5103, July 2019. doi: 10.1093/mnras/stz1084.

Peter J. Wheatley, Richard G. West, Michael R. Goad, James S. Jenkins, Don L. Pollacco, Didier Queloz, Heike Rauer, Stéphane Udry, Christopher A. Watson, Bruno Chazelas, Philipp Eigmüller, Gregory Lambert, Ludovic Genolet, James McCormac, Simon Walker, David J. Armstrong, Daniel Bayliss, Joao Bento, François Bouchy, Matthew R. Burleigh, Juan Cabrera, Sarah L. Casewell, Alexander Chaushev, Paul Chote, Szilárd Csizmadia, Anders Erikson, Francesca Faedi, Emma Foxell, Boris T. Gänsicke, Edward Gillen, Andrew Grange, Maximilian N. Günther, Simon T. Hodgkin, James Jackman, Andrés Jordán, Tom Louden, Lionel Metrailler, Maximiliano Moyano, Louise D. Nielsen, Hugh P. Osborn, Katja Poppenhaeger, Roberto Raddi, Liam Raynard, Alexis M. S. Smith, Maritza Soto, and Ruth Titz-Weider. The Next Generation Transit Survey (NGTS). *MNRAS*, 475(4):4476–4493, April 2018. doi: 10.1093/mnras/stx2836.

J. Wilms, A. Allen, and R. McCray. On the Absorption of X-Rays in the Interstellar Medium. *ApJ*, 542(2):914–924, October 2000a. doi: 10.1086/317016.

J. Wilms, A. Allen, and R. McCray. On the Absorption of X-Rays in the Interstellar Medium. *ApJ*, 542(2):914–924, October 2000b. doi: 10.1086/317016.

Thomas G. Wilson, Elisa Goffo, Yann Alibert, Davide Gandolfi, Andrea Bonfanti, Carina M. Persson, Andrew Collier Cameron, Malcolm Fridlund, Luca Fossati, Judith Korth, Willy Benz, Adrien Deline, Hans-Gustav Florén, Pascal Guterman, Vardan Adibekyan, Matthew J. Hooton, Sergio Hoyer, Adrien Leleu, Alexander James Mustill, Sébastien Salmon, Sérgio G. Sousa, Olga Suarez, Lyu Abe, Abdelkrim Agabi, Roi Alonso, Guillem Anglada, Joel Asquier, Tamas

Bárczy, David Barrado Navascues, Susana C. C. Barros, Wolfgang Baumjohann, Mathias Beck, Thomas Beck, Nicolas Billot, Xavier Bonfils, Alexis Brandeker, Christopher Broeg, Edward M. Bryant, Matthew R. Burleigh, Marco Buttu, Juan Cabrera, Sébastien Charnoz, David R. Ciardi, Ryan Cloutier, William D. Cochran, Karen A. Collins, Knicole D. Colón, Nicolas Crouzet, Szilard Csizmadia, Melvyn B. Davies, Magali Deleuil, Laetitia Delrez, Olivier Demangeon, Brice-Olivier Demory, Diana Dragomir, Georgina Dransfield, David Ehrenreich, Anders Erikson, Andrea Fortier, Tianjun Gan, Samuel Gill, Michaël Gillon, Crystal L. Gnilka, Nolan Grieves, Sascha Grziwa, Manuel Güdel, Tristan Guillot, Jonas Haldemann, Kevin Heng, Keith Horne, Steve B. Howell, Kate G. Isaak, Jon M. Jenkins, Eric L. N. Jensen, Laszlo Kiss, Gaia Lacedelli, Kristine Lam, Jacques Laskar, David W. Latham, Alain Lecavelier des Etangs, Monika Lendl, Kathryn V. Lester, Alan M. Levine, John Livingston, Christophe Lovis, Rafael Luque, Demetrio Magrin, Wenceslas Marie-Sainte, Pierre F. L. Maxted, Andrew W. Mayo, Brian McLean, Marko Mecina, Djamel Mékarnia, Valerio Nascimbeni, Louise D. Nielsen, Göran Olofsson, Hugh P. Osborn, Hannah L. M. Osborne, Roland Ottensamer, Isabella Pagano, Enric Pallé, Gisbert Peter, Giampaolo Piotto, Don Pollacco, Didier Queloz, Roberto Ragazzoni, Nicola Rando, Heike Rauer, Seth Redfield, Ignasi Ribas, George R. Ricker, Martin Rieder, Nuno C. Santos, Gaetano Scandariato, François-Xavier Schmider, Richard P. Schwarz, Nicholas J. Scott, Sara Seager, Damien Ségransan, Luisa Maria Serrano, Attila E. Simon, Alexis M. S. Smith, Manfred Steller, Chris Stockdale, Gyula Szabó, Nicolas Thomas, Eric B. Ting, Amaury H. M. J. Triaud, Stéphane Udry, Vincent Van Eylen, Valérie Van Grootel, Roland K. Vanderspek, Valentina Viotto, Nicholas Walton, and Joshua N. Winn. A pair of sub-Neptunes transiting the bright K-dwarf TOI-1064 characterized with CHEOPS. *MNRAS*, 511(1):1043–1071, March 2022. doi: 10.1093/mnras/stab3799.

A. Wolszczan and D. A. Frail. A planetary system around the millisecond pulsar PSR1257 + 12. *Nature*, 355(6356):145–147, January 1992. doi: 10.1038/355145a0.

Hans Wolter. Spiegelsysteme streifenden Einfalls als abbildende Optiken für Röntgenstrahlen. *Annalen der Physik*, 445(1):94–114, January 1952. doi: 10.1002/andp.19524450108.

Brian E. Wood and Jeffrey L. Linsky. Resolving the ξ Boo Binary with Chandra, and Revealing the Spectral Type Dependence of the Coronal "FIP Effect". *ApJ*, 717(2):1279–1290, July 2010. doi: 10.1088/0004-637X/717/2/1279.

Brian E. Wood, J. Martin Laming, and Margarita Karovska. The Coronal Abundance Anomalies of M Dwarfs. *ApJ*, 753(1):76, July 2012. doi: 10.1088/0004-637X/753/1/76.

J. T. Wright, G. W. Marcy, A. W. Howard, John Asher Johnson, T. D. Morton, and D. A. Fischer. The Frequency of Hot Jupiters Orbiting nearby Solar-type Stars. *ApJ*, 753(2):160, July 2012. doi: 10.1088/0004-637X/753/2/160.

Nicholas J. Wright and Jeremy J. Drake. Solar-type dynamo behaviour in fully convective stars without a tachocline. *Nature*, 535(7613):526–528, July 2016. doi: 10.1038/nature18638.

Nicholas J. Wright, Jeremy J. Drake, Eric E. Mamajek, and Gregory W. Henry. The Stellar-activity-Rotation Relationship and the Evolution of Stellar Dynamos. *ApJ*, 743(1):48, December 2011. doi: 10.1088/0004-637X/743/1/48.

Nicholas J. Wright, Elisabeth R. Newton, Peter K. G. Williams, Jeremy J. Drake, and Rakesh K. Yadav. The stellar rotation-activity relationship in fully convective M dwarfs. *MNRAS*, 479(2):2351–2360, September 2018. doi: 10.1093/mnras/sty1670.

M. C. Wyatt, Q. Kral, and C. A. Sinclair. Susceptibility of planetary atmospheres to mass-loss and growth by planetesimal impacts: the impact shoreline. *MNRAS*, 491(1):782–802, January 2020. doi: 10.1093/mnras/stz3052.

Dongdong Yan, Jianheng Guo, Chenliang Huang, and Lei Xing. Atmosphere Escape Inferred from Modeling the Hα Transmission Spectrum of WASP-121b. *ApJ*, 907(2):L47, February 2021. doi: 10.3847/2041-8213/abda41.

Roger V. Yelle. Aeronomy of extra-solar giant planets at small orbital distances. *Icarus*, 170(1):167–179, July 2004. doi: 10.1016/j.icarus.2004.02.008.

N. Zacharias, C. T. Finch, T. M. Girard, A. Henden, J. L. Bartlett, D. G. Monet, and M. I. Zacharias. VizieR Online Data Catalog: UCAC4 Catalogue (Zacharias+, 2012). *VizieR Online Data Catalog*, art. I/322A, July 2012.

J. P. Zahn. Tidal friction in close binary systems. *A&A*, 57:383–394, May 1977.

Li Zeng, Stein B. Jacobsen, Dimitar D. Sasselov, Michail I. Petaev, Andrew Vanderburg, Mercedes Lopez-Morales, Juan Perez-Mercader, Thomas R. Mattsson, Gongjie Li, Matthew Z. Heising, Aldo S. Bonomo, Mario Damasso, Travis A. Berger, Hao Cao, Amit Levi, and Robin D. Wordsworth. Growth model interpretation of planet size distribution. *Proceedings of the National Academy of Science*, 116(20):9723–9728, May 2019. doi: 10.1073/pnas.1812905116.

Michael Zhang, Heather A. Knutson, Lile Wang, Fei Dai, Leonardo A. dos Santos, Luca Fossati, Gregory W. Henry, David Ehrenreich, Yann Alibert, Sergio Hoyer, Thomas G. Wilson, and Andrea Bonfanti. Detection of Ongoing Mass Loss from HD 63433c, a Young Mini-Neptune. *AJ*, 163(2):68, February 2022. doi: 10.3847/1538-3881/ac3f3b.

Michael Zhang, Heather A. Knutson, Fei Dai, Lile Wang, George R. Ricker, Richard P. Schwarz, Christopher Mann, and Karen Collins. Detection of Atmospheric Escape from Four Young Mini-Neptunes. *AJ*, 165(2):62, February 2023. doi: 10.3847/1538-3881/aca75b.